ABSTRACT

Title of dissertation: MEASUREMENT OF THE SURFACE AND UNDERGROUND FAST NEUTRON SPECTRA WITH THE UMD/NIST FAST NEUTRON SPECTROMETERS

Thomas J. Langford, Doctor of Philosophy, 2013

Dissertation directed by: Professor Elizabeth J. Beise
Department of Physics

The typical fast neutron detector falls into one of two categories, Bonner sphere spectrometers and liquid scintillator proton recoil detectors. These two detector types have traditionally been used to measure fast neutrons at the surface and in low background environments. The cosmogenic neutron spectrum and flux is an important parameter for a number of experimental efforts, including procurement of low background materials and the prediction of electronic device faults. Fast neutrons can also cause problems for underground low-background experiments, through material activation or signals that mimic rare events. Current detector technology is not sufficient to properly characterize these backgrounds.

To this end, the University of Maryland and the National Institute of Standards and Technology designed, developed, and deployed two Fast Neutron Spectrometers (FaNS) comprised of plastic scintillator and ^{3}He proportional counters. The detectors are based upon capture-gated spectroscopy, a technique that demands a delayed coincidence between a neutron scatter and the resulting neutron cap-

ture after thermalization. This technique provides both particle identification and knowledge that the detected neutron fully thermalized. This improves background rejection capabilities and energy resolution.

Presented are the design, development, and deployment of FaNS-1 and FaNS-2. Both detectors were characterized using standard fields at NIST, including calibrated ^{252}Cf neutron sources and two monoenergetic neutron generators. Measurements of the surface fast neutron spectrum and flux have been made with both detectors, which are compared with previous measurements by traditional detectors. Additionally, FaNS-1 was deployed at the Kimballton Underground Research Facility (KURF) in Ripplemead, VA. A measurement of the fast neutron spectrum and flux at KURF is presented as well. FaNS-2 is currently installed in a shallow underground laboratory where it is measuring the muon-induced neutron flux and spectrum.

Measurement of the Surface and Underground Neutron Spectra with the UMD/NIST Fast Neutron Spectrometers

by

Thomas J. Langford

Dissertation submitted to the Faculty of the Graduate School of the
University of Maryland, College Park in partial fulfillment
of the requirements for the degree of
Doctor of Philosophy
2013

Advisory Committee:
Professor Elizabeth J. Beise, Chair/Advisor
Professor Thomas D. Cohen
Professor Michael A. Coplan
Professor Carter Hall
Dr. Jeffrey S. Nico

Dedication

To my wife.
Without whom,
I never would have made it.

Acknowledgments

There are an innumerable number of people who have helped and supported me throughout grad school. I am indebted to each and every one of them. First and foremost, I want to thank my trio of advisors: Betsy, Herbert, and Jeff. Betsy, thank you for convincing me to come back to nuclear physics, I am grateful every day. Herbert, thank you for instilling so many important experimental techniques and a slight packrat mentality for equipment. Jeff, thank you for your ample help with analysis, but more for your support when I transitioned to working at NIST. I would never have made it without you all!

My time at UMD has been greatly enhanced by some truly fabulous people, starting with the staff who make the world go 'round: Judy for doing purchases at 3:55 on a Friday; Linda for always having candy and a kind word; and Lorraine, Paulina, and Jane for being able to work magic.

Many thanks are owed to my fellow grad students that I have had the privilege to work with. To Chris and Robert and the house on the corner with all the Swagger; to Brian for taking afternoon tea when things were not working; to Liz for our numerous Chipotle trips; and to Evan for fantastic puns and riddles that made that difficult times much easier; thank you all. When all the ENP people were away, TQHN took me in and deigned to let an experimentalist eat lunch with them, which always lead to interesting discussions, and some fools errands. Thanks to Kyle, Dave, and the other coolUMD2008 list for always providing something

interesting/funny/bizarre to distract me when I needed it. Thanks to the Grass Clowns for the many games of soccer that helped to keep me sane.

I also want to thank my fellow ENP members: Attila, Simon, Ruey, Clayton, Colleen, Doug, and Lisa. When you haven't been at WIPP or Homestake, it's been great to work with you! Attila, you and I have seen that lab transform from storage space to bustling lab, it's a good thing we don't have to move it! To my undergraduate help: Dylan, Geoffrey, and Anna, thank you for doing some of the work I really didn't want to do. To my co-KURF-ites: Graham, Paddy, and Derek, thanks for helping us operate FaNS-1 from afar; I promise the result is coming soon!

I have had an equal privilege of working full time at NIST for the past few years. I would especially like to thank Chris and Craig for many discussions on FaNS, Pieter for your many distractions, Alan for always being up for espresso, and the Astoria espresso machine which has helped many times when nothing else would!

Thanks to Marco and the other people at CAEN who helped us find solutions for our desired DAQ. I am very grateful for your continued support and help; FaNS-2 would never have happened without it. You were the best hosts when I visited Viareggio, and I hope I can repay the favor some day.

My family has been incredibly supportive through all stages of my career, but especially grad school. Thanks to my sister Nattie for talking me through difficult stages and helping me keep everything in perspective. To my sisters-in-law Alexis, Marisa, and Zabrina, thank you for all your encouragement and support. Thanks so much to Jenna for random text messages of excitement and inspiration, and for being the best house guest ever. Thanks to my mom for teaching me to never be

afraid of school and to love learning. Finally, there are not enough words to express my thanks to my wife, Lauren. I am more lucky and blessed to have you every day. I could never have done this without you.

Table of Contents

List of Tables

List of Figures

Chapter 1

Introduction

The UMD/NIST collaboration has designed, built, and characterized two fast neutron spectrometers (FaNS-1 and FaNS-2) based on the concept of capture-gated spectroscopy. The FaNS detectors are arrays of plastic scintillator and ^{3}He proportional counters. The high efficiency, large dynamic range detectors have been deployed in a variety of locations measuring neutrons from sources and the environment. This thesis will discuss the FaNS detectors and present measurements of the surface and underground fast neutron spectra.

This chapter contains a brief overview of fast neutrons as they relate to underground particle and nuclear physics. It will begin with a discussion of the origin of fast neutrons and the energies typically found for each source. Following that is an overview of the impact of fast neutrons on underground physics experiments. Current standard detection techniques are presented, focusing on moderated ^{3}He proportional counters and liquid scintillator proton recoil detectors. Finally, capture-gated spectroscopy will be discussed, including how the FaNS detectors utilize this technique to improve upon previous measurements.

1.1 Fast neutrons and their origins

Neutrons are classified by their energies into three main classes: thermal neutrons, cold/ultra cold neutrons, and fast neutrons. Thermal neutrons are those which have equilibrated in a room temperature environment and have a Boltzman energy distribution peaked around 25 meV. Cold neutrons, with energies between 1 and 5 meV, are produced by moderating higher energy neutrons in cryogenic targets such as liquid hydrogen or deuterium ice. These neutrons are useful for a wide range of experimental efforts, including neutron interferometry, precision measurements of the neutron lifetime, and many others [1–6]. Finally, neutrons can be cooled even further through the use of down-scattering in superfluid helium or using a gravitational trap [7]. This produces ultra cold neutrons that can be stored in a bottle for high-sensitivity measurements, like the neutron electric dipole moment or lifetime [8, 9]. Fast neutrons have energies much higher than cold or thermal neutrons. Typically, they are classified as having energies greater than 100 keV. These neutrons are generated by a few distinct sources, in order of increasing energies: 1) spontaneous fission, 2) radioisotope production and (α, n), 3) fusion of light nuclei, 4) cosmic-ray induced spallation, and 5) muon-induced reactions. Each of these will be discussed as they pertain to the FaNS detectors.

1.1.1 Spontaneous fission of heavy nuclei

Spontaneous fission is a process in which a nucleus, without external intervention, breaks apart into many fragments. These fission events can emit multiple

neutrons along with gammas and lighter nuclei. Though rare, spontaneous fission isotopes can be found in the decay chains of uranium and thorium. The neutron energy spectra from these isotopes are normally characterized by a Watt or Maxwellian parameterization, which are peaked at ∼1 MeV and have a roughly $1/E$ shape of the high energy tail.

The most common spontaneous fission neutron source is ^{252}Cf, which is commonly used to calibrate detectors and irradiate samples for other analysis. The ^{252}Cf spectrum from the ENDF-VII set of standards is shown in Figure 1.1 [10].

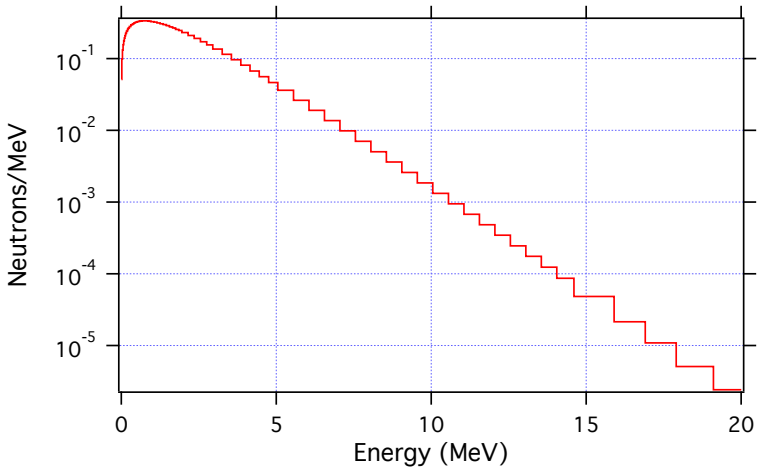

Figure 1.1: The ENDF-VII parameterization of the ^{252}Cf spontaneous fission neutron spectrum [10].

Though the spectrum extends to ∼20 MeV, the majority of neutrons are at lower energies, with a mean energy of ∼2 MeV. Each ^{252}Cf spontaneous fission results in an average of 3.7 neutrons and ∼20 gammas (80% of which have energies below 1 MeV). There is no preferred direction of the reaction, so the particles are emitted isotropically [11]. ^{252}Cf has a particularly large neutron yield of 2.3×10^6 $n/s/\mu g$, therefore high activity sources may be made in small quantities [12]. Unlike other

spontaneous fission sources, ^{252}Cf has a short half-life of 2.65 years. This makes maintaining a high activity source difficult, as the activity is reduced by an order of magnitude every decade.

1.1.2 Radioisotope (α,n) reactions

Another method of generating fast neutrons is through (α,n) reactions [13], an example of which is shown here:

$$ {}^{4}_{2}\alpha \; + \; {}^{9}_{4}Be \; \rightarrow \; {}^{12}_{6}C \; + \; {}^{1}_{0}n \; (+5.71 \; MeV). \tag{1.1} $$

An energetic alpha is captured by a Be nucleus, which then emits an energetic neutron. Typically $\mathcal{O}(10^{-4})$ neutrons are emitted for every alpha decay, though the reaction probability increases with incident alpha energy [12].

These reactions occur naturally in material that contains trace amounts of uranium and thorium. The decay chains of these two elements emit numerous alpha particles, which can then interact with light nuclei in the surrounding material. These are the most common neutrons found in underground environments where low background experiments operate. An attempt to systematically characterize the various (α, n) spectra for underground environments has been made in Reference [14].[1]

[1]The authors of that work have also published a website that will produce rough neutron spectra from uranium and thorium decay chains in different isotopic mixtures [15]. The calculations make the assumption that the decay chains are in isotopic equilibrium, which is not always accurate.

A compact neutron source based upon (α, n) reactions may be made by mixing an alpha emitting isotope, like ^{241}Am, with a light target nucleus, like beryllium. The neutron energy spectrum of an Am-Be source is shown in Figure 1.2. These source have much longer half-lives than ^{252}Cf(^{241}Am has a half-life of 432 years), and will therefore be much more stable in their activities.

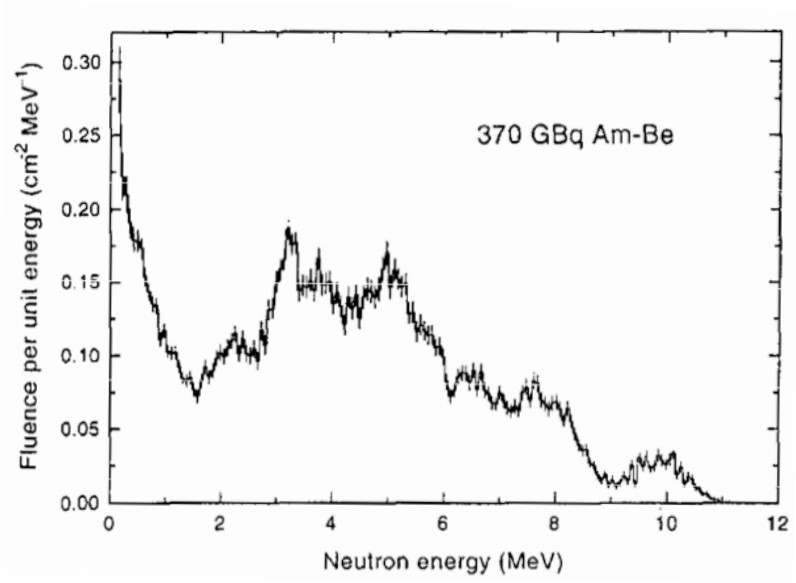

Figure 1.2: The measured spectrum of emitted neutrons from an Am-Be (α, n) neutron source. Figure from Reference [16].

The neutron energy spectrum is harder than that of the spontaneous fission sources and contains multiple peaks. This makes (α, n) sources attractive for testing neutron detectors, because they have features that can demonstrate detector resolution.

However, the production rate and resulting neutron energy are dependent on the energy of the alpha. The spectra of these sources can therefore vary greatly. In particular, it has been shown that the packing of the alpha emitter and absorber

isotopes inside a source container may change the output spectrum [12]. Thus, without an energy resolving detector, knowing the absolute spectrum of emitted neutrons is difficult.

The energy spectrum variability creates difficulties in estimating the neutron spectrum from (α, n) reactions underground. It is not normally possible to know the exact distribution of the alpha emitting isotopes in the local material, and so simulating the spectrum is exceptionally challenging.

1.1.3 Fusion of light nuclei

It is also possible to generate neutrons through the fusion of light nuclei. For example, by fusing different isotopes of hydrogen, it is possible to generate neutrons with energies from a few MeV (deuterium-deuterium fusion) up to 14 MeV (deuterium-tritium fusion):

$$ {}^{2}_{1}H \ + \ {}^{2}_{1}H \rightarrow \ {}^{3}_{2}He \ + \ {}^{1}_{0}n + 3.26 \text{ MeV}, \tag{1.2} $$

$$ {}^{2}_{1}H \ + \ {}^{3}_{1}H \rightarrow \ {}^{4}_{2}He \ + \ {}^{1}_{0}n + 17.6 \text{ MeV}. \tag{1.3} $$

In the final states of these two reactions, the neutron receives 2.45 MeV and 14.1 MeV, respectively, via kinematics. These reactions require enough energy to overcome the Coulomb barrier, which is typically a few keV. By accelerating deuterium into tritium or deuterium nuclei, it is possible to induce fusion in a laboratory.

Currently, there are a number of manufacturers of compact neutron generators based on small accelerators with deuterium and tritium gas [17–19]. These gener-

ators produce between 10^8 and 10^{10} n/s, and have typical operational lifetimes of 2000 hours.

Both the DD and DT fusion reactions produce mono-energetic neutrons that can be used to characterize and calibrate detectors. These generators will be discussed in more detail when the calibrations of the FaNS detectors are presented later.

1.1.4 Spallation of nuclei from high energy cosmic rays

The highest energy neutrons are produced from spallation by high energy particles. This occurs naturally from high energy cosmic rays interacting in the atmosphere and high energy muons interacting underground.

When energetic cosmic rays are incident on the upper atmosphere, they rapidly lose their energy through collisions with the molecules in the air. As seen in Figure 1.3a, the initial energies of these particles can exceed 10^5 GeV.

These collisions trigger air-showers that can exceed hundreds of meters in diameter when they reach sea-level. While propagating down, various particles are created, including protons, neutrons, electrons, gammas, pions, kaons, and muons. These secondary particles are the source of much of the ambient radioactivity at the surface. Figure 1.3b shows the simulated fluxes of various particles generated in the showers. The simulation is based on the CRY Cosmic Ray Generator [20].

Neutrons produced in cosmic ray showers have energies that extend from thermal to beyond 10 GeV. Their energies are determined by the incident cosmic ray

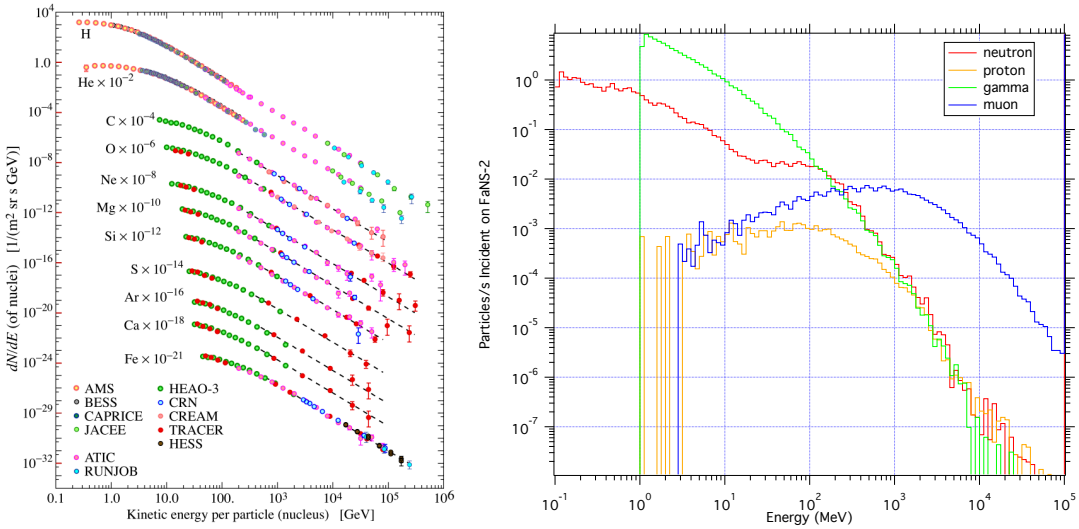

Figure 1.3: Left: The fluxes of the primary cosmic radiation in terms of energy per nucleus. Figure from Reference [11]. Right: The fluxes of neutrons, protons, muons, and gamma rays generated by cosmic rays in the atmosphere. These data were generated with the CRY Cosmic Ray Generator simulation.

that created the shower and the various energy loss mechanisms that the neutron encounters as it travels down to sea-level. There are two main energy regions of the cosmogenic fast neutron spectrum: the "evaporation" peak centered around 1 MeV, and the "cascade" peak centered around 100 MeV. The evaporation peak is composed of neutrons that have been emitted by the de-excitation of nuclei in the atmosphere. The cascade peak is populated by neutrons that are knocked out of nuclei by high momentum transfer interactions [21, 22].

There have been many measurements of the cosmic-ray induced neutron spectrum, but these have mainly been performed with passively moderated ^{3}He counters, known as Bonner spheres [23–27]. These detectors lack energy resolution and rely on complicated unfolding procedures, as will be discussed in more detail in Section 1.3.1. There is considerable spread in the measured flux and spectrum from

these data, related to various environmental considerations, including weather, barometric pressure, geomagnetic cutoff, and solar cycle. Figure 1.4 shows the neutron spectrum recorded with the same detectors for three different days with varying conditions. There is a wide fluctuation between the three measurements, with almost a factor of two in total flux among them.

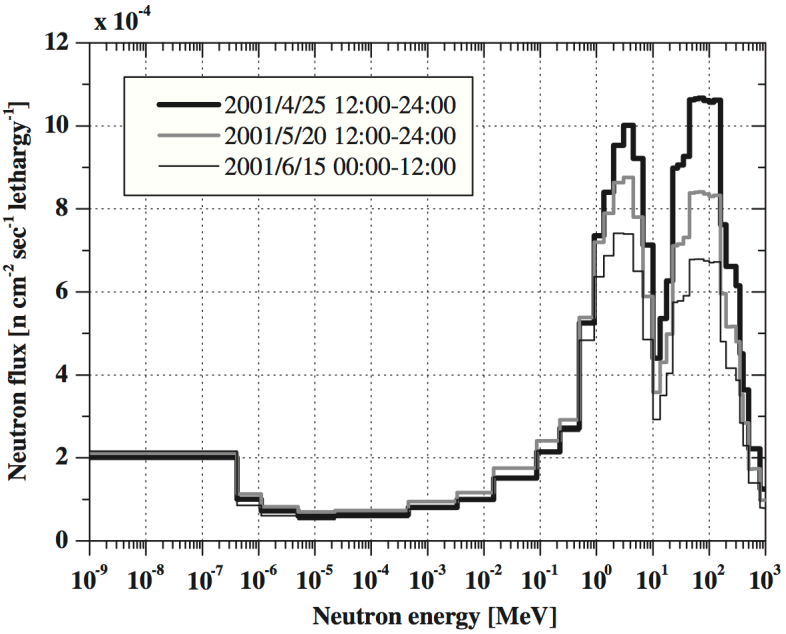

Figure 1.4: The recorded neutron energy spectra (in units of $E \times d\phi/dE$) at a single location using the same Bonner sphere array on three different dates. Significantly different neutron fluxes are observed. Figure from Reference [24].

There have been a few measurements of the surface fast neutron spectrum with different detector types, including phoswich[2] neutron detectors [28, 29], liquid scintillator [30], and double scatter neutron telescopes [31, 32]. Each measurement provides slightly different insight to the cosmic-ray induced neutron spectrum. In Reference [30], a large Gd-doped liquid scintillator volume was placed at ground level

[2] "Phoswich" is a portmanteau of "phosphor" and "sandwich". These detectors are made of two scintillator materials with different pulse shape characteristics. This allows for particle ID to separate neutron interactions from gammas.

outside of Gran Sasso National Laboratory. The detectors were at approximately 42°25′11″ N, 13°31′2″ E, rigidity cutoff 6.3 GV, and altitude 970 m above sea level.[3] Figure 1.5 shows their reported neutron energy spectrum.

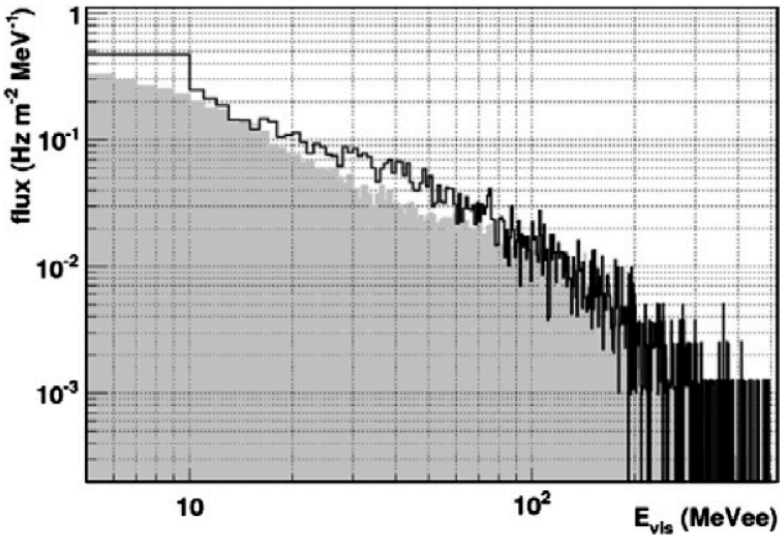

Figure 1.5: The recorded neutron energy spectrum from a large Gd-doped liquid scintillator detector at ground level at Gran Sasso National Laboratory. Figure from Reference [30].

They were able to make a measurement of the total flux above two thresholds, 10 and 20 MeV:

$$\Phi(E > 10\ MeV) = (4.7 \pm 0.5) \times 10^{-3}\ n/cm^2/s, \tag{1.4}$$

$$\Phi(E > 20\ MeV) = (4.2 \pm 0.4) \times 10^{-3}\ n/cm^2/s. \tag{1.5}$$

[3]The cosmic ray flux depends upon the location within the earth's magnetic field, which is not aligned with the usual longitude and latitude. Thus, it is useful to include the rigidity cutoff, which is a measure of the energy required for cosmic rays to penetrate the magnetosphere [33].

This is the first capture-gated measurement of the cosmic-ray induced fast neutron spectrum and flux. This measurement will be compared to the FaNS measurements in later chapters.

The azimuthal dependence of the neutron spectrum, for 80 MeV $< E_n <$ 300 MeV, has been shown to be proportional to $\cos^m\theta$ with $m = 3.5 \pm 1.2$ and θ oriented at the zenith [34]. Figure 1.6 shows this distribution, with the shaded region showing the uncertainty.

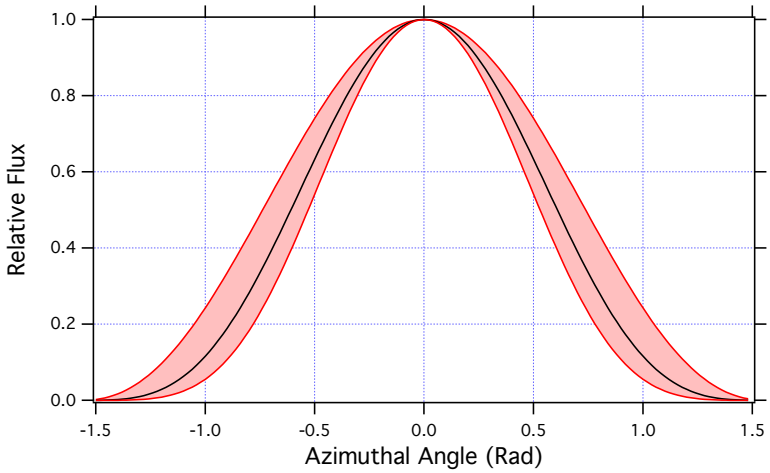

Figure 1.6: The azimuthal dependence ($\cos^m\theta$ with $m = 3.5 \pm 1.2$) of the cosmogenic neutron flux as reported in Reference [34]. The shaded region highlights the uncertainty.

The angular distribution of lower energy neutrons is expected to be highly dependent on the local environment. A recent measurement has shown that the angular distribution for neutrons between 1 and 10 MeV also follows a $\cos^m$ shape. However, statistics have limited their ability to quantify the power of the distribution [31].

1.1.5 Muon-induced interactions

Muons created by cosmic rays are deeply penetrating and are one of the largest backgrounds for underground experiments. Muons may interact directly in a detector, or induce radioactivity as it interacts with the local material. Muon-induced neutrons are generated by either spallation, like the cosmic-ray interactions previously discussed, or through negative-muon capture. The Feynman diagram for muon spallation is shown in Figure 1.7.

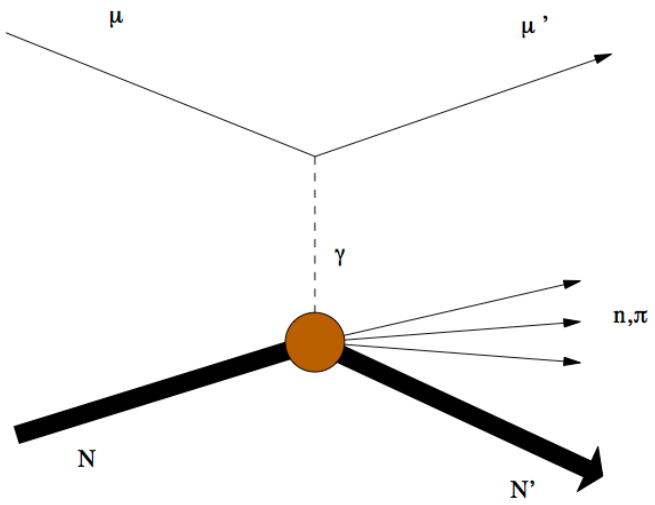

Figure 1.7: The Feynman diagram of neutron production via muon spallation. Here an energetic muon exchanges a virtual photon with a nucleus, which then de-excites via neutron emission. Figure from Reference [35].

The rate of muon-induced neutron production is suppressed at underground locations due to the attenuation of the muon flux passing through the earth. Figure 1.8 shows the muon and muon-induced neutron fluxes at various underground laboratories.

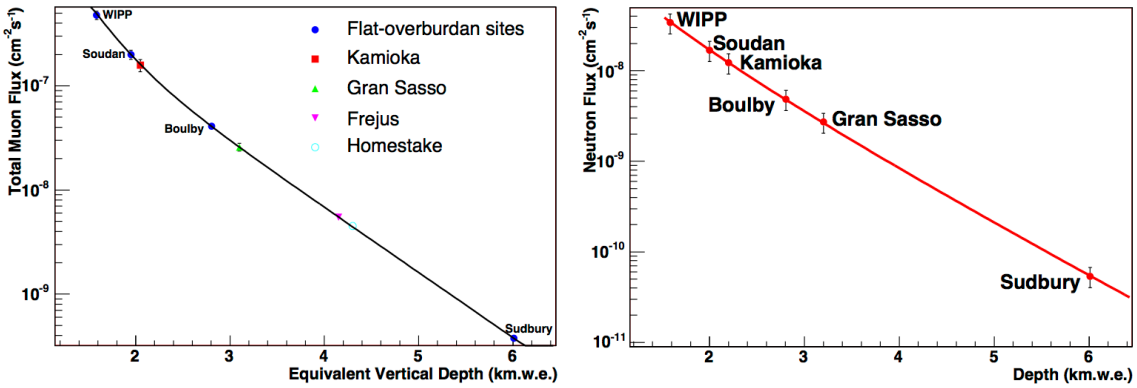

Figure 1.8: Left: Measured muon fluxes at various underground sites. Right: The deduced neutron fluxes for various underground laboratories. Figures from Reference [36].

Reference [36] includes a parameterization of the muon-induced neutron flux as a function of overburden depth, shown in Equation 1.6.

$$\Phi(n) = P_0 \left(\frac{P_1}{h_0}\right) e^{-h_0/P_1} \tag{1.6}$$

P_0 and P_1 are fit parameters and h_0 is the equivalent vertical depth (in km.w.e). They found fit values of $P_0 = (4.0 \pm 1.1) \times 10^{-7}/\text{cm}^2/\text{s}$ and $P_1 = 0.86 \pm 0.05$ km.w.e. This parameterization will be used later to estimate the expected flux of muon-induced neutrons at the Kimballton Underground Research Facility.

The energies of the muon induced neutrons extend to beyond 1 GeV, as shown in Figure 1.14. The data in this figure are generated using a FLUKA simulation of input muons interacting in the rock walls of the laboratories. A detailed theoretical treatment of muon spallation may be found in Reference [35].

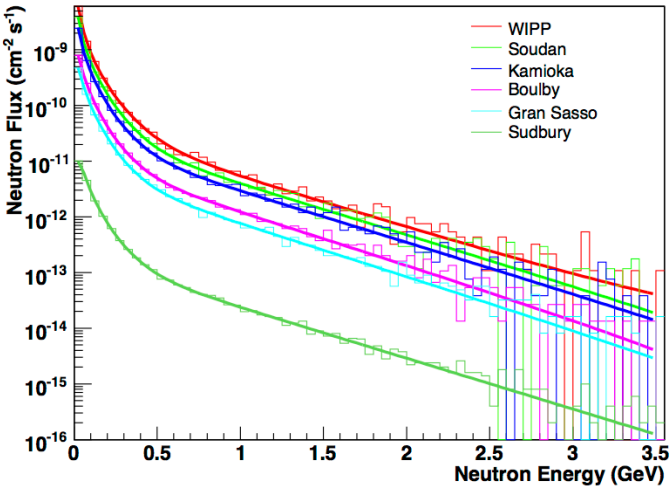

Figure 1.9: The calculated differential neutron energy spectra for different underground laboratories. Figure from Reference [36].

At lower muon energies, there is a finite probability that the muon will be stopped completely and capture on a nearby nucleus. The resulting nucleus is excited in the range of 10 - 20 MeV, which is enough energy to emit one or more neutrons [37]. The emitted neutrons may carry up to the kinematic limit of 100 MeV, though the most probable energy is around 1 MeV. This process is largest in heavy nuclei, which have a larger probability to capture muons. However, even in the lighter nucleus ^{12}C, neutron production via muon capture has been observed [38]. Figure 1.10 shows the detected energy spectrum of neutrons produced from a muon beam incident on a carbon target.

At shallower depths, where the average muon energy is comparatively low, neutron production by stopped muons may be the dominant source. These neutrons can be produced in the detector and shielding material directly, making a complicated optimization problem for shallow underground experiments. Better

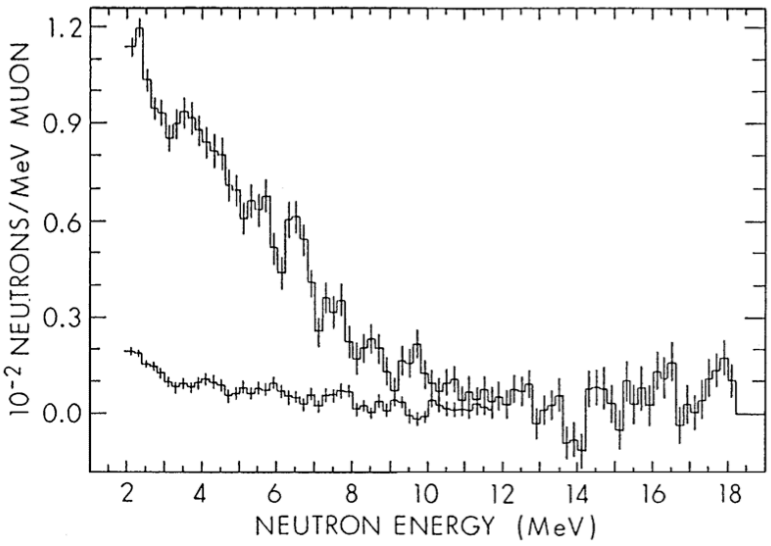

Figure 1.10: The detected energy spectrum of neutrons produced by muon capture on a carbon target. The spectrum of background neutrons is shown in the lower curve. Figure from References [38].

knowledge of the production cross-sections for these interactions would improve the ability to estimate these backgrounds.

1.2 Physics motivation

While there are a variety of uses for a fast neutron detector, this section will focus on only three of them. This section will cover three areas of research where a high sensitivity, high efficiency fast neutron spectrometer would be useful. First, the cosmic-ray induced fast neutron spectrum at sea-level will be discussed, followed by a discussion of the muon-induced and radioactive neutron backgrounds in shallow and deep underground environments. Finally, there is a discussion of neutron spectroscopy and dosimetry, which are of particular interest for the National Institute for Standards and Technology.

1.2.1 Fast neutron activation of low background material at sea-level

The fast neutron background at the surface can cause a variety of problems for low background experiments. The largest concern is neutron activation of detectors and shielding material. Low background experiments go to great lengths to procure and produce materials with low levels of radioactivity [39–41]. The materials are then stored underground to prevent activation from high energy cosmic rays.[4]

Fast neutrons are a major source of activation of common shielding materials, such as copper and lead [43], and detector materials such as germanium [44]. The isotopes produced have long half-lives and frequently emit radiation in the signal region for various experiments. Germanium in particular has a neutron-induced peak (from the $^{76}\mathrm{Ge}(\mathrm{n},\mathrm{n}'\gamma)$ interaction) only 15 keV below the expected Q-value for neutrinoless double beta decay. Figure 1.11 shows the production cross-sections for ^{68}Ge and ^{60}Co in germanium as functions of the incident fast neutron energies.

Many of these materials must still be transported above ground or even by plane. Any time spent at sea-level or at airplane altitude must be accounted for and the activation of the material calculated and included in the Monte Carlo of the full experiment.

To calculate the cumulative activation by cosmogenic neutrons, a precise knowledge of the fast neutron spectrum between 1 MeV and 1 GeV is required. Figure 1.12

[4] A database of materials assay results has been published online [42]. The database contains results of approximately 350 assays of common materials available for general use.

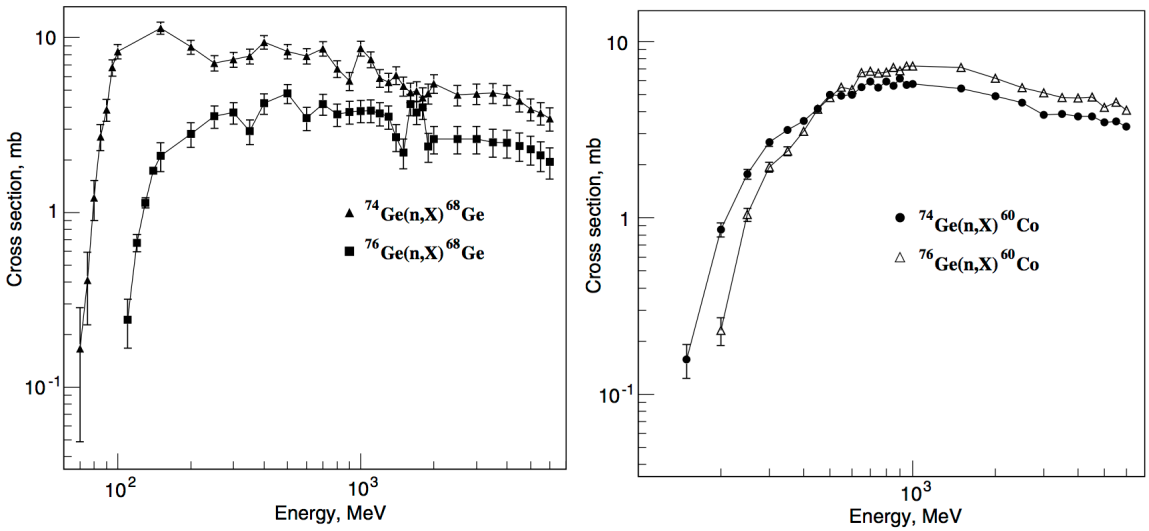

Figure 1.11: The production cross-sections for two radioactive isotopes (Left: ^{68}Ge, Right: ^{60}Co) from fast neutron interactions in germanium. Figures from Reference [44].

shows a comparison between three cosmogenic neutron spectra reported by different papers.[5]

The spectra are different in both shape and in absolute flux. These differences can lead to significant variations between calculations of activation. Reference [46] includes a systematic study of the neutron activation of germanium for multiple cosmic ray neutron energy spectra. The authors observed more than an order of magnitude difference in activation rates of enriched germanium. Better knowledge of the fast neutron spectrum would greatly improve their ability to design and optimize shielding at sea-level.

[5]The neutron spectrum is roughly 1/E in shape and covers many orders of magnitude. Thus, it is often more illustrative to show the spectrum in units of $E \times d\phi/dE$, which highlights the details of the spectrum.

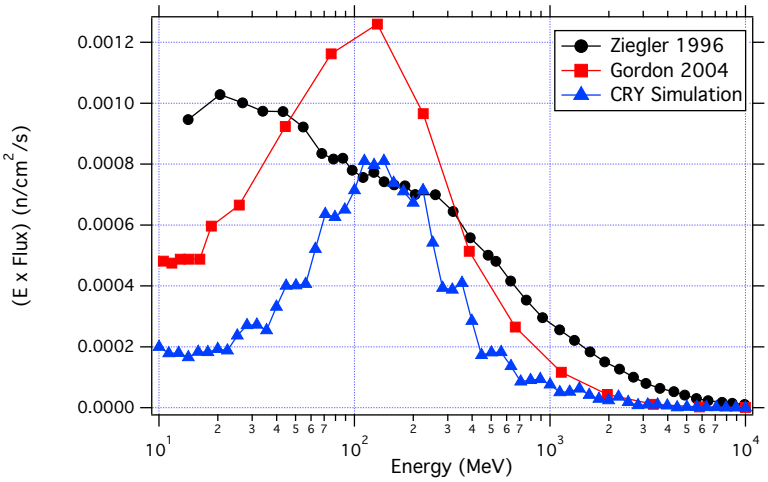

Figure 1.12: A comparison between three different reported cosmogenic neutron spectra. Ziegler [45] and Gordon [23] are measurements with Bonner spheres, and CRY is a Monte Carlo Simulation [20].

1.2.2 Fast neutrons from muon interactions and local radioactivity underground

Fast neutrons are a particular problem for rare event experiments operating underground. Fast neutrons can mimic signatures of these rare events, often with significantly higher frequency than the desired event. As an example, the effect of fast neutron backgrounds on WIMP dark matter searches will be discussed here.

Weakly interacting massive particles (WIMPs) are the leading theoretical explanation of gravitational anomalies observed over the past half century. The rotation curves of galaxies show evidence of non-visible matter that increases the rotational speeds at large radii. Using the required relic density to account for these anomalies, one finds that the interaction cross sections are on the order of the weak nuclear force [47, 48].

Due to their weak nature, WIMPs are proposed to interact via nuclear recoils. This gives WIMP dark matter searches a powerful tool for discriminating between background signals and potential WIMP signals. Many detectors are able to separate the two recoil types by measuring multiple modes of energy transfer: light, heat, or ionization. Electronic recoils, from gammas and electrons, deposit energy in different ratios of these quantities than nuclear recoils. By detecting at least two of these quantities for each event, it is possible to effectively distinguish between electron and nuclear recoils. Figure 1.13 shows the discrimination power for the Xenon10 experiment, which detects the light and ionization from each event.

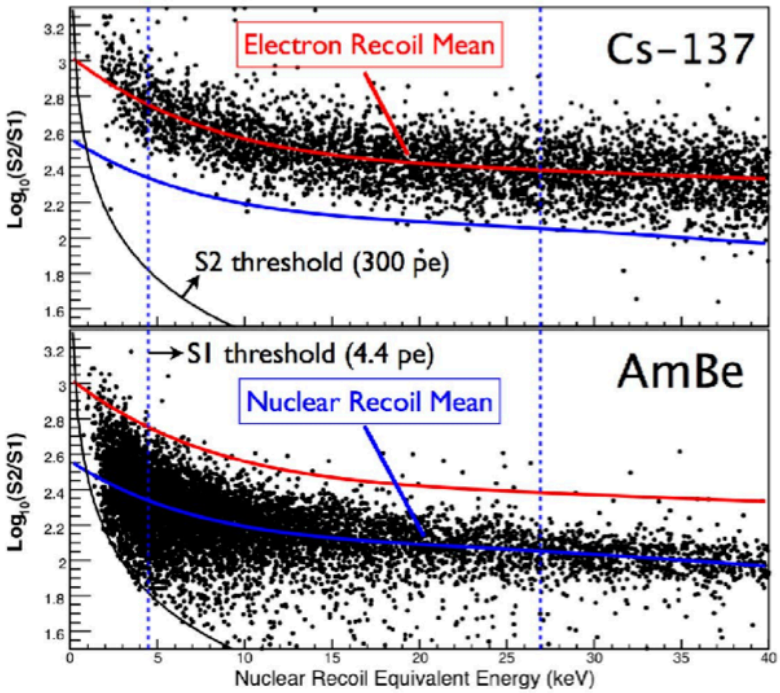

Figure 1.13: The discrimination between electronic and nuclear recoils from the Xenon10 experiment based on the ratio of the amount of light and ionization produced for each event. Nuclear recoil events are generated from an Am-Be neutron source, while the electronic recoils are from a ^{137}Cs gamma source. Note the separation between the mean of the two bands [49].

Because the most common background in the underground environments in which these experiments operate is due to electronic recoils, this technique is exceptionally powerful. However, fast neutrons will not be rejected by this technique, since they too interact via nuclear recoils. Thus it is vitally important to know the fast neutron background in the lab so that it can be shielded against [50–58]. Fast neutrons in underground labs typically are produced from two main sources. Naturally occurring radioactive isotopes in the local environment, like uranium and thorium, have neutron emitting isotopes in their decay chains. Separately, decay alphas may interact with light nuclei to produce (α,n) neutrons. These neutrons range from 1 MeV to 15 MeV, with the (α,n) neutrons having a harder spectrum. Figure 1.14 shows the relative fast neutron spectra from (α,n) and muon interactions with and without shielding from Reference [36]. The shielding design used in this work featured an inner layer of 10 cm of copper, followed by 40 cm of lead, and finally 10 cm of polyethylene.

The low energy neutrons from (α, n) reactions are effectively shielded, but the muon-induced neutron spectrum is relatively unchanged above 20 MeV. The total muon flux is reduced substantially by operating in an underground environment, as shown previously in Figure 1.8. However, increasing the shielding material can also increase the neutron production from muons. This can be seen in the increase from the red circles (μ: Rock/Cavern Boundary) to the blue crosses (μ:After Lead + Copper Shielding). The muon-induced neutron yield for specific materials should be taken into consideration when designing a shield.

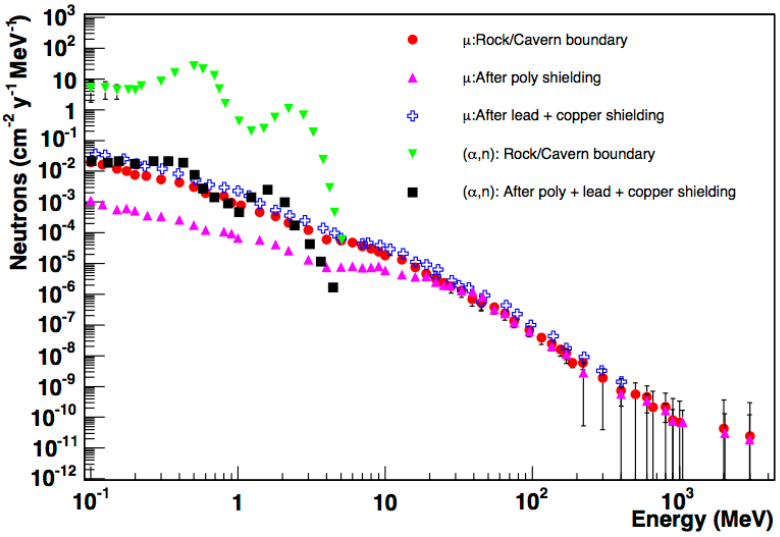

Figure 1.14: A comparison between simulated fast neutron spectra from muon and (α,n) interactions with and without shielding materials. Figure from Reference [36].

Many experiments have worked to measure the muon-induced neutron yield in rock, scintillator and lead in underground environments [51, 52, 57, 59–62]. These measurements have typically been side projects of larger experiments using the neutron shield as a detector. However, these experiments have focused on measuring the muon-induced neutron yield and not the energy spectrum of the produced neutrons. Therefore, much uncertainty remains about the muon-induced neutron energy spectrum.

To systematically study the muon induced neutron yield from common shielding materials in a controlled environment, the NA55 experiment was performed at CERN using a mono-energetic 190 GeV muon beam incident on different targets [63]. Three liquid scintillator detectors were positioned at different angles (45°, 90°, and 135°) and the count rates in each detector were recorded. Figure 1.15 shows the measured neutron yield (solid points) for lead (solid triangles), copper

(solid squares), and carbon (solid circles). The histograms are from simulations performed with two different models of high energy physical processes[6] [64].

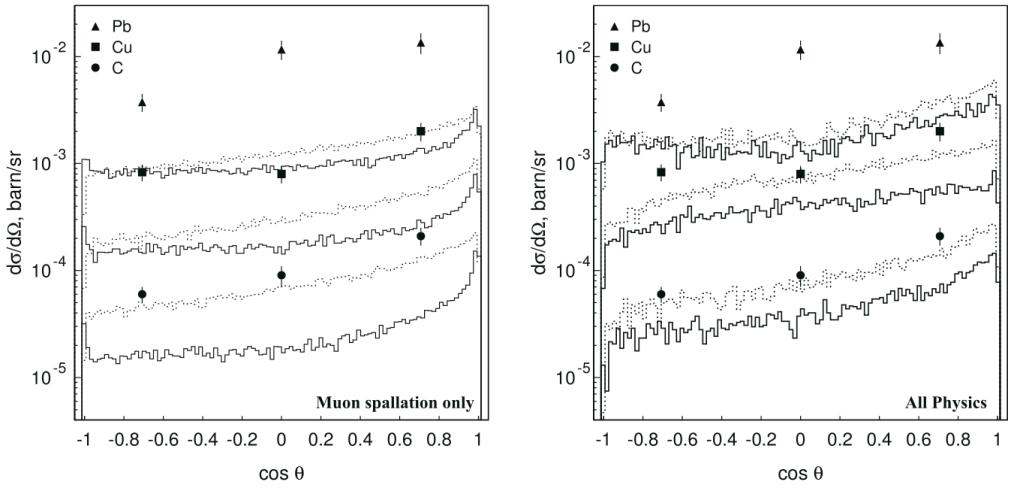

Figure 1.15: Differential neutron production cross sections as measured with mono-energetic muons at CERN in the NA55 experiment (solid points) and simulated with Geant4 using two different physics lists (solid and dashed lines). Left shows the simulated response for each target when only muon spallation physics is included, while Right shows the effect on the simulated responses when an improved physics model is used. The simulation data, from top to bottom, are for Pb, Cu, and C. Note the large discrepancy that remains for neutron yield in lead. This change highlights the uncertainties in simulations even for a simple geometry. Figures from Reference [64].

NA55 found a significant discrepancy between the predicted and measured neutron yields, even with the improved physics modeling. For lead, the data is an order of magnitude higher than the simulation. This highlights the need for new measurements with calibrated detectors.

Low energy accelerator and reactor-based neutrino oscillation searches typically cannot take advantage of operating deep underground, and so must understand their expected cosmogenic backgrounds. At shallow depths of tens of meters wa-

[6]These are also known as "Physics Lists", which are user selectable in simulation packages like Geant4.

ter equivalent these experiments have significant backgrounds from muon induced fast neutrons. These neutrons are generated by muon spallation and negative muon capture in the surrounding material, and frequently in the detector itself.

1.2.3 Benchmark simulations

As underground detectors have become increasingly more sensitive, the requirements for background characterization and suppression have also increased. The ability to measure neutron backgrounds at these facilities has not kept pace with the experimental goals. This has led to a reliance on Monte Carlo simulations to estimate the neutron backgrounds from various sources present in the underground environment. The most commonly used simulation package for underground physics is Geant4 [65].

A recent study of the muon-induced neutron production in lead using the Geant4 software package has produced interesting results. The authors ran the same simulation with eight different combinations of physics lists and Geant4 versions. They found a steady increase in the neutron production rate with each newly released physics list. Their measured value remains $\sim$20% higher than the simulated value [57].

These simulations rely on cross sections for neutron production and propagation that have large uncertainties, and frequently are based on models rather than measurements. This is an active area of research that will require more measurements of muon induced neutron yields and energy spectra.

1.2.4 Neutron spectroscopy

Measurements of the neutron emission spectrum from different sources could have a large impact on the choice of standards and calibrations. The common neutron source used for calibrations at NIST is ^{252}Cf. However, this source has a relatively short half-life, 2.645 years, that makes maintaining high activity sources difficult. If there were a different neutron source with a longer half-life that had a well characterized spectrum, it would be useful to replace the ^{252}Cf sources.[7]

The increased use of (α, n) sources is an area that would benefit from a neutron spectrometer. As discussed earlier in Section 1.1.2, the spectrum of neutrons emitted by (α,n) sources depends on the energies of the incident alpha particles and the distribution of the alpha-emitting isotope within the source [67]. Similarly, a recent result comparing the ISO standard Am-Be neutron spectrum to multiple Am-Be sources found significant discrepancies [68]. A neutron spectrometer with good energy resolution would greatly improve the ability to characterize neutron sources and calibrate other detector systems.

1.3 Previous detection techniques

There are many types of fast neutron detectors, ranging from lithium glass to ^{3}He recoil detectors to time of flight spectrometers. For this work, the focus will be placed on two of the most common detector techniques, passively moderated ^{3}He

[7] There is also concern that obtaining ^{252}Cf sources will become increasingly more difficult now that Oak Ridge National Lab has significantly increased the cost of production [66].

proportional counters (Bonner Spheres) and proton recoil detectors using organic liquid scintillator.

1.3.1 The Bonner sphere detector

The Bonner Sphere was first developed in 1960 as a technique for adjusting the energy response of ^{3}He proportional counters [69, 70]. The ^{3}He proportional counter is a thermal neutron detector and has a very low efficiency for fast neutrons. By adding a neutron moderator, typically hydrogen-rich polyethylene, around a ^{3}He counter, it is possible to increase the response for higher energy neutrons. The moderator allows higher energy neutrons to thermalize and then be captured by the ^{3}He counter. A Geant4 model of a 7" Bonner sphere is shown in Figure 1.16 [71]. The green tracks are from neutrons thrown at the detector from above, while the red center is the ^{3}He counter.

For energies between 1-15 MeV it is possible, though experimentally challenging, to compare the calculated response function with measurements of monoenergetic neutrons. Outside this range, it becomes increasingly difficult to find a standard neutron source that can be measured. Therefore, response functions for high energy neutrons are calculated typically using Monte Carlo simulations. It is difficult to estimate the uncertainties in these response functions but few unfolding codes will allow the inclusion of uncertainties. Correct understanding of the uncertainty in the final result is challenging [72].

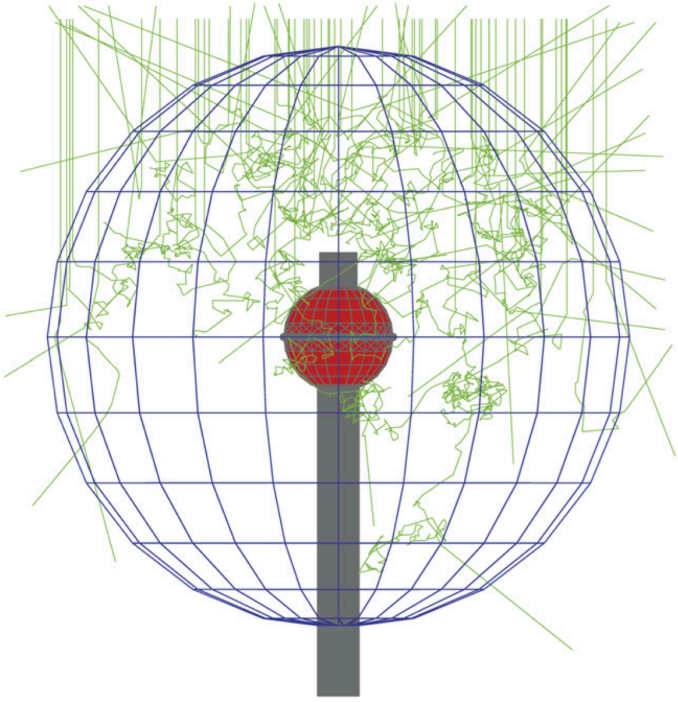

Figure 1.16: A Geant4 simulation of a 7" Bonner sphere from Reference [71]. The red center is the ^{3}He thermal neutron detector, while the green tracks are neutrons thrown at the detector from above.

With the addition of cadmium (a thermal neutron capture agent) and/or lead to the moderator, the response can be further adjusted to reject thermal neutrons or to increase the response to very energetic neutrons, respectively [23]. Work was done to show that arrays of Bonner Spheres, each with a different amount of moderator, could map out the energy spectrum of a large energy range, from thermal (0.025 eV) to hundreds of GeV. Figure 1.17a shows an array of 14 Bonner spheres deployed on the roof of a building. Figure 1.17b shows the various response functions for the different spheres used in Reference [23]. The responses are in units of counts/(neutron/cm^2), which is a measure of the detection efficiency for a isotropic neutron fluence.

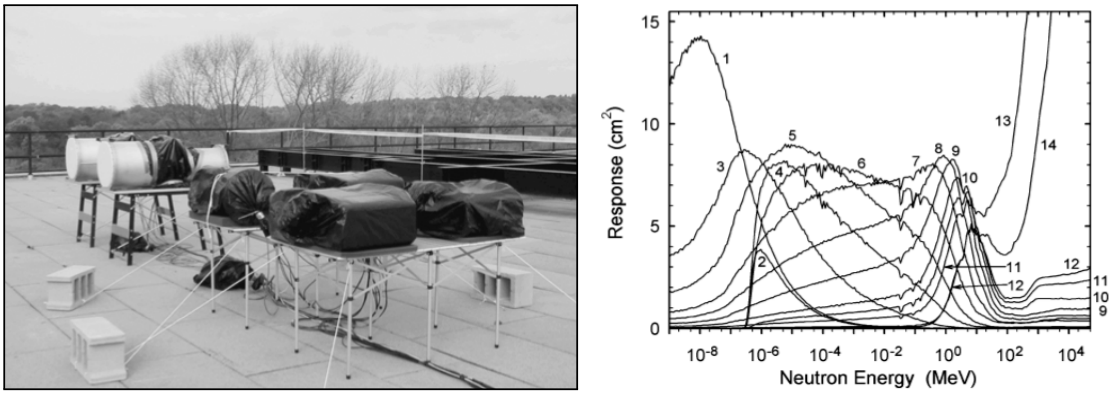

Figure 1.17: Left: The 14 element Bonner sphere array used in Reference [23]. This array has a quoted sensitivity to 100 GeV. Right: The MCNP calculated response functions for the 14 Bonner spheres from Reference [23]. The responses are in units of counts/(neutron/cm^2), which is a measure of the efficiency to a isotropic neutron fluence. The detectors with increasing response at high energy have layers of lead that act as multipliers for very energetic neutrons.

Using the energy response function for each sphere, an unfolding procedure can be performed that finds the most likely incident neutron spectrum that would produce the count rates observed in the ^{3}He counters. A common unfolding procedure is to minimize a χ^2 value, usually defined in terms of the difference between the measured count rate and the expected count rate for each sphere.

$$\chi^2 = \sum_{i=1}^{M} \left(\frac{(M_i - C_i)}{\sigma_i} \right)^2 \tag{1.7}$$

M_i and C_i are the measured and expected count rates for the ith sphere, while σ_i is the uncertainty in the measured readings [72].

Work in Reference [71] shows variations that occur from unfolding. The cosmic-ray induced neutron spectrum was measured with 16 Bonner spheres, including two that contained layers of lead, 1.25 cm and 2.5 cm thick. Figure 1.18a

shows the raw rates of the Bonner spheres. The high count rates of two spheres with 9 in diameter are from the lead layers that act as neutron multipliers. The observed count rates were then unfolded using four different response function calculations, two from MCNP and two from Geant4. Note the large fluctuations in the unfolded spectra for the evaporation and cascade peaks.

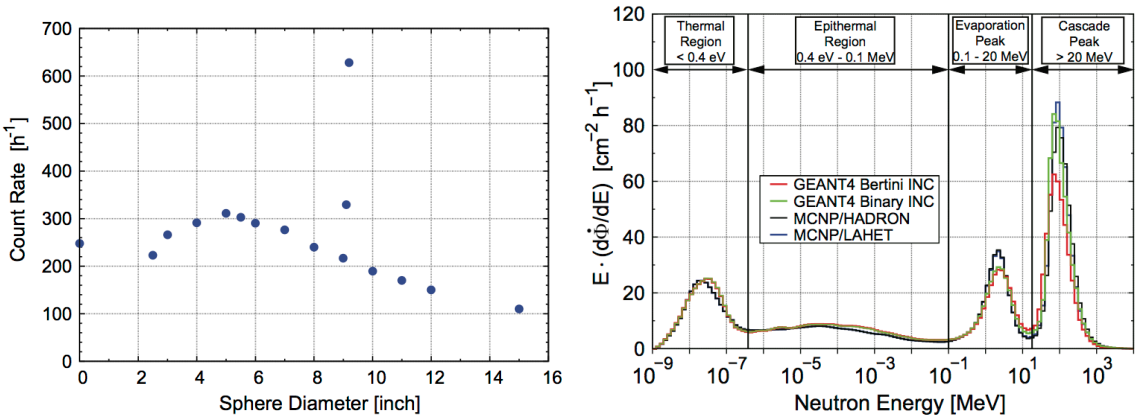

Figure 1.18: Left: The raw count rates in the 16 Bonner spheres used in Reference [71]. Note, the enhanced rates in the 9 inch detectors are from the addition of 0.5 inch and 1 inch of lead to the detectors. Right: The unfolded spectra from the same count rates, using four different simulations of the detector response. More detail is in the text. Figures from Reference [71].

There are a number of difficulties encountered with the use of Bonner sphere arrays, including poor energy resolution and non-directional response. Ideally, an array would consist of an infinite number of elements with infinitely narrow energy responses. Since there are a finite number of elements in the array, however, the final energy sensitivity is limited to the similarity of the response functions for each sphere. If the responses of two spheres are too similar, their measurements become degenerate, and no extra benefit is gained from having both. It is important that the

detectors span the desired energy range with non-degenerate responses to decrease errors in the unfolding procedure.

Another limitation of Bonner spheres is their completely isotropic response. There is no inherent way to determine the angular distribution of the incident neutron flux. Recent work has been done to develop directional spheres, but these have yet not been fully benchmarked [73, 74].

Bonner sphere arrays have excellent dynamic range, measuring neutrons from thermal energies to beyond 1 GeV. However, the uncertainties in the detector responses and the complications from unfolding make them non-ideal for many situations.

1.3.2 The liquid scintillator proton recoil detector

The liquid scintillator proton recoil detector is perhaps the opposite of the passively moderated ^{3}He counter. Rather than detecting the capture of a thermalized neutron, these detectors function by detecting the recoil proton from a neutron collision. With their large hydrogen content, liquid organic scintillators are highly effective neutron moderators. Depending upon the mass of the recoiling nucleus, a neutron can transfer any fraction of its energy, up to a certain cutoff energy.

$$E_r = \frac{4A}{(1+A)^2}(\cos^2\theta)E_n \tag{1.8}$$

$$E_r|_{max} = \frac{4A}{(1+A)^2}E_n \tag{1.9}$$

E_r is the energy of the recoiling nucleus, A is the atomic number of the nucleus, θ is the angle (in the lab frame) of the recoil, and E_n is the incident neutron energy. For hydrogen, the neutron can transfer all of its energy to the recoiling proton. For carbon, the other main element in organic scintillator, the recoil nucleus can receive a maximum of 0.28 E_n [12]. Carbon recoils do not produce light in the scintillator, but manifest themselves as a loss of up to 28% of the total neutron energy.

Liquid scintillator also possesses the important ability to distinguish between nuclear recoils and electronic recoils using the shape of the resulting pulse of light. Nuclear recoils excite longer-lived excitations (triplet vs singlet state) in liquid scintillator which lead to a slightly longer pulse of light. Figure 1.19 shows example traces of typical gamma and neutron interactions in liquid organic scintillator. The two signals shown have the same total integral, but the longer tail of the neutron signal yields a smaller overall amplitude.

For each trace, the total charge in two integration regions, Q_{short} and Q_{long}, are calculated. By comparing the charge in the short and long regions using Equation 1.10, neutron and gamma interactions may be effectively separated. Figure 1.20 shows a 2D scatter plot of the PSD variable versus the deposited energy for events from a ^{137}Cs gamma source (red) and a 2.5 MeV neutron generator (blue).

$$PSD = \frac{Q_L - Q_S}{Q_L} \tag{1.10}$$

Liquid scintillators have the added advantages of being relatively inexpensive, highly versatile in shape, and relatively high in light yield. However, the energy

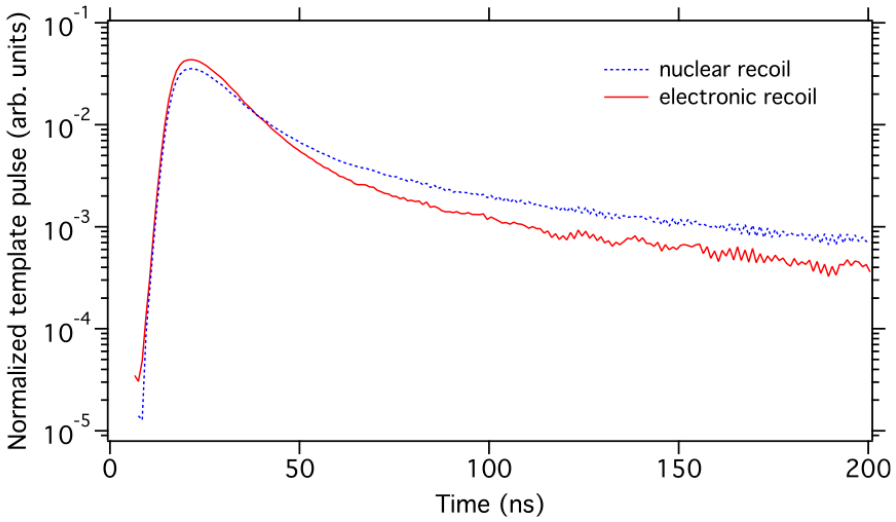

Figure 1.19: Signals from neutron (blue) and gamma (red) interactions in liquid scintillator with the same integrals. The two signals have equal integrals, but the neutron pulse is lower in amplitude and has an enhanced tail. Figure from Reference [75].

spectrum of neutron interactions in scintillator is dependent on multiple processes, including partial energy depositions, nonlinear light response for proton recoils, neutron scattering on carbon, and the intrinsic resolution from photon statistics. The effects of each of these are shown in Figure 1.21. The nonlinearity of organic scintillator to heavy charged particles causes a difference in observed light for a neutron that scatters multiple times rather than just once. This will be discussed in more detail in Chapter 2. Neutron interactions on carbon are effectively lost energy, since the recoiling nucleus produces effectively no light. This leads to a slight peak in the spectrum at $0.72E_n$. There is extensive literature characterizing the response of liquid organic scintillators to neutron fields. For example, Figure 1.22, from Reference [76], shows the response functions for NE-213 liquid scintillator calculated by the SCINFUL code [77].

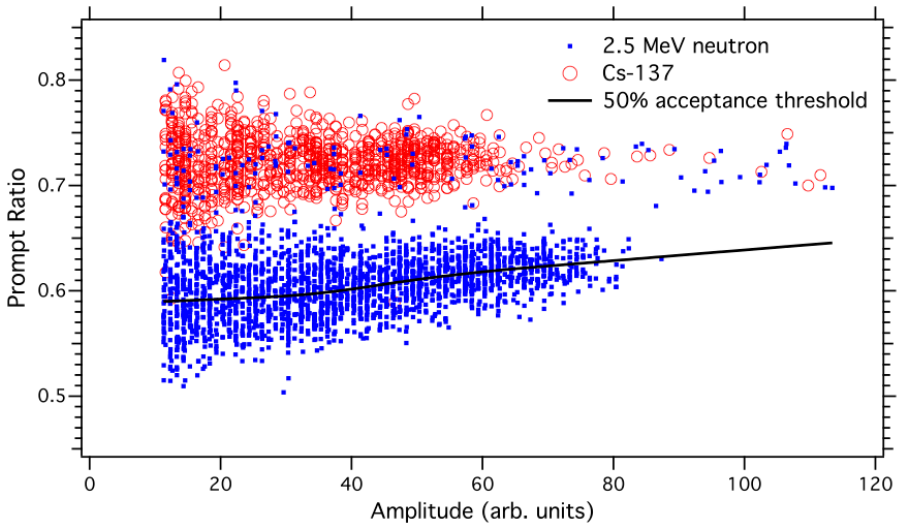

Figure 1.20: A 2D plot of the ratio of prompt signal integral to full integral versus the total amplitude of events from an 2.5 MeV neutron generator (blue) and a ^{137}Cs gamma source (red). Two bands are clearly visible, and the separation between them improves at higher energies. The few gamma-like events in the 2.5 MeV data are likely from neutron capture gammas from $n+p \rightarrow d+\gamma+2.2$ MeV. Figure from Reference [75].

The response functions are roughly step functions with an enhanced low energy tail. Typically, these response functions will be used to unfold a detected spectrum into its components. A comparison of multiple neutron unfolding codes may be found in Reference [78]. An example of a 2.5 MeV mono-energetic neutron source spectrum undergoing unfolding is shown in Figure 1.23.

The unfolded spectrum accurately reproduces the calculated spectrum generated by the neutron source. However, the unfolding is driven by the upper edge of the spectrum, so a large amount of data is necessary to carry out the unfolding procedure accurately. In the presence of an unknown neutron spectrum, the unfolding is highly variable and must be performed off-line. For use in low-neutron fields, this can be problematic. In an underground environment, where typical gamma fluxes

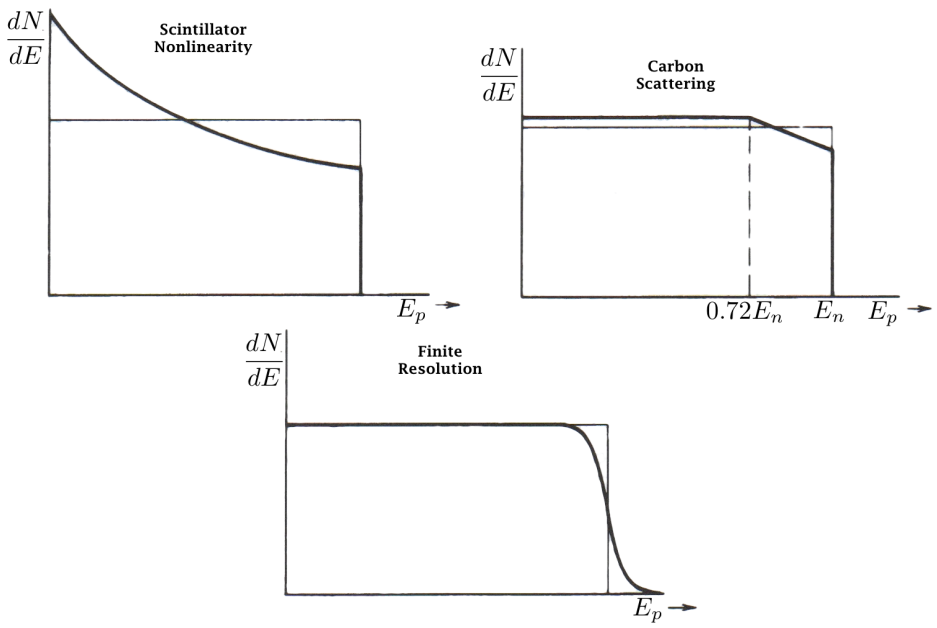

Figure 1.21: Three main processes that shape the spectrum of neutron energy deposition in organic scintillator. For each, the spectrum starts as a rectangle from (n,p) scattering kinematics. Left to right shows the effects of scintillator non-linearity, scattering on carbon, and the finite resolution from photon statistics. These are discussed in more detail in the text. Figures from Reference [12].

are many orders of magnitude larger than neutron fluxes, it is not possible to see neutron interactions in real time.

1.4 Improved neutron detection through capture-gated spectroscopy

The work in this thesis combines these two different detection concepts by merging the direct energy measurement of the proton recoil detectors and the neutron particle identification of the Bonner sphere systems. The FaNS detectors are arrays of plastic scintillator and ^{3}He proportional counters based on the principal of capture-gated spectroscopy [80, 81].

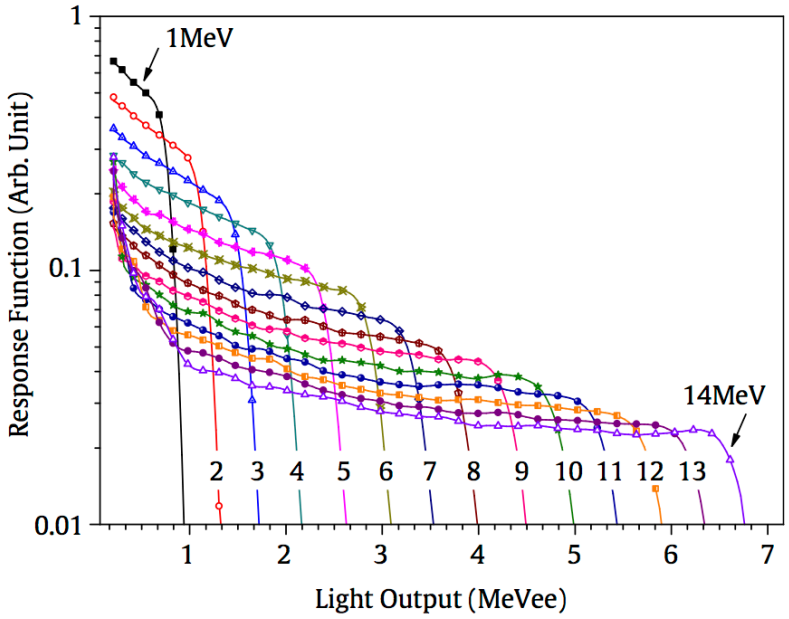

Figure 1.22: The calculated response functions for a 12.7 cm cylinder of NE-213 liquid scintillator to mono-energetic neutrons from 1-14 MeV using the SCINFUL code [77]. Figure from Reference [76].

By detecting a coincidence between a neutron thermalization and a neutron capture, a capture-gated spectrometer can efficiently reject non-neutron backgrounds while actively detecting the energy of the incident neutron on an event-by-event basis. The capture requirement demands that the neutron deposits its full energy, which eliminates partial energy depositions that lead to the broad response in proton recoil detectors. As will be shown later, a capture-gated detector will measure peaks from a mono-energetic source without the need to unfold a spectrum.

This thesis will cover the design, construction, and operation of two capture-gated spectrometers. Chapter 2 will discuss the general techniques behind capture-gated spectroscopy with plastic scintillator and ^{3}He proportional counters. Chapters 3 and 4 present the design, calibration, and measurements of the surface and underground fast neutron spectra recorded with the FaNS-1 detector at the National

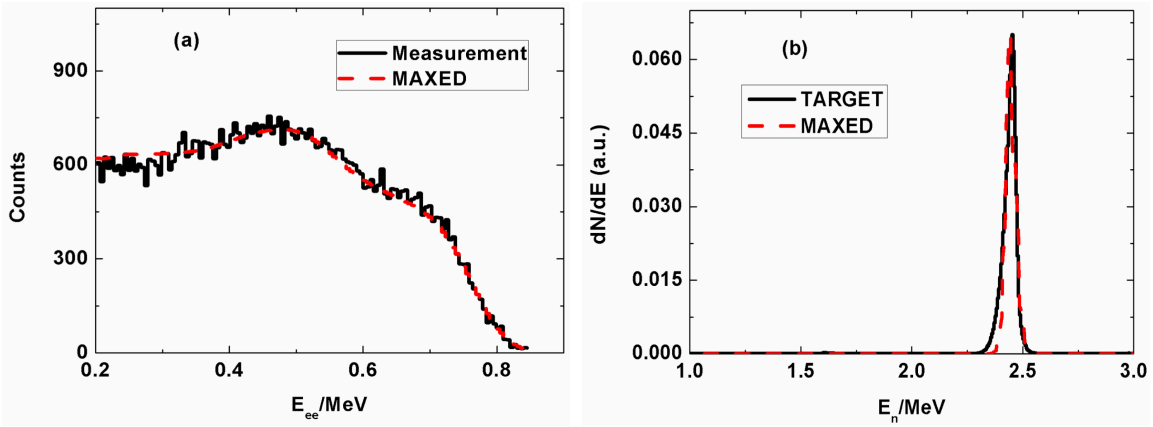

Figure 1.23: Left: A comparison between the reconstructed energy spectrum from the MAXED unfolding code and the measured spectrum from a 2.5 MeV monoenergetic neutron source. Right: The unfolded spectrum from the unfolding code MAXED compared with a calculated spectrum from the neutron source. Figures from Reference [79].

Institute of Standards and Technology in Gaithersburg, MD and at the Kimballton Underground Research Facility in Ripplemead, VA.

Chapter 5 covers the design and construction of the upgraded FaNS-2 detector, a significant improvement over FaNS-1. Chapter 6 presents the measurements of FaNS-2 in calibrated neutron fields. Finally, Chapter 7 presents the measurement of the ambient neutron flux and spectrum at NIST, Gaithersburg from 1 MeV to 1 GeV. In Chapter 8 the final results are discussed and future measurements for both FaNS detectors are presented.

Chapter 2

Capture-gated spectroscopy with plastic scintillator and ^{3}He proportional counters

Neutron detectors typically operate in environments where the neutron interaction rate is substantially lower, sometimes by many orders of magnitude, than the rate of gamma interactions. Thus, it is important to be able to separate neutron interactions from non-neutron interactions. For some types of detectors, this can be done by pulse-shape discrimination, as discussed earlier. However, this technique normally is done in post processing, causing a large fraction of the data recorded to be backgrounds. Also, many neutrons incident on a detector will scatter once and leave, depositing only a fraction of their full energy in the detector. This causes a large distortion to the neutron energy spectrum, which is dominated by partial energy depositions.

A technique that avoids this problem is capture-gated spectroscopy, which involves introducing a neutron capture agent into the detector. A coincidence between a scatter-like event and a capture-like events is demanded, greatly improving the signal to background ratio. Since the neutron capture cross section for most materials is highly peaked at low energies and rapidly falls off as the energy increases, knowing that a neutron captured implies that the neutron deposited all of its energy in the detector.

Work has been done with capture-gated spectroscopy in liquid scintillators doped with a neutron capture agent [75, 82, 83]. By suspending the capture agent directly in a scintillator cell, the light from either a neutron scatter or capture can be detected. When a neutron thermalizes in the detector volume, it then randomly walks until it captures on a nucleus or leaves the volume, as illustrated in Figure 2.1.

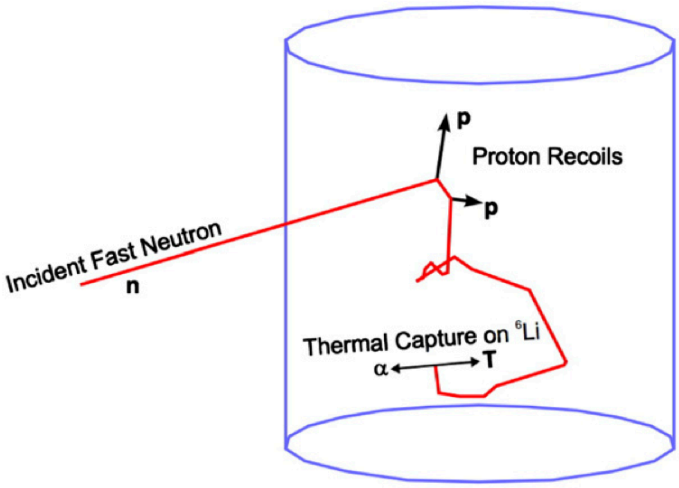

Figure 2.1: A schematic of a neutron interaction in a liquid scintillator-based capture gated detector. A neutron enters the detector, thermalizes through multiple proton recoils, and then is captured by ^{6}Li. Figure from Reference [75].

The signature of such an event is two pulses of light within a few microseconds of each other. The first signal contains information about the energy of the incident neutron, while the second signal contains information about the energy of the capture. An example of such a signal is shown in Figure 2.2.

Though a very simple detector, there is a significant disadvantage to having both the recoil and capture signals in the same data stream; it is difficult to tell the

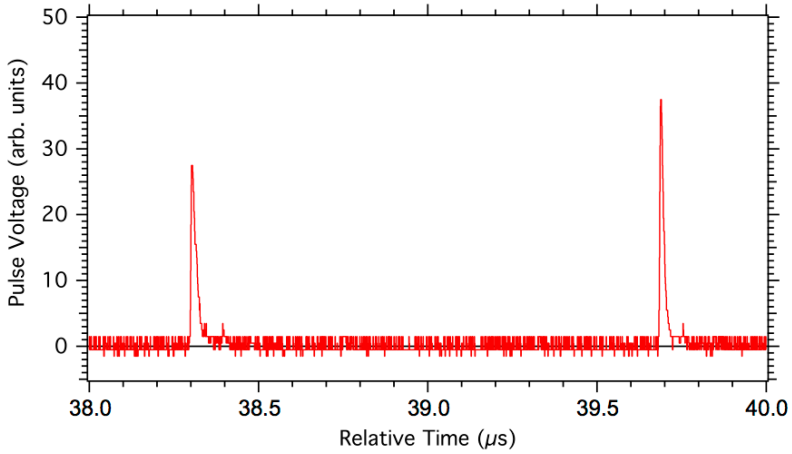

Figure 2.2: An example of a neutron thermalization event followed by a neutron capture event in a ^{6}Li-doped liquid scintillator. Figure from Reference [75].

two signals apart. This leads to a high rate of random coincidences, which can be difficult to deal with.

2.1 Segmented capture-gated spectroscopy with plastic scintillator and ^{3}He proportional counters

A different approach from using doped liquid scintillator is to have the capture agent separated from the active neutron moderator. This is the concept behind using ^{3}He proportional counters to detect the thermalized neutron. By separating the two signals, recoil and capture signals are positively identified. Because the ^{3}He counter is primarily sensitive to thermal neutrons, the rates of triggers in the ^{3}He counters are significantly lower than the PMT signals, improving the ability to detect low activities of neutrons, even in a field of high gamma activity [84].

For plastic scintillator, which does not have the ability to distinguish between neutrons and gammas using pulse shape[1], capture agents can be have a dramatic effect on the quality of the measurement. In this chapter using plastic scintillator and ^{3}He proportional counters together in a segmented, capture-gated spectroscopy setup is discussed. Also covered are some techniques that will be applied for both detectors, including segmentation, accounting for the nonlinear light response of plastic scintillator, a method for improving the dynamic range of the electronics, and pulse shape identification in ^{3}He proportional counters. Each of these techniques are important to the FaNS detectors.

2.2 Nonlinear light response of plastic scintillator

As discussed in the Chapter 1, organic scintillator provides a high density of protons that efficiently thermalize incident neutrons. The amount of energy a neutron can deposit in a single scatter is governed by kinematics, as shown previously in Equation 1.8. When a neutron scatters off a proton it can deposit up to its full energy, with uniform probability. The average deposition is half its initial energy. The proton recoils and produces scintillation light that is detected by photomultiplier tubes. The neutron then encounters another proton, and again deposits on average half its energy. This process continues until the neutron is fully thermalized or leaves the scintillator volume.

[1]There is a new type of plastic scintillator that was jointly developed between Livermore National Lab and Eljen Technologies that does display pulse shape discrimination between neutrons and gammas. Currently, the largest detector that can be made is a 5 cm cylinder [85].

A neutron will scatter many times before reaching thermal energies, but these scatters all occur within ∼10 ns. Conventional photomultiplier tubes are not fast enough to distinguish between each of the individual scatters. Thus, the recorded signal is the sum of multiple interactions. However, for heavy charged particles, the light response as a function of energy is not linear. The light produced by multiple energy depositions, E_i, is not the same as the light produced by one deposition of the same total energy:

$$L(\sum(E_i)) \neq \sum(L(E_i)). \tag{2.1}$$

This nonlinearity leads to a distorted determination of the neutron energy when there are multiple scatters in the same light producing volume. However, by segmenting the detection volume, as shown in Figure 2.3, it is possibly to convert the energy of each scatter separately, and reconstruct the true neutron energy.

If the specific energy loss is known for the particular material, it is possible to calculate a light response function including fit parameters that are experimentally tuned [86–88]. NIST provides an extensive database for calculating the stopping power and range of protons and alphas in various materials, including a version of plastic scintillator similar to those used for the FaNS detectors [89]. This specific energy loss will be used for this work.

This method is based upon the concept that the reduction in light production for heavy charged particles stems from recombination of electrons and ions. For heavy charged particles, which have high specific energy loss and deposit most of

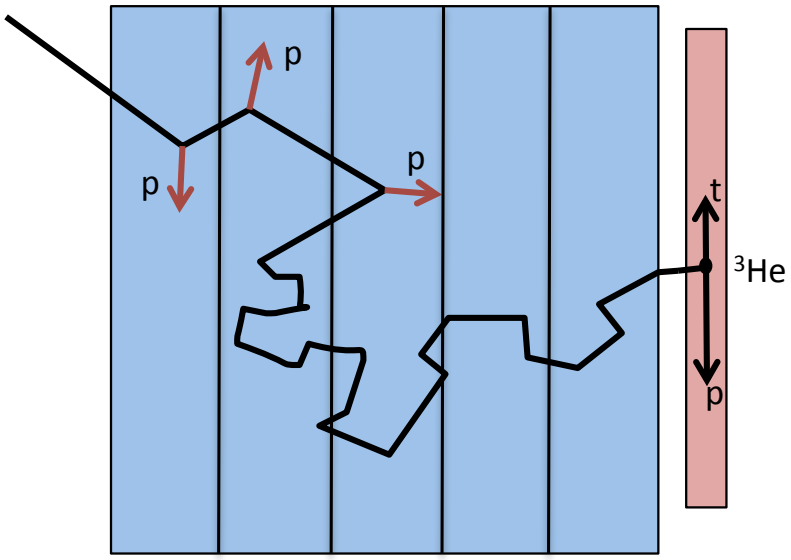

Figure 2.3: A schematic of a neutron multiple scattering in separate scintillator segments before thermalizing and capturing on a helium proportional counter. By converting from light to energy for each scatter individually, and then summing the energies, it is possible to reconstruct the incident neutron energy.

their energy in a very small range, this quenching is increased by the density of electrons and ions. These pairs recombine, and therefore do not produce light. Craun and Smith have derived a fitting function to produce the light response of protons:

$$dL/dx = S(dE/dx)\left[1 + kB(dE/dx) + C(dE/dx)^2\right]^{-1}, \tag{2.2}$$

where dL/dx is the light produced in path length dx, E is the particle's energy, dE/dx is the specific energy loss of the particle at the specific energy, and kB and C are fitting parameters [87]. The total light is the result of summing over the full range of the particle.

The fit parameters are known to vary between scintillator type and manufacturer [88]. Therefore, it is better to measure the light response of the specific

scintillator in question to a range of energies and use those data to fit a light response function.

2.2.1 NIST neutron time of flight setup

To measure the light response of the scintillator used in this work, a neutron time of flight apparatus based upon a ^{252}Cf spontaneous fission source was set up [90]. When californium undergoes spontaneous fission, an average of four neutrons are emitted, along with an average of four gammas with energies greater than 1 MeV [11]. By using a separate detector close to the source, the gammas can be used as a start clock for a time of flight measurement, as shown in Figure 2.4.

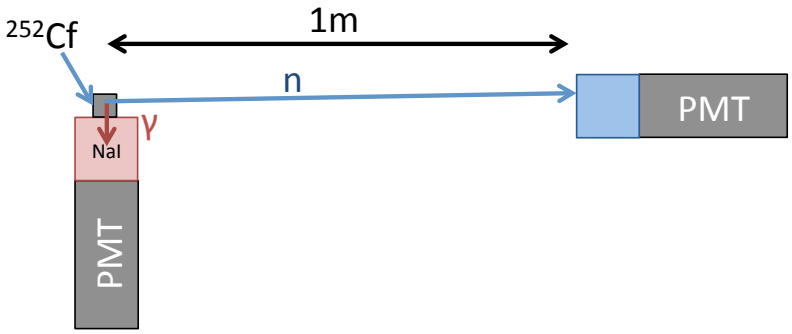

Figure 2.4: A schematic of the neutron time-of-flight setup at NIST. The ^{252}Cf source is placed one meter away from the test scintillator (blue) and directly next to a gamma tagging scintillator (red). The gamma tag detector is used as a start signal for the time of flight, and the test scintillator is the stop signal.

A near detector is placed directly below a ^{252}Cf source. This detector is a NaI crystal coupled to a photomultiplier tube, which is excellent for gamma detection and insensitive to neutrons. The start signal for the time of flight is provided by the NaI detector. The plastic scintillator that is under test is placed at a distance of one meter from the ^{252}Cf source. The stop signal, which is calibrated in light

units by a gamma check source, comes from the test scintillator. The ^{252}Cf neutron energy spectrum peaks at about 1 MeV, which corresponds to a neutron velocity of 0.04 c. A 1 MeV neutron will take about 75 ns to travel 1 m, while a gamma will take 3.3 ns. This large time difference allows for high fidelity separation of neutrons and gammas, as can be seen in Figure 2.5.

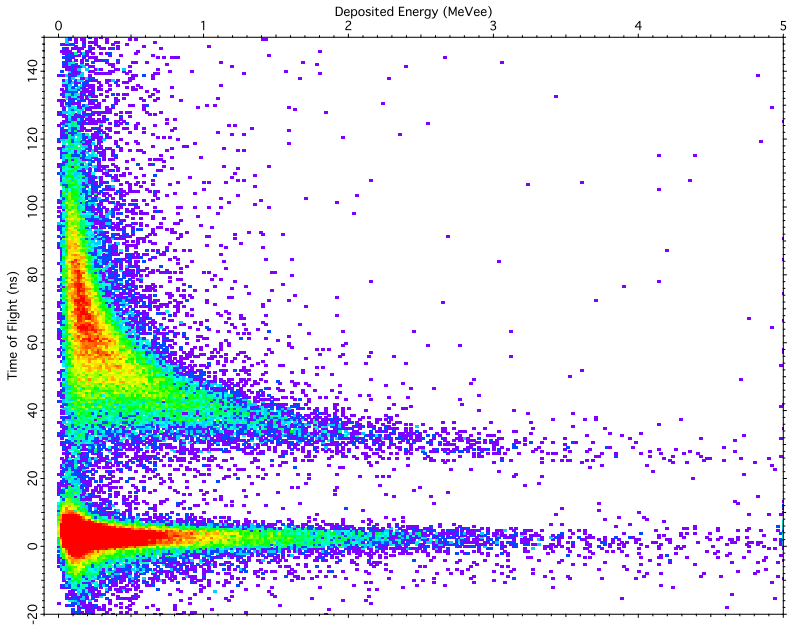

Figure 2.5: Two dimensional histogram of the time difference between the gamma start detector and the test scintillator's stop signal versus the deposited energy (in light units of MeVee) in the test scintillator. This clearly shows the two bands of signals in time of flight; small time differences are gamma interactions, while longer time differences are from neutrons.

There are two main coincidence modes: 1. Gammas interact in both detectors, 2. A gamma interacts in the start detector and a neutron in the stop detector. The former coincidence time difference gives an accurate measure of the distance between the two detectors. The latter coincidence time difference gives the incident energy of the neutron. Comparing the time of flight energy with the deposited energy in the test scintillator can yield the light response of the scintillator. The ^{252}Cf neutron

spectrum goes out beyond 10 MeV, so it is possible to map out the light response though most of the nonlinear regime.

By making cuts in the neutron time-of-flight energy, the scintillator bar's response to neutrons can be explored over a range of energies. The energy cuts are defined to be with in ±10% of the specified energy. Figure 2.6 shows the response of a segment of EJ-200 scintillator to 3 MeV neutrons. The half height of this distribution is the electron-equivalent energy for the scintillator.

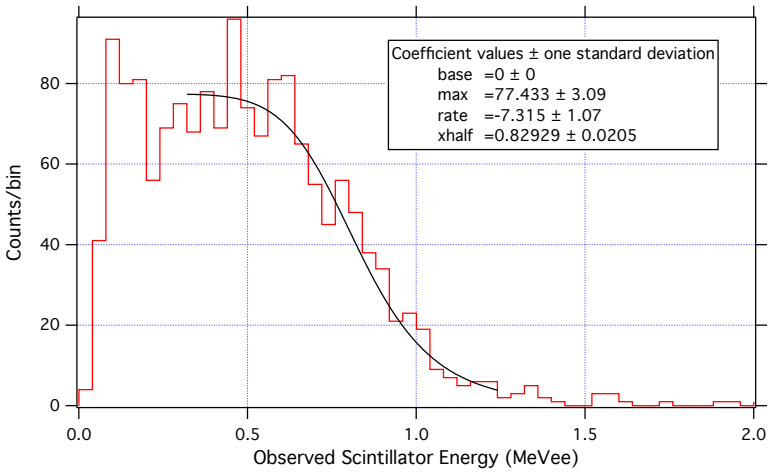

Figure 2.6: Shown here is the response of a segment of EJ-200 scintillator to 3 MeV neutrons. The incident energy is determined from the neutron time-of-flight as described in the text. Also shown is a fit to the data to extract the half-height of the distribution, which provides the conversion from MeVee to MeV.

By making many of these slices, the scintillator's response to a range of neutron energies was mapped out. Figure 2.7 shows the 2D histogram of the time-of-flight energy versus the deposited energy. Overlain are the light response data points obtained from measuring the half-heights of multiple time-of-flight slices.

The fit parameters in Equation 2.2 are adjusted to match the measured values. The resulting calculated light response and data are shown in Figure 2.8. For the

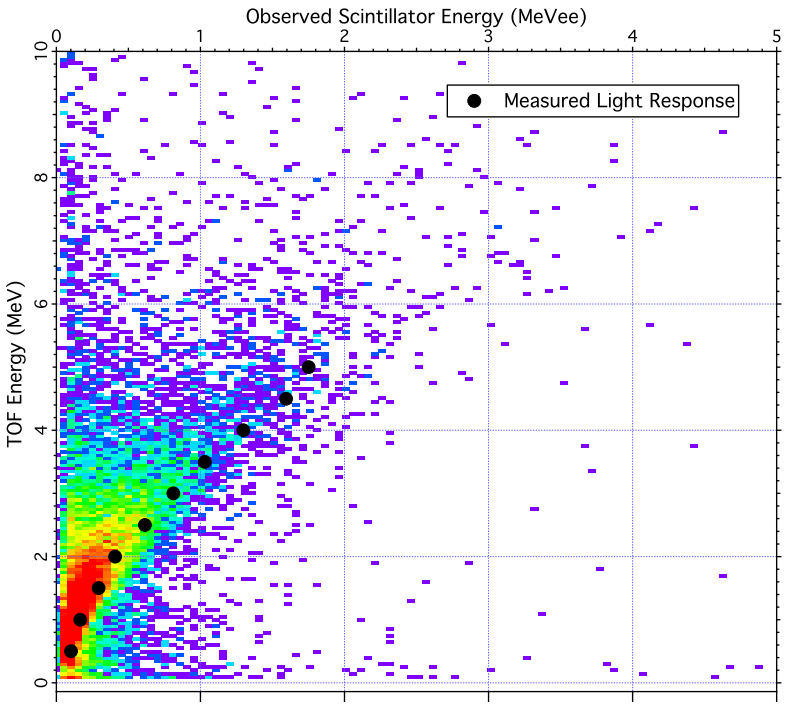

Figure 2.7: A 2D histogram of the incident neutron energy (measured by the time of flight) versus the deposited neutron energy in the scintillator. Also shown are the data from measuring the half-heights in time-of-flight slices of the data to generate a light response function.

measured data, values of $kB = 0.0095$ and $C = 1 \times 10^{-5}$ were obtained iteratively. This light response, which extends to greater than 200 MeV, can be used when reconstructing energy depositions in data and MCNP. Further improvements could be made by a least-squares fitting of the parameters, as well as improving the statistics for nTOF data at higher energies ($E_n > 5$ MeV).

2.2.2 Improved energy resolution through segmentation

The main consequence of the nonlinearity in light response for proton recoils is that if a neutron scatters multiple times in the same light producing volume, there will be an incorrect energy reconstruction that will degrade energy resolution. If,

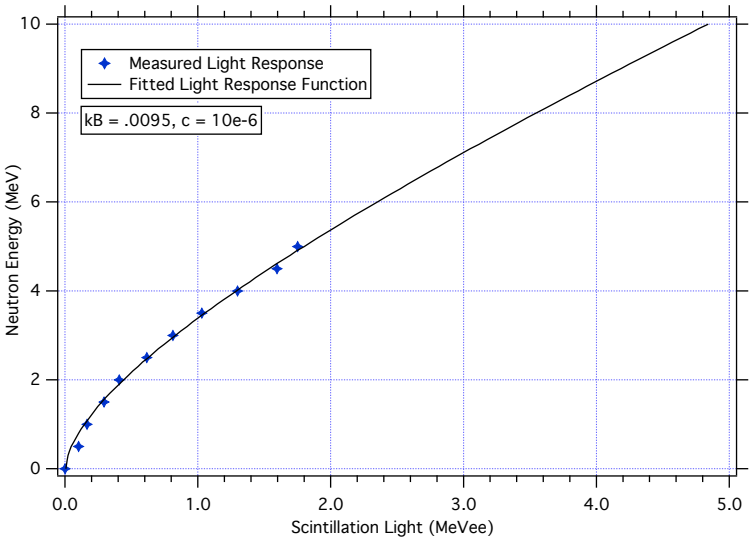

Figure 2.8: Data collected by measuring the edge of pseudo-monoenergetic neutron distributions from the neutron time of flight apparatus. Overlaid is the parameterization that will be used for the rest of this work.

however, the light from each scatter is captured separately, and the light response is known, it is possible to correctly reconstruct the incident neutron energy [91]. By segmenting the detector volume into pieces that are smaller than the mean free path of the incident neutrons, most events will only scatter once in each segment. Similarly, a cut can be placed to demand that neutrons interact in at least two segments, to better ensure the reconstruction accuracy.

To study the effect of segmentation on monoenergetic neutron response, a simulation was done with a finely segmented liquid scintillator detector. The modeled detector was a 50 cm $\times$ 50 cm $\times$ 50 cm cube composed of 1 cm^3 segments. The detector was exposed to 10 MeV neutrons in MCNP, and the deposited energies recorded. Analysis was done with and without the segmentation. The results are shown in Figure 2.9. Note the improvement of both the energy reconstruction and peak resolution. Two main features in the reconstructed spectrum remain even with

fine segmentation. First is the inflection at 8.5 MeV from events that scatter off carbon, and lose 23% of their energy without producing any scintillation light. Second is the peak at 5 MeV from inelastic carbon interactions. For neutrons with energies above a threshold, it is possible for the neutron interaction to break up the carbon nucleus. This results in a loss of ∼5 MeV in the reconstructed energy. These are unavoidable aspects of working with organic scintillator.

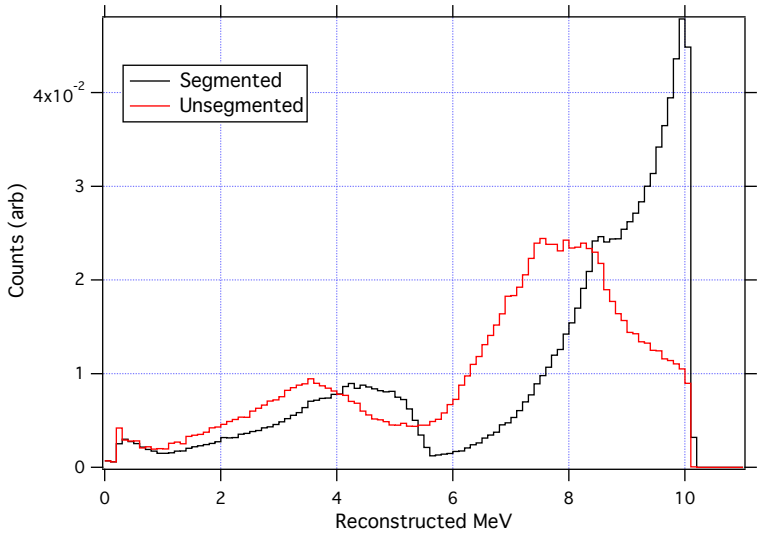

Figure 2.9: Reconstructed energy spectra from a simulation of 10 MeV neutrons incident on a finely segmented detector. The red curve is the detector's response from summing the light before converting into neutron energy. In black is the response of the detector when segmentation is taken into effect.

The optimum size of each segment is energy dependent; more energetic neutrons can have larger segments without suffering significant response degradation. The choice of geometry for a real detector therefore depends upon the neutron energy range of interest. An example of the effect of segmentation on the reconstruction of monoenergetic neutrons will be shown in Chapter 6*NOTE:NEW*.

2.3 Splitter/Summer modules for increased dynamic range

The data acquisition systems used for this work have limited dynamic ranges. To counteract the limited range of the DAQ, a novel signal processing module was developed that increases the dynamic range by a factor of ten. This is achieved by asymmetrically splitting each PMT signal, delaying one signal branch, and then re-summing the two. A schematic of this process is shown in Figure 2.10. An example of a resulting signal can be seen in Figure 2.11.

The system was prototyped for the FaNS-1 detector, using a cable delay and a NIM Linear Fan In/Fan Out module to re-sum the signals. For the FaNS-2 system, a custom printed circuit board was developed that makes use of analog delay chips, which simplify the operation of the setup and allow for the increase of channels seen in FaNS-2.

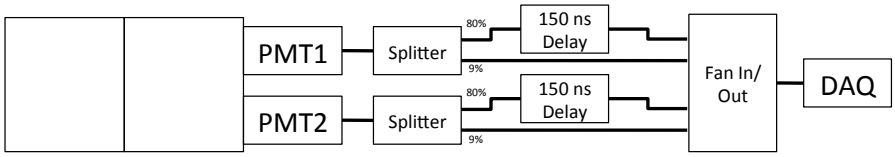

Figure 2.10: A schematic of the photomultiplier branch of the electronics for one scintillator block of FaNS-1. The two PMTs signals are combined

This technique provides a factor of ten increase in dynamic range, allowing for simultaneous acquisition of both large and small signals. It is possible to measure the exact conversion between the full and attenuated pulses by comparing the integrals of output signals that do not saturate the data acquisition system. Figure 2.12

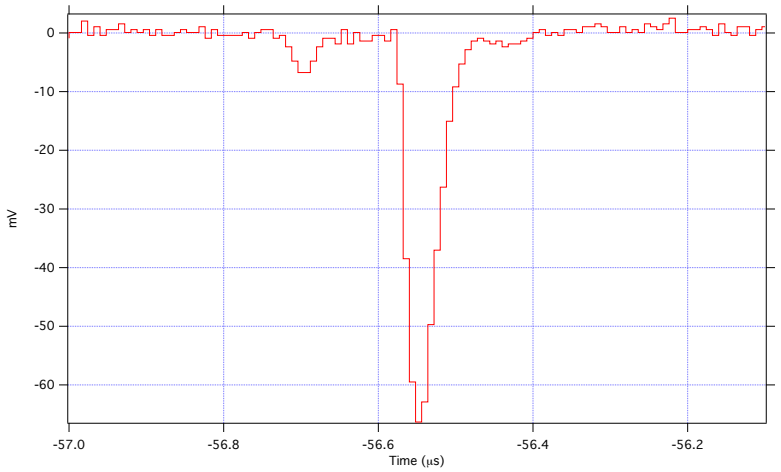

Figure 2.11: A sample trace of one photomultiplier signal that has gone through the FaNS-1 electronics. The pre-pulse is a 1/10 attenuated copy of the larger pulse, which allows for a factor of ten increase in dynamic range.

shows a two dimensional scatter plot of the attenuated signal versus the full signal. There are four discernible regions:

1. Small full scale pulses without a good attenuated signal;
2. Good signals on both the full and attenuated branches;
3. The full signal has saturated the digitizer, while the attenuated signal is still valid;
4. Both the attenuated and full signals are saturated.

These regions are clearly seen in the scatter plot in Figure 2.12. The conversion factors for each channel are extracted by fitting the linear region this plot. These are used to convert attenuated signal integrals into energy.

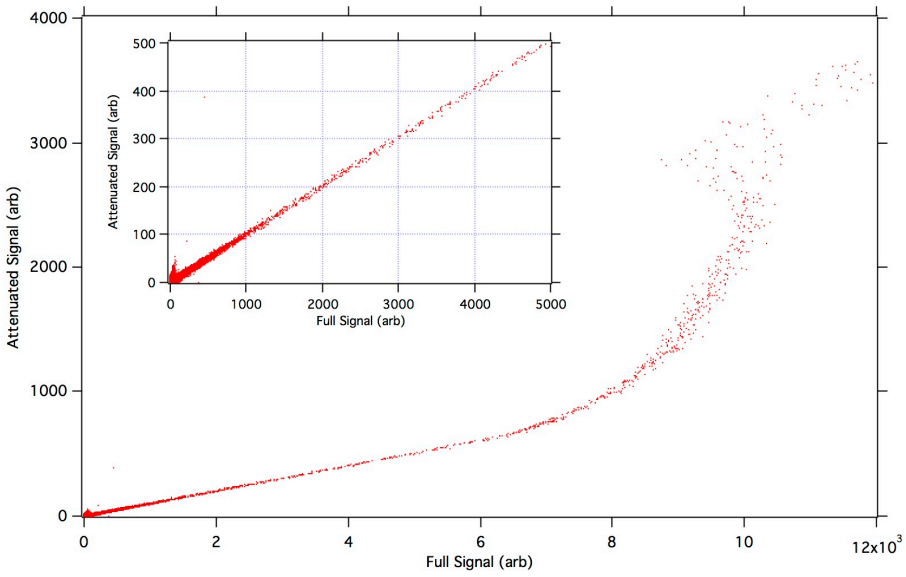

Figure 2.12: A scatter plot showing the attenuated signal integral versus the full signal integral for a given PMT. The slope of the linear section is the conversion factor between the full pulse and the attenuated pulse. Inset is a zoom-in on the lower energy region where both signals are fully captured by the digitizer. At large full signals, a curvature can been seen that is due to the full pulse saturating.

2.4 ^{3}He proportional counters

^{3}He has been used to detect thermal neutrons for more than half a century [92–95]. ^{3}He has a high thermal neutron capture cross section ($5330 \times 10^{-24}\,\mathrm{cm}^2$) and a final state that consists of charged particles, with no resulting gamma radiation. A neutron is captured by a ^{3}He nucleus, resulting in a proton and a triton, which share 764 keV of kinetic energy

$$n + {}^3\mathrm{He} \rightarrow p + t + 764 \ \ \mathrm{keV}. \tag{2.3}$$

Unlike other neutron capture agents, including gadolinium, boron, and lithium, ^{3}He is a gas at room temperature. Therefore, the most convenient detector type

is the gaseous proportional counter. Typically, proportional counters operate by having a volume of gas with an anode wire set at a high potential. Incident particles ionize the gas, liberating electron-ion pairs, which drift in the electric field.

Cylindrically shaped detectors have an added benefit of an increasing electric field gradient. The electric field of concentric cylinders is

$$\mathcal{E} = \frac{V_o}{r \ln(b/a)}, \tag{2.4}$$

where a is the diameter of the central anode wire, b is the diameter of the detector body, and r is the radius at which the $\mathcal{E}$ is evaluated. As the electrons drift towards the central anode wire, they experience an increasing electric field. When the electric field reaches a critical level, the electrons begin to ionize the gas themselves. This creates an avalanche of charge, which multiplies the initial deposited energy, creating a detectable current.

There are three main regions of operating a cylindrical gas detector, shown in Figure 2.13. First, when the applied voltage is low, no avalanche occurs and the current detected is equal to the charge deposited. This is the "ion chamber" region. Second, when the applied voltage is sufficient for avalanche, there is a region of proportionality where the deposited charge is amplified. Finally, if the applied voltage is sufficiently high, any amount of deposited charge is enough to cause breakdown of the detector. This final region is the Geiger-Muller region.

Because the neutron capture on ^{3}He has a two body final state, the charged particles will be emitted in opposite directions. If the ionization tracks are parallel to

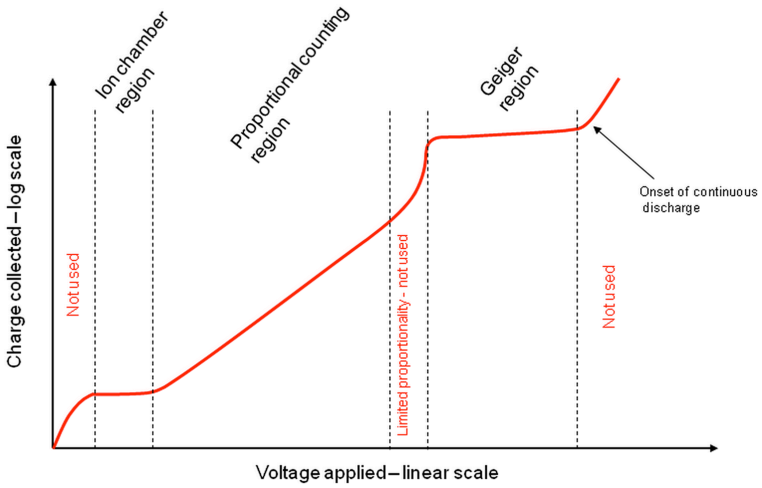

Figure 2.13: A diagram of the various regions for operating a proportional counter. More detail is provided in the text [96].

the central anode wire, all of the charge will be collected at approximately the same time, leading to a short risetime of the detected signal. However, if the particles are emitted perpendicular to the anode wire, one particle will be moving towards the wire while the other is moving away. The collected charge will be spread out in time due to the radial variation caused by the track geometry [97].

Typically, a ^{3}He proportional counter is biased through a preamplifier, and the resulting signals are sent through a shaping amplifier to be analyzed with a multi-channel analyzer or peak-sensing analog-to-digital converter. However, shaping the preamplifier signal smoothes out the slight deviations in signal shape caused by the track geometry. With high-speed waveform digitizers, it is possible to study the shape of preamplifier signals directly and apply digital signal processing to each event to identify the type of incident radiation. This is particularly useful for low-neutron environments, where backgrounds from alpha emission from the detector walls become problematic. This will be discussed in more detail shortly.

2.4.1 Specific energy loss and particle range

To demonstrate the expectation that the pulse shape of ^{3}He proportional counter signals can be used for particle identification, it will first be shown that the ranges of different particles in the detector vary significantly. By simplifying the Bethe Bloch equation, it can be shown that the specific energy loss of non-relativistic charged particles with charge Z, mass m, and kinetic energy E_{kin}, is approximately proportional to:

$$-\frac{dE}{dx} \propto \frac{Z^2 m}{E_{kin}}. \tag{2.5}$$

Thus, the track length for a given E_{kin} decreases with increasing mass and charge of the projectile. For neutron capture on ^{3}He the proton is emitted with 573 keV and the triton with 191 keV. The stopping power and particle ranges can be accurately determined using the TRIM software package [98]. At these energies, the proton has a range of 5.76 mm and the triton has a range of 1.6 mm for the gas mixture of the proportional counters used in this work. Because the proton and triton are emitted back-to-back, this yields a total track length of 7.36 mm for a neutron capture. An alpha particle with the same energy as the neutron capture, 764 keV, will have a track 2.54 mm long.

Beta emitters, electrons from γ-interactions, and cosmic rays leave long tracks and deposit little energy, resulting in small signals with a wider range of risetimes. Alpha particles with much higher specific energy loss leave shorter tracks and deposit more of their energy, which yield large signals with a relatively fast risetime.

These features can be exploited in analysis to help identify the original radiation. Details about the energy loss of charged particles and the resulting pulse shapes in proportional counters can be found elsewhere [12, 97, 99–102].

2.4.2 Microdischarges

Helium proportional counters have been shown to occasionally exhibit spurious signals. Microdischarges from the high voltage feedthrough to the grounded case of the counter are an example of such non-physical signals. A recorded trace of a microdischarge signal is shown in Figure 2.14 along with neutron-capture and alpha-particle signals of a similar amplitude. This is a known effect in ^{3}He proportional counters, and a thorough treatment of the origin of these signals can be found in Ref. [103]. The microdischarge is seen by the preamp as a current pulse and is treated as a normal signal. When sent through a shaping amplifier, there is no way to distinguish a discharge from a signal generated by an incident particle. By using the preamplifier signal, it is possible to measure the fast risetime of these spurious signals and discriminate against them.

2.4.3 Helium detectors for FaNS

In this work, 2.54 cm outer diameter, 46.3 cm active length, aluminum-bodied, cylindrical ^{3}He proportional counters manufactured by GE-Reuter Stokes are used. The ^{3}He partial pressure in the counters is 404 kPa (4 atm)[2] with a buffer gas

[2]The total pressure of ^{3}He has been confirmed using transmission measurements with a monochromatic cold neutron beam at NIST. The total transmission was found to be 0.07 for 5.6 meV neutrons. Using the diameter of the detectors and an assumed wall thickness (1.5 mm), this

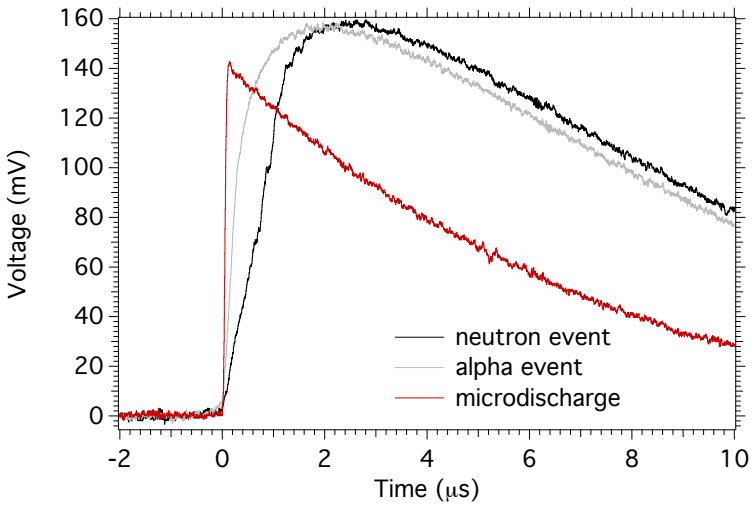

Figure 2.14: Example of the raw preamplifier traces showing the risetimes from three different sources. Shown here, in sequence of increasing risetime (left to right), are a microdischarge, an alpha-particle trace, and a neutron trace.

consisting of 111 kPa (1.1 atm) of krypton. Helium does not have a high stopping power for heavy charged particles. Therefore, manufacturers add a buffer gas with higher stopping power to ensure full energy deposition from the capture products. The krypton increases the stopping power of the gas for charged particles but has little effect on neutron capture.

Figure 2.15 shows an energy spectrum from a moderated ^{252}Cf source measured by one of the proportional counters used in this work. Note that although the neutron capture reaction is monoenergetic, there are still features in the energy spectrum related to when one of the particles interacts in the counter wall, leading to reduced energy deposition. This well-known wall effect is clearly seen in the two edges around 200 keV and 600 keV in Figure 2.15. By integrating the lower portion of the spectrum, the fraction of events that interact in the wall is found

yields a pressure of 4.24±0.1 atm. If the wall thickness is assumed to be 0.75 mm, the total pressure reduces to 4.0 atm.

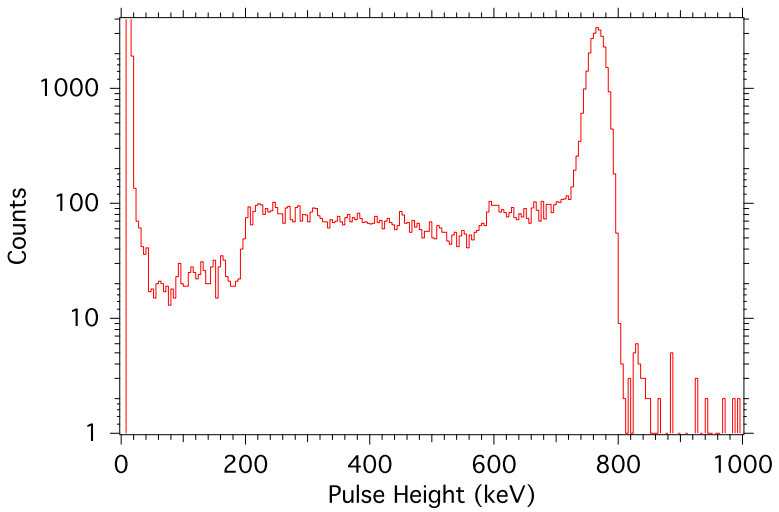

Figure 2.15: Typical energy spectrum of neutron capture events in one of the ^{3}He proportional counters used in this study. The dominant feature is the full-deposition peak at 764 keV. The two edges in the spectrum near 200 keV and 600 keV are related to partial energy deposition in the gas when either the proton or the triton interacts in the detector wall.

to be approximately 25-30%. This agrees with previous work done with similar detectors [104], and a simple Monte Carlo simulation that randomly distributed tracks and tallied those which intersected the wall. The same simulation can be used to estimate the fraction of events that lose both particles into the wall. This double wall effect is found to occur in 0.3% of neutron captures and is therefore ignored for the rest of this work. Events below 200 keV are largely electrons liberated from the counter body by gammas from the ^{252}Cf source. Typical energy resolution for these detectors at the thermal neutron capture peak is roughly 2-3%.

By exposing these detectors to various types of source radiation, it is possible to characterize their response. Figure 2.16 shows the risetime versus pulse height scatter plots for a single detectors response to thermal neutrons (2.16a), gammas (2.16b), and betas (2.16c). Also shown are two figures that are from long back-

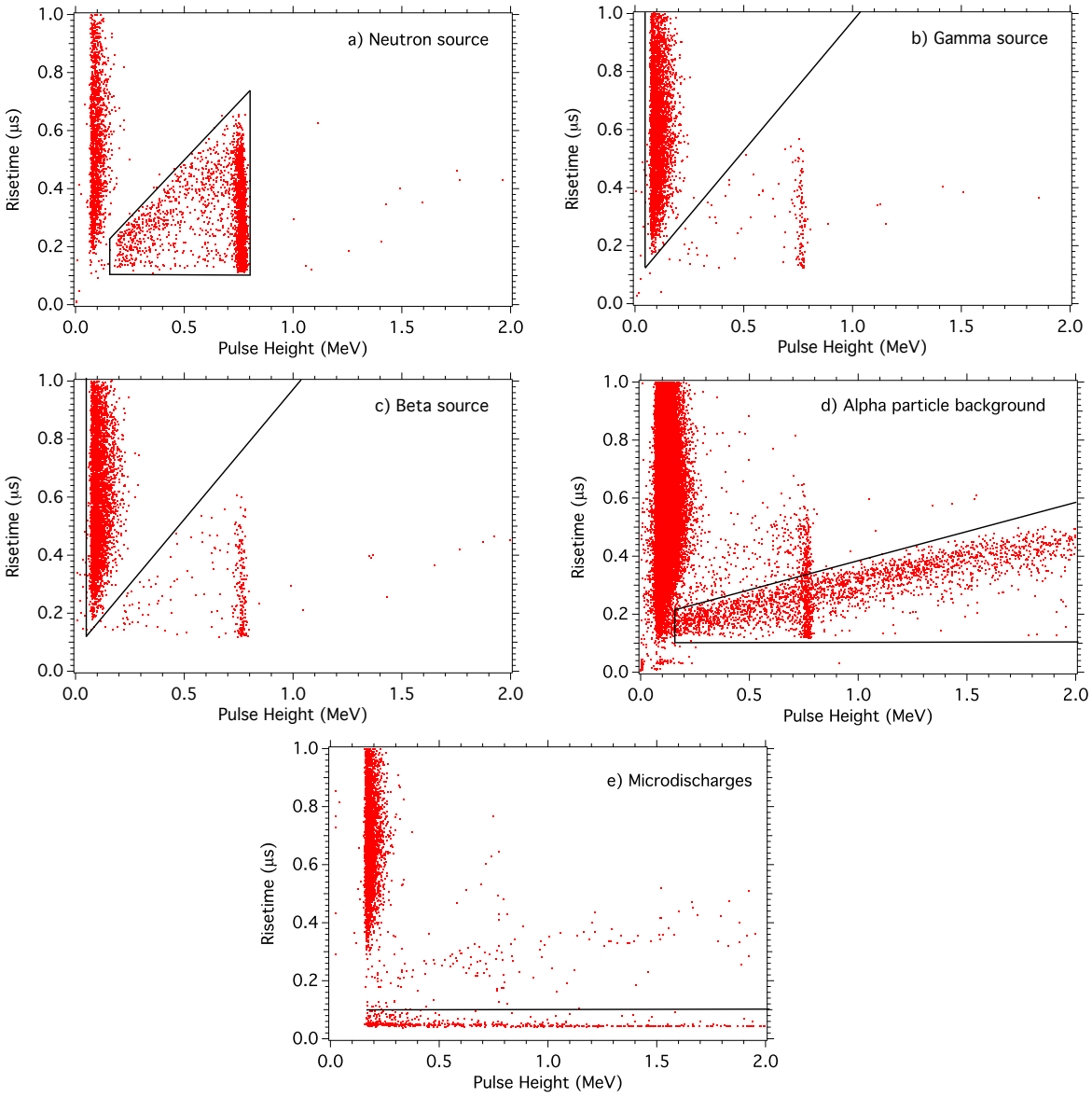

Figure 2.16: Scatter plots showing the risetime versus pulse height from different sources of radiation and microdischarges in ^{3}He proportional counters: a) neutron source data; b) ^{137}Cs gamma source data; c) ^{90}Sr beta source data; d) alpha-particle background data; and e) microdischarges. The solid black lines illustrate regions where the indicated events occur. Betas and gammas deposit a small fraction of their energies in the detectors, and therefore produce small signals. Alpha particles are emitted from the detector walls, where they deposit part of their energy. Therefore the alpha spectrum is broad.

ground runs that highlight alpha contamination in the detector walls (2.16d) and microdischarges (2.16e). The microdischarge figure shows an example of a detector with a clear band of fast (< 100 ns) risetime events that span a wide range of pulse height. The rate of such events may vary significantly among proportional counters, even for counters made by the same manufacturer.

By making a careful study of each helium proportional counter, the best tubes for use in the detector arrays may be selected. Each detector was counted for an extended period of time to characterize the internal background rate and the microdischarge rate. The detectors with the lowest alpha emission rate were selected for use in the FaNS detector arrays. ^{3}He counters with moderate rates of microdischarges are acceptable for this work, since these events are easily discriminated against.

2.4.4 Sensitivity of the FaNS ^{3}He counters

To characterize the overall sensitivity of the ^{3}He counters used in this work, a configuration of detectors was simulated and measured with a calibrated ^{252}Cf neutron source at different distances. The count rates of each detector position were compared between data and MCNP. The ratios of detected count rates to simulated neutron capture rates give insight to the accuracy of the model and potential detection inefficiencies. Figure 2.17 shows the ratios for three ^{3}He counters exposed to the source at three distances. These are averaged to obtain an average detection

efficiency of 84±10% compared to the MCNP simulation. This number will be used to account for detector sensitivity in the Monte Carlo predictions.

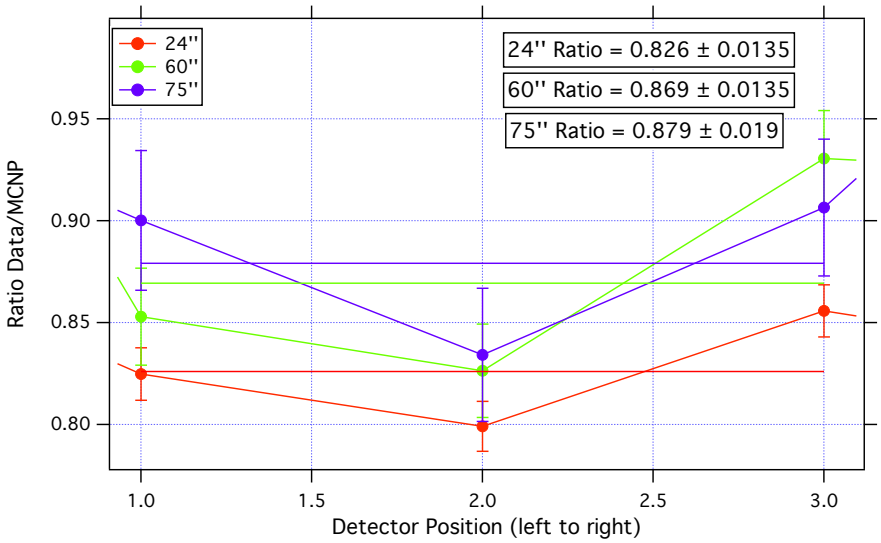

Figure 2.17: The ratios of observed neutron count rates to simulated neutron capture rates for three counters in three different source configurations (24", 60", and 75" above the detectors). These ratios are averaged to obtain an effective detection efficiency for use in the following chapters.

The best method for characterizing the ^{3}He counters is to expose the entire detector to a uniform calibrated thermal neutron beam. This is currently not possible at NIST; the thermal neutron column has not been operational for approximately 10 years. However, there is a collimated monochromatic beam of 5.6 meV neutrons that may substitute for the thermal column with corrections for the (^{3}He, n) cross-section taken into account. To characterize the sensitivity as a function of position along the ^{3}He counter, the detector is shielded except for a small slit that can translate the length of the tube. The slit is then exposed to the monochromatic beam, and the neutron count rate in the detector is observed. This measurement is then repeated over the length of the detector, mapping out the sensitivity profile of the

detector, which is then summed to obtain the full sensitivity. This measurement is being planned and will hopefully occur within the next few months at NIST.

2.5 The Monte Carlo N Particle (MCNP) simulation package

To simulate neutron interactions, a software package was developed by Los Alamos National Lab called *Monte-Carlo N Particle* (MCNP). This Monte-Carlo software package was designed to simulate nuclear processes, particularly those in nuclear reactors. It has been continually updated and expanded to better model higher energy processes of interest to nuclear and particle physics. Both MCNP5 and MCNPX were used to model the fast neutron response of detector arrays in this work.

For all calculations of neutron spectra, the particle tracking (PTRAC) option of MCNP was used. PTRAC tracks individual particles throughout the detector volume, including secondary gammas and electrons created by neutron interactions. It also allows for the light response of each particle to be taken into account on an event-by-event basis. This allows the simulation to account for multiple scattering and segmentation effects as discussed in Section 2.2.2.

PTRAC analysis programs were written to convert deposited energy into light, according to each particle's light response. For protons, the calculated light response discussed in Section 2.2.1 was used. However, for heavier particles, like alphas and carbon nuclei, a technique was used to appropriately scale the proton response.

From Birks' formulation, Equation 2.2, it can be shown that the light response depends upon the specific energy loss, dE/dx, of the particle in question. The specific energy loss depends on a particle's velocity, rather than its energy [12]. Therefore, to convert from the proton light response to any other particle, the following relation is used:

$$L' = L_p\left(\frac{E'}{m'}\right) \times m', \tag{2.6}$$

where L_p is the proton light response function, E' and m' are the energy and mass of the particle in question, and finally L' is the adjusted light response. This method has been fully detailed in [105].

To account for various running parameters, the PTRAC analysis programs output pseudo-data, which could then be passed through the same series of conditions as the real data. These include thresholds, number of separate scatters, time to capture, and others. These cuts will be discussed at length for each detector. For FaNS-2, an effort was made to also account for photon statistics in the Monte-Carlo, which will also be discussed in more detail in Section 5.6.

2.6 The FaNS detectors

Using these techniques, the UMD/NIST collaboration has produced two Fast Neutron Spectrometers (FaNS) to measure broad spectrum, low fluence, neutron sources. The rest of this thesis will focus on the application of these techniques to the design, construction, calibration, and deployment of FaNS-1 and FaNS-2 at

sea-level and underground. The upcoming chapters will refer to these techniques throughout.

Part I

FaNS-1

Chapter 3

The UMD/NIST Fast Neutron Spectrometer (FaNS-1)

The UMD/NIST Fast Neutron Spectrometer (FaNS-1) was designed to be sensitive to neutrons with energies from 500 keV to 150 MeV with good energy reconstruction. The detector system consisted of six segments of plastic scintillator (BC-400) and six helium proportional counters. FaNS-1 was constructed in 2008 and was commissioned and calibrated at the NIST Californium Neutron Irradiation Facility [106] before moving to a low-overburden lab to measure the surface neutron spectrum. In the summer of 2010, the detector was installed at the Kimballton Underground Research Facility (KURF) in Ripplemead, VA [107] to measure the fast neutron flux and energy spectrum. It operated for two years, with intermediate upgrades to electronics and detectors, before being decommissioned in the fall of 2012.

3.1 Detector design

Initially intended as a prototype of the detection techniques, the main components of FaNS-1 were repurposed from previous experiments. This allowed for rapid assembly and deployment of a test detector while the design effort of the full detector, FaNS-2, was undertaken. The feasibility of a plastic scintillator and helium proportional counter capture-gated spectroscopy system was tested with FaNS-1.

With this in mind, FaNS-1 proved to be a far more successful detector than was initially anticipated.

3.1.1 Scintillator segments for FaNS-1

Originally, the FaNS-1 scintillator segments were designed and used as part of a proton telescope on an experiment at the Paul Scherrer Institute in Switzerland [108]. The six plastic scintillator segments in FaNS-1 are identical and are constructed of BC-400 scintillator and UV-transmitting light guide. A schematic of one scintillator assembly is shown in Figure 3.1. Both the scintillator and light guide portions of the assembly are 9±0.1 cm × 18.5±0.1 cm × 15±0.1 cm, which yields a combined size of 9 cm × 18.5 cm × 30 cm. Each segment is wrapped in aluminized mylar for increased reflectivity and then covered with black vinyl tape for light tightness. The active volume of each scintillator segment is 2.50±0.03 liters.

Two 7.5 cm photomultiplier tubes are mounted via optically transparent potting silicone (GE Silicones RTV615) to cylindrical light guide posts on the light guide side of the assembly. The large light guide was originally included to ensure that each photomultiplier tube has uniform light collection for events that occur anywhere in the scintillator. The photomultipler tubes used for FaNS-1 were Hamamatsu model R3036. To improve the pulse linearity of the PMTs, a tapered voltage divider base was used to set the potentials on each of the 12 PMT stages. The tapered divider provided linearity of better than 5% up to 100 mA, or roughly 5 V in a 50 Ω load.

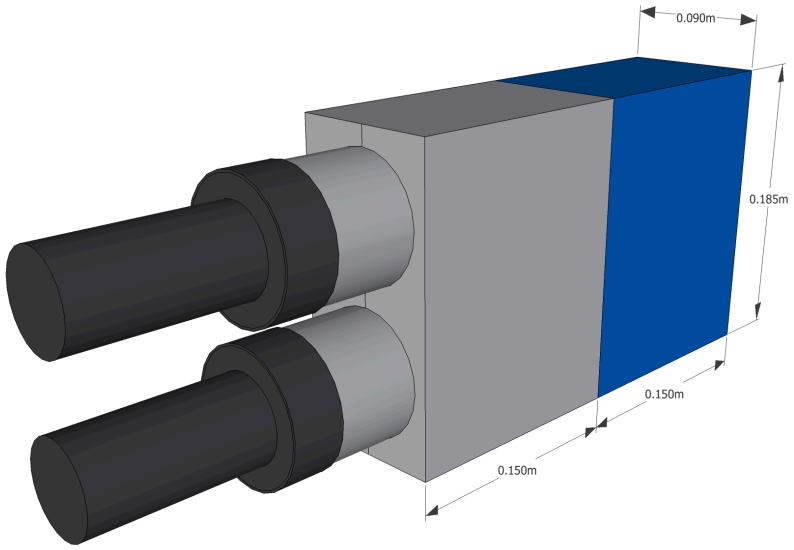

Figure 3.1: A single segment of the FaNS-1 scintillator. The blue region is the active volume of scintillator, while the grey region is ultraviolet-transmitting light guide. The addition of light guide flattens out the spatial light collection of the photomultiplier tubes, seen on the end.

3.1.2 Helium proportional counters for FaNS-1

The helium proportional counters used in FaNS-1 are 2.5 cm diameter aluminum-bodied cylindrical detectors manufactured by Reuter Stokes, model RS-P4-0819-103. They are filled with a mixture of 4 atm of high purity ^{3}He and 1.1 atm of ^{nat}Kr to increase the stopping power of the gas for charged particles. Because krypton has a low neutron cross-section, the addition of krypton does not contribute to neutron interactions. These detectors were originally part of a neutron scattering experiment at the NIST Center for Neutron Research. The large number of helium counters available allowed us to select detectors which had particularly low levels of alpha and gamma backgrounds.

3.1.3 Optimization of detector geometry

The geometry and relative position of individual components influences the overall performance of the full detector. For FaNS-1, this effect is enhanced by the large light guides in the scintillator assemblies. Neutrons thermalize equally in both the scintillator and the light guide, but only events that occur in the scintillator produce detectable light. Therefore, any energy deposited in the light guide is lost, and the incident neutron energy is incorrectly reconstructed. This effect degrades the energy resolution of the detector.

Approximately four arrangements of scintillator segment and ^{3}He counters were simulated and experimentally tested. Designs with helium proportional counters overlapping the light guides led to an increase of neutron events that had interactions in the light guide, degrading the ability to accurately reconstruct the incident neutron energy. These designs also had an increase of random coincidences caused by neutrons that fully thermalized in the light guide, depositing no energy in the scintillator.

To minimize the detection of neutrons that may have interacted in the light guides, the individual components were arranged with the scintillator active volumes pointing towards a central channel where the helium proportional counters were vertically stacked. Figure 3.2 shows how the individual components were arranged. Including small spacers between them, the six helium proportional counters completely spanned the 18.5 cm height of the scintillator segments. To shield external thermal neutrons, a boron-loaded silicone rubber, Boroflex, covered the active

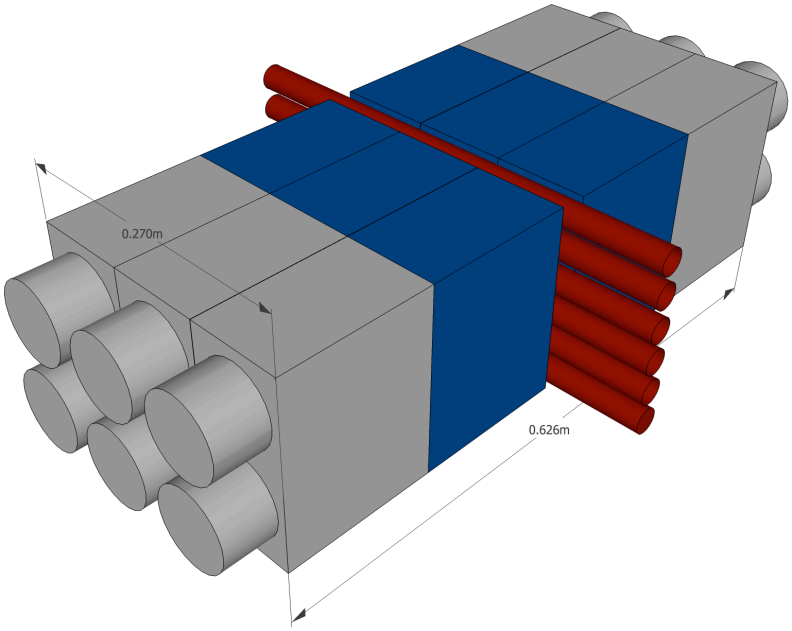

Figure 3.2: A schematic of the full array of FaNS-1. Each side of the detector consists of three segments of plastic scintillator with their active volume (blue) facing inwards and light guides (grey) facing out. In the central channel, six helium proportional counters (red) are vertically stacked.

volume of the detector. This was also wrapped around the ends of the ^{3}He counters that were not surrounded by scintillator. This helped to reduce random coincidences from thermal neutron captures without energy deposition in the scintillator.

3.2 Electronics and Data Acquisition

The data acquisition system was based on an 8 channel, 125 MSample/s, 12 bit, waveform digitizer manufactured by GaGe Applied Technologies, model CSE8289 [109]. The helium detectors provided the trigger for acquisition, at which point all PMT channels were digitized. This allowed for maximum flexibility for tuning the different cuts and analysis parameters, including thresholds, coincidence level, and coincidence window. Figure 3.3 shows the block diagram of the FaNS-1

electronics. A custom data acquisition software package was developed to control the digitizers.

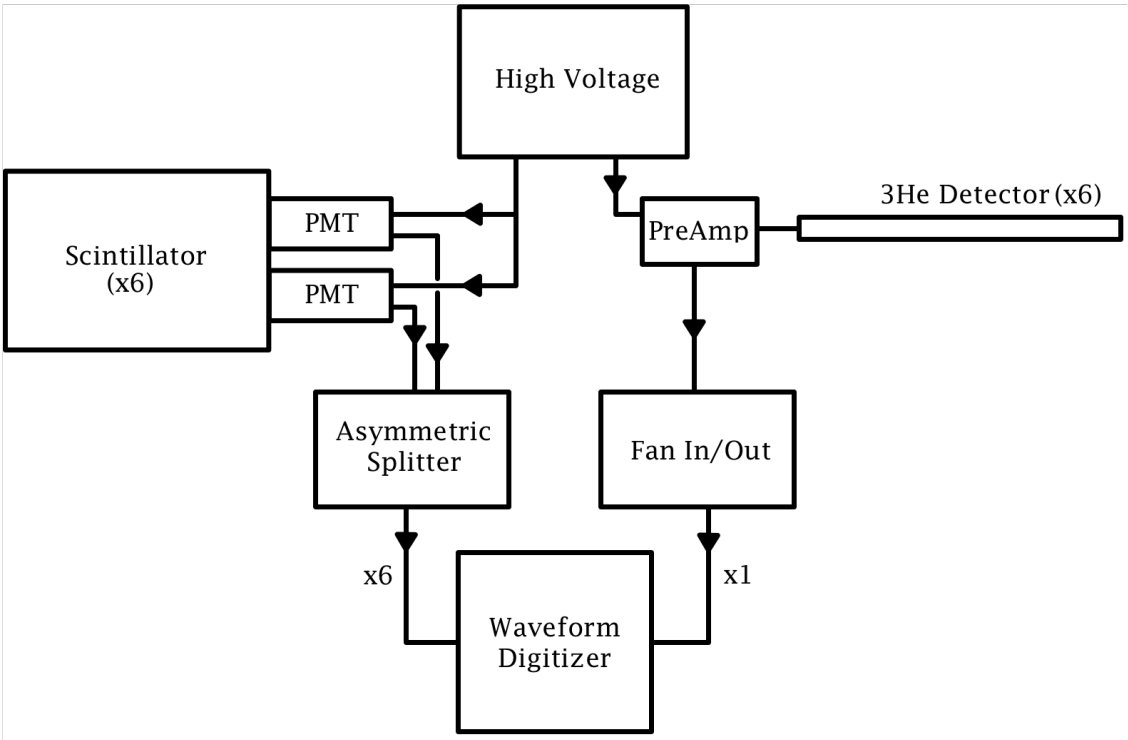

Figure 3.3: The block-diagram of the electronics for the FaNS-1 data acquisition. For simplicity, only one of the scintillator segments and helium proportional counters are shown. More detail is provided in the text.

High voltage was provided to the helium counters and the PMTs by a modular, ethernet-controlled high voltage power supply crate manufactured by Wiener, Plein and Baus Corp (model MPOD Mini) [110]. The crate contained two high voltage cards, manufactured by Iseg HV [111], capable of providing positive high voltage for the helium detectors, +3 kV/500 μA, and negative high voltage, -3 kV/3 mA, for the PMTs. The crates were controlled by Simple Network Management Protocol (SNMP) commands, which allowed for remote and automatic setting of gains. Python scripts monitored the high voltages during the underground operation.

3.2.1 Phototube branch

Signals from the two photomultiplier tubes on each scintillator segment are summed before being sent into the custom splitter-summer unit discussed in Section 2.3. The outputs of the splitter-summer modules are fed into the digitizer, one scintillator segment per channel. The PMT channels had a maximum voltage setting of 1 V.

3.2.2 Helium tube branch

The helium tubes in FaNS-1 were biased through separate Canberra 2006 preamplifiers and gain-matched through varying the bias high voltage. The raw preamp signals were summed in a NIM linear fan-in fan-out and sent into one channel of the waveform digitizer. Care was taken to minimize the length of cabling between the preamplifiers and the detectors to reduce electronic noise pickup.

3.2.3 Digitization

The phototubes and the helium tubes were sent into the GaGe waveform digitizer through SMB cables. A large window for data acquisition was set to ensure effective capture of the coincidence between the scintillator and ^{3}He counters. The helium detectors act as the trigger for the data acquisition. The acquisition window was centered around the ^{3}He trigger. The helium signal was AC coupled in the digitizer to counteract any baseline fluctuations which might cause an inconsistent trigger level. A thorough study was carried out to ensure that AC coupling did not

effect the resolution or efficiency of the helium detectors. A sample digitized trace is shown in Figure 3.4.

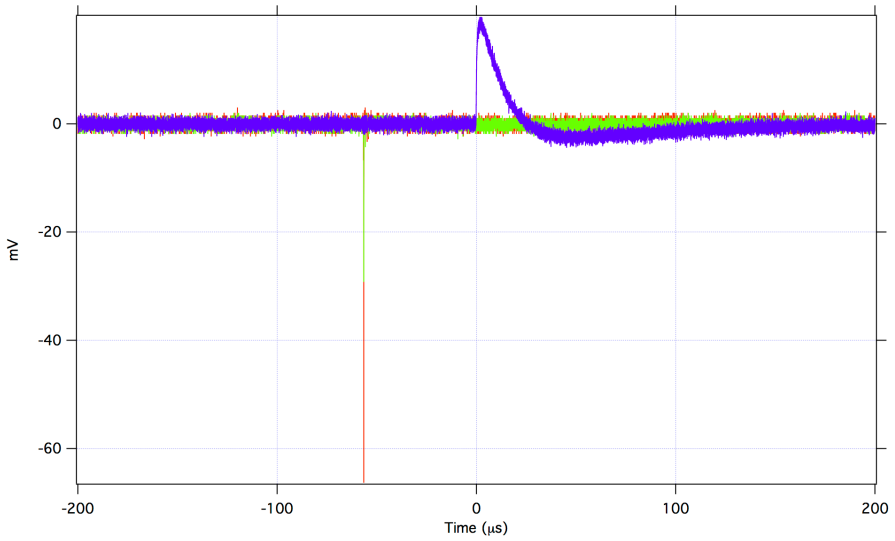

Figure 3.4: A sample digitized event for FaNS-1. Shown are a helium signal in purple and a pair of PMT signals (green and red) from a neutron interaction. The two PMT signals (located at -60 μs) are from two scintillator blocks firing in coincidence, due to a neutron multiple scattering before being captured by a ^{3}He nucleus.

When the digitizer triggers, signals from all eight channels are written to disk, although the ability to suppress channels which did not pass a simple threshold was used for high-rate source data. This feature was implemented to reduce dead time and the amount of data written to disk. However, the ability to set a threshold in software later on would have been greatly diminished. Therefore, for ambient neutron operation of FaNS-1, all channels were recorded for each trigger. A screen shot of the data acquisition program is shown in Figure 3.5.

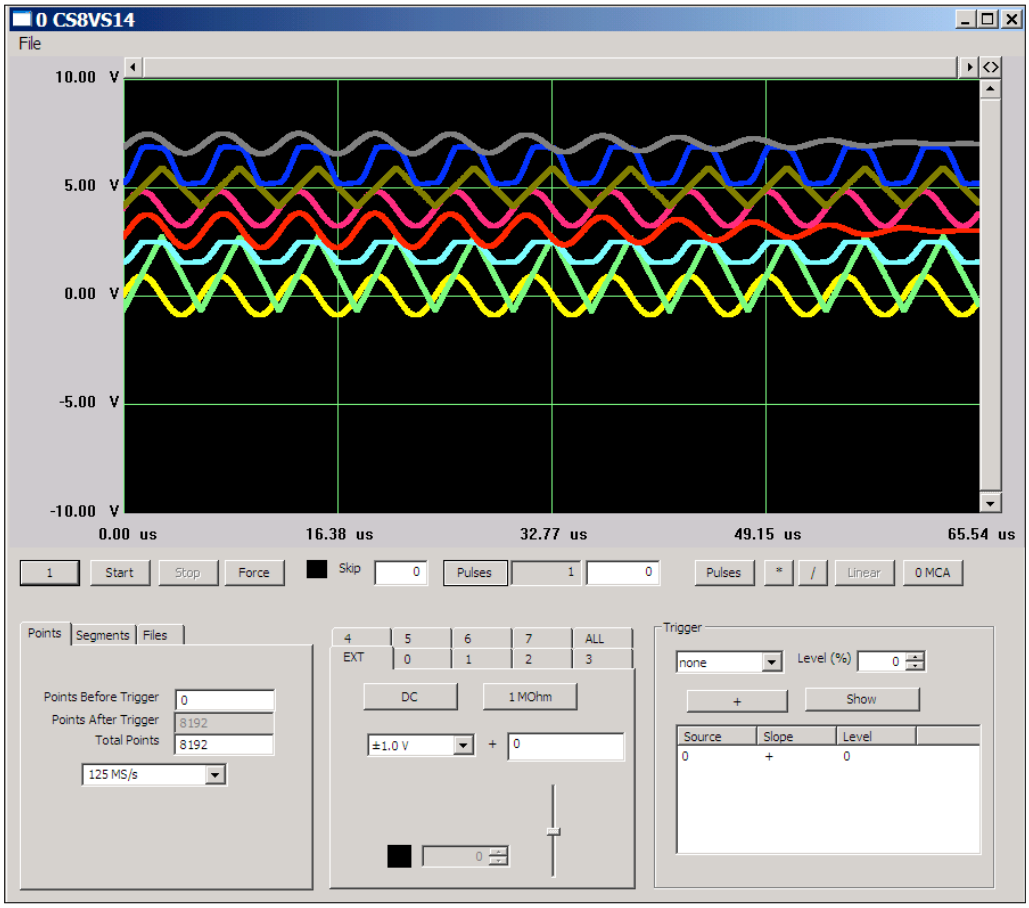

Figure 3.5: A screen shot of the custom control software for the GaGe waveform digitizer. The program can control all the settings of the digitizer, as well as impose certain filters for data before being written to disk.

3.3 FaNS-1 data analysis

The software to analyze the recorded data was based on the IGOR Pro 6 [112] software package. The code was structured into three main sections: 1) reading raw data and producing physics data, 2) performing cuts on physics data, and 3) identifying and subtracting random coincidences.

3.3.1 Reading raw data and producing physics data

The digitized traces are stored in a binary file with an ASCII header containing run parameters for each channel as well as a timestamp for the start of acquisition. Each event begins with a header containing information about which channels are digitized and a timestamp for that particular event. The timestamp is a 44-bit number based on the sample frequency of the digitizer, which increments every 8 ns. The timestamps were zeroed at the beginning of each data file, which typically ran for one hour. The event timestamps are converted into absolute time using the data file timestamp from the header. Thus, each event time is known to approximately 1 second, the resolution of the time stamp in the header. The waveforms are stored in two-character, big-endian, signed integer format. The analysis program reads one event at a time for analysis.

From the helium signals, the location of the trigger, the baseline, the amplitude, and the risetime (defined as the time difference between 10% and 50% of the full amplitude, discussed in Section 2.4) are all extracted. Because the helium detector signals are passed through charge-integrating preamplifiers, the energy in-

formation is in the amplitude of the signals, not the integral. The ^{3}He tubes are self-calibrating; the thermal neutron capture peak is distinct and can be used to accurately calibrate the energy scale when the detectors are operated in the proportional regime.

From each scintillator signal, the integrals of the full and attenuated pulses are converted into energies/energy spectra through gamma calibration data, using either ^{137}Cs or ^{60}Co gamma sources. Figure 3.6b shows an example of the energy spectrum from one detector exposed to a ^{137}Cs source. During long periods of operation, the calibration of the detectors was monitored using ambient background gamma rays. This will be discussed at length in Section 4.2.3.1.

Because plastic scintillator is a low-Z material, the dominant feature in the gamma energy spectrum for plastic scintillator is the Compton edge. To achieve an accurate calibration, the data were compared to a simulated spectrum generated by the MCNP package, previously discussed in Section 2.5. To account for detector resolution, a Gaussian smoothing routine is applied. The smoothed MCNP spectrum is then fit to the data. This process is repeated for varying smoothing parameters, and the fit quality is tracked by the resulting χ^2. Figure 3.6a shows the MCNP spectrum for a ^{137}Cs source before and after smoothing. Figure 3.6c shows the effect of varying the smoothing parameter for the quality of fit and the output calibration factor.

All the extracted parameters from each event are stored in a large 2D matrix, along with the timestamp of the event and the location in the data file. This matrix was written to disk and saved for future analysis.

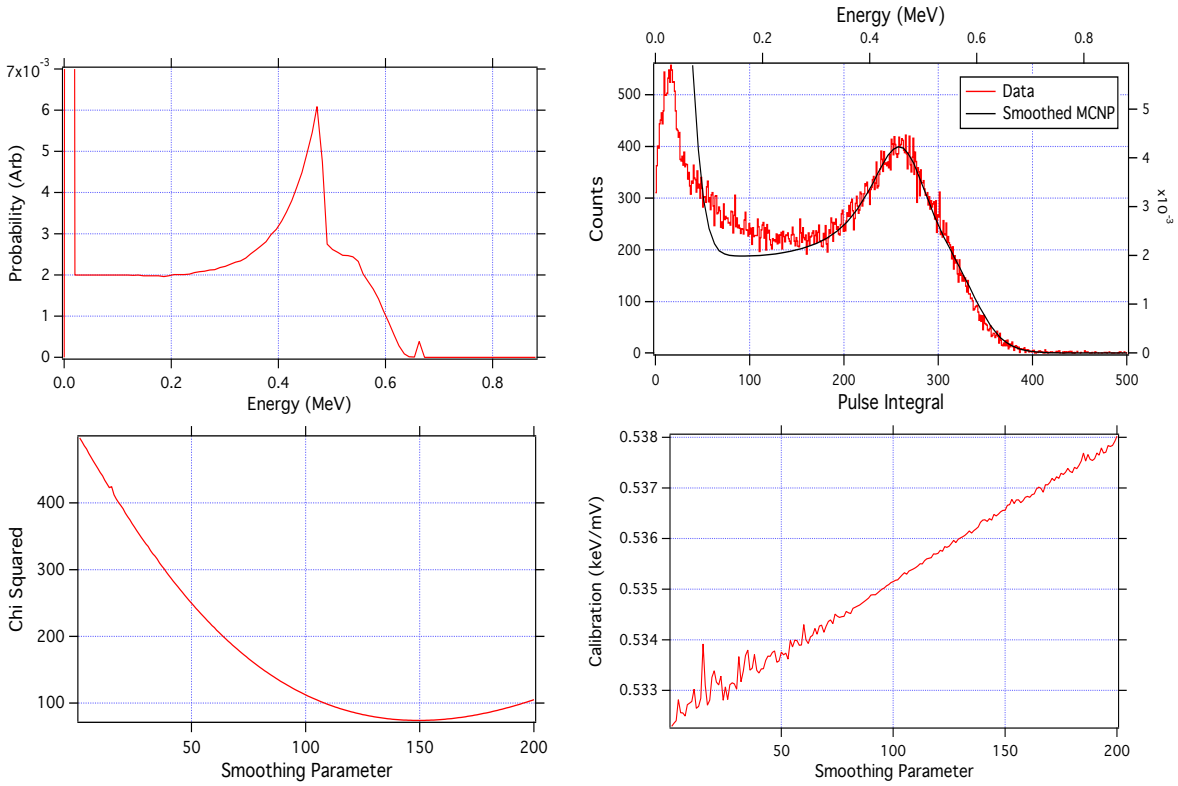

Figure 3.6: Top Left: The spectrum generated by the MCNP simulation for a ^{137}Cs source placed above one FaNS-1 scintillator segment. Top Right: The spectrum of deposited energy from a ^{137}Cs gamma source. Overlaid is the smoothed spectrum from MCNP. Bottom Right and Left: the effects on the fit quality and calibration parameter from varying the smoothing parameter.

3.3.2 Performing cuts

The second part of the analysis involved applying cuts to the analyzed data; Table 3.1 indicates the parameters and the cut ranges used. The cut on energy deposited in the photomultiplier tubes is set to be approximately 3σ above the RMS noise level of the channels. The energy cut on ^{3}He signals is set to the energy range of thermal neutron capture, which is highly peaked at 764 keV, but due to wall effects, extends down to $\sim$200 keV. The cut on the risetime of the ^{3}He signals is designed to reject fast microdischarge noise events without eliminating any neutron-like signals.

Table 3.1: Cut parameters and typical values for FaNS-1 analysis. These cuts are applied to the data using the IGOR Pro software package. See the text for more detail about each parameter.

Parameter	Typical Cut Range
He Energy	(100 keV - 800 keV)
He Risetime	(100 ns - 1 μs)
PMT Energy	(30 keVee - 150 MeVee)
Time Separation	(0 μs - 200 μs)

Occasionally, a trigger will have scintillator signals that are sufficiently separate in time to not be the same particle. It is not possible to discern which scintillator signal was the neutron scatter that lead to the ^{3}He signal and which was an unrelated background gamma. For the analysis in FaNS-1, these multiple site triggers are completely rejected to prevent biasing the data or the background subtraction.

3.3.3 Identifying and subtracting random coincidences

The third main step in the analysis is subtraction of random coincidences. A key feature of the FaNS version of capture-gated spectroscopy is that the scattering event and capture event are in separate detectors. A neutron signal has a definite time-ordering; first the neutron thermalizes in the scintillator, then it is captured in the helium proportional counter. By looking for events where the helium detector fires *before* the PMT signal, a distinctly non-physical coincidence, the random coincidence rate is continually monitored. This can be seen in the histogram, shown in Figure 3.7, of the time separation between the photomultiplier signals and the helium signal.

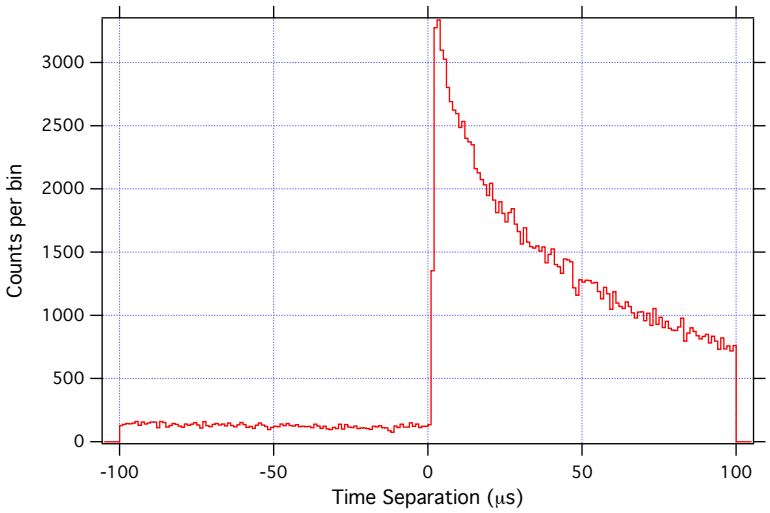

Figure 3.7: Histogram of the time separation between the PMT signals and the helium capture signal. Positive time separation is when the PMT signals precede the helium capture. Negative time separation is when the helium signal precedes the PMT signals, and thus are random coincidences.

By gating on the negative timing events, an energy spectrum of random coincidences can be generated. This can then be subtracted from the positive timing

energy spectrum to yield a true background subtracted energy spectrum. There are a few key advantages to this technique. First, since the random coincidences are measured at the same time as the real events, there is no systematic error from any variation in the run parameters (calibration, temperature, etc). Secondly, any transient source of random events, such as transportation of a source near the detector, can easily be accounted for.

The random coincidence rate can also be calculated with the raw trigger rates of the helium proportional counters and the scintillator bars:

$$\Gamma_r = \Gamma_{scint} \times \Gamma_{helium} \times \tau_{window}, \tag{3.1}$$

where Γ_{scint} and Γ_{helium} are the raw trigger rates in the scintillator segments and helium detectors, and τ_{window} is the coincidence window.

3.4 Neutron calibration of FaNS-1

Characterizing the neutron response of FaNS-1 was accomplished through two distinct types of calibration. First, to understand neutron energy reconstruction, FaNS-1 was exposed to two mono-energetic neutron fields. Second, a calibrated californium neutron source was used to measure the absolute neutron detection efficiency. By detecting the neutron capture rate in FaNS-1 with the neutron source at multiple distances, the efficiency can be decoupled from room-return and other backgrounds.

3.4.1 Monoenergetic Source Calibration at NIST

The Californium Neutron Irradiation Facility (CNIF) at NIST provides an ideal location to calibrate fast neutron detectors. The facility features a boron-loaded thermal neutron shield inside of a larger lab space. The lab is approximately 10 m.w.e. underground, which greatly reduces the cosmic-ray-induced fast neutron background. Housed in the CNIF are the two mono-energetic neutron sources that are used in this work. Figure 3.8 shows the engineering drawing of the CNIF. The location of the boron-loaded shielding is shown by the red rectangle, with the approximate location of FaNS-1 during operation marked by the 'x'.

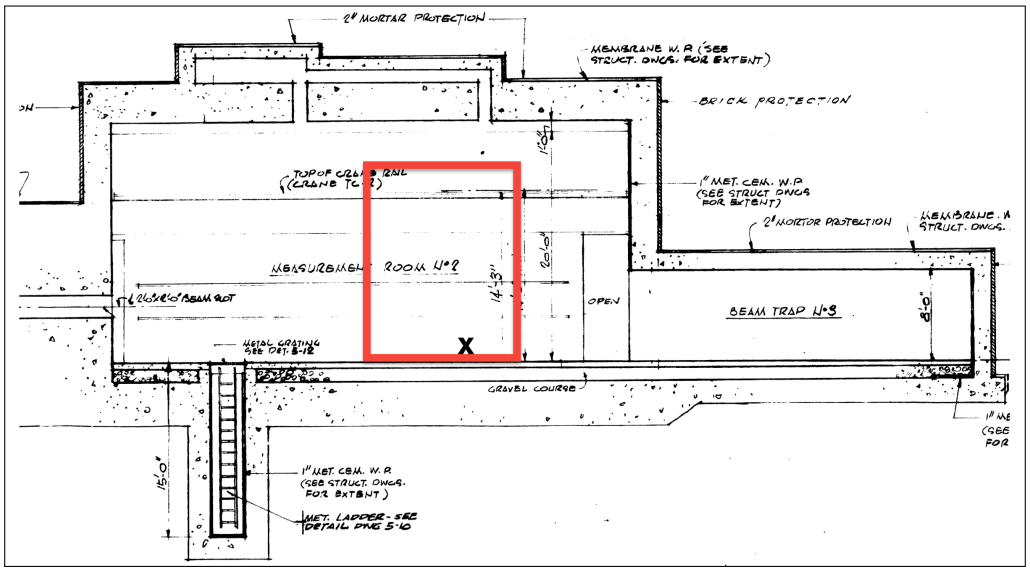

Figure 3.8: Shown is the engineering drawing of the Californium Neutron Irradiation Facility at NIST. The walls are high-density concrete, and the ceiling of the measurement room is approximately 6 meters below grade. The red rectangle shows the position of the boron-loaded shielding walls. The location of FaNS-1 during operation is marked by the 'x' inside the boron shielding walls.

The generators are based on deuterium-deuterium and deuterium-tritium fusion reactions and are manufactured by Thermo-Fisher Scientific [17]. These gener-

ators produce neutrons via the following reactions:

$$D + D \rightarrow {}^{3}\mathrm{He} + n + 3.3\ \mathrm{MeV}, \tag{3.2}$$

$$D + T \rightarrow {}^{4}\mathrm{He} + n + 17.6\ \mathrm{MeV}, \tag{3.3}$$

which result in 2.5 MeV and 14.1 MeV mono-energetic neutrons, respectively. The generators are used to test the detector's energy reconstruction and resolution.

FaNS-1 was operated on the floor of the thermal-neutron-shielded room, approximately 4.5 m below the neutron generators. Figures 3.9a and 3.9b show the detected energy spectrum of the DD and DT neutron sources, respectively. Overlaid are the simulated responses from MCNP.

As can be seen in those histograms, a large fraction of detected events have significantly less energy than expected. After comparison with MCNP and studies of the CNIF, it was concluded that these are from two distinct sources, room-return neutrons and inelastic carbon interactions. Room-return neutrons, those which scatter from the concrete walls before entering the detector, are present in both DD and DT generator data. However, in the DT data, there is a significant fraction of neutrons that inelastically scatter from carbon in the scintillator. These scatters result in either a gamma being emitted by the excited carbon nuclei, or the carbon nucleus breaking up via:

$${}^{12}\mathrm{C} + n \rightarrow \alpha + {}^{9}\mathrm{Be}, \text{ or} \tag{3.4}$$

$${}^{12}\mathrm{C} + n \rightarrow 3\alpha. \tag{3.5}$$

Gammas emitted have a decreased probability of depositing their full energy in the scintillator, and thus energy is lost. Similarly, alpha particles emit significantly less scintillation light than protons and also appear as events with missing energy. These interactions have a threshold of 6.17 MeV and 7.98 MeV respectively, and are therefore not present in the DD neutron data [12].

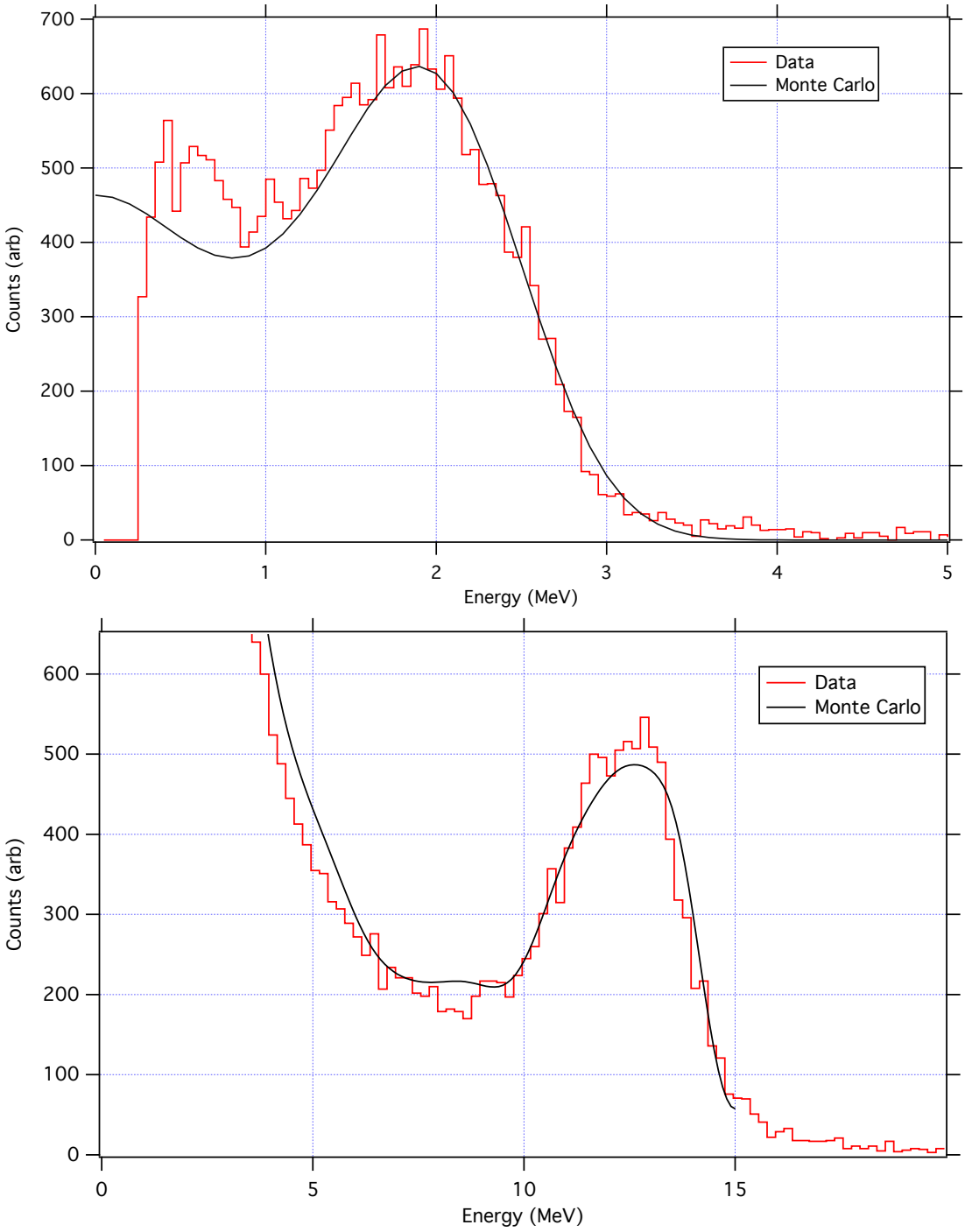

Figure 3.9: Energy spectra of the DD (top) and DT (bottom) neutron generators measured with FaNS-1 in the CNIF. Overlaid are MCNP simulations for the two configurations.

3.4.2 Efficiency calibration at KURF

A ^{252}Cf source was brought to the KURF lab and measurements were taken at several distances to measure the absolute efficiency of FaNS-1. The parameters from these data runs are shown in Table 3.2. The total neutron activity of the source was calibrated by NIST to be 4335 /s at the time of the measurement. For this analysis, two experimental thresholds were used, 1 MeV and 2 MeV. This gives an idea of how the detector's efficiency varies with energy. Using the ENDF-VII standard Maxwellian parameterization of the ^{252}Cf neutron spectrum, $P \propto \sqrt{E}\, e^{E/1.4\ MeV}$ [113], the neutron activities above these two thresholds are estimated at 3385.7 /s and 2006.6 /s. These will be used later in the calculation of the efficiency.

Because the detector is not small compared to the distance at which the source is placed, a simple inverse square law relation cannot be used to estimate the solid angle for each height. Instead, the solid angle subtended is calculated at the average interaction depth for ^{252}Cf neutron energies, which is approximately 3.5 cm [114],

$$\Omega = \int_{SA} \frac{h + z_0}{(x^2 + y^2 + (h + z_0)^2)^{3/2}}\, dx\, dy, \tag{3.6}$$

where x and y map the coordinates on the top surface of the detector, z_0 is the average interaction depth of neutrons in the detector, and h is the height is the distance above the top of the detector where the source was placed. The longest source-data distance was 812.8 cm, with the source across the room, where data were collected for ten days. The side of the detector was facing the source, rather than

the top of the detector. This has been accounted for in the solid angle calculations by using the dimensions of the side of the detector, rather than the top.

To account for dead time in the detector, a scalar module tallied the absolute number of triggers sent to the digitizer. The *time to next event* technique is used to measure the dead time and real event rate directly from the data [12]. The time interval between events are extracted from the timestamps of successive triggers in the digitized data. This technique relies on the Poisson nature of trigger events; the time interval between sequential events, I_1, can be shown to be:

$$I_1(t)dt = re^{-rt}dt, \tag{3.7}$$

where r is the average rate of events. This has a simple exponential form, with the event rate as the decay parameter. By binning and fitting the distribution of intervals between events, the dead-time-independent rate of events can be measured. An example of this is shown in Figure 3.10. The histogram shows the exponential distribution of the intervals. The fit of the distribution yields the event rate for use in the efficiency calculations. The absence of events at short time intervals yields a direct measurement of the dead time for a single event; there are no intervals shorter than 10 ms.

To measure the background-subtracted rate for each distance, the time interval distributions are fit for positive and negative timing events. Then the rates are subtracted as discussed in the previous chapter. The results of each distance are

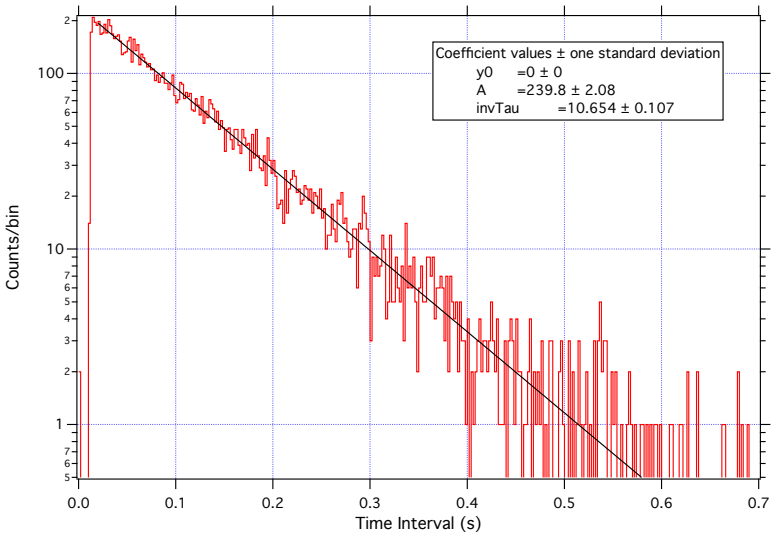

Figure 3.10: A histogram of the time intervals between successive events in FaNS-1 data for a ^{252}Cf source at 29.9 cm above the center of the detector. The line is an exponential fit, with the decay constant equal to the dead-time-free neutron rate. Note the absence of events at the beginning of the histogram, with time intervals shorter than 10 ms; this is a measure of the dead time for each event.

shown in Table 3.2. The total rate R_{tot} above threshold is given by

$$R_{tot} = \epsilon A_{\mathrm{Cf}} \Omega + R_{rr} + R_b, \tag{3.8}$$

where ϵ is the detector efficiency, A_{Cf} is the neutron source activity, and Ω is the fractional solid angle subtended by the detector from the source, as discussed earlier. R_{rr} is the rate in the detector due to room-return neutrons (i.e., those source neutrons that scatter from the surrounding environment into the detector), and R_b is the background rate in the detector when there is no source present.

The ambient neutron rate is small at KURF, approximately 1 /day, and can be ignored for these measurements. The room return term depends on the geometry and material composition of the room. The rate is largely constant over the range

of measurement positions for a given source activity [115, 116]. To determine R_{rr}, measurements were taken with the source placed at several distances, r, from the detector. The intercept of a linear fit to the total rate in the detector versus fractional solid angle gives the value of R_{rr}. Figure 3.11 shows the fit for data acquired at five distances.

Table 3.2: Data from efficiency measurements taken with ^{252}Cf neutron source. Note, there was a source of noise that prevented the 1 MeV analysis of the 120 cm data.

Distance (cm)	Exposure (s)	Fractional Solid Angle	Rate above 1 MeV (n/s)	Rate above 2 MeV (n/s)
812.8	878400	$(6.6\pm0.3)\times10^{-5}$	$(1.7\pm.2)\times10^{-3}$	$(8\pm3)\times10^{-4}$
120.0	71762.5	$(4.2\pm0.2)\times10^{-3}$		0.098±0.003
90.17	48086.6	$(7.1\pm0.4)\times10^{-3}$	0.314± 0.004	0.208±.003
49.53	1984.1	$(2.1\pm0.1)\times10^{-2}$	0.86±0.07	0.55±0.03
29.85	1073.5	$(4.8\pm0.2)\times10^{-2}$	1.94±0.08	1.35±0.08

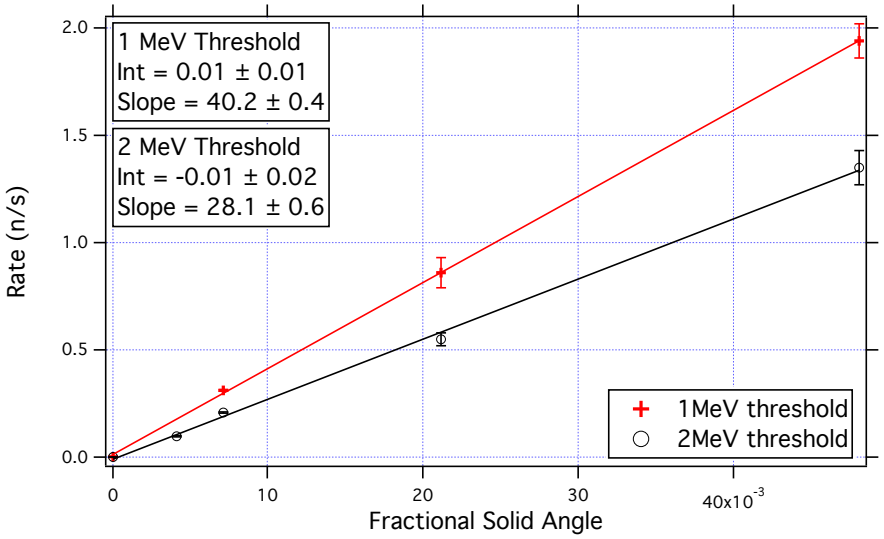

Figure 3.11: Detected rate of neutrons from ^{252}Cf source placed at various distances from the detector versus the fractional solid angle subtended by the detector. The red crosses are for analysis threshold of 1 MeV and the black circles are for a threshold of 2 MeV. Y-error bars shown are the fit errors of the time interval distributions. The line is a fit to the data.

From the slope and intercept of the linear fit, the efficiency and room return are determined, respectively. The room return is equal to the y-intercept of the fit, which for both of these analyses is consistent with zero. The efficiencies for each threshold are shown here:

$$\varepsilon = \frac{slope}{\Gamma_s}, \tag{3.9}$$

$$\varepsilon_{(1\text{ MeV})} = \frac{40.2 \pm 0.8\ n/s}{3385.7 \pm 300\ n/s} = 1.2 \pm 0.12\,\%, \tag{3.10}$$

$$\varepsilon_{(2\text{ MeV})} = \frac{28.1 \pm 0.6\ n/s}{2006.6 \pm 200\ n/s} = 1.4 \pm 0.14\,\%. \tag{3.11}$$

The leading error in this analysis is due to the uncertainty in z, the depth at which the neutrons interact, as included in the calculation of the effective solid angle (Equation 3.6). By varying the effective depth of the detector and noting the effect on the fitted slope, an uncertainty of 2% in the slope is estimated. The uncertainty in the activity is due to placing a threshold in the ^{252}Cf spectrum. There is some discrepancy between models of the ^{252}Cf neutron energy spectrum, as well as the uncertainty in the absolute threshold. This uncertainty is estimated at 10%.

The efficiency calibrations have been performed in identical settings as the underground measurements performed at KURF, including all the same cuts. This efficiency can therefore be used to convert detected neutron rates at KURF into incident neutron flux.

3.4.3 Calibration conclusions

FaNS-1 has been shown to accurately detect neutrons from mono-energetic and broad spectrum sources. The neutron generator data highlight the power of capture-gated spectroscopy. By rejecting partial energy deposition events, a neutron energy spectrum with a well-defined peak is detected. The ^{252}Cf measurements provide important characterization of the detection efficiency that will be used later to estimate the total neutron flux at the surface and underground. These data are featured in the next chapter.

Chapter 4

Surface and underground results from FaNS-1

For production data, FaNS-1 was operated in two different environments. First, it was used to measure the comsmogenic neutron energy spectrum outside of the Radiation Physics building (Building 245) at NIST, Gaithersburg. FaNS-1 was then installed approximately 1450 m.w.e. underground at the Kimballton Underground Research Facility in Ripplemead, VA, where it was used to measure the ambient neutron spectrum and flux.

4.1 Surface measurement at the Radiation Physics Building, NIST

The surface fast neutron energy spectrum and flux have been extensively measured using Bonnor sphere arrays, as discussed in Chapter 1. However, there are distinct disadvantages of these detector systems. These detectors do not directly measure the energy of neutron interactions. Rather, they monitor the count rates of detectors with different energy acceptances. A main source of uncertainty in previous measurements is the reliance on unfolding procedures to produce a neutron spectrum from Monte Carlo generated response functions. Determining uncertainty in the output spectrum from unfolding is exceptionally difficult and convoluted.

Uncertainty in the spectrum and flux of cosmogenic fast neutrons is a concern for the production and transport of low radioactivity materials used in underground

experiments [43]. A more accurate, direct measurement would help reduce these uncertainties. To this end, FaNS-1 was installed in a low-overburden lab to measure the fast neutron energy spectrum. The detector was located at approximately 100 m above sea level.

Cosmogenic neutrons also serve as a convenient source of high energy neutrons to test the response of the detector. The highest energy neutron source available at NIST is 14 MeV, while the surface neutron spectrum extends well beyond 1 GeV. A measurement of the cosmogenic neutron spectrum acts as a separate calibration of the detector and can be validated with MCNP.

To model the response of FaNS-1 to the cosmogenic fast neutron spectrum, a Monte Carlo simulation was performed using MCNP. The input neutron spectrum was that reported in JEDEC standard 89A[1] [117]. This standard is based upon a measurement performed in New York City using an array of Bonner spheres, and subsequently unfolded using the MAXED 3.1 software package [23, 118]. The spectrum is shown in Figure 4.1. This spectrum includes neutrons that have backscattered off of the concrete pad on which the detectors operated.

Outside NIST Building 245, a standard cargo container was installed to test the response of portal monitors to various source configurations [119]. This container, shown in Figure 4.2, provided a convenient location to measure the ambient cosmic-ray-induced neutron spectrum. The container is constructed of thin steel, which should ensure that the neutron energy spectrum to which FaNS-1 is exposed

[1] JEDEC Solid State Technology Association is a trade organization that represents over 300 members, including IBM, Samsung, and Intel. Fast neutron interactions create faults and errors in microchips, which cause device failures. This is a particular problem for the aerospace industry, where the electronics are exposed to a significantly higher dose.

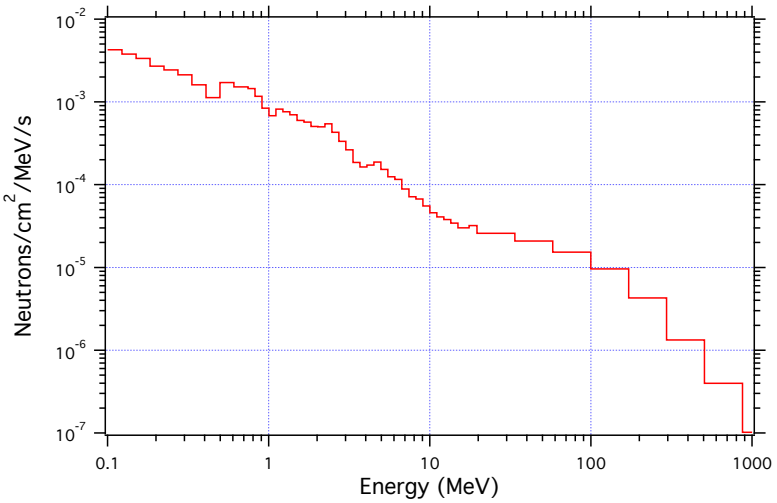

Figure 4.1: The JEDEC standard ambient fast neutron energy spectrum at sea-level as measured with a Bonner Sphere array in Reference [23, 117]. This spectrum includes neutrons that have backscattered off of the concrete pad on which the detectors operated.

is altered as little as possible from the incident spectrum. The container is approximately 1.6 m above a concrete pad. This reduces the probability that neutrons could scatter off the ground and into the detector, which would distort the energy spectrum of events.

Within the container, FaNS-1 was placed on the floor, directly on top of a sheet of 3 mm thick boron-loaded rubber (boroflex) to shield thermal neutrons. The detector was approximately 7 m from the concrete wall of Building 245. The building shields the detector a negligible amount, and does not effect the measurement. Using the technique discussed in Chapter 3, FaNS-1 was calibrated with a ^{137}Cs gamma source and data were collected for approximately three days.

Figure 4.2: Arial photo of the cargo container (white, center) outside of building 245 at NIST. This standard ISO container has been outfitted with power and was a convenient location to install FaNS-1. The detector's location is marked by a red 'x'.

4.1.1 Gamma calibration

Following the procedure laid out in the previous chapter, the calibrations for the surface run were determined. Figure 4.3 shows the pre-calibration pulse integral histograms for each scintillator block of FaNS-1 when exposed to ^{137}Cs. The resulting calibration and smoothing parameters are shown in Table 4.1. The reasonable gain matching allows us to use consistent thresholds between the channels in analysis.

With the use of the splitter summer modules discussed earlier, these calibrations yield an effective upper limit of ∼150 MeV /segment. Above this energy, the

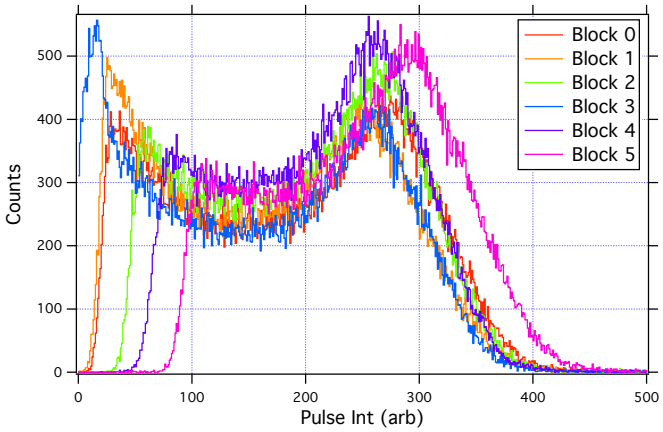

Figure 4.3: Histograms of the pulse integrals for gamma calibration data from a ^{137}Cs source placed above each of the FaNS-1 scintillator segments. These histograms are subsequently fit with an MCNP template and the calibration factor is extracted, as discussed in Section 3.3.

electronics saturate and energy information is lost. If events saturate a channel, they are excluded from the analysis.

An issue with the scintillator thresholds was discovered during the analysis of FaNS-1. As a proof-of-principle detector, careful studies of the photon statistics of the PMTs were not undertaken. Thus, the efficiency for detecting events close to the threshold suffer from photon fluctuations that have not been included in the Monte Carlo simulations. The uncertainty is estimated at 20% through experimental variations in the analysis thresholds. This is an area that has yielded important lessons learned from FaNS-1, and great effort has been undertaken to account for them in FaNS-2.

Table 4.1: Table of the different calibration factors for the surface data series. The pulse integrals are multiplied by the calibration parameters to convert from pulse integral into energy. The Full/Attenuated pulse ratios are calculated by averaging the ratio of full to attenuated pulses for each event. These ratios are used in the analysis to convert the attenuated signals to energy.

Segment	Calibration (MeV/integral)	Full/Attenuated Pulse Ratio
Block 0	0.00167	9.93
Block 1	0.00179	10.42
Block 2	0.00172	10.33
Block 3	0.00176	10.38
Block 4	0.00174	9.99
Block 5	0.00157	10.32

4.1.2 Run conditions

The data used in this analysis were collected between May 28, 2010 and May 30, 2010. These data are selected based upon the reasonable gain-match between the PMTs and stability of the data acquisition system. The data were recorded in 1800 second long files, each with the same base name and incrementing run numbers. The total accumulated data for this series was approximately 100 GB.

It was discovered afterwards that a few of the ^{3}He proportional counters had high rates of alpha particle and micro-discharge events. Evidence for these events can be seen in the number of counts with energies above the neutron capture peak. To mitigate these backgrounds, a tight cut is placed on the neutron capture peak of plus/minus twice the width of the peak, as shown in Figure 4.4. By making a similar cut in neutron source data, the fraction of neutron captures that survive this cut is determined to be $77 \pm 2\%$.

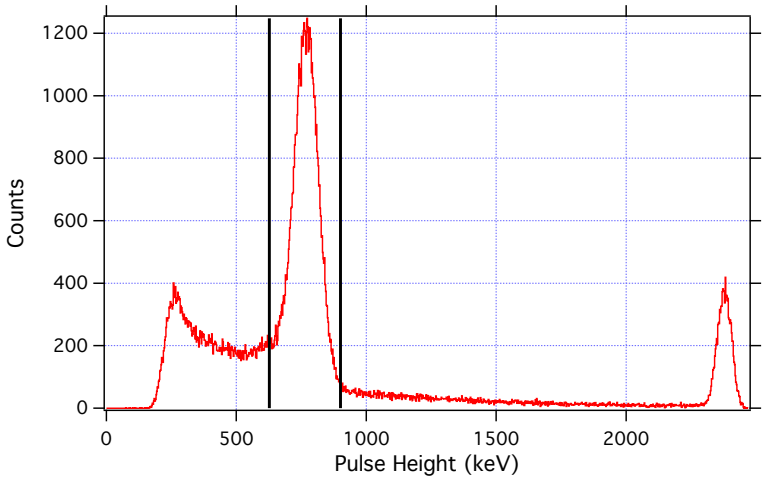

Figure 4.4: Uncut energy spectrum of ^{3}He triggers in the surface data set. The vertical bars shown are the locations of the cuts applied to the ^{3}He energy: $\pm 2\sigma$, with σ being the peak width. This eliminates much of the backgrounds from alpha particles and micro-discharges. Note, the peak at approximately 2.3 MeV is from saturation of the electronics.

4.1.3 Surface Results

During the period of operation, 131,252 events were recorded in 1.62×10^5 seconds, for a raw trigger rate of 0.81 /s. For this analysis, the threshold of neutron energy was set to 1 MeV$_n$. After applying coincidence requirements and basic cuts on the neutron capture energy in the helium detectors, 1.18×10^4 events remained, for a post-cut rate of 0.073 /s. After subtraction of the random coincidences, 5133 events remained for a final detected neutron rate of 0.032 /s. A plot of the pre- and post-cut data rates is shown in Figure 4.5. Large fluctuations can be seen in the pre-cut rate that are due to noise in the helium detectors. The noise trigger rate increased with the temperature in the trailer, which reached above 38° Celcius when the sun shone directly on it in the morning. However, the post-cut event rate does not show such a variation.

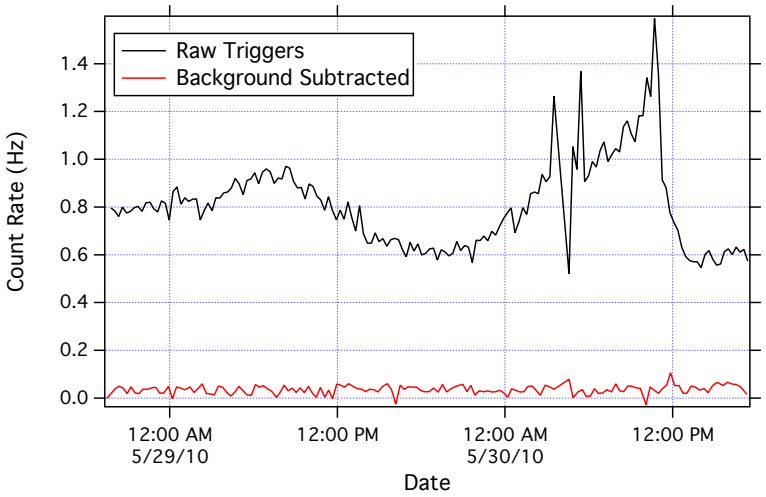

Figure 4.5: The pre- and post-cut event rates for FaNS-1 operating at the surface on May 29-30, 2010. The large fluctuations in the pre-cut rate are due to temperature fluctuations in the trailer, which exceeded 40 degrees Celsius during the morning when the sun was shining directly on the trailer.

A histogram of the time separation of each event is shown in Figure 4.6a. For this data set, the acquisition window was extended to (-100,+300 μs) to improve coincidence efficiency. Since the detector operated at a low trigger rate, this did not increase dead-time or cause other performance issues. After investigation with MCNP, it is estimated that truncating the time separation to 300 μs eliminates $6 \pm 2\%$ of the captures. This loss will be corrected in the final result. Figure 4.6b shows the energy spectra for the random and real+random events as determined by the timing distribution.

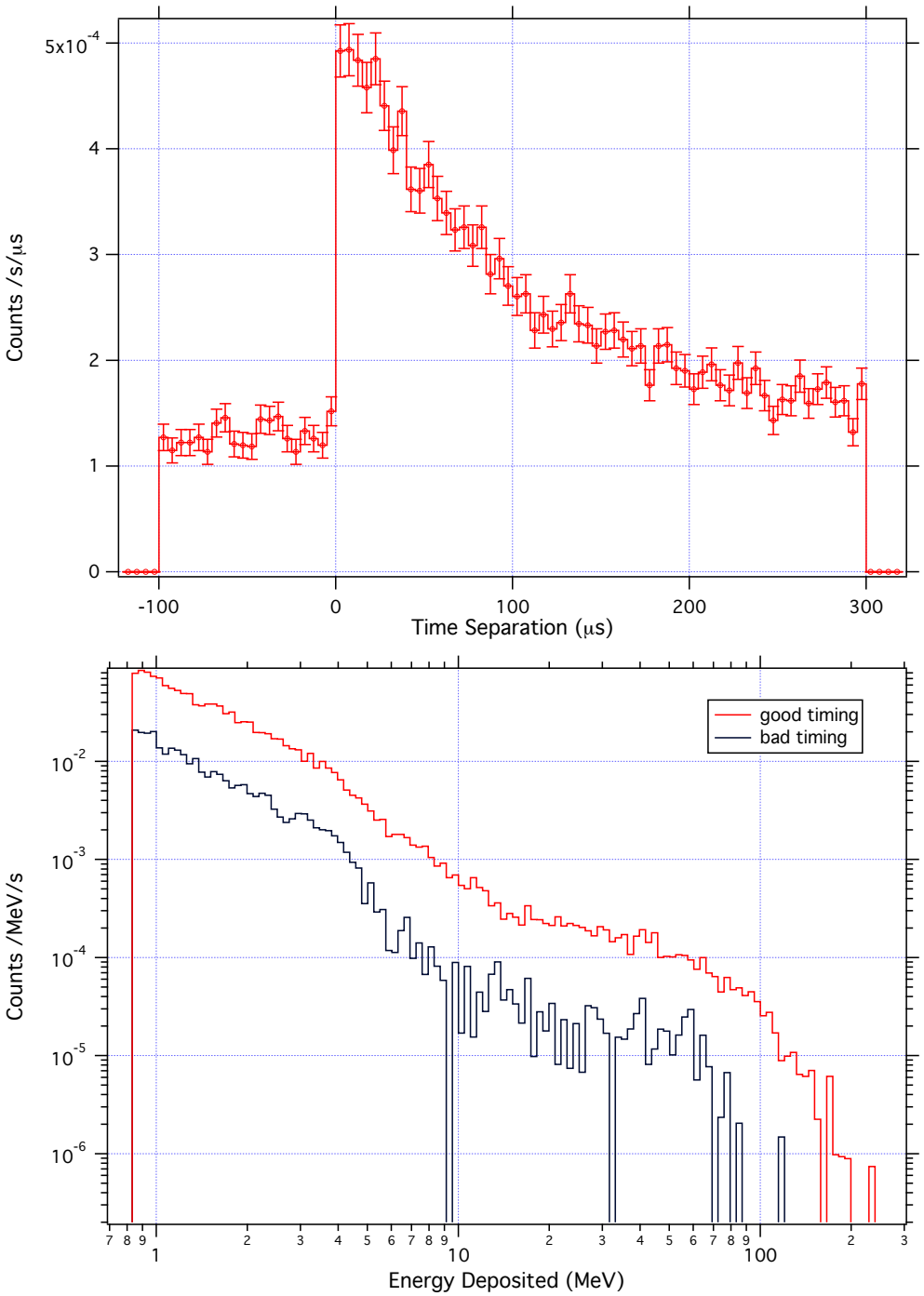

Figure 4.6: The timing spectrum from a data run of 1.62×10^5 s live at NIST Gaithersburg. Note the larger acceptance window $(-100, +300\mu s)$ for coincidences improved detection efficiency, but due to low trigger rate, did not increase dead-time. Energy spectra of the positive and negative timing events. The negative timing events are subtracted from the positive timing events to generate the detected neutron spectrum.

Using the same background subtraction and pulse height method as before, the neutron spectrum shown in Figure 4.7 is generated. The detectors response to the measured neutron spectrum shown in Figure 4.1 was simulated for neutrons with energies above 0.122 MeV. The truncation of the energy spectrum minimizes simulation time and prevents an artificial suppression of the efficiency from including neutrons below the experimental threshold (1 MeV). The Monte Carlo was performed by simulating 2×10^7 neutrons isotropically thrown from a sphere 75 cm in radius. This corresponds to a neutron fluence of 1.13×10^3 n/cm^2 with energies above 0.122 MeV, and a fluence of 891.8 n/cm^2 with energies above 1 MeV inside the detector volume.

After applying the experimental cuts to the Monte Carlo, a total of 10962 events remained. Using the aforementioned fluence (891.8 n/cm^2), and the overall ^{3}He detection efficiency of (84±10)%, as discussed in Section 2.4.4, the detector was found to have an average sensitivity to the cosmic ray fast neutron spectrum above 1 MeV:

$$\epsilon = \frac{10962 \pm 100\ n}{(8.91 \pm 0.4) \times 10^2\ n/cm^2} \times 0.84 \pm 0.1 \tag{4.1}$$

$$\epsilon = 10.3 \pm 2.5\ n/(n/cm^2). \tag{4.2}$$

This sensitivity is comparable to an efficiency weighted by the incident neutron spectrum. The effect of truncating the coincidence time to 300 μs is included in the MCNP response. Combining this with the number of neutrons detected and the

total exposure time, the detected neutron flux can be determined:

$$\Phi(n) = \frac{N}{\tau_e \times \epsilon} \times \frac{1}{\epsilon_{He}} \tag{4.3}$$

$$\Phi(n) = \frac{5133 \pm 1000\ n}{1.62 \times 10^5\ s \times (10.3 \pm 2.5)\ n/(n/cm^2)} \times \frac{1}{0.77 \pm 0.02} \tag{4.4}$$

$$\Phi(n) = (4.0 \pm 1) \times 10^{-3}\ n/cm^2/s, \tag{4.5}$$

where N is the number of background subtracted neutrons, τ_e is the exposure time, ϵ is the MCNP generated efficiency, and ϵ_{He} is the cut efficiency of the ^{3}He signals. The uncertainty in the counts shown here is dominated by the 20% uncertainty in the location of the thresholds.

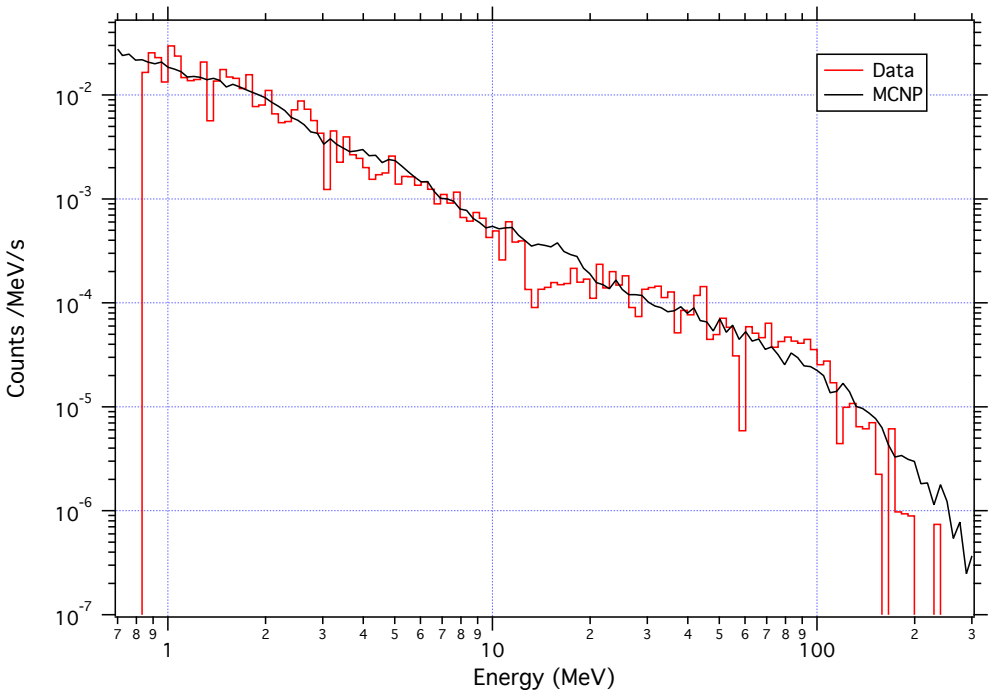

Figure 4.7: The detected neutron energy spectrum at NIST Gaithersburg. Overlaid is an MCNPX simulation of the detector's response to the reported spectrum from Reference [23]. The Monte Carlo has been scaled to overlay the data.

4.1.4 Surface conclusions

There is very good agreement between the measured and simulated energy spectra shape over a broad range of energies. Using the Monte Carlo generated sensitivity for FaNS-1, the surface fast neutron flux above 1.0 MeV at NIST is found to be $(4.0 \pm 1) \times 10^{-3}\ n/cm^2/s$.

There are no other sources available for testing FaNS-1 with such high energy neutrons. Operation of FaNS-1 in the cargo container demonstrated that the detector has a large dynamic range, with a sensitivity to fast neutrons from 1 MeV up to 300 MeV. In less than two days of exposure, a detailed spectrum was measured with FaNS-1 that agrees with previous measurements. The measurement of the cosmic-ray induced fast neutron spectrum demonstrates the detector's sensitivity, which can now by applied to a measurement of the ambient fast neutron spectrum and flux at the Kimballton Underground Research Facility.

There are two major uncertainties in the flux measurement performed with FaNS-1, both of which relate to the comparison between data and simulation. First is the uncertainty in the experimental thresholds caused by photon statistical fluctuations. This leads to an imprecise and non-uniform application of thresholds based upon Poisson fluctuations in the number of detected photons. The second major uncertainty is due to inconsistencies between the data and Monte Carlo simulation of the ^{3}He proportional counter sensitivity. These two uncertainties dominate the measurement, and they will guide improvements made when designing and operating FaNS-2.

4.2 Operation at Kimballton Underground Research Facility

The FaNS-1 spectrometer also operated at the Kimballton Underground Research Facility (KURF), located at Lhoist North America's Kimballton mine in Ripplemead, VA. The facility is located in a vein of high purity limestone at a depth of 1450 meters water equivalent (m.w.e.) and provides a good low-radioactivity counting environment [107]. FaNS-1 was commissioned at KURF in the summer of 2010.

4.2.1 The Kimballton Underground Research Facility

The KURF lab is a large enclosure, built in 2007, in a drift of the 14 East level of the mine. The drift is approximately 12 m wide and 30 m high in the area of the lab, and the enclosure itself is 10.5 m wide $\times$ 30 m long $\times$ 6.1 m high, as shown in Figure 4.8. There are currently more than 10 experiments operating at KURF, ranging from screening facilities for materials selection [107, 120] to prototypes of larger detectors [121,122] and full experiments [123]. The experiments need to know the fast neutron background to properly account for it in their analyses.

There are two main sources of neutron backgrounds at KURF. First are neutrons from radioactive decays, both spontaneous fission and (α,n), of U and Th in the surrounding limestone. These neutrons typically range in energy from 1 to 10 MeV. Second, although highly suppressed by the overburden above the lab, is muon spallation of the surrounding material that produce neutrons with energies from a few MeV to greater than 100 GeV.

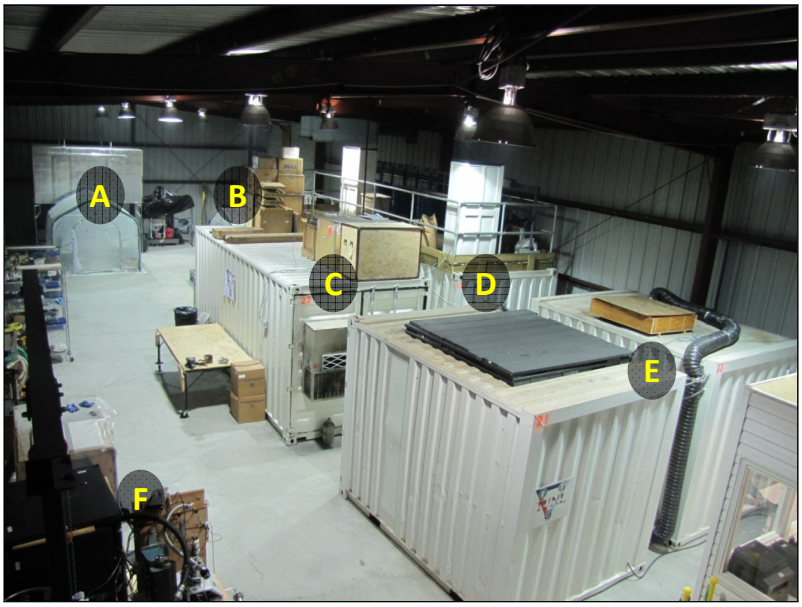

Figure 4.8: A photo of the enclosure for KURF. The various experiments are labeled A) MiniLENS [121], B) FaNS, C)TUNL $\beta\beta$ Decay [123], D) Low Background Screening [107], E) MALBEK [120], and F) DarkSide argon test [122].

For 1450 m.w.e., an estimate of the muon-induced neutron flux is obtained using the method of Mei and Hime [36]. They have generated a parameterization for the muon-induced neutron flux as a function of depth:

$$\phi_n = P_0(P_1/h_0)e^{-h_0/P_1}, \tag{4.6}$$

where h_0 is the vertical depth in km.w.e. The fit parameters are $P_0 = 4 \pm 1.1 \times 10^{-7}$ /cm^2/s and $P_1 = 0.86 \pm 0.05$ km.w.e. For the depth of KURF, there is an expected muon-induced neutron flux of 4.4×10^{-8} n/cm^2/s. To estimate the fraction of muon-induced neutrons with energies above 1 MeV and 10 MeV, the simulated values for a laboratory at a similar depth are scaled by the relative depth. For the Waste Isolation Pilot Plant (WIPP), located at 1585 m.w.e., Mei et al. have

simulated a total muon-induced neutron flux of 3.4×10^{-8} n/cm^2/s, with 3.2×10^{-9} n/cm^2/s between 1 MeV and 10 MeV, and 7.5×10^{-9} n/cm^2/s above 10 MeV. The corresponding fluxes for KURF can be estimated by scaling the WIPP results by the ratio of the total fluxes, as shown in Table 4.2.

Table 4.2: Estimates of the muon-induced neutron fluxes, in units of 10^{-9} n/cm^2/s, at WIPP and KURF. The WIPP data are from Reference [36], and the KURF data have been scaled by the ratio of the calculated total muon-induced neutron fluxes at WIPP and KURF.

Lab	Total Flux	1 MeV - 10 MeV	10 MeV - 100 MeV	<100 MeV
WIPP	34	3.2	5.9	1.56
KURF	44	4.1	7.6	2.0

The neutron flux and spectra from radioactivity in the lab is harder to predict, as it depends on the local composition of the materials. The majority of these neutrons are due to (α, n) reactions within the rock and surrounding material, which range in energy up to 8-10 MeV. The flux and spectra depend greatly on the alpha energies and material composition. Figure 4.9a shows different (α, n) spectra that have been simulated for two rock compositions.

Estimating the absolute flux of (α,n) neutrons is difficult. The rate is highly dependent on the distribution of isotopes within the material as well as neutron transport out of the rock and concrete. Measuring the neutron spectrum in situ is an important tool to constrain the (α, n) backgrounds that can cause problems for the other experiments at KURF.

Mei et al. have also simulated a comparison between the (α,n) and muon-induced neutrons at Gran Sasso National Laboratory in L'Aquila, Italy. Figure 4.9b

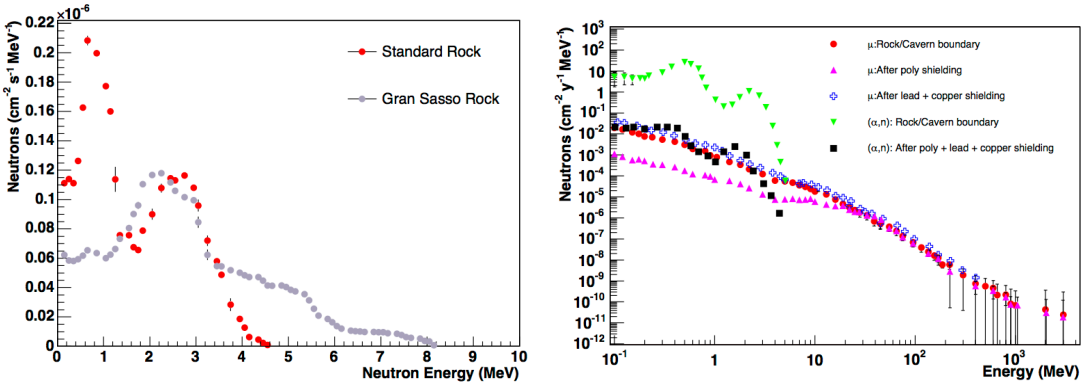

Figure 4.9: Left: The energy spectra for neutrons from (α, n) reactions in two different rock compositions. Note, these spectra are both harder than that of spontaneous fission. Right: The neutron energy spectra from various sources at Gran Sasso National Lab in L'Aquila Italy. The two curves of interest to this work are the muon-induced neutrons at the Rock/Cavern boundary (red circles) and the (α,n) at the Rock/Cavern boundary (green triangles). Figures from Reference [36].

shows the neutron energy spectra for both (α,n) and muon-induced neutrons at Gran Sasso. The spectral shape of muon induced neutrons is similar to the cosmogenic neutron spectrum at the surface. For the final analysis, the detector response of FaNS-1 at the surface will be used to convert the measured neutron rate into an incident neutron flux.

4.2.2 The UMD/NIST installation at KURF

Each group working at KURF has a designated area for their operations. Many groups use standard ISO containers to enclose their experiments. It was decided to minimize external shielding of the detector by using a thin plastic-walled tent. This provided appropriate space delineation, as well as allowing for a fixed volume of air for purification, using a HEPA filter. Air quality is a key concern at KURF due to the excessive amount of diesel soot generated by mining equipment. Diesel

soot is conductive and can generate shorts in electronics and high voltage power supplies, generating noise or failure. The HEPA filter deployed in the enclosure performed well, minimizing the build up of soot on the electronics. However, after approximately 1.5 years of operation, small leakage currents developed in the high voltage power supplies. An attempt to throughly clean the units was made during one visit, with mixed success.

The tent was kept at approximately 27° Celsius and 40% relative humidity using a ceramic heater and a standard dehumidifier. The temperatures in and around the enclosure were monitored using a USB thermocouple data logger from Omega (model TC-08) [124]. The temperatures inside the enclosure, in the main lab, inside the DAQ computer, and internal to the data logger are shown in Figure 4.10a as a function of date and time. Small temperature fluctuations caused by the dehumidifier cycling on and off every few minutes are observed[2].

Limits were set up to alert any over-temperature conditions, which were defined as any temperature exceeding 40° Celsius. This was specifically to ensure that in the event of a fan failure, the data acquisition could be shut down in time to prevent damage being done to the GaGe digital oscilloscope. During the operation at KURF no alerts were received. The relative humidity was also monitored, for a limited period of time, using an Omega OM-EL-USB-RT data logger [125]. A selection of the data is shown in Figure 4.10b. The external humidity in the Kimballton Mine is approximately 100% due to water spraying for dust mitigation. This level

[2]There are larger fluctuations of 1-2 degrees Celsius. These have been correlated with researchers entering the lab and turning on the lights.

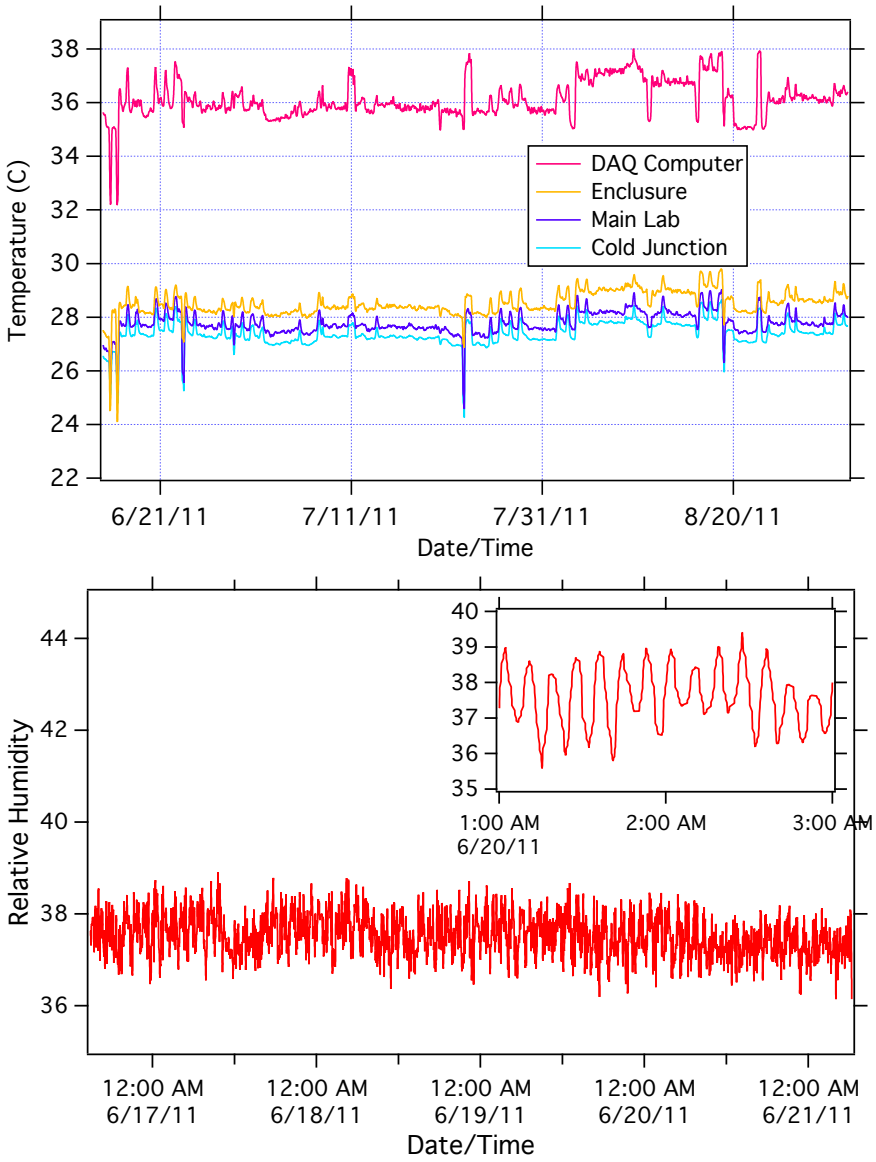

Figure 4.10: Top: The recorded data from the temperature monitoring system in the UMD/NIST enclosure at KURF. Shown are the readings from thermocouples positioned inside the enclosure, inside the DAQ computer, and in the main lab. Also shown is the internal "Cold Junction" that acts as a reference point to the other measurements. The temperatures were quite stable over the course of the selected data sets. The periodic up-ticks in the temperature are due to other researchers turning on the lights in the lab when they were working. Bottom: A selection of the humidity data recorded with the OM-EL-USB-RT monitor. Note the stability of the humidity, which doesn't vary more than a few percent. The inset figure shows a zoomed-in section that highlights the cycling of the dehumidifier.

of humidity would be dangerous to operate the high voltage, as condensation would lead to shorts and sparks. Figure 4.10b shows the effectiveness of the dehumidifier.

4.2.3 Final data run at KURF

The two years of operation at KURF can be divided into three main data sets. The first led to the discovery of high alpha particle backgrounds in the ^{3}He counters. The second set was carried out after a complete overhaul of the ^{3}He system to install low-background detectors and upgrade the preamplifiers to allow for pulse-shape discrimination. However, these data were plagued with PMT calibration drift and could not be salvaged. The final data set followed a resurrection of the PMTs and a complete gain match between the channels. This final set is what is analyzed and presented in this chapter.

4.2.3.1 Gamma calibration

An initial calibration was performed using a ^{60}Co gamma source. The recorded gamma spectra are shown in Figure 4.11. Note, one of the channels, Ch1, has a substantially lower response than the others. Due to the decrease in gain in the PMTs, sufficient high voltage could not be supplied to these tubes to match the other channels. It was decided that corrections could be made in analysis for this difference.

To monitor the gamma calibration during the operation at KURF, 100 s of PMT free-trigger data were collected every hour. The energy spectrum of these

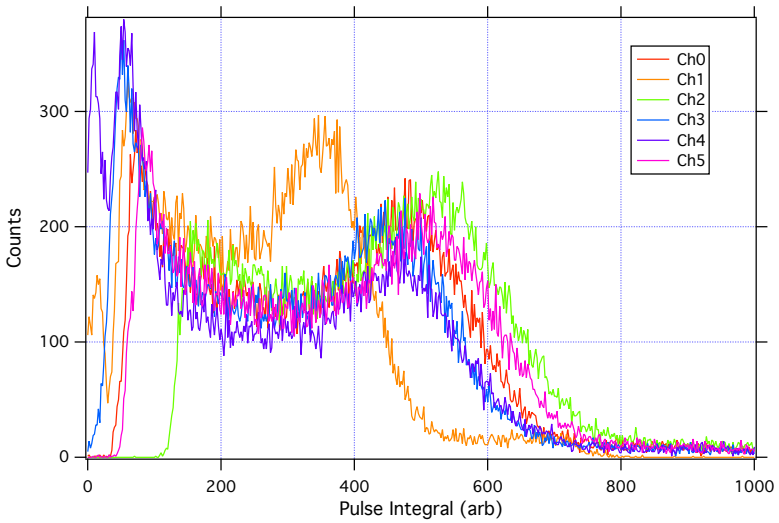

Figure 4.11: The energy spectra recorded by each scintillator bar in FaNS-1 when exposed to a ^{60}Co gamma source. By fitting these spectra, the starting gamma calibration factors used in the analysis are obtained.

calibration runs was dominated by two main gamma backgrounds present in the lab: ^{40}K and ^{208}Tl with energies of 1.4 MeV and 2.6 MeV respectively. Gamma spectra recorded by a germanium detector and a FaNS-1 plastic scintillator block are shown Figure 4.12. The germanium detector has a few prominent energy peaks, most notably the ^{208}Tl peak at the highest energy.

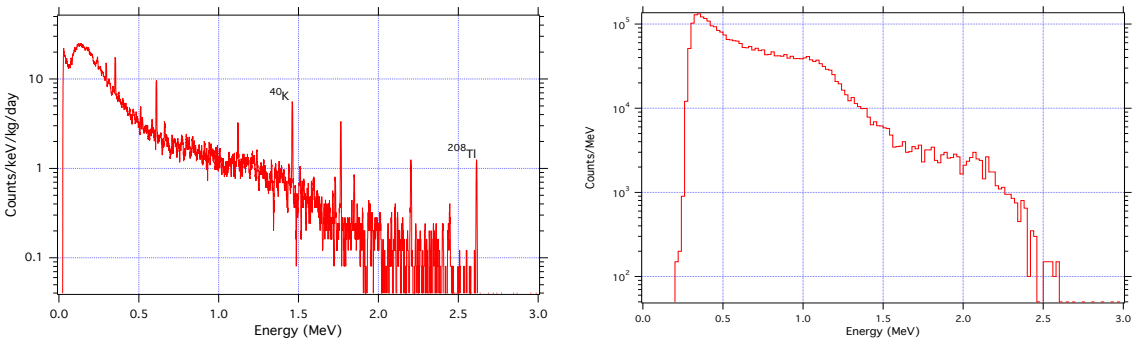

Figure 4.12: Left: The measured gamma spectrum at KURF from the VT-1 germanium detector [107]. Right: The gamma spectrum measured with one of the FaNS-1 plastic scintillator bars. Note the Compton edges from ^{40}K and ^{208}Tl in the spectrum at approximately 1.2 and 2.4 MeV.

During the long operation at KURF, photomultiplier tube gains decreased.[3] Figure 4.13a shows a collection of gamma spectra taken with the same block of scintillator over the course of two months; the colors highlight the progression in time of the drift. The upper edge of the spectrum begins at approximately channel 2600, but drifts downwards to below channel 2000.

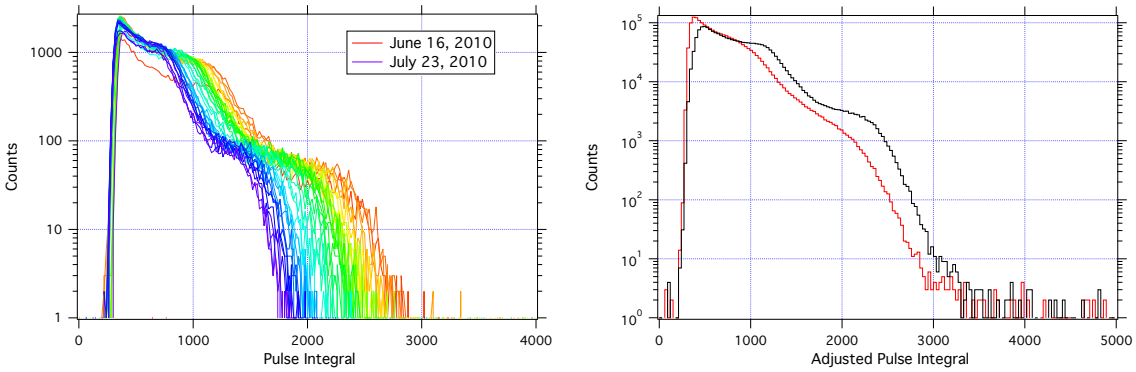

Figure 4.13: Left: Energy spectra for a single block of scintillator operating at KURF over the course of two months. In the beginning, the upper edge of the gamma spectrum is located at approximately channel 2600, but after two months has drifted down below channel 2000. Right: The gamma spectra from a single block of FaNS-1 scintillator before and after the corrected calibration factor has been applied. Note the appearance of sharp edges in the post-correction spectrum.

By monitoring the ^{208}Tl edge, the calibration drift can be tracked and corrected for in analysis. The effectiveness of this correction can be shown using the gamma calibration data. Figure 4.13b shows the gamma spectrum from one scintillator bar before and after the correction has been applied. Note the clear edges present in the post-correction spectrum that are completely absent from the pre-correction spectrum.

[3]The photomultiplier tubes were repurposed from a previous experiment that operated in 1995. It is not unusual for these detectors to fail after such a long period of operation.

Figure 4.14 shows the drift of the calibrations, in keV/mV, as a function of time over the two months used for this analysis. Each channel shows a gradual drift towards larger calibration factors (lower gain), while two of the channels also exhibit a sharp change in calibration. The gradual loss of gain has been attributed to the aging of the PMTs, while the sharp change is due to one of the two PMTs on a scintillator block dying. Using the timestamp from each event, an interpolated calibration factor is applied to each scintillator signal integral.

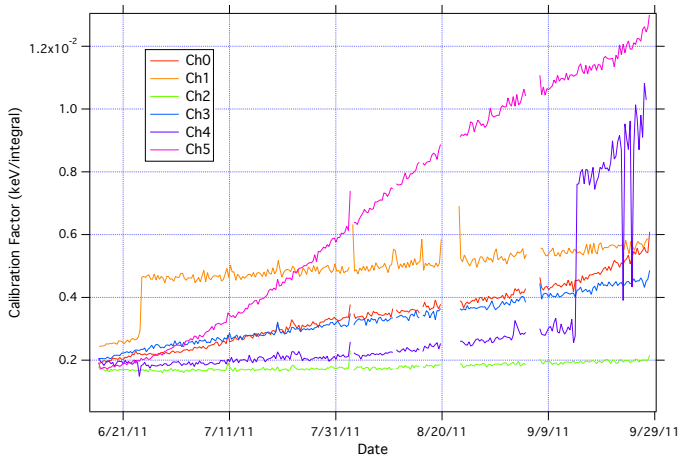

Figure 4.14: Shown are the calibration factors (in keV/unit integral) for each scintillator channel of FaNS-1. These are measured by tracking the ^{208}Tl Compton edge over the operational period at KURF. The scintillator pulse integrals are multiplied by the calibration factors to convert them into energy.

4.2.3.2 Prompt alpha/gamma coincidences

Despite selecting the lowest background ^{3}He counters, the proportional counters chosen are likely to still contain trace amounts of U and Th. Alpha decays from these isotopes are frequently accompanied by gamma rays in prompt coincidence, within picoseconds of the alpha. The alpha can interact in the ^{3}He counter,

while the prompt gamma can be detected by the scintillator. Such coincidences are correlated, and are therefore not removed by the subtraction of negative timing events. To measure this effect, likely alpha events with helium proportional counter energies higher than the neutron capture peak are studied. The timing spectrum of alpha-like ^{3}He events is shown in Figure 4.15.

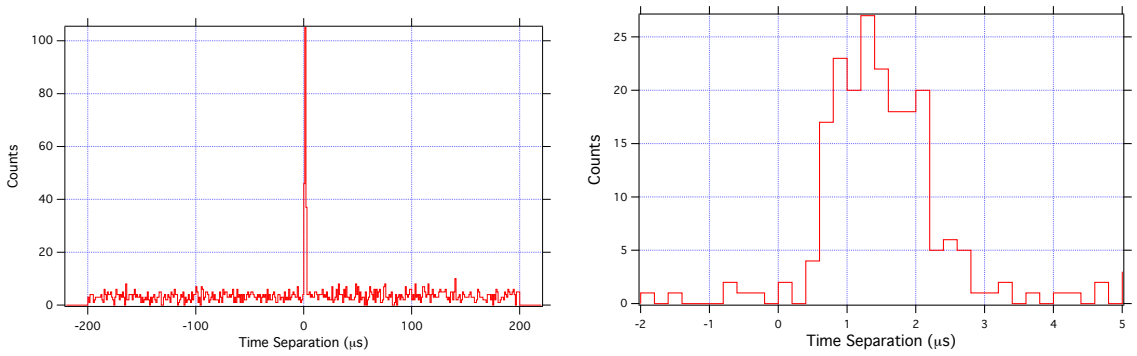

Figure 4.15: Left: The timing spectrum of alpha-like coincidences with ^{3}He energies above 0.8 MeV. This spectrum should be compared to the normal timing spectrum from neutron coincidences, such as in Figure 4.6a. Right: Zoom-in to highlight the large peak at $\Delta t \simeq 1.5$ μs due to prompt coincidences between alpha and gamma decays of uranium and thorium in the aluminum body of the ^{3}He counter.

The prompt coincidences do not extend past 3 μs. Therefore, these events are eliminated simply by rejecting events in that portion of the time window. Ten events are found within the prompt time window of $(0, 3\ \mu\text{s})$, and are not included in the full analysis. There is some probability that real neutron events could be rejected by this exclusion, which can be estimated using source data. By comparing the number of events that pass all cuts, but fall in this time region, a systematic shift in the observed neutron rate is estimated. Using ^{252}Cf source data collected at KURF, excluding this time region rejects approximately 1.9% of neutron captures, which is accounted in the final analysis.

4.2.3.3 Total exposure time

The data used in this analysis range from the end of June, 2011 through August, 2011. These data were chosen by defining an upper limit on acceptable calibration factors of 1×10^{-2} MeV/integral. This ensures that each channel has a high enough gain to be reasonably included in the analysis. The total exposure time is calculated using the total number of data files collected while all the calibration factors are below 1×10^{-2} MeV/integral, each of which are 3600 s long. Between 6/31/11 and 9/1/11, a total of 1038 data files were recorded, for a total exposure time of 3.737×10^6 seconds. The uncertainty of this parameter is taken to be one data file, or 3600 s. This is approximately 0.1 % of the total exposure time.

4.2.3.4 Applying cuts to KURF data

The analysis cuts can be applied piecewise to understand which cuts play the most important roles. The main cuts used are on the ^{3}He risetime and the ^{3}He energy. First, Figure 4.16 shows the ^{3}He risetime versus energy scatter plot. Note the vertical band of events between 0.75 MeV and 0.85 MeV from full-energy deposition of the neutron capture. There is also a large horizontal band of events with risetimes shorter than 150 ns, which are micro-discharge noise events. Figure 4.17 shows the effects of the various cuts.

The three timing spectra shown in Figure 4.17 are produced by placing cuts on ^{3}He signal properties. The top spectrum (black) shows the timing distribution after only demanding a coincidence between a ^{3}He counter and a scintillator signal.

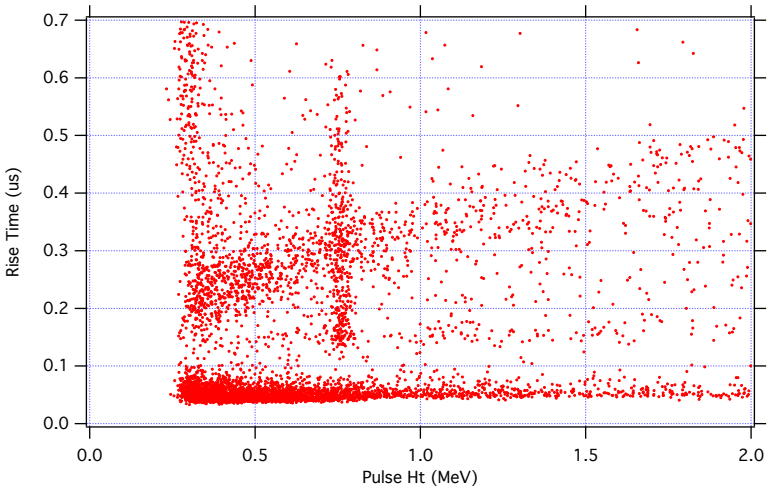

Figure 4.16: The scatter plot of ^{3}He risetime versus energy for the final dataset collected at KURF. Note the three main features; first, a strong vertical band of events around 0.75 MeV from neutron captures; second, there is a strong horizontal band of events with fast risetimes from micro-discharge noise events; finally there is a diagonal band of events that are from alpha particle interactions.

Note the flat spectrum with a prominent peak around 0 μs. This peak contains correlated alpha and gamma events arising from sequential decays of uranium and thorium in the aluminum body of the ^{3}He counters, as discussed in Section 4.2.3.2.

After rejecting all microdischarge events, the timing spectrum shown in blue is obtained. Microdischarges are completely uncorrelated with any scintillator signal, thus the effect of this cut is a uniform reduction across all times. Finally, after placing a tight cut on the ^{3}He energy, the red spectrum in Figure 4.17 is produced. The prompt peak is significantly reduced and an asymmetry in the number of counts with positive versus negative timing is seen. Figure 4.18a shows the final post-cut timing spectrum on a linear scale to highlight the asymmetry.

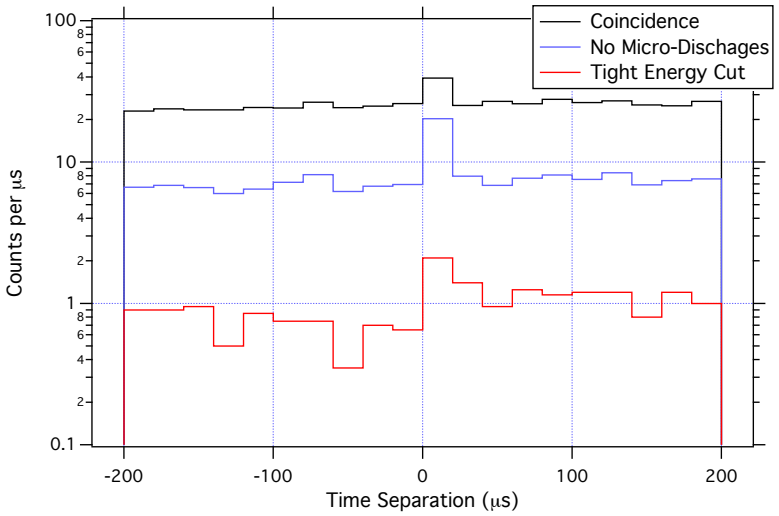

Figure 4.17: The timing spectra from three stages of the analysis. First (in black) is the spectrum from only demanding a coincidence between the ^{3}He counters and a scintillator signal. Second (in blue) is the spectrum from removing the micro-discharge noise events. Finally (in red) is the resulting spectrum from placing a tight cut on the ^{3}He energy.

4.2.3.5 Measurement of fast neutrons up to 10 MeV

In approximately 2 months of operation (with a live time of 3.74×10^6 seconds), 384 coincident events with scintillator energies greater than 1.4 MeV were detected. Of these, 10 were rejected for being in the prompt alpha/gamma coincidence region. The timing spectrum for these events can be seen in Figure 4.18a. Figure 4.18b shows the energy spectra for the positive and negative timing coincidences.

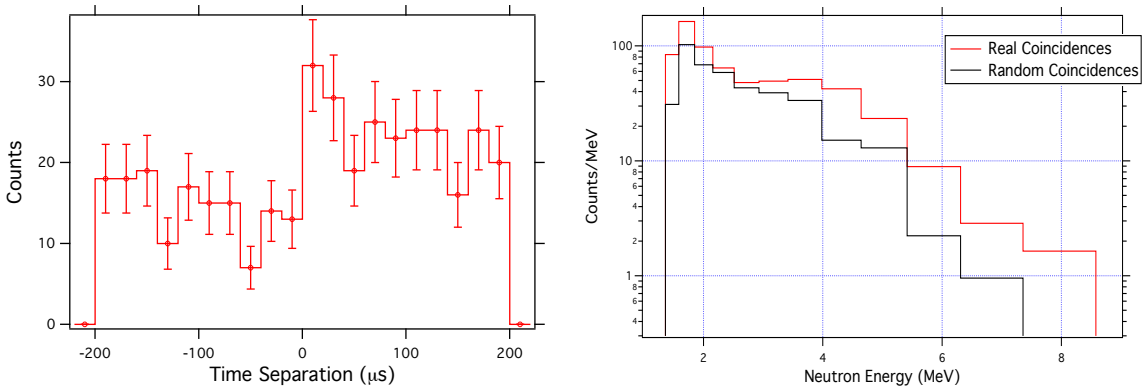

Figure 4.18: Left: The post-cut timing spectrum from the final data run at KURF. Right: The energy spectra for positive and negative timing coincidences from the final run at KURF.

To determine the total rate of detected neutrons, the *time to next event* technique, as discussed in Section 3.4.2, is used. This technique provides a simple method of determining the deadtime-free event rate. Figure 4.19 shows histograms of the time between events for the positive and negative timing coincidences at KURF.

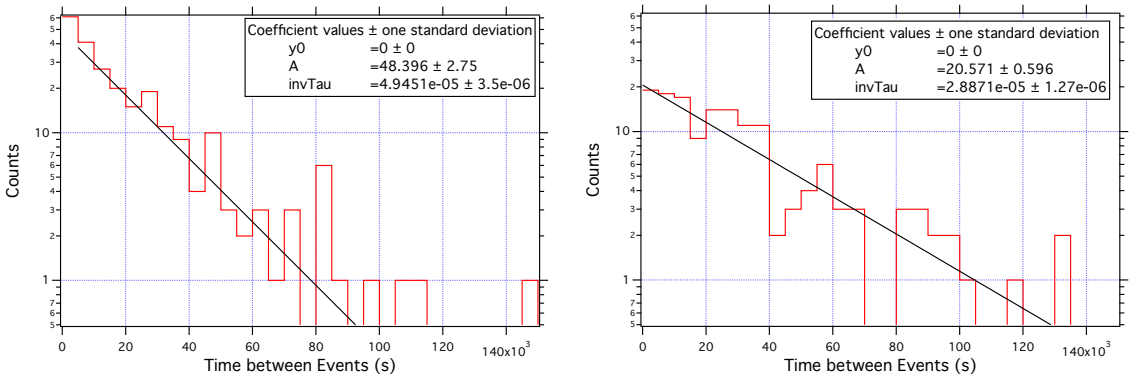

Figure 4.19: Histograms of the time between successive events for the positive (left) and negative (right) timing coincidences at KURF. The fit lines shown are single exponentials with the y-offset held at zero. The exponential decay parameter from the fit is equivalent to the deadtime-free rate of events.

The exponential parameter from fitting these histograms provides the absolute rate in counts/s. For these data, rates of $(4.94 \pm 0.35) \times 10^{-5}$ /s and $(2.89 \pm 0.13) \times$

10^{-5} /s are found for the positive and negative timing coincidences, respectively. By subtracting the negative timing from the positive, a measurement of the background subtracted neutron count rate of $(2.05 \pm 0.37) \times 10^{-5}$ /s is made.

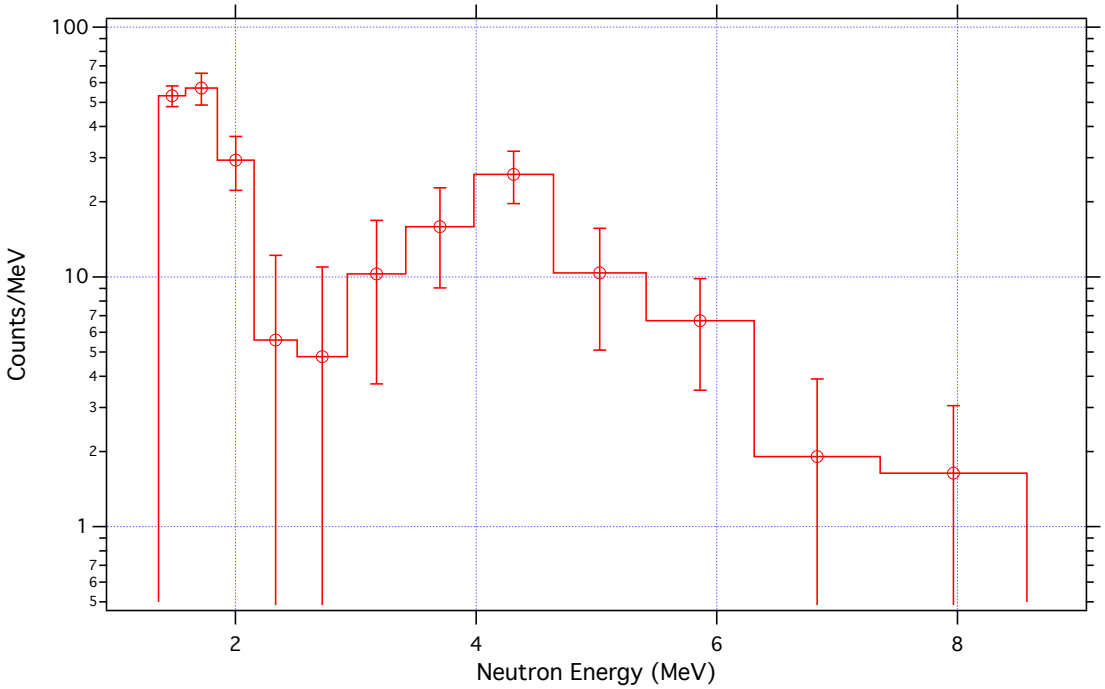

Figure 4.20: The energy spectrum of 89 detected neutron events recorded in 3.737×10^6 s of operation at KURF.

To obtain the ambient neutron flux from this measurement, the total efficiency and exposed surface area must be accounted for. As measured with the ^{252}Cf source in Section 3.4.2, FaNS-1 has an absolute efficiency of $\varepsilon = (1.3 \pm .1)\%$ for neutrons in this energy range directed at the top of the detector. The total exposed surface area, SA, of scintillator in FaNS-1 is 2957.5 cm^2. Combining these with the measured

neutron rate, the total neutron flux above 1.4 MeV is found to be:

$$\begin{aligned}\Phi_n(E_n > 1.4 \text{ MeV}) &= \Gamma_{meas} \times \frac{1}{SA} \times \frac{1}{\varepsilon} \times \frac{1}{\varepsilon_{He}} \times \frac{1}{\varepsilon_{prompt}} \\ &= (2.05 \pm 0.37) \times 10^{-5} \text{ n/s} \times \frac{1}{2957.5 \text{ cm}^2} \\ &\quad \times \frac{1}{.013 \pm 0.01} \times \frac{1}{0.77 \pm 0.02} \times \frac{1}{.98} \\ &= (6.5 \pm 2) \times 10^{-7} \text{ n/cm}^2\text{/s},\end{aligned}$$

where the total uncertainty is found from combining the uncertainties in threshold, statistics, and prompt and ^{3}He cut corrections as detailed in Table 4.3.

Table 4.3: Uncertainty budget for FaNS-1 operational at KURF.

Source	Correction	Uncertainty
Exponential Fit		18%
Efficiency		10%
Threshold		20%
Exposure		2%
Prompt (α,γ)	1.9%	5%
^{3}He Cut Efficiency	23%	2%

4.2.3.6 Limit on the muon-induced neutron flux

No events were observed with energies greater than 10 MeV during the period of operation. A confidence level based on a null observation is estimated using Poisson statistics. The functional form of the Poisson distribution is:

$$f_p(x) = \frac{e^{-a}a^x}{x!} \tag{4.7}$$

where a is the mean value. For an observation of zero events, Equation 4.7 yields a 90% confidence limit of 2.3 events, while the 95% CL is found to be 3.0 events.

A limit on the neutron flux above 10 MeV may be placed, assuming the muon-induced spectrum is comparable to the cosmogenic spectrum at the surface. Using the same Monte Carlo technique discussed in Section 4.1.3, FaNS-1 has an average response to neutrons above 10 MeV of (3.5±0.7) n/(n/cm^2). Recall, this is the number of neutrons predicted to be detected above 10 MeV per neutron fluence above 10 MeV, including the time to capture cutoff of 200 μs. Combining this with the exposure time of (3.737±0.004)×10^6 seconds and the Poisson upper limit of 3.0 events, the upper limit of the neutron flux above 10 MeV is:

$$95\%\ CL = \frac{3.0\ \text{n}}{(3.737 \pm 0.004) \times 10^6\ \text{s} \times 3.5\ \text{n/(n/cm}^2)} \tag{4.8}$$

$$95\%\ CL = 2.3 \times 10^{-7}\ \text{n/cm}^2\text{/s}. \tag{4.9}$$

This limit is considerably higher than the expected rate of 7×10^{-9} n/cm^2/s from the estimates made of the muon-induced neutron rate above 10 MeV discussed in Section 4.2.1. Extrapolating from this sensitivity, FaNS-1 would be expected to observe approximately one muon-induced neutron per year of operation.

4.2.4 Discussion of KURF Results

Operating FaNS-1 in the Kimballton Underground Research Facility provided important and useful understanding of how to operate a detector in a low background environment. Of the two years installed at KURF, many improvements

were made to the detector. The final data set consists of two months of production data. A measurement of the ambient fast neutron flux and spectrum from natural radioactivity in the surrounding rock was made with FaNS-1.

An experimental limit on the neutron flux above 10 MeV in KURF has also been made. In order to determine the muon-induced neutron spectrum, a larger and more robust detector system is required and it would either have to operate for a significantly longer time at KURF or be situated in a shallower location. To this end, a more optimized detector system was designed and constructed and is the subject of the remainder of this thesis.

4.3 Conclusions

The first generation of the Fast Neutron Spectrometer operated in a variety of environments, ranging from high rate calibrations with calibrated sources to high energy exposure at the surface to low rates deep underground. In each regime, FaNS-1 performed exceptionally well considering the repurposed nature of many of the components. The detector's ability to reconstruct mono-energetic neutron sources into peaks without the use of unfolding techniques was demonstrated. The absolute efficiency of FaNS-1 was measured with two thresholds (1 MeV and 2 MeV) to be 1.3% and 1.4% respectively. The operation at the surface shows that the technique of capture-gated spectroscopy with separated detectors can be used to effectively measure neutrons with energies beyond 150 MeV. Finally the detector successfully operated in a low background environment and measured the fast neutron spectrum and flux at the Kimballton Underground Research Facility. This measurement will be used by the other researchers at KURF to constrain their backgrounds and improve their analysis.

Part II

FaNS-2

Chapter 5

The UMD/NIST Fast Neutron Spectrometer 2 (FaNS-2)

Based on lessons learned from the operation of FaNS-1, the design of a dedicated system, FaNS-2, began in 2011. Priority was given to improving the detection efficiency at high energies to better determine the spectrum of cosmic-ray induced neutrons. The design, optimization, construction, and installation of the FaNS-2 detector array is discussed in this chapter. In Chapters 6 and 7, results from source measurements and a measurement of the surface fast neutron spectrum with FaNS-2 are discussed, respectively. Finally, in Chapter 8 future measurements that may be made with FaNS-2 are presented.

5.1 Geometry of the FaNS-2 array

To optimize the detector size and layout, many design configurations were considered and compared in simulation. The main goal was to balance good energy reconstruction with high sensitivity to high energy neutrons. Figure 5.1 shows a selection of the designs considered in MCNP.

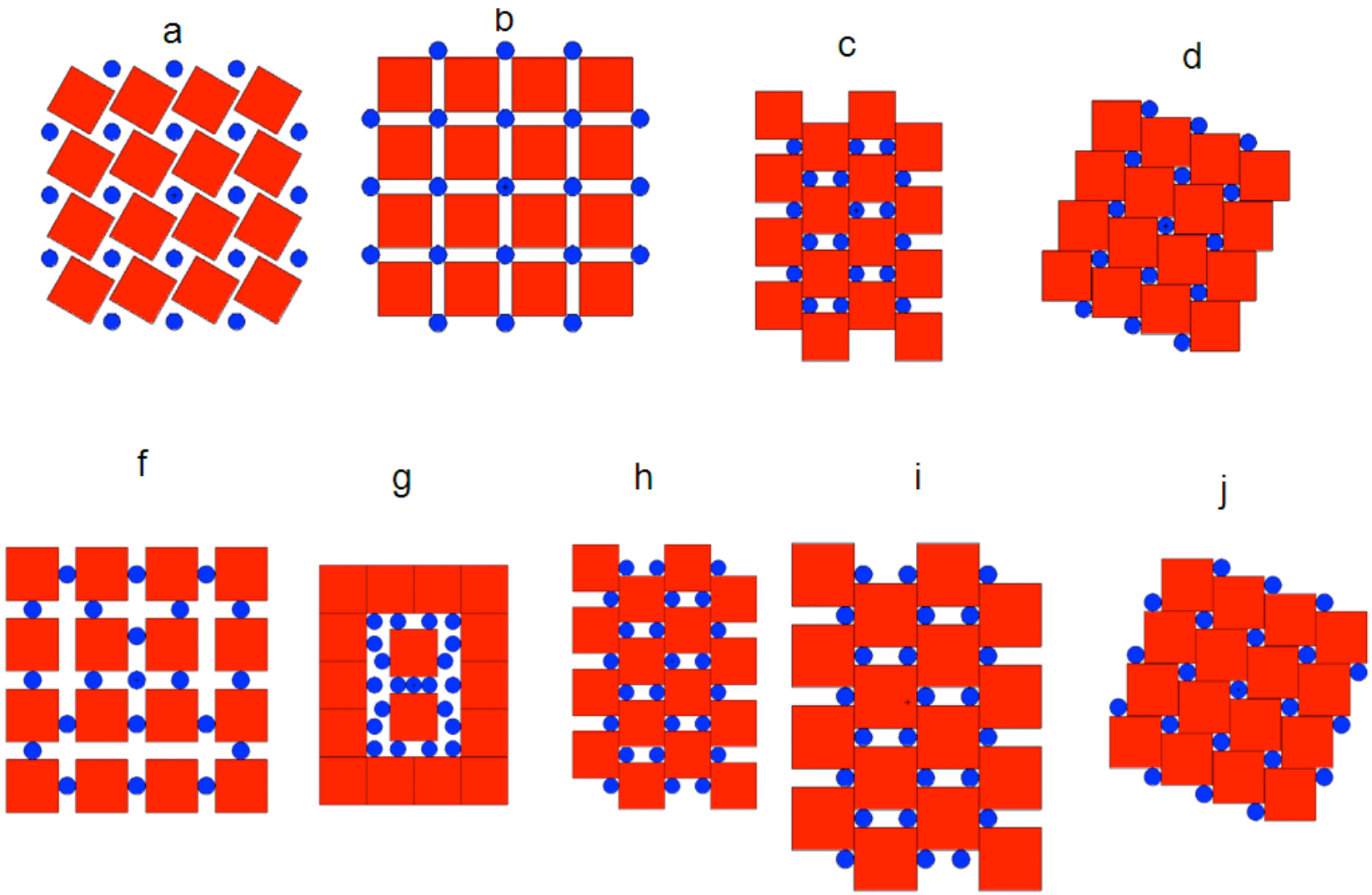

Figure 5.1: A selection of the various designs that were considered in Monte Carlo for FaNS-2. The red squares are scintillator bars, while the blue circles are ^{3}He proportional counters. More detail is in the text.

The design goal was to have sufficient scintillator volume to have sensitivity to neutrons above 500 MeV. For optimization, a few items were fixed as constraints. First, the length of the scintillator needed to be well matched to the active length of the ^{3}He counters, which is 46 cm. Secondly, the detector had to be reasonably symmetric to minimize directional variation in the detector's efficiency. Finally, discussed later in Section 5.2.3, the PMTs for FaNS-2 are 5 cm diameter, so the scintillator segments needed to have reasonable light collection into a cylindrical, 5 cm diameter light guide. A separate Monte Carlo was performed to study the light collection of the scintillator bars, as discussed in more detail in Section 5.2.4.

The final selection was Design A from Figure 5.1. This design met most of the criteria, especially the symmetry constraint. The spacing between the scintillator and ^{3}He counters is required to mechanically mount the ^{3}He counters and the scintillator bars. These spacings were made as small as possible, since tight packing of the detectors yielded high neutron detection efficiency. Figure 5.2 shows a larger depiction of the final geometry, including the space required to mount the ^{3}He counters.

The layout is highly symmetric, which decreases directional differences in detector response. The tilt in the scintillator bars allows for tight packing on the ^{3}He counters. It also ensures that there is no direct path through the detector that does not intersect a scintillator segment, which improves detector efficiency. MCNP studies show that this geometry improves the high energy response (neutron energies above 100 MeV) between a factor of 15 and 30 over the response of FaNS-1.

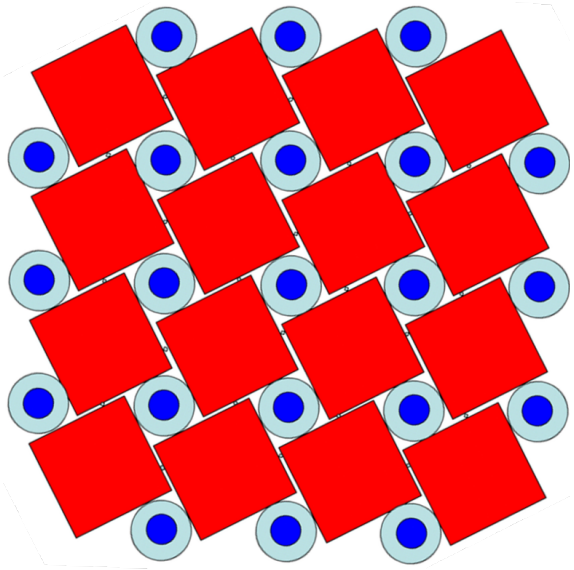

Figure 5.2: A schematic of the FaNS-2 layout. The red squares are 9 cm × 9 cm × 56 cm plastic scintillator segments, the blue circles are ^{3}He proportional counters, and the light blue circles are the spacing required to mount the ^{3}He counters. More detail is included in the text.

5.2 Components

FaNS-2 is an array of identical plastic scintillator segments interspersed with ^{3}He proportional counters. In this section the details of each component are discussed.

5.2.1 Helium proportional counters

FaNS-2 uses 21 of the same Reuter-Stokes ^{3}He proportional counters as were used in FaNS-1. These counters, model RS-P4-0819-103, have an active region 46 cm long and a ^{3}He partial pressure of 4 atm. An additional buffer gas of 1.1 atm ^{nat}Kr improves the operation of the counters. A technical drawing of one is shown in Figure 5.3. During construction, a thin coating of nickel was applied to the inner

surface of the aluminum cylinder to reduce alpha particle emission from the body of the detectors [126].

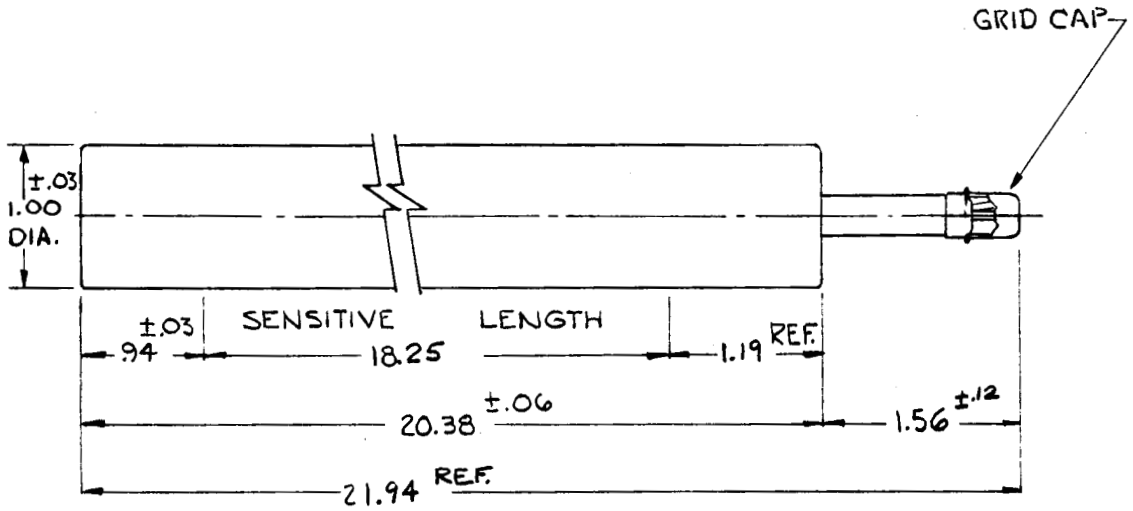

Figure 5.3: Technical drawing of the ^{3}He proportional counters used in FaNS-2 as provided by the manufacturer [126].

Approximately 80 ^{3}He counters were surveyed, using the technique discussed in Chapter 2, to measure their internal alpha backgrounds and rate of microdischarge noise. The 21 detectors with lowest alpha rates were selected for inclusion in FaNS-2. The ^{3}He proportional counters are operated at approximately 2100 V, with slight variations to gain match energy responses. This gain setting places the full-energy thermal neutron capture peak (0.764 MeV) at approximately 200 mV.

5.2.2 Plastic scintillator

FaNS-2 contains 16 segments of EJ-200 plastic scintillator manufactured by Eljen Technologies [127]. Each segment is 9.0 cm × 9.0 cm × 56.0 cm, with 5.0 cm diameter, 9.6 cm long, light guides coupled to each end, as shown in Figure 5.4. The

total volume of scintillator in the detector is 72.6 liters. The bars are wrapped in aluminized mylar to increase light collection and covered in black vinyl sheets for light-tightness.

Figure 5.4: A diagram of one FaNS-2 scintillator bar, manufactured by Eljen Technology. The body is 9 cm × 9 cm × 56 cm and is composed of EJ-200 general purpose plastic scintillator. The light guides on each end are 5 cm diameter and 9.6 cm long and are made of UV-Transmitting plastic.

This particular polyvinyltoluene-based scintillator was chosen to match the light response of the Phillips 5 cm PMTs, discussed in Subsection 5.2.3, that are used in FaNS-2. Figure 5.5 shows the light output of the scintillator and the light response of the PMTs. EJ-200 has been shown to produce 10,000 photons per MeV of energy deposited and has an attenuation length greater than 3 m. It has a pulse width of approximately 2.5 ns and a refractive index of 1.58 [127].

5.2.3 Photomultiplier tubes

The photomultiplier tubes used in FaNS-2 are 5 cm diameter, Photonis model XP2262 [128]. The detectors are 12-stage tubes that have been repurposed from the G0 experiment at Jefferson Laboratory [129–131]. A diagram of the detector assembly is shown in Figure 5.6. The tubes are housed in a light-tight enclosure that also contains mu metal magnetic shielding.

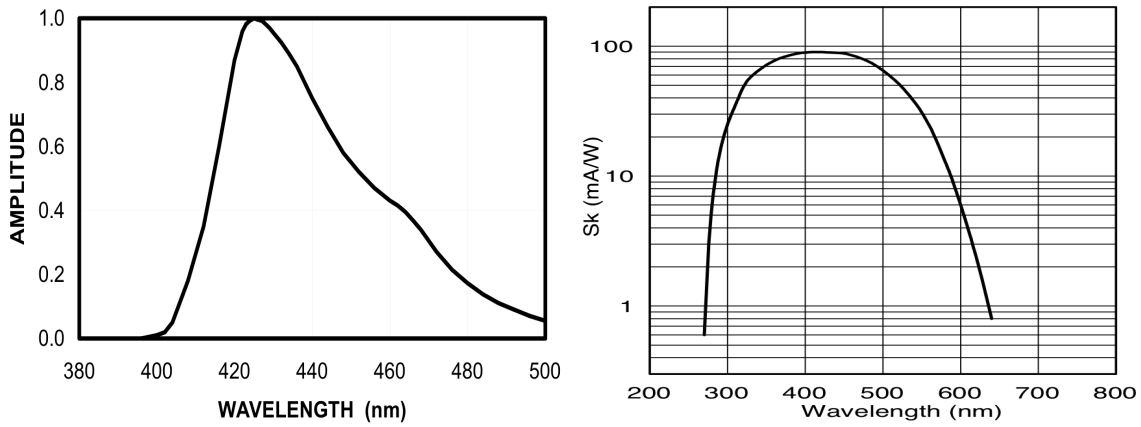

Figure 5.5: Left: The light emission spectrum for EJ-200 polyvinyltoluene scintillator. [127] Right: The optical response (in mA/W) of the XP2262 PMT used for FaNS-2.

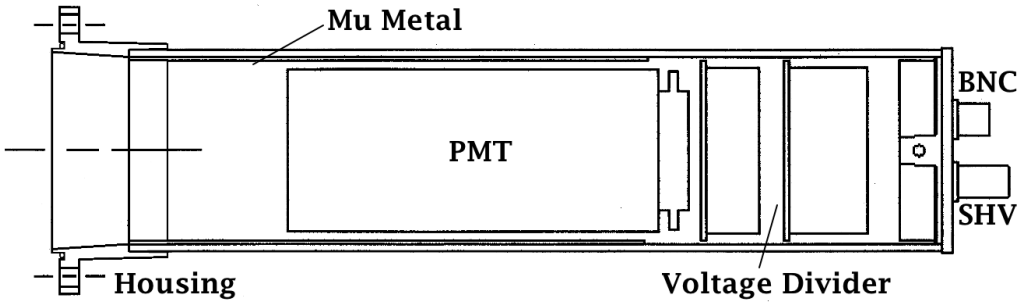

Figure 5.6: Mechanical drawing of the housing for the XP2262 PMTs.

The enclosure is constructed of black ABS plastic with a mounting flange on the front face. This flange contains an O-ring groove that provides the light-tight seal to the overall FaNS-2 enclosure. The PMT base is located within the light-tight enclosure and has two compression springs that provide pressure between the PMT and the light guide, ensuring a quality optical seal[1].

[1]During the transportation of FaNS-1 into KURF, seven of the 12 optical joints between the light guides and PMTs broke. This effectively halved the light collection for each of those PMTs. A lesson learned was the importance of axial pressure to hold the PMTs in place. This also lead to the use of silicone optical pads that can repair their seal after a shock.

The PMTs are coupled to the light guides using 5 cm diameter, 3 mm thick, EJ-560 silicone optical pads. The pads have an index of refraction of $n = 1.43$, which is a reasonably close match to the indices of refraction for the light guides and the PMT glass. Matching the indices of refraction maximizes the light transmission at the boundary between PMT and light guide. The silicone also provides mechanical cushion between the tubes and the light guides to prevent damage caused by vibration during transportation.

5.2.3.1 Linearity

An extensive study was conducted to improve and measure the linearity of the PMTs using attenuated laser pulses. A tube was illuminated by an ultra-fast pulsed laser (100 ps width) that was sent through 15 different neutral density filter combinations with a range of attenuation of two orders of magnitude. Approximately ten different base designs were tested, and ultimately a new design was chosen based upon optimizing linearity up to 10 V and minimizing nonlinearity above 10 V. Figure 5.7 shows the linearity of the original base compared to the linearity of the selected base design. Note the improved linearity above 10 V and the maintained linearity below 10 V.

The final base design is shown in Figure 5.8. The design exhibits the best linearity in the region where the best statistics are expected; the detectors operate at a gain setting where 10 V is approximately 100 MeV_{ee}. For events that do cross this region, a correction can be made to adjust for the nonlinearity.

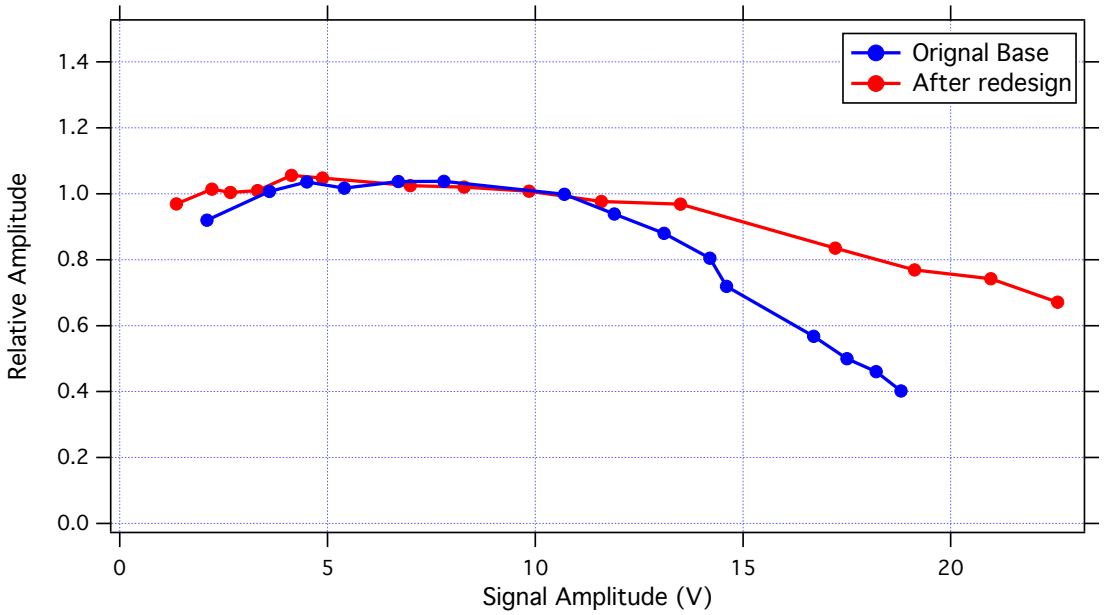

Figure 5.7: The ratio of measured amplitude to expected amplitude for the original base design (blue) and post-modification base design (red) versus the recorded signal amplitude.

5.2.3.2 Single photo-electron and photo-statistics

Measurements of the single photo-electron (SPE) peaks for each PMT were used to characterize photo-statistics for threshold placement and total energy resolution of FaNS-2. Figure 5.9 shows a typical single photoelectron spectrum from one of the XP2262 PMTs. To extract the width and peak of the SPE distribution, the spectrum is fit with a Gaussian plus an exponential.

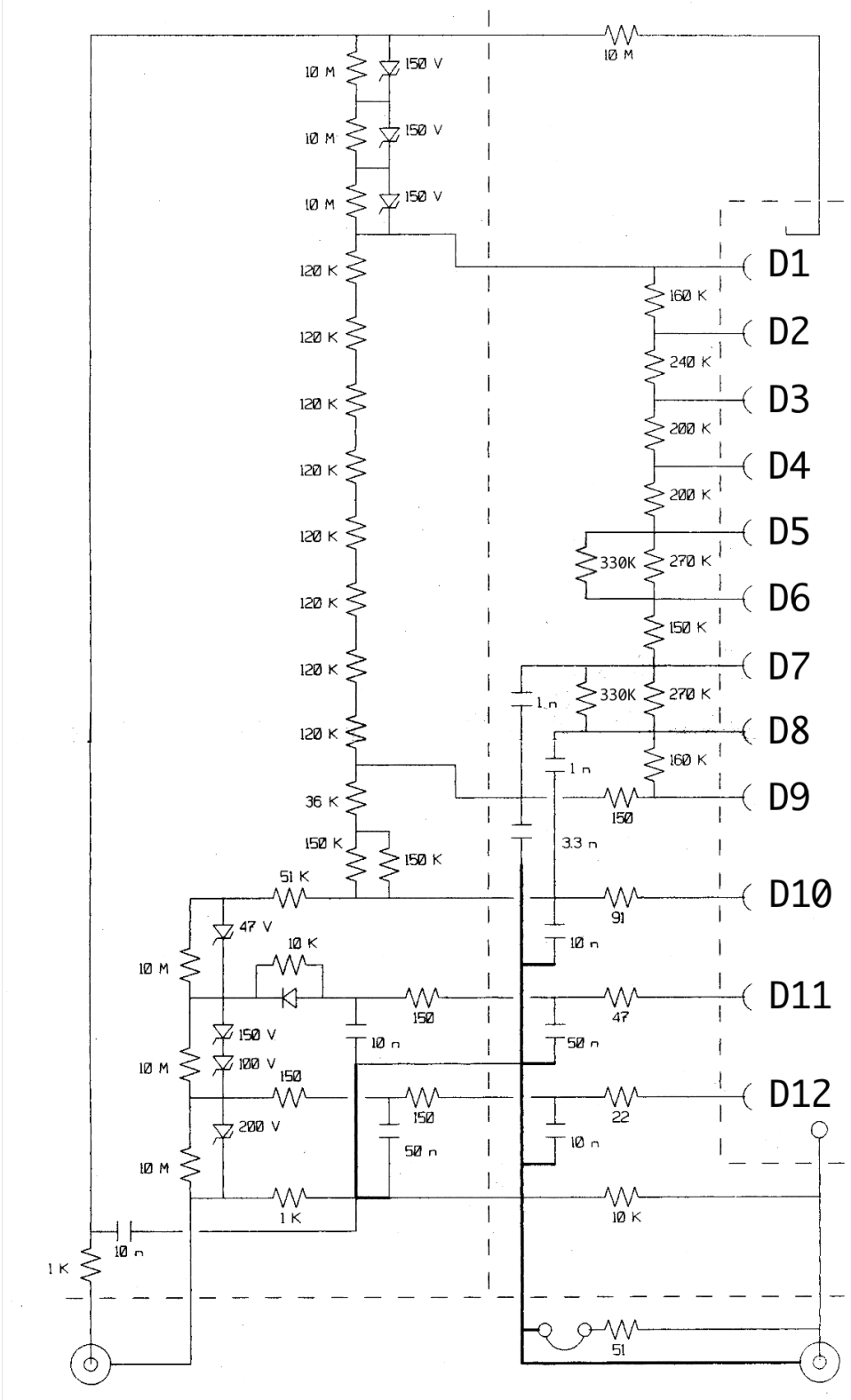

Figure 5.8: The final design of the PMT bases for FaNS2.

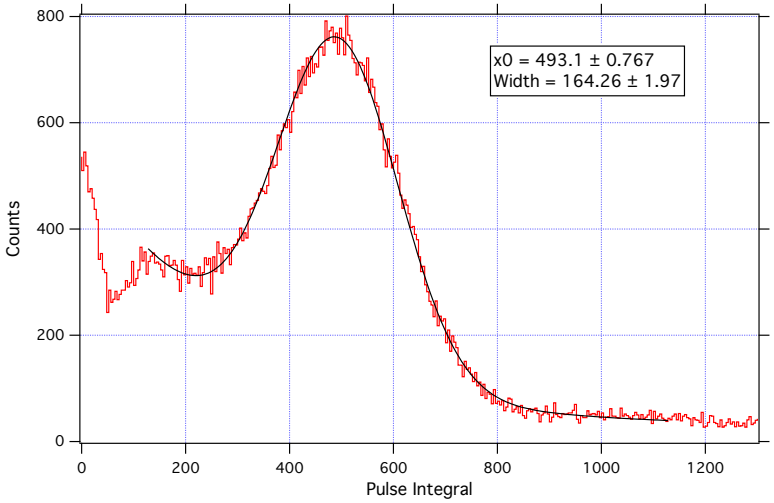

Figure 5.9: A typical single photoelectron spectrum of one of the XP2262 PMTs used in FaNS-2. The black line is a fit to the data of a Gaussian plus an exponential tail. The Gaussian width is used to characterize the inherent resolution of the PMT.

When the primary photo-electron strikes the first dynode of the PMT, a certain number of secondary electrons are emitted, depending on the work function of the surface. The width of the single photoelectron peak is determined by the electron statistics of the first dynode [12]. For the SPE spectrum shown in Figure 5.9, the FWHM is approximately 80% of the peak. This is consistent with the expected width obtained from Phillips [132]. From the width of the gaussian, approximately nine electrons are estimated to be emitted from the first dynode; this is slightly less than the expected value of 11 from the PMT data sheet. This width determines how precisely the PMTs are able to measure the number of photoelectrons in a given signal. This result will be used when determining thresholds and comparing the experimental data with Monte Carlo.

5.2.4 Light collection simulation

Extensive simulations were done to optimize the quantity and uniformity of the light collected in each PMT. Using the GuideM Monte-Carlo code [133], photons were randomly emitted throughout the whole body of the scintillator bar, and collection efficiencies were recorded as a function of location. The simulation included losses from scattering from the scintillator surface, attenuation, and from lack of total internal reflection. The model included the light guides, aluminized mylar, the silicone optical coupling pads between the light guide and PMT, and the front glass face of the PMT.

Two different methods of mounting the PMT to the scintillator were studied: 1) tapered light guides, and 2) cylindrical light guides. These two options are shown in Figure 5.10.

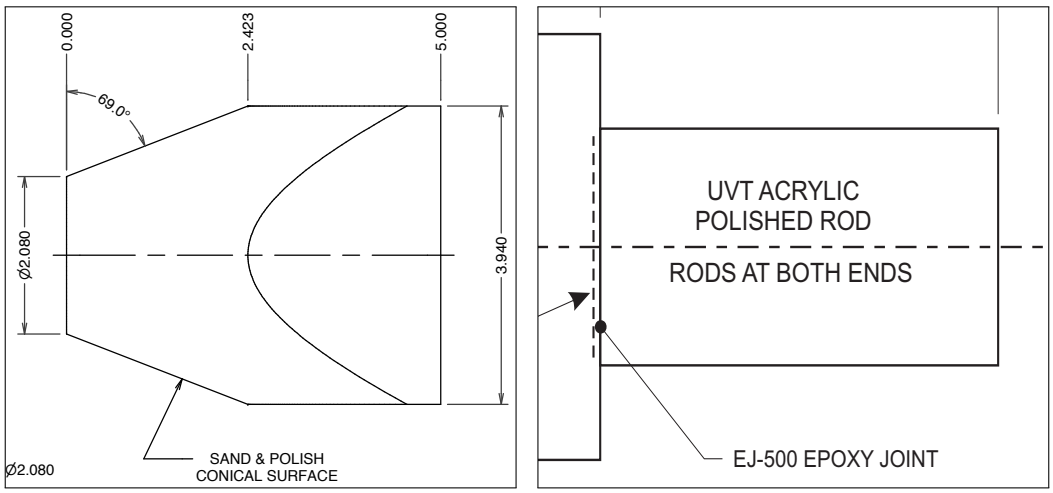

Figure 5.10: The two different light guide concepts studied for the FaNS-2 scintillator bars. Left: Tapered light guides, Right: Straight, cylindrical light guides.

The tapered light guide showed an overall higher average light collection efficiency than the straight, cylindrical light guides. However, the increase was not

uniformly distributed throughout the detector, as can be seen in Figure 5.11. A non-uniform light collection leads to a decrease in the achievable energy resolution. Thus it was decided to use the straight cylindrical light guides for FaNS-2.

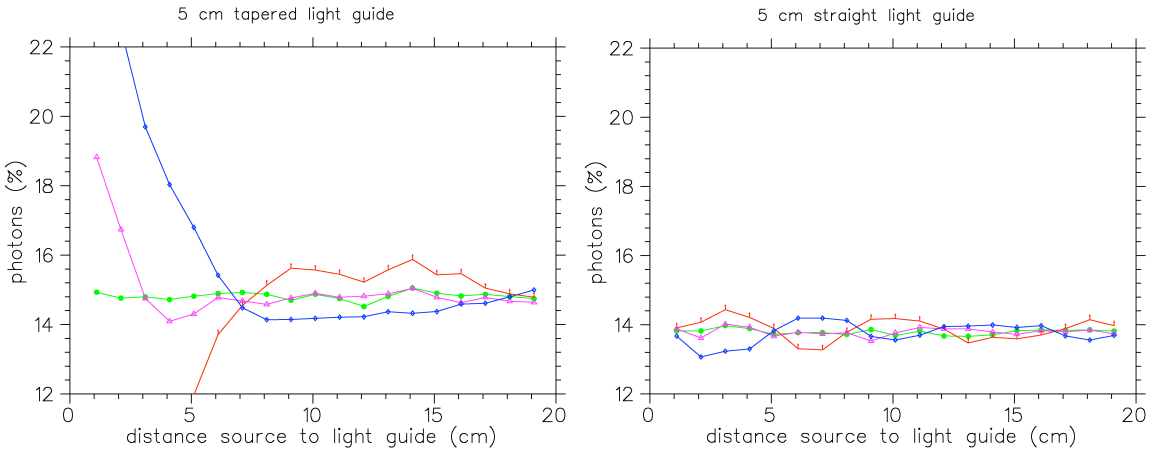

Figure 5.11: Shown is a comparison between the two light guide designs for FaNS-2, tapered and straight. A 4π source of photons was placed at multiple locations in the scintillator volume. Each color represents a different source location in the simulation. Though the tapered design has a higher overall light collection efficiency, the increase is non-uniformly distributed, leading to a position dependence of the light collection. To minimize this position dependence, FaNS-2 was constructed with straight light guides.

Once the final design of the scintillator assembly was chosen, a full Monte Carlo was performed to measure the light collection efficiency for FaNS-2. The reflectivity of the scintillator surface was set at 98.7%. The surfaces of the scintillator are diamond-tool finished, which has a reflectivity between that of cast surfaces (99.5% or better), and polished surfaces (around 97%). The aluminized mylar was separated from the scintillator surface by an air gap, and has a reflectivity of 95%. Table 5.1 shows the various components used in the Monte Carlo calculations.

To simulate the position dependent light collection efficiency, the scintillator volume is divided into cells of 0.5 cm $\times$ 0.5 cm $\times$ 1.0 cm (with 1 cm in the long axis

Table 5.1: Table of parameters used in the GuideM Monte-Carlo simulation of the light collection for FaNS-2. More details are in the text.

Component	Index of Refraction	Reflectivity	Attenuation Length (cm)
EJ-200 Scintillator	1.58	.987	450
EJ-560 Optical Coupler	1.43	.987	∞
PMMA Light Guide	1.49	.987	450
PMT Glass	1.54	1	∞
Aluminized Mylar		.95	

of the detector). Each cell is populated with 5×10^5 photons, and the collection efficiency for a given cell is recorded. Figure 5.12 shows the results for one section of the scintillator volume. Note, due to the highly symmetric nature of the FaNS-2 scintillator bars, only 1/8 of the possible cells are simulated, with the remaining cells filled using symmetries.

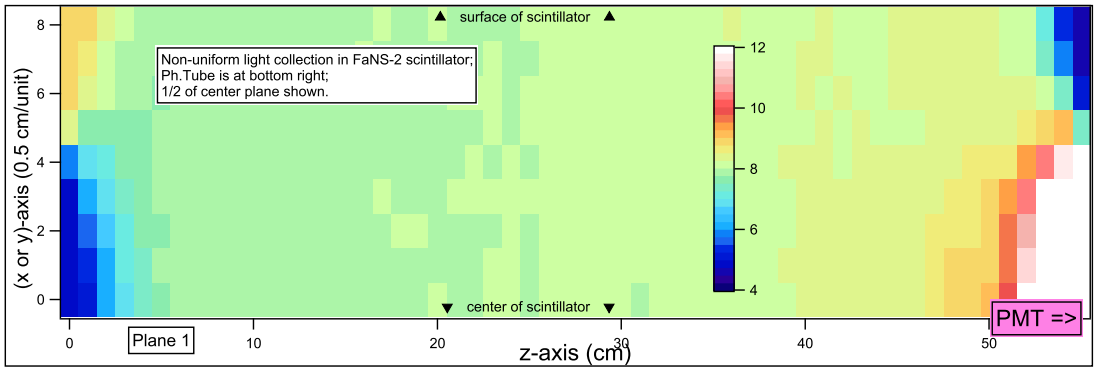

Figure 5.12: A heat-plot showing the distribution of light collection efficiency (percent of photons detected versus photons emitted) for the FaNS-2 scintillator bars. Only one half of the scintillator bar is shown in this figure, because the light collection is symmetric. The PMT is on the right, note the high light collection efficiency directly in front of the PMT face. Figure from [134].

On average, 8% of the emitted photons arrive at each of the PMTs attached to the scintillator for a total of 16% of the initial photons incident on the PMTs.

Throughout the bulk of the scintillator, there is very little variation from uniform light collection. However, at the ends of the scintillator, hot and cold spots in the collection efficiency are observed. Directly in front of the a PMT there is a hotspot of collection, while directly in front of the opposing PMT there is a corresponding cool spot. The hot spot is due to solid angle effects, while the cool spot is due to the opposing PMT collecting photons. Similarly, there are slight hot and cold areas in the corners due to reflections and shadowing, respectively. However, these variations even out when the light collected from both PMTs are summed.

This non-uniformity leads to a slight degradation of the achievable energy resolution of the detector. The size of this effect can be compared with the inherent resolution of the scintillator based upon Poisson statistics. Figure 5.13 shows a comparison between the spread of detected photons when considering only the non-uniform light collection and when Poisson statistics are also considered.

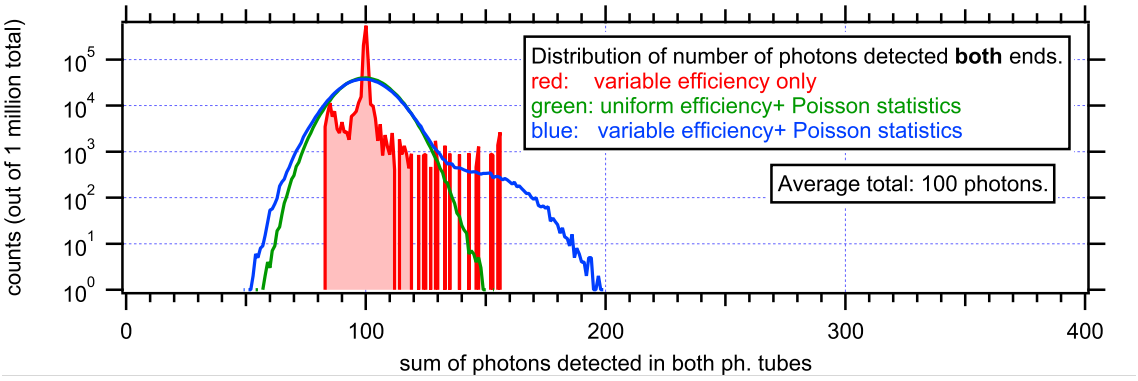

Figure 5.13: The spread of collected photons for and average of 100 photons from: 1) non-uniform light collection (red), 2) uniform light collection with Poisson statistics (green), and 3) both non-uniform collection and Poisson statistics (blue). The Poisson statistics dominate the width of the distribution. Figure from [134]

For typical energies of a few MeV$_n$, the uncertainties from Poisson statistics dominate the resolution. Thus, for the rest of this work the scintillator will be assumed to have a uniform 8% light collection efficiency.

As a check of the simulation, the average light collection in one of the FaNS-2 scintillator bars is shown in Figure 5.14. The average light collection is determined by measuring the single photoelectron peak and the distribution from a known gamma source. Due to its single gamma energy, ^{137}Cs is an excellent source for this study. ^{137}Cs emits a gamma of 662 keV, with a Compton edge at 478 keV. Using the light production of the scintillator provided by the manufacturer (10^4 ph/MeV), each event at the Compton edge will generate 4780 photons. The GuideM simulation estimates 382 photons will hit the PMT front face. The typical quantum efficiency for the PMTs in this work is 15-20 % [132], which yields an estimation of 57-76 pe at the ^{137}Cs Compton edge. Figure 5.14a shows a typical single photoelectron spectrum from the two PMTs attached to a single scintillator segment. Figure 5.14b shows the summed response of those PMTs to a ^{137}Cs source.

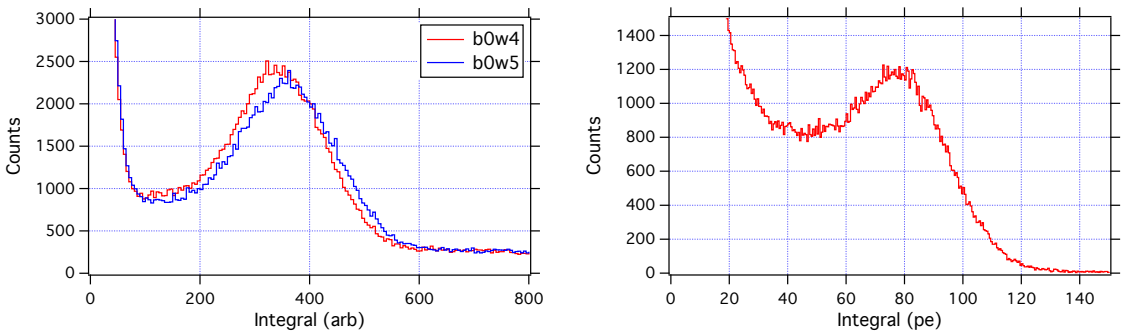

Figure 5.14: Left: The SPE spectra from the two PMTs attached to a scintillator segment. Right: The energy spectrum of the summed PMT response to a ^{137}Cs source placed at the center of the same scintillator segment. The energy is shown in units of photoelectrons (pe).

With the fitted value of the SPE peak location for each channel, the number of photoelectrons detected for a given energy deposition in each scintillator can be determined. After being summed, the two PMTs collect approximately 200 pe for 1 MeV_{ee} of energy deposited in the scintillator for a light conversion of $\sim$5 keV_{ee} per detected photon. Although this value is slightly lower than the predictions from Monte Carlo calculations, the experimental number is used to characterize the thresholds placed on each signal and the resolution of the detector.

5.2.5 Construction

FaNS-2 was constructed at the University of Maryland in the summer of 2012. Extensive work was done in collaboration with the UMD Physics Machine Shop to design and machine the mechanical structure and light-tight enclosure for FaNS-2. The entire detector was modeled in SolidWorks CAD, shown in Figure 5.15.

The support structure is based upon the 80/20 aluminum framing system [135]. A set of 80/20 (1 in$\times$3 in) rails are assembled into a base frame, upon which a 61.8 cm $\times$ 57 cm $\times$ 1.3 cm base plate is bolted. Vertical 80/20 rails are bolted to the base plate, which act as the mounting support for the scintillator bars. Two external mounting plates are bolted to the edges of the base plate. These provide the support for the ^{3}He counters and the PMTs.

The scintillator bars are supported by aluminum angle brackets on each corner with foam rubber pads to act as vibration isolation. The brackets are secured at their ends by 0.6 cm thick aluminum manifolds shown in Figure 5.16. Each manifold has

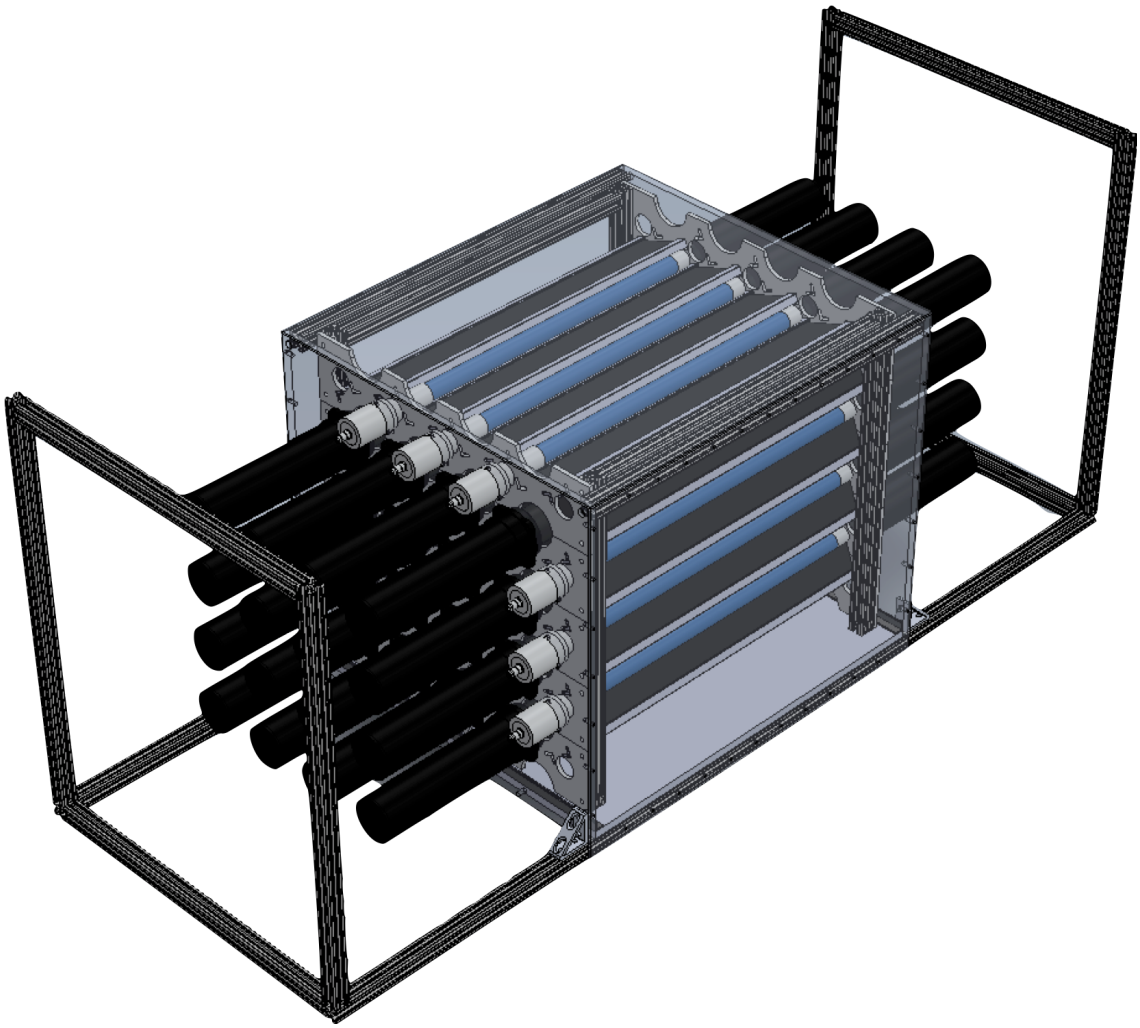

Figure 5.15: The FaNS-2 detector, as drawn in SolidWorks CAD.

through holes for the light guides and the ^{3}He counters. Ten of these brackets (five on each side) are bolted to vertical supports made from 80/20 extruded aluminum framing. These plates are flush to the ends of the scintillator bars with only the cylindrical light guides extending through them. Foam rubber shims are used to keep the scintillator bars fixed in place between the plates.

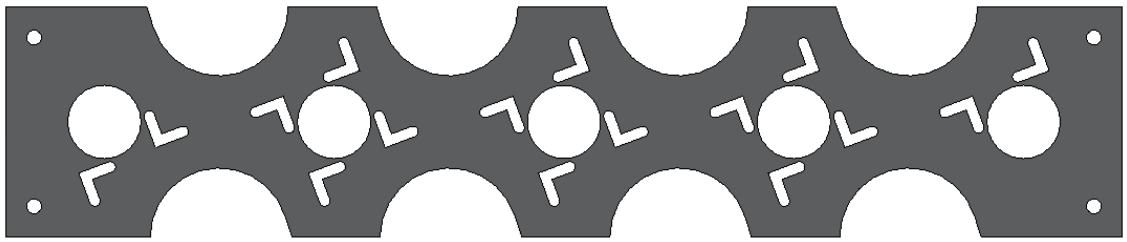

Figure 5.16: The aluminum bracket that holds the scintillator bars in place. The angle cut-outs are through holes for the aluminum rails that support the scintillator, while the circular holes in the center are through holes for the ^{3}He counters.

On each end, the PMT and ^{3}He support plates are bolted to the edge of the base plate and are secured at the top with an 80/20 cross-beam. The seams between the base plate and the end plates are made light-tight with an aluminum angle bracket and black foam rubber. The angle is bolted into the base plate with the foam compressed by the end plates. The 1.3 cm thick aluminum plates have tapped mounting holes for the PMT assemblies. Since the ^{3}He counters are supported on one end, only one of the plates has their mounting mechanism.

The ^{3}He counters lock into place using a bayonet-style mechanism developed by the UMD machine shop. Using four pins to hold the ^{3}He counter in place, an O-ring seal is made between the outside of the ^{3}He counter body and the aluminum

mounting plate, shown in Figure 5.17. The O-ring seal provides both mechanical stability and light tightness.

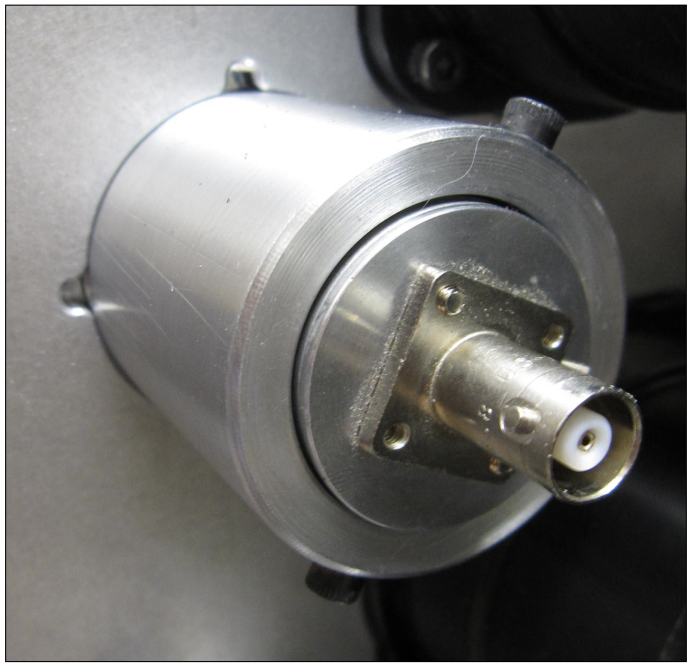

Figure 5.17: A photograph of a ^{3}He counter mounted in the outer enclosure of FaNS-2. Note the notches for the bayonet pins.

Surrounding the scintillator and ^{3}He counters is 3 mm thick boron-loaded silicone rubber, Shieldwerx model SWX-238 "Flexi-Boron" [136], to shield the detector from thermal neutrons. The silicone rubber contains 25.3% natural boron, which provides a thermal neutron attenuation factor of 259. Effort was taken to maximize the shielding of the detector, including the areas surrounding the light guides and ^{3}He counters. The top, bottom, and sides are all completely shielded, while the ends have cutouts to allow the ^{3}He counters and light guides to exit the detector volume. Figure 5.18 shows the boron shielding as it is being installed inside the enclosure.

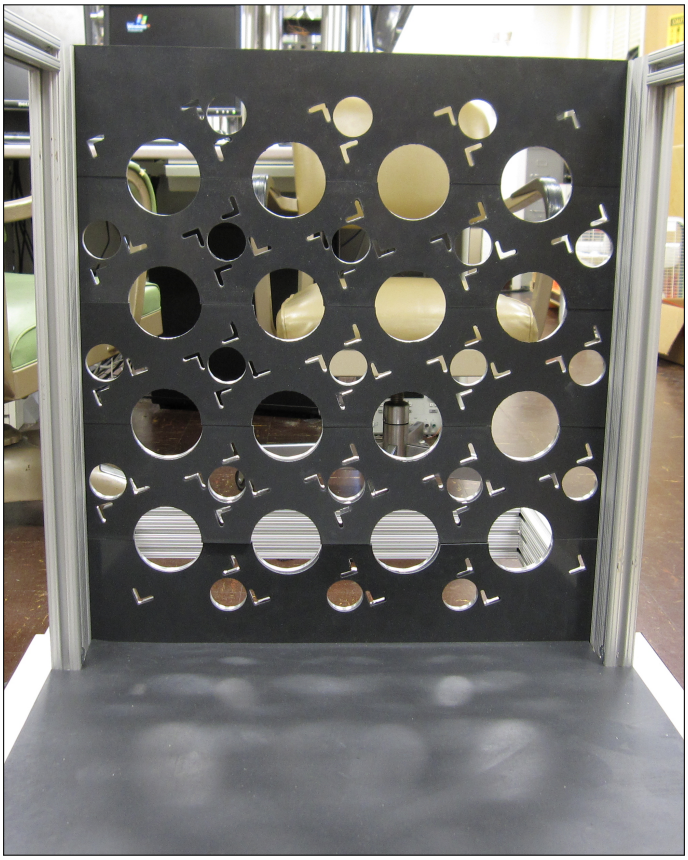

Figure 5.18: A photograph showing the thermal neutron shielding (grey rubber) as it is being installed. Note the cutouts for the ^{3}He counters and the scintillator light guides.

The top and sides of the enclosure are covered with thin (1.5 mm) aluminum sheeting for mechanical protection and light tightness while minimizing the material through which neutrons pass. These are mounted to the 80/20 framing with black foam rubber as a light seal. A close-up of the foam sealing is shown in Figure 5.19. The whole apparatus is mounted on top of 13 cm diameter wheels that for mobility.

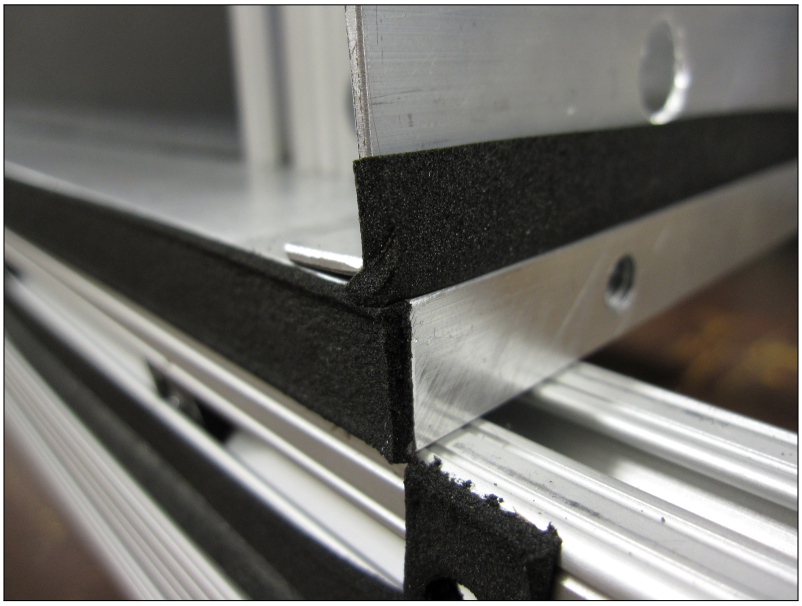

Figure 5.19: A photograph showing the baseplate with black foam rubber along the edges to light-tight the enclosure.

5.3 Electronics

The FaNS-2 electronics setup is a significant increase in complexity over that used for FaNS-1. Ultimately, FaNS-1 was operated simply using a PCI-based waveform digitizer with minimal external electronics. Given the number of channels in FaNS-2, it was more practical and cost-effective to use a more scalable system.

To handle the large increase in the number of channels, a new data acquisition system based upon seven VME waveform digitizers manufactured by CAEN Technologies was used. The V1720B digitizer features 8 channels, 12 bits of dynamic range, and a 250 MS/s digitization speed (4 ns/point). FaNS-2 is comprised of 32 channels of photomultiplier signal lines (each PMT is digitized separately) and 21 ^{3}He signal lines. Any of the ^{3}He counters may provide the trigger for data acqui-

sition, and therefore an external trigger system is necessary to ensure synchronous trigger distribution.

Figure 5.20 shows the overall schematic of the FaNS-2 detector array. The 32 PMTs are powered by an ISEG high voltage power supply in an MPOD Mini high voltage crate, and the signal lines are fed into the second generation Splitter/Summer modules. The output of these modules is sent through an amplifier that restores lost amplitude from the Splitter/Summer module and also acts as over-voltage protection for the digitizers. The 32 channels are split into four groups (one for each layer of the detector) and sent into the V1720 digitizers. The ^{3}He proportional counters are biased through 4 channel CAEN model A1422 preamplifiers [137], which also receive high voltage from an ISEG high voltage power supply. Their signal lines are passed through AC couplers to remove any baseline fluctuations and are fed into three V1720 digitizers, ordered by their position in the array, starting at the top left.

To handle the increase in PMT channels, improved splitter/summer modules were manufactured, consisting of custom printed circuit boards with eight channels each of splitter/summer circuitry. The centerpiece of the circuit is a passive delay chip that replaced the delay cables used in the FaNS-1 setup. This allows for a significantly increased channel density and reduces noise pickup in the cable delays. Each circuit board is fitted into a single-width NIM unit for ease of use.

The upgraded preamplifiers provide a factor of 10 higher gain, which puts the neutron capture peak at approximately 200 mV, rather than 20 mV. This improves energy resolution and allows for a lower threshold for acquisition. Separately, the

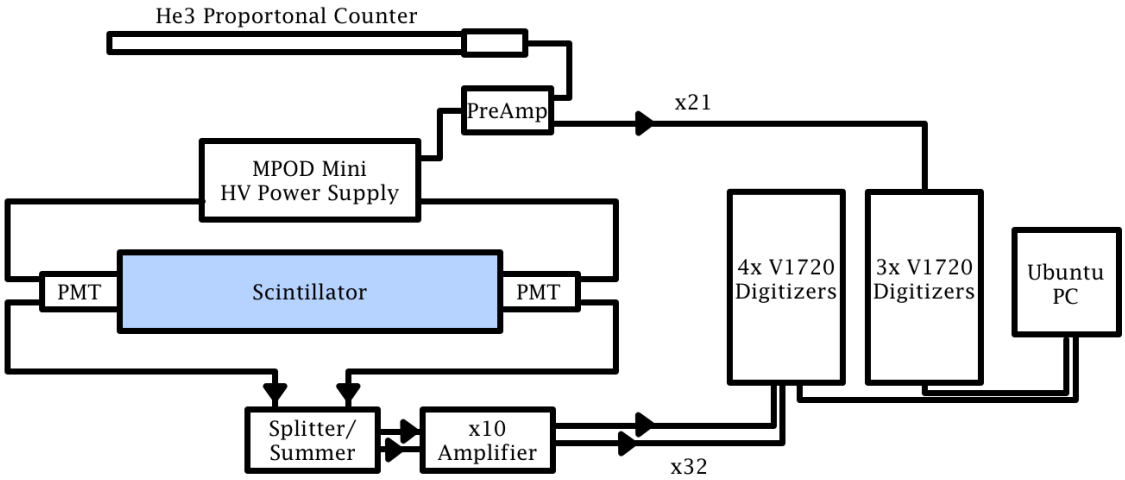

Figure 5.20: An overview schematic of the detectors in the FaNS-2 array. Note that though only one scintillator bar and one ^{3}He counter are shown, there are 16 scintillators and 21 ^{3}He proportional counters in FaNS-2.

increase in channel density simplifies the experimental setup, without compromising the ability to set individual high voltages for gain matching. Figure 5.21 shows the ^{3}He energy spectrum for the three preamplifiers used in the FaNS detectors: the initial Mechtronics model 400 used at the surface, the Canberra model 2006 used at KURF, and finally the new CAEN 1422 preamplifiers used for FaNS-2.

By improving the ^{3}He electronics, the energy resolution at the neutron capture peak improves from 8.9% with the Mechtronics model, to 5.8% with the Canberra unit, and finally to 2.6% with the CAEN preamplifier. This will allow for a tighter cut on the ^{3}He energy, which reduces backgrounds from alpha events in the ^{3}He proportional counters.

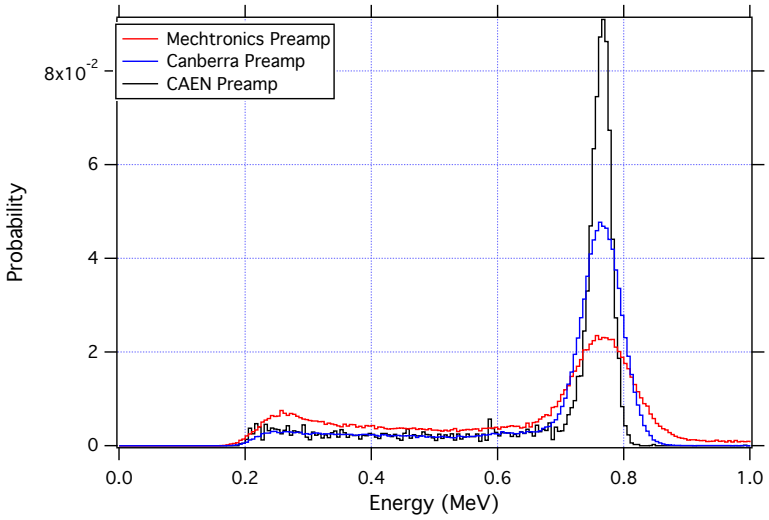

Figure 5.21: A comparison between the three preamplifiers used in the FaNS detectors. Shown are the probability distributions for each manufacturer (Mechtronics 400, Canberra 2006, and CAEN 1422), and highlights the improvement of the CAEN preamplifier over the previous units.

5.3.1 Trigger system

To control the synchronous triggering of the detector array, an external trigger propagation system is used. The trigger system is based upon NIM logic signals that are generated by the digitizers when they trigger. These logic signals are then sent through a Linear Fan In/Out and are directed to each of the digitizers' Trigger In port. A diagram of the trigger system is shown in Figure 5.22.

Either the PMT digitizers or the ^{3}He digitizers may generate a global trigger. Having this set up in hardware allows the operator to control the trigger flow in software. The digitizers optionally generate or receive external triggers. These settings are controlled via software, which is discussed further in Section 5.4.

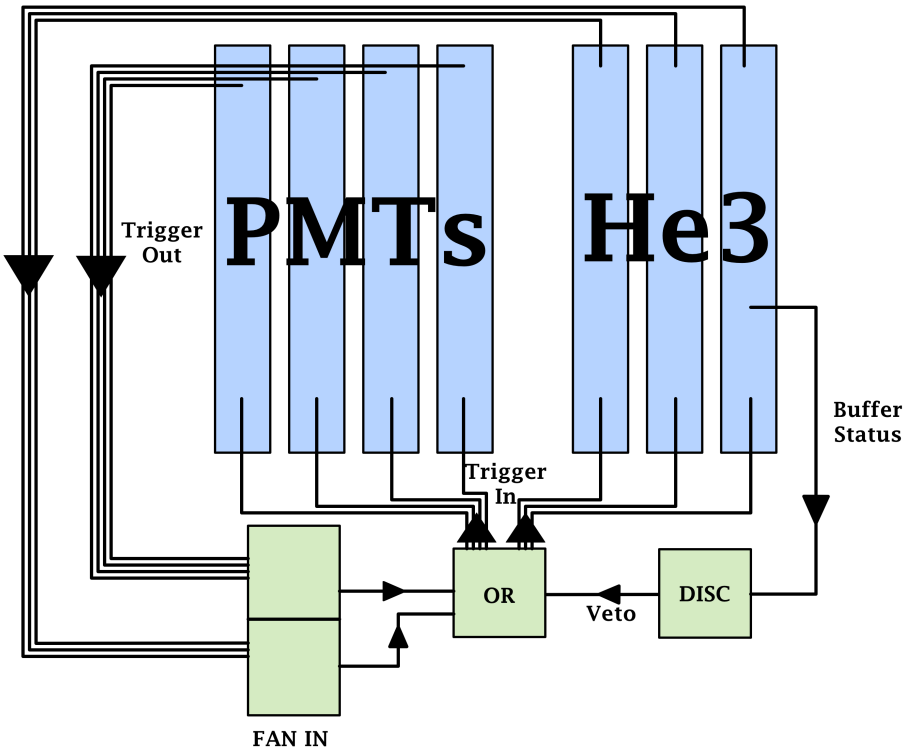

Figure 5.22: A schematic of the trigger system for FaNS-2. The digitizers (blue) are split into two sets, one for PMTs and one for ^{3}He counters. The trigger logic (green) controls which digitizer set is generating the global trigger. More details are in the text.

5.4 Data acquisition control

The waveform digitizers are controlled by a PC running Ubuntu Linux over two optical fiber cables, one for the ^{3}He digitizers and one for the PMT digitizers, each of which has a data throughput of 80 MB/s. The DAQ is controlled by a custom software program, a screen shot of which is shown in Figure 5.23.

The DAQ program is controlled by a Python-based interface that allows all settings to be controlled automatically. A typical running script can be found in Appendix D. Acquisition is segmented into discrete cycles of running time, typically

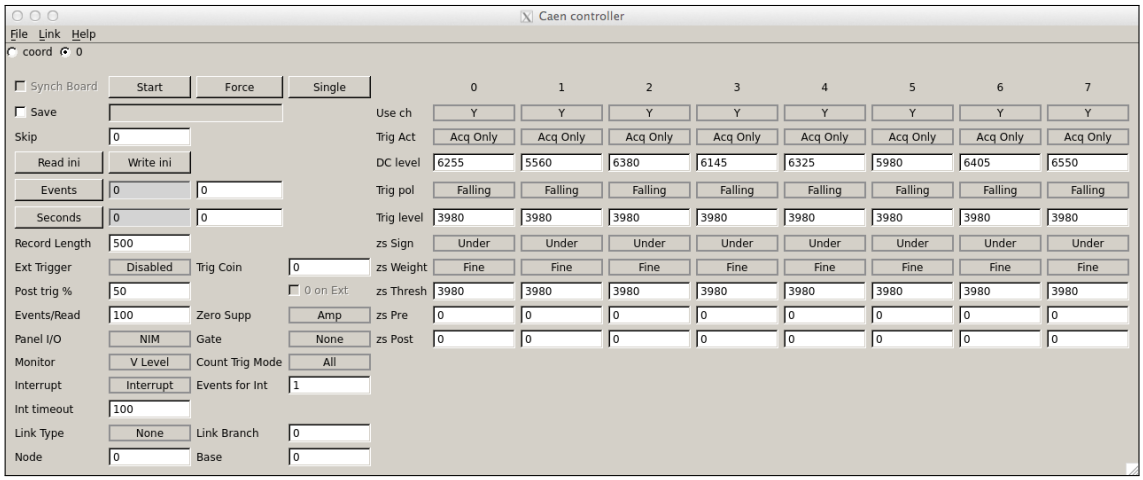

Figure 5.23: A screenshot of the CAEN controller DAQ program. Here all the settings of an individual board can be controlled. A separate panel is used to control the synchronous operation of multiple cards.

one hour. At the beginning of a run cycle, a series of calibration runs are performed. A typical running cycle is shown here:

1. Gamma Calibration - Low PMT thresholds are applied, with synchronous triggering for the scintillator digitizers (100 s long data set).

2. Muon Calibration - High trigger thresholds are applied, with low zero-suppression thresholds, and synchronous triggering for scintillator digitizers (100 s long data set).

3. NaI Calibration - The NaI detector free triggers alone, monitoring gamma backgrounds with better resolution than organic scintillator. (100 s long data set).

4. Neutron Data - Any ^{3}He counter triggers all digitizers synchronously (3600 s long data set).

For all data acquisition modes, the sampling clock is daisy-chained from the first digitizer to the others. The digitizers contain an analog output (labeled "Mon/Σ") that can be controlled via register. The Mon/Σ output from one of the digitizers is used to generate a gate for acquisition that is sent through a Fan In/Fan Out to each digitizer synchronously. The time stamps are initialized when acquisition begins, yielding a uniform trigger timestamp across the digitizers for each event.

For gamma and muon data acquisition modes, only the PMT digitizers are operated. The acquisition windows are shortened to reduce pileup and minimize dead-time. Any PMT that triggers generates a Trigger Out that is propagated to all four digitizers simultaneously. The gamma calibration mode used a low trigger threshold to record events with energies below 3 MeV. For muon data acquisition, the trigger threshold is increased to $\sim$ 3 MeV, to reject gamma events.

For neutron triggering, all seven digitizers are operated synchronously. Any ^{3}He signal triggers the full detector array. The digitizer that contains the triggering channel outputs a Trigger Out NIM logic signal, which is passed through a Fan In/-Fan Out and is sent to the Trigger In for each digitizer. This guarantees synchronous triggering regardless of which digitizer generated the trigger.

5.5 Data analysis

The increase in complexity of the FaNS-2 detector is mirrored in the complexity of the data collected. The analysis, therefore, must also be modified to handle this

increase. The data structure and updated analysis software are presented in this section.

5.5.1 Data structure

The FaNS-2 data structure is based on the standard data format generated onboard the digitizer. First, an ASCII file-header contains the complete settings of the digitizers, as well as the date and time at which acquisition began. The file-header information is used to set up the analysis code to correctly read the binary data. The file-header begins with a key, consisting of four 32-bit longwords, that denotes the total length of the header. Each event also begins with a header of four 32-bit longwords that contain the size of the event, the board ID, the event counter, and a 32-bit trigger time stamp. A diagram of the structure of one event is shown in Figure 5.24.

The CAEN digitizers also have a separate data handling concept that is more complicated, called Zero-Length Encoding (ZLE). ZLE allows for a threshold to be set in the digitizer's field-programmable gate array (FPGA) that is applied to each event as it is collected. If a signal does not pass the threshold, it is not included in the data stream from the digitizer to the PC. If a signal does pass the threshold, a fixed amount of data before and after the threshold crossing is sent back to the PC. A few examples of this are shown in Figure 5.25.

The raw data generated with ZLE have a more complicated structure, shown in Figure 5.26. The header has a single bit (bit 24 of the second longword) set

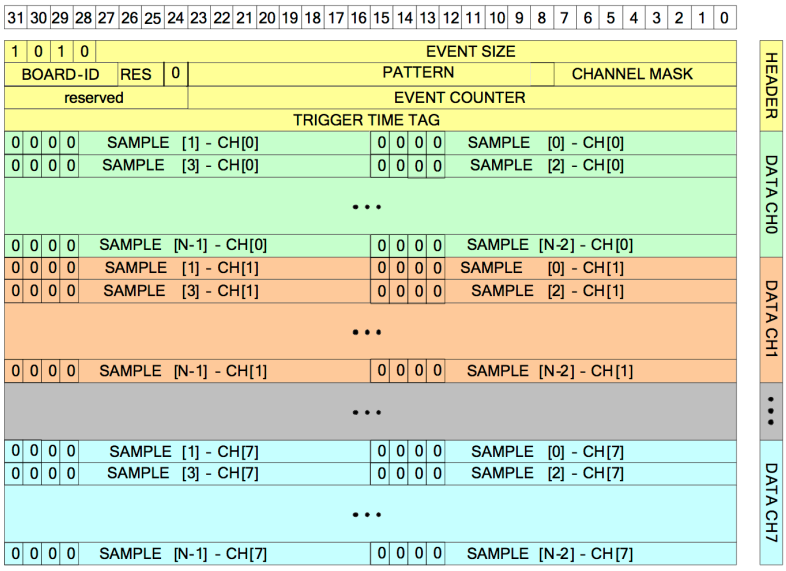

Figure 5.24: The default data structure for a single event, as generated by the digitizer. Note the four 32-bit longword header containing the event size, board ID, event counter, and timestamp. Figure from [138].

to indicate that the data are zero-length encoded, but is otherwise the same. The event-by-event data, however, are structured by Control Words (CW). A CW==1 indicates that either data is present, while a CW==0 indicates the number of samples skipped by the zero-length encoding. A single channel of data is structured:

- Total number of 32bit longwords transferred for this channel
- Control Word
- Stored data, if CW==1, or nothing if CW==0
- Control Word
- Stored data, if CW==1, or nothing if CW==0
- ...
- Control Word
- Stored data, if CW==1, or nothing if CW==0

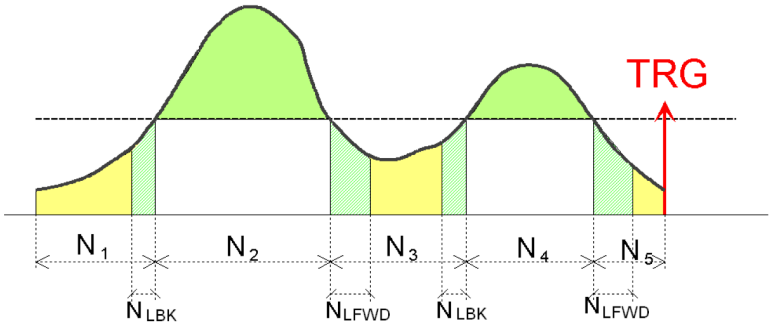

Figure 5.25: A sample event that has been collected with ZLE. Shown are two regions that cross the threshold (in green). User-defined "look back" (N_{LBK}) and "look forward" (N_{LFWD}) regions are set to include a number of samples before and after a threshold crossing. These chunks of data are transferred to the PC, while the data below threshold (yellow) are ignored. Figure from [138].

The pattern of Control Word/data/Control Word/data is repeated through the whole event. Due to large acquisition windows during neutron operation, FaNS-2 data are zero-length encoded. Without ZLE, a single event would be 21.2 MB, with ZLE enabled, the same event can be as little as 30 kB in size. This helps minimize dead-time and reduce the final file size on disk.

The FaNS-2 components are arranged into the data stream according to the detector type and location in the array: the PMTs are grouped by layer into digitizers 0-3 (the top layer of four scintillators/eight PMTs are fed into digitizer 0, the next layer into digitizer 1, etc.) and the ^{3}He counters are fed into digitizers 4,5, and 6. There are three spare channels in digitizer 6 devoted to monitoring backgrounds. A full channel listing is included in Appendix C. A NaI detector and a bare ^{3}He proportional counter measure the gamma and thermal neutron rates, respectively. These provide insight into the backgrounds present in the environment, as well monitoring any transient backgrounds, such as a gamma check source being used by a

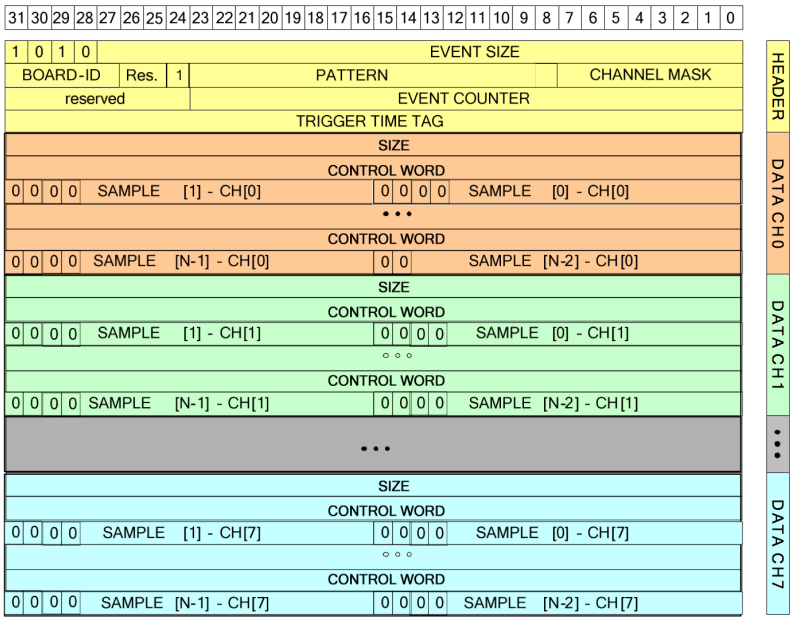

Figure 5.26: The ZLE data structure for a single event, as generated by the digitizer. Note the 24th bit of the second longword is now set to 1, indicating that the data following are zero-length encoded. Figure from [138].

different experiment in the same facility. Should any significant increase in either of these rates occur, those data sets are removed from the analysis.

5.5.2 Python data analysis

In order to handle the more complex structure of the FaNS-2 data, relative to FaNS-1, the data analysis software was transitioned from IGOR Pro to Python. Completely Object-oriented, the Python analysis is better suited for the complex data generated by FaNS-2. The code is structured in four main steps: 1) read raw data from the binary files, 2) perform peak finding algorithm on each trace and generate clusters of scintillator signals, 3) group clusters into physics data coincidences, and 4) perform cuts on those coincidences. The first three steps are performed on

every data file in parallel, the physics data are stored in Python dictionaries and written to disk using the cPickle module. The data are then sequentially loaded back into Python and cuts are applied to each event.

5.5.2.1 Reading raw data

Each data file is processed by the Python analysis. Using the Multiprocessing module, any number of data files may be processed in parallel. A key distinction made in the FaNS-2 analysis is the separation between trigger and event objects. A trigger object contains the raw traces, file position, date/time of the trigger, name of the file, the PMT calibrations for that specific time, and the light response conversion. When the trigger object is analyzed, each cluster of PMT signals is treated as a separate event. An array of event objects is returned for each trigger. A diagram showing the breakup of one trigger into multiple events is shown in Figure 5.27.

The event class contains all the calculated parameters from a specific coincidence between a PMT cluster and a ^{3}He signal. This includes the ^{3}He risetime and energy, the PMT energies, cluster location, combined energy of the event, and the geometry of the event (where each signal occurred in the detector). These are parameters that will be cut upon later.

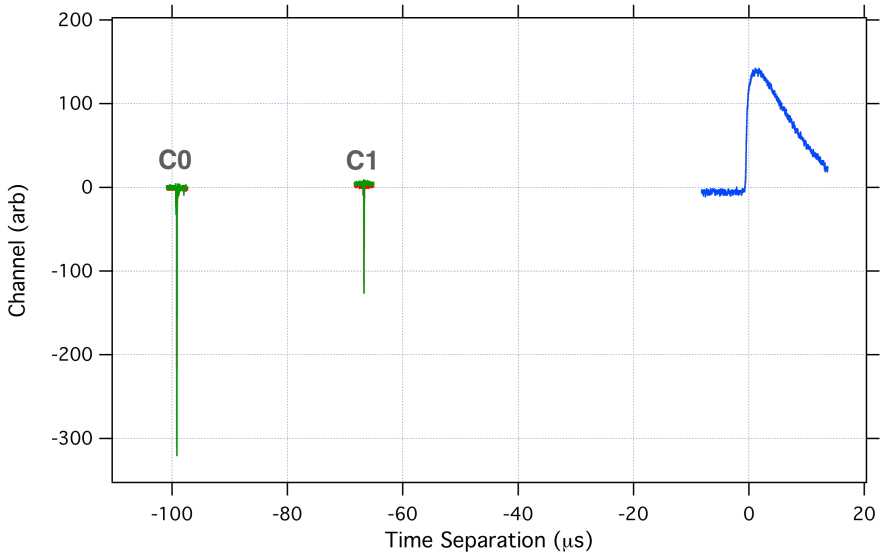

Figure 5.27: An example of a trigger with two separate scintillator clusters ("C0" at -95 μs, and "C1" at -65 μs). These two clusters are both treated as valid events and all relevant parameters are calculated.

5.5.2.2 Cluster finding and generation of physics data

One of the key features of the analysis is locating and analyzing multiple clusters of PMT signals in a given trigger. Each cluster of scintillator signals represents a separate event in the analysis. During typical operation, a trigger has on average three to four events. However, during certain source calibrations, upwards of 10 separate events in a single trigger are observed.

A scintillator cluster is defined as a group of PMT signals occurring within 8 μs of each other. This is a broad enough window to exclude PMT after-pulsing, but is still tight enough to minimize random scintillator coincidences. To locate the multiple clusters of PMT signals, a recursive peak finder searches for scintillator signals above a threshold in each trace. When a peak is found, it is added to an array of locations.

After the full event has passed through the peak finding, the PMT traces are sent through a separate routine to determine the physics data for each cluster. This includes integration of the full and attenuated peaks, conversion of integrals to electron-equivalent energy detected (MeV_{ee}), conversion of light units to neutron deposited energy (MeV_n), and finally summing the energy deposited in each scintillator bar to generate the total energy of an event. The analysis of individual PMT signals is discussed in more detail in Section 5.5.3. The PMT clusters and ^{3}He signals are paired into coincidences, and their timing separation is calculated. The resulting events are stored in a Python array, ready for analysis.

5.5.3 Scintillator analysis

For FaNS-2, each PMT signal is digitized and stored for offline analysis. A pair of example traces from the PMTs on a single scintillator segment is shown in Figure 5.28. Note the pre-pulse generated by the Splitter/Summer module discussed earlier. After the pulses, small ripples can be seen in the traces. These are a combination of the PMTs after-pulsing and a small amount of noise caused by the Splitter/Summer module.

For each photomultiplier signal, several parameters are calculated. First, the baseline is calculated by averaging the first 10 samples, then it is subtracted from the trace. Next, a recursive peak-finding algorithm is applied that searches for peaks over a certain threshold. Finally, the integrals and amplitudes for each signal are

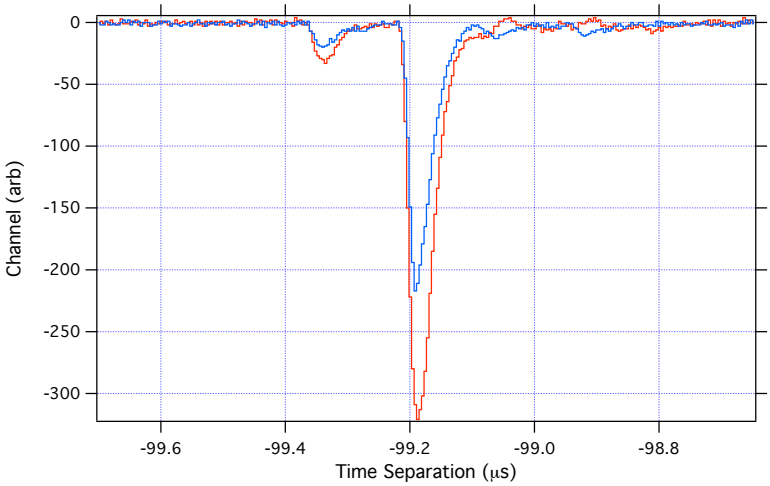

Figure 5.28: An example of two PMT signals from a single scintillator bar. Note slight variations in amplitude caused by statistical fluctuations in the number of photons detected in each.

calculated by integrating the full and attenuated pulses. These values are stored in arrays, and returned as part of a specific "event" object.

For long running data sets, it is possible for the PMT gains to drift. To account for this, the pulse integrals are converted into energies by applying a time-varying calibration factor. A discussion of generating the calibration factors is included in Section 5.5.4. For a specific cluster, each scintillator's energy is converted from MeV_{ee} to MeV_{n} using the non-linear light response. Then all the energies are summed to determine the total deposited energy of the event.

5.5.4 Scintillator calibration

Throughout the operation of FaNS-2, two different techniques have been used to calibrate the photomultiplier tubes. The first uses gamma sources, while the

second relies on the ambient radioactivity present in the lab. When combined, these calibrations give time-varying calibrations for each detector.

The construction of FaNS-2 presents a challenge for calibration. To ensure that the detected gamma energy is the "true" energy, it is important to place the source directly next to the scintillator. However, unlike FaNS-1, there is no direct access to each scintillator bar while the detector is assembled. Specifically, the center four detectors and the bottom detectors are shielded from the outside by the other scintillator bars and the aluminum baseplate, respectively.

To address this problem, a removable calibration inset was fabricated that swaps in for a ^{3}He counter. This allows a gamma source to be inserted into the void that normally contains a ^{3}He counter. There are four calibration points used to calibrate the full detector, which are indicated in Figure 5.29.

All the scintillator segments are exposed to the same gamma source, and an initial calibration parameter is extracted in analysis. As was performed for FaNS-1, the recorded gamma spectra are fit with a Monte Carlo generated template, shown in Figure 5.30.

A standard procedure for gamma calibration of organic scintillator is to use the the half-height of the edge as the location of the Compton edge. However, since the scintillator bars are not small, there is a probability that gammas will Compton scatter multiple times. Thus the half-height of the energy spectrum cannot be assumed to be the location of the Compton edge. The spectra are instead fitted by a smoothed template generated by MCNP. When the calibration parameters obtained

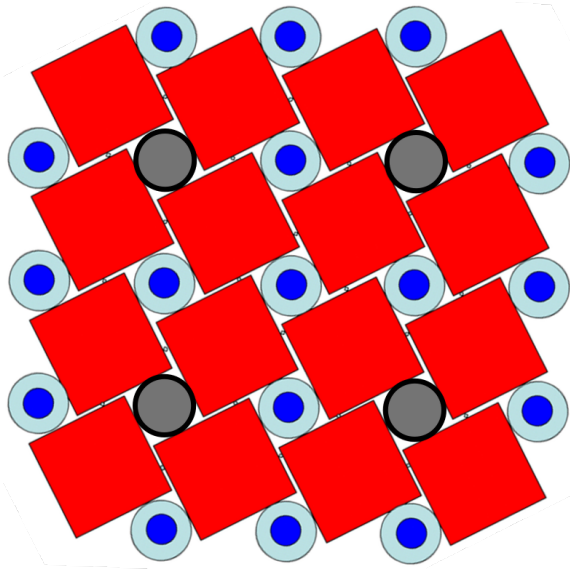

Figure 5.29: A schematic showing the four calibration locations for FaNS-2 (dark grey circles). A light-tight tube is inserted into these ^{3}He ports that allows for the insertion of a gamma source. Thus each scintillator bar is calibrated with a source directly incident upon it. There is no self shielding from the surrounding detectors or support structure.

by fitting the spectrum are compared with the half heights of the distribution, a 15% shift in the energy scale is observed.

An important lesson learned with FaNS-1 is that the collection of periodic gamma calibration data is exceptionally important. PMTs drift over time, and the ability to track their gain can salvage data that otherwise would have been lost. To this end, FaNS-2 is operated in a scintillator free-trigger mode every hour to monitor the response of the PMTs. These data are analyzed and an instantaneous calibration factor is extracted. The histogram of one channel from a gamma run is shown in Figure 5.31.

A level crossing within the steepest section of the spectrum is chosen to be tracked. In Figure 5.31, the steepest section is between pulse integrals 2000 and

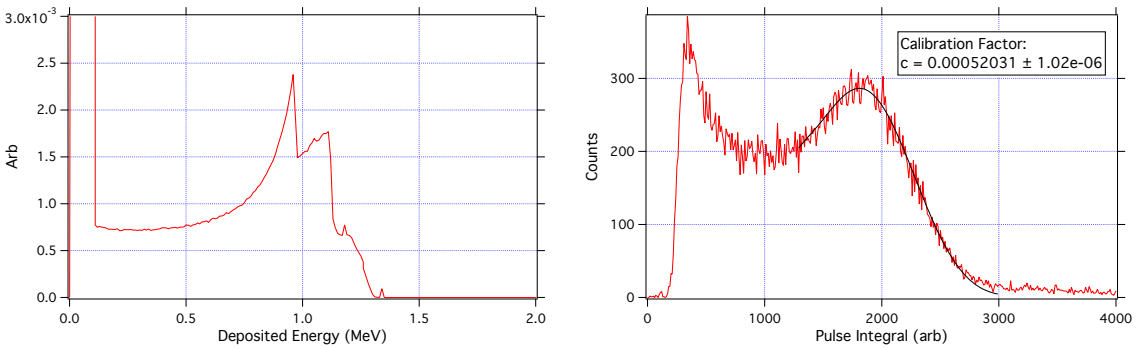

Figure 5.30: Left: The Monte Carlo generated template for ^{60}Co that is fitted to the data. Right: The recorded energy spectrum from illumination of a single scintillator bar, along with the fitted spectrum. The calibration factor is in units of *integral/MeV* to convert the raw integrals into energy. Note: the fitted spectrum has been smoothed with a simple Gaussian smoothing algorithm to account for detector resolution.

3000. To track any changes in the location of this section, the place where the spectrum crosses a threshold is followed. In this case, a reasonable threshold is 50 counts/bin. For all subsequent calibration files, the location of this threshold is stored. If the calibration shifts, this location will change and the calibration of that channel can be adjusted accordingly. This procedure is repeated for each channel and for each calibration file. When finished, a variable calibration factor for each time step is produced. These are stored in a text file with a timestamp for further analysis.

To use the time varying calibration factors, the time of the event is first determined. This is done by adding the event timestamp to the start time of data acquisition, which is stored in the data file's header. Then, for each event, the calibration factors for the scintillator are found by interpolating between nearest calibration points in the varying calibration array.

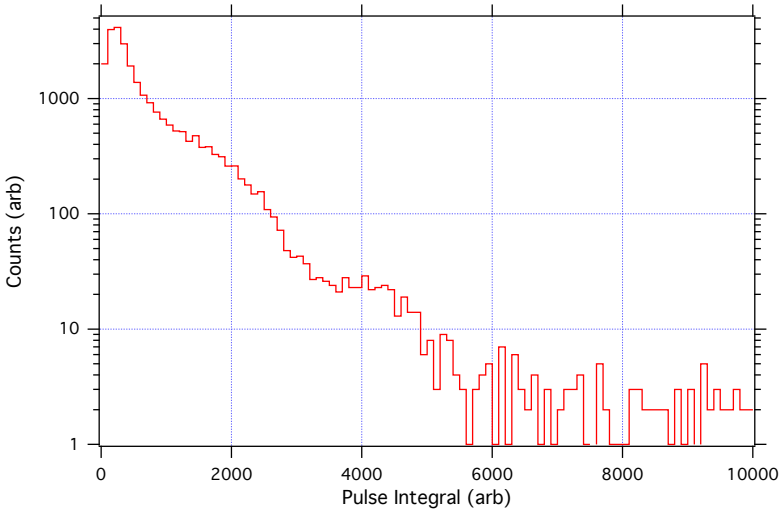

Figure 5.31: A spectrum recorded with one of the PMTs in FaNS-2 during a free trigger calibration run.

5.5.5 ^{3}He analysis

Figiure 5.32 shows an example of a ^{3}He signal recorded with FaNS-2. The analysis of each ^{3}He signal is similar to that used for FaNS-1. First, the baseline is removed by averaging over the first 10 samples. The amplitude of the resulting signal is stored as the energy of the specific signal. For the risetime analysis, a linear interpolation is performed to find the level crossings at 10% and 50% of the signal's full height. Finally, the location of the ^{3}He signal is taken to be the 50% point. These parameters are all returned and stored in each event object for a given trigger.

5.5.6 Performing cuts

After the initial generation of multiple events from a trigger, the events are treated as independent entities. This prevents biasing the analysis by choosing one

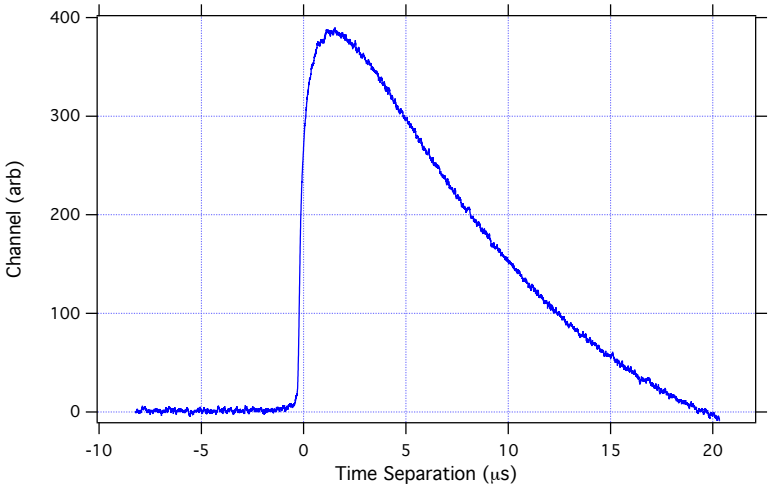

Figure 5.32: An example of a ^{3}He signal recorded with FaNS-2. Note, the ^{3}He signals are passed through AC couplers to remove large-scale baseline fluctuations.

event per trigger over the others. In order to ensure the cuts and subtraction of random events is done correctly, every event must be kept. To perform cuts on the FaNS-2 data, a series of conditions is determined. Approximately 200 Boolean conditions are tested against each event. These can be combined in any fashion to produce more complicated cut logic. The following section outlines these conditions and how they are generated.

5.5.6.1 PMT-specific cuts

A series of cuts is performed on the photomultiplier signals. First, a cut is placed that demands that both PMTs on a given scintillator bar are over a small threshold. A second threshold is placed on the sum of the light collected from a single scintillator bar. A cut can be placed on the multiplicity of the event to single out the effect of multiple scattering and segmentation effects, if desired.

After cuts are made, the total energy and multiplicity are recalculated. This ensures that if a signal is below threshold, it will not contribute to the final analysis of that event. A brief study of the effects of varying the analysis threshold is presented in Chapter 6.

5.5.6.2 ^{3}He-specific cuts

The main cuts on the ^{3}He signals are on the energy and risetime of the signal. The ^{3}He energy must be less than 0.9 MeV to reject alpha interactions in the detectors. Cuts are also placed in the risetime versus energy space to reject gamma, alpha, and microdischarge events:

$$\tau_r > 0.1\ \mu\text{s} \tag{5.1}$$

$$\tau_r < \frac{0.45\ \mu\text{s}}{0.59\ \text{MeV}} \times E + 0.15\ \mu\text{s}, \tag{5.2}$$

where τ_r is the 10% to 50% risetime for the helium signal and E is the total energy of the pulse. Cut 5.1 rejects microdischarge sparks by eliminating fast rising pulses. Cut 5.2 eliminates beta/gamma-like events that have low energies and long risetimes. These cuts are discussed in detail in Chapter 2. The effects of these cuts are shown in Figure 5.33.

The ^{3}He cuts effectively remove gamma/beta and microdischarge noise events while rejecting a minimum of neutron captures. The neutron cut efficiency is very high, with only a small fraction of neutron captures being rejected.

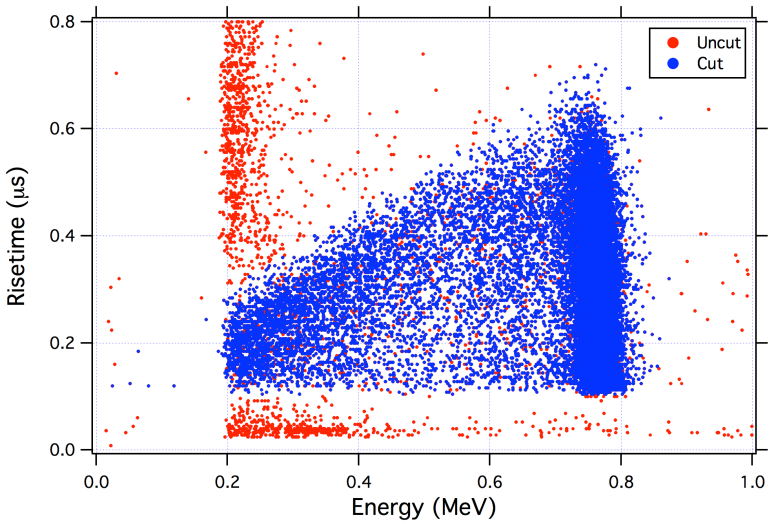

Figure 5.33: A scatter plot of showing the risetime versus energy of the ^{3}He signals. Shown in red are the uncut data, while the blue markers are the events that pass the 2D risetime/energy cuts.

5.5.6.3 Subtraction of random coincidences

As with FaNS-1, events with negative time separations are used to monitor the random coincidence rate in FaNS-2. These events are completely uncorrelated from the neutron capture and so appear uniformly in time. Because the scintillator and ^{3}He count rates can vary with time, tracking the random coincidence rate in real-time is the most effective method to ensure proper background subtraction. Events with positive time separation could be either real neutron coincidences or random coincidences. The negative and positive timing events will be referred to as "random only" and "real+random" events in the rest of this work. This is shown in Figure 5.34.

The energy spectrum of "random only" events is subtracted from the energy spectrum of the "real+random" events. FaNS-2 was operated with an asymmetric time window that spans from -200 μs to +600 μs. Thus, the "random only" energy

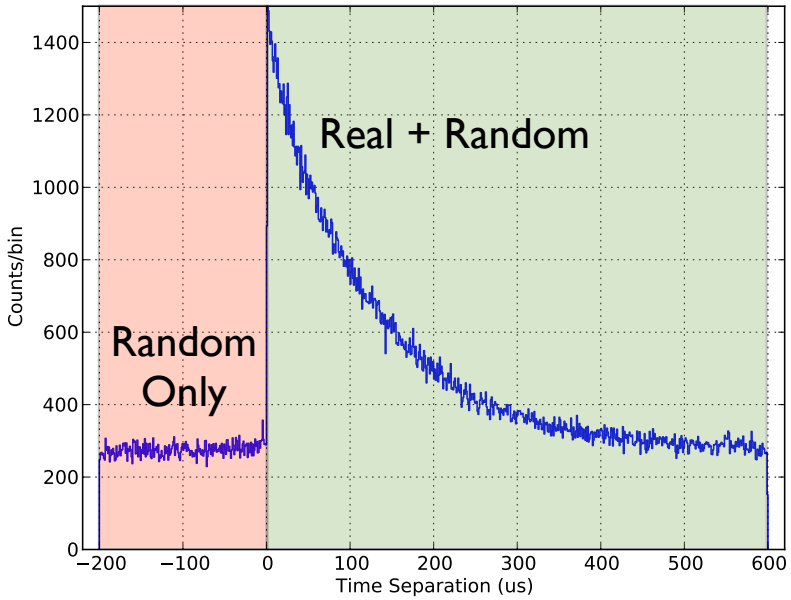

Figure 5.34: The distribution of time separations between ^{3}He signals and PMT clusters for FaNS-2. The negative timing events, labeled "Random Only" are when the ^{3}He signal occurs before the PMT cluster, which is a non-physical event. Random events are uniform in time, and so are found in the positive timing events as well.

spectrum must be scaled by the relative size of the acceptance windows (nominally a factor of three). A bin-wise subtraction is performed resulting in the background-subtracted energy spectrum. When working with source data, it is important to also subtract any ambient neutron events that occur. Since these are real neutron signals, they will not be removed from this subtraction.

During long background data collection, a significant number of prompt coincidences ($\Delta t < 2$ μs) that are correlated but not real neutron events were observed. In FaNS-1, these were dominated by prompt gamma emission following alpha decays in the ^{3}He counters. Therefore any event that occurs with a time separation between 0 μs and 2μs will be rejected. This will be discussed further with the measurement of the ambient neutron spectrum in Chapter 7.

5.5.6.4 Effects of cuts

To study the relative effects of these cuts, they are applied to a sample set of data with a ^{252}Cf neutron source centered at ∼110 cm above FaNS-2 . Each of the aforementioned cuts are applied separately to show their relative effects. The results are listed in Table 5.2.

Table 5.2: A table listing the effects of each cut placed on data collected with a ^{252}Cf neutron source above ∼110 cm above FaNS-2.

		Total Events:	113833
	Cut Parameter	Cut Range	Events After Cut
^{3}He Cuts	^{3}He Energy	0.2 MeV < E < 0.8 MeV	113101
	^{3}He Spark Cut	$\tau_r > 0.1$ μs	112614
	^{3}He β Cut	Diagonal in τ_r vs E	110249
	All ^{3}He Cuts		109729
PMT Cuts	Scintillator Energy	E > 1.0 MeV$_n$	52007
	Prompt Δt Cut	Removal of $0 < \Delta t < 2$ μs	112836
Combined			49642
$\Delta t > 0\mu$s			40538
$\Delta t < 0\mu$s			9090
After subtraction			13268

The dominant cut is the threshold on the scintillator signals. This is due to the large number of neutrons emitted by ^{252}Cf that are below the 1 MeV$_n$ threshold used in this test. These neutrons enter the detector, thermalize, and may capture on a ^{3}He counter. However, they are not energetic enough to produce a signal in the plastic scintillator and are therefore cut.

5.6 FaNS-2 MCNP

FaNS-2 has been modeled in MCNPX, including the support structure and enclosure. The simulations use the default model physics (based on the Bertini Intranuclear Cascade model [139]) for neutrons greater than 20 MeV [140]. One major change to the simulation is the exclusion of gamma ray production. MCNPX is designed to reproduce the correct branching ratios for certain processes on a statistical basis, not on an event-by-event basis. This leads to non-physical events where a single neutron may capture on two different nuclei. For a capture-gated detector, this becomes problematic; neutrons are observed that capture on ^{3}He and yet still produce a 2.2 MeV gamma from capturing on hydrogen. These events skew the energy spectra produced by the simulation. Therefore, gamma ray production has been removed from the simulation.

Unlike what was used for FaNS-1, the simulation output is now treated on a event-by-event basis. The output file contains the light generated in each scintillator segment, the ^{3}He counter where the neutron captured, and the time between the neutron scatter and capture. These data are fed into the Python data analysis and the same experimental cuts are placed on them as the experimental data.

An important lesson-learned from FaNS-1 is the sensitivity of the analysis thresholds on photon statistics. To better address this, the calculation of photon statistics and PMT resolution has been added to the MCNP analysis. The light generated in each scintillator bar is converted from MeV$_{ee}$ into a number of photons detected using the measured light collection efficiency. Then, a random number is

selected from a Poisson distribution with an expected value equal to the number of photons. The output from that random number generator is then converted back into MeV_{ee}. This technique appropriately accounts for the effects of light collection on the achievable energy resolution. This should vastly improve the ability of the Monte Carlo to match the data.

The photomultiplier tubes also contribute to the resolution of the detected spectra. As discussed in Section 5.2.3.2, the Gaussian full-width half-max (FWHM) of the single-photoelectron peak is approximately 80%. This can be used to determine the gain of the first stage of the PMTs. A Gaussian with FWHM of 80% corresponds to a gain of 9 electrons created from a single photon.

The change in energy reconstruction based on different photon statistics is shown in Figure 5.35. Here the light collection has been varied from effectively infinite to 0.04 MeV_{ee}/photon. As discussed in Section 5.2.3.2, the measured light collection for the FaNS-2 PMTs is 0.005 MeV_{ee}/photon.

Accounting for photon statistics also provides a method for applying a consistent threshold for both the data and simulation. This is important for the comparison of the detection efficiency between ^{252}Cf source data and MCNP. Since the ^{252}Cf energy spectrum above 1 MeV is exponentially shaped, a small variation in the effective threshold can create a large change in the number of neutrons accepted. For the efficiency measurements, this would create a constant offset between the data and the Monte Carlo.

The full MCNP process is shown here:

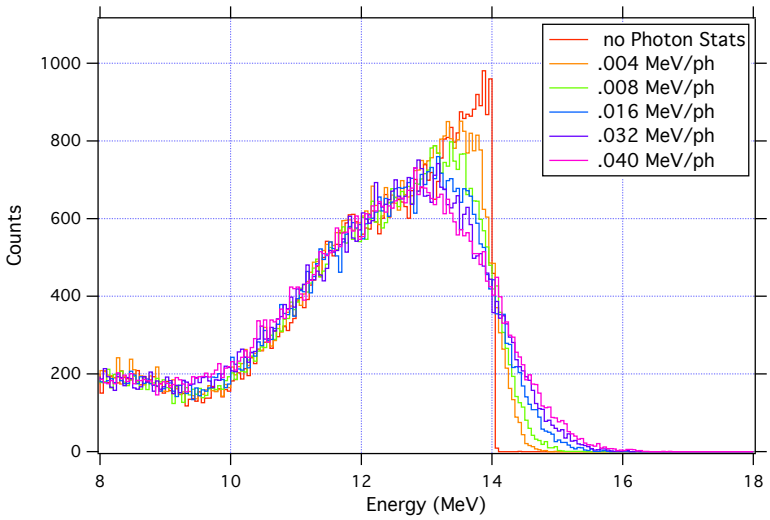

Figure 5.35: The resulting spectra from an MCNP simulation of the 14 MeV neutrons on FaNS-2 with different photon statistics. The measured light collection for FaNS-2 is 0.005 MeV_{ee}/photon.

1. Neutrons are thrown at FaNS-2 in MCNPX based upon the input source distribution.

2. MCNPX generates the tracks of each event using the PTRACK file format.

3. Filters select events that have a scatter in a scintillator cell and a ^{3}He capture.

4. Particle tracks are converted into energy depositions (in MeV_{ee}) in each scintillator.

5. These energy depositions are written to a file, along with the location of scatters, the location of ^{3}He capture, and the time between scatter and capture.

6. The MCNP output is converted into pseudo-data:

   - Energy is converted into photons detected (including Poisson statistics).

- The number of photons detected is smeared by a Gaussian random number to account for the measured PMT resolution.
- Each MCNP event is stored in the same Event object as the real data.

7. The simulated events are passed through the same cuts as the real data.

Throughout the MCNP analysis, the measured light response function of the FaNS-2 plastic scintillator is used, as discussed in 2.2.1.

To compare MCNP to the experimental data, each measurement setup is carefully modeled. For the mono-energetic neutron generators discussed in the next chapter, the center of the generator is matched with a point source of isotropic, mono-energetic neutrons. MCNPX has a built-in standard for the ^{252}Cf neutron energy spectrum, which is based upon the ENDF-VII standard [10]. A ^{252}Cf point source was placed at the same distances used for the efficiency measurements, discussed in the next chapter, and the total number of detected neutrons is compared. The Monte Carlo results are directly compared with the experimental data in the next chapter.

As was discussed in Section 2.4.3, the sensitivity of the ^{3}He proportional counters was measured to be 16% lower than the MCNP model produces. This manifests in a higher overall calculated efficiency efficiency for FaNS-2 than is realized. The root cause of this effect is currently under study, with new measurements required for confirmation. To adjust for this difference, a detection efficiency of 0.84 ± 0.1 is applied to the MCNP.

In Chapter 6, MCNP simulations are compared to each of the source measurements, including mono-energetic neutron generators and a calibrated ^{252}Cf neutron source. In Chapter 7, a simulation is used to determine the weighted efficiency of FaNS-2 to the cosmogenic neutron spectrum as reported by Reference [117]. This is applied to the recorded data to produce a measurement of the incident fast neutron flux.

Chapter 6

FaNS-2 results from calibrated sources at NIST

Presented in this chapter are the results from source calibrations performed with FaNS-2 at NIST. First is a brief discussion of the environment in which the detector operated. Then, the results of efficiency measurements with a calibrated ^{252}Cf neutron source are presented. Finally, measurements made with two mono-energetic neutron generators are shown. Throughout, comparisons between data and Monte Carlo simulations are highlighted. A brief discussion about how these results affect the measurement of the ambient fast neutron spectrum presented in the next chapter is included in the conclusions of this chapter.

6.1 The NIST Low Scatter Lab

As discussed in Section 3.4, NIST houses a number of neutron sources ideal for calibrating detectors. These include calibrated ^{252}Cf sources with activities known to $\sim$2% and two mono-energetic neutron generators at 2.5 MeV and 14 MeV. These sources have been used to fully characterize FaNS-2 and prepare the detector for measuring the surface fast neutron spectrum. The ^{252}Cf neutron sources are calibrated using a manganese sulfate bath. A source is inserted into a 1.27 m diameter sphere of $MnSO_4$ liquid. Neutrons are absorbed by the $MnSO_4$, and the activation of ^{56}Mn is continuously measured with a scintillation counter. A photograph

of the apparatus is shown in Figure 6.1. Neutron sources are compared against the NIST standard Ra-Be photoneutron source, NBS-1. Source activities are typically measured to 1.2% using the NIST calibration setup. As the ^{252}Cf source decays, different neutron-emitting fission daughters build up, and the uncertainty in the calibration grows. The total activity of the source used to calibrate FaNS-2 is known to 2% [141, 142].

Figure 6.1: A photograph of the $MnSO_4$ neutron calibration apparatus at NIST. The blue sphere is the 1.27 m diameter volume in which neutron sources are calibrated. Figure from Reference [143].

After operating FaNS-1 in the Californium Neutron Irradiation Facility (CNIF), it was discovered that a significant fraction of the detected neutrons had deposited some of their energy into the walls of the lab. This led to a large low-energy tail of detected events, known as room-return. To mitigate this problem, the characterization of FaNS-2 was performed in the Low Scatter Facility at NIST. This lab is surrounded by low-density walls that minimize room-return neutrons. The Low

Scatter Facility is primarily used for neutron calibrations of personal dosimetry and hand-held neutron monitors [144]. The lab is a large (12 m × 13 m) two-level room with thin, metal walls and ceiling. The main level has an aluminum floor to further reduce backscattering neutrons. There is one high-density concrete shielding wall that separates the lab from the main building.

FaNS-2 was deployed in the corner of the lab that is farthest away from the main building. A schematic of the location is shown in Figure 6.2. This location was chosen to minimize the shadowing effects of the building when measuring the surface fast neutron spectrum. The detector rested on top of a 15 cm thick concrete slab.

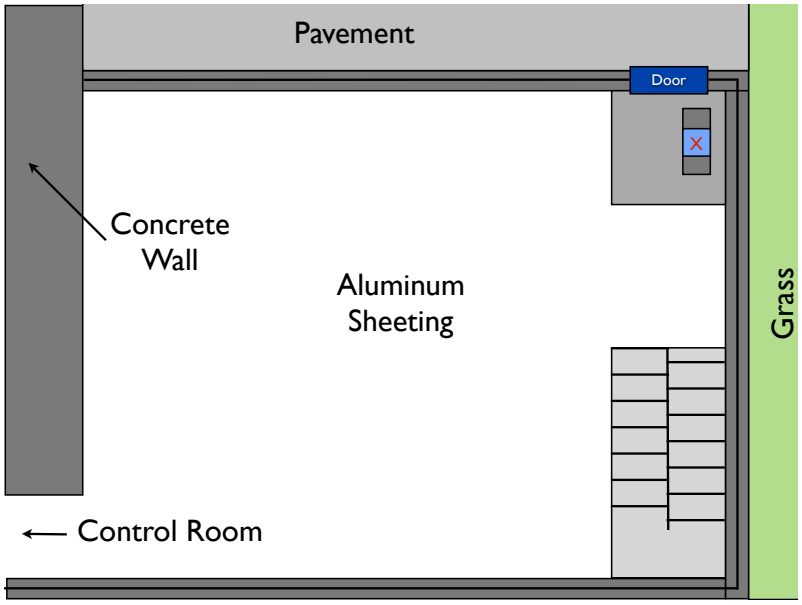

Figure 6.2: Schematic showing the location of FaNS-2 (red 'x') in the Low Scatter Room at NIST. The active volume of the detector is shown in blue. The high density concrete wall is on the left, while a small berm (30 cm high) runs around the rest of the room supporting the aluminum walls. The main area of the lab has aluminum sheeting for a floor. The detector is located on top of a 15 cm thick concrete pad.

The detector was powered through a uninterruptible power supply (UPS) that protected the system from power surges and filtered the incoming AC power. The data acquisition electronics were kept separate from the high voltage, which was also separate from the PC and monitor. This helped to minimize any noise pickup over the power lines on the data acquisition. Similarly, the high voltage power supplies were operated in a separate electronics rack to minimize any noise caused by the switching power supplies.

6.2 Efficiency calibration with a ^{252}Cf source

To measure the absolute neutron detection efficiency of FaNS-2, a ^{252}Cf neutron source was positioned at a range of distances above the detector. A vertical frame was assembled overtop of the detector to provide consistent and reproducible positioning of the source. The frame consists of two 3 m long 80/20 segments with two cross braces. The source can either be hung from the top cross piece, or can be placed on top of the lower cross piece, which has a platform to allow the inclusion of lead shielding.

6.2.1 Source description

The ^{252}Cf source used in this calibration is DHS-9667. It was last calibrated on September 3, 2009 with a neutron activity of (14,900±180) /s [145]. Using the lifetime of ^{252}Cf, $\tau = 3.816$ years, the average remaining activity for the dates the

data were collected, April 24 to May 20, 2013, is:

$$\Gamma = \Gamma_0 \times e^{-t/\tau}$$

$$\Gamma = 14,900 \text{ n/s} \times \text{Exp}(-3.675 \text{ years}/3.816 \text{ years})$$

$$\Gamma = 5690 \pm 150 \text{ n/s}.$$

This is the total neutron activity of the ^{252}Cf source at the time of measurement. The uncertainty here has been increased from 1.2% to 2% of the source activity to account for slight variations in decay rates of different isotopes in the source [66]. There is also an uncertainty related to the variation in activities across the month the data were collected. The difference between the rate at the beginning and the end of the ^{252}Cf measurements is $\sim$100 n/s. This has been included in the above uncertainty.

The source is enclosed in a stainless steel encapsulation, shown in Figure 6.3a. The source is situated 0.8 cm from the bottom of the encapsulation. The stainless steel encapsulation changes the shape of the energy spectrum of the emitted neutrons. This was not an issue for FaNS-1 because a different source was used with significantly thinner encapsulation. However, for FaNS-2 the effect is noticeable, as shown in Figure 6.3b. Therefore, the simulated spectrum is used for the remainder of this section.

As with FaNS-1, only the neutron activity above the experimental threshold is included in the analysis. This prevents the reported efficiency from being artificially suppressed by the portion of the ^{252}Cf spectrum that is below threshold. To estimate

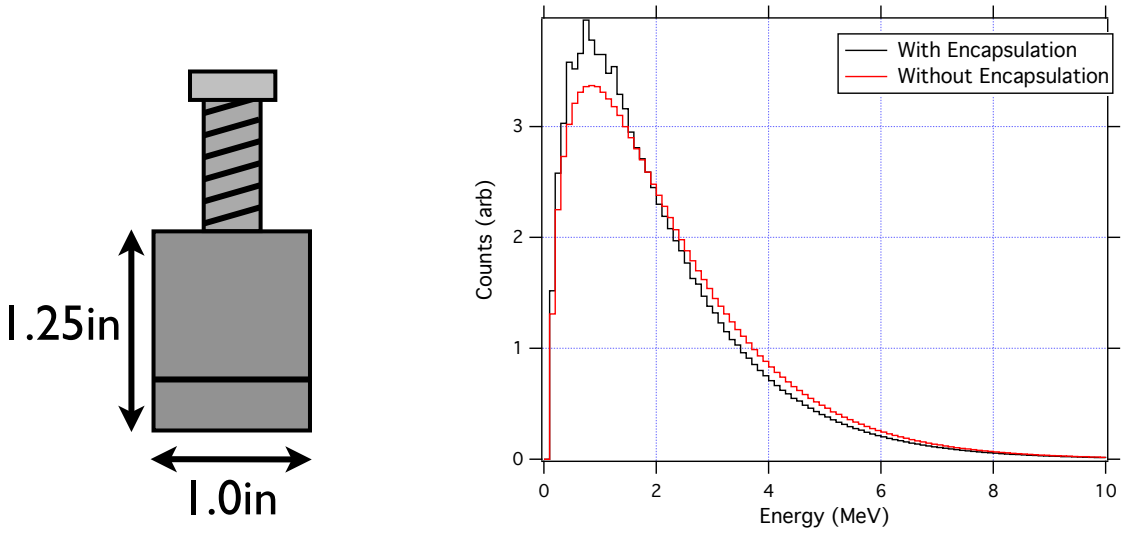

Figure 6.3: Left: A diagram of the encapsulation of ^{252}Cf source DHS-9667 used to calibration FaNS-2. The body of the encapsulation is stainless steel. Right: The effect of the encapsulation on the energy spectrum emitted by the source in MCNP. Note how the spectrum is shifted down in energy, increasing the number of neutrons below 1.5 MeV.

activity of the source over the experimental thresholds, the normalized ^{252}Cf energy spectrum generated by MCNP is integrated above each threshold. The activity is then corrected by this fraction. For these data, an analysis threshold of 2 MeV$_n$ is set, yielding a neutron activity of:

$$\Gamma_{E_n>2.0\ \mathrm{MeV}} = 2137 \pm 85\ \mathrm{n/s}. \tag{6.1}$$

The uncertainty in the above rate is based upon a 3.5% uncertainty in the absolute calibration, and a 2% uncertainty in the shape of the ^{252}Cf energy spectrum [10].

6.2.2 Description of the data

The ^{252}Cf source was placed above the detector at seven distances ranging from 85.15 cm to 238.3 cm. The spread in distances and the number of measurements allows for coverage of a large range of neutron capture rates and solid angles. Since the detector is not small compared to the distances at which the source was positioned, a simple $1/r^2$ estimate of the solid angle cannot be used. The solid angles, Ω, have been calculated using a two-dimensional integral:

$$\Omega = \int_{SA} \frac{h + z_0}{(x^2 + y^2 + (h + z_0)^2)^{3/2}} \, dx \, dy, \tag{6.2}$$

where x and y are taken to be in the plane of the surface of the detector, z_0 is the average interaction depth of neutrons in the detector, and h is the height is the distance above the top of the detector where the source was placed. The integration limits are taken from the extent of the top plane of the detector. Table 6.1 shows the run parameters of the data for the calibration data. The distances are measured from the bottom of the source enclosure to the center of the first layer of scintillator, which is the expected depth of interaction for ^{252}Cf energy neutrons [114].

To monitor for dead time, a scalar was used to count the absolute number of triggers sent to the digitizers. Should the memory buffers of the digitizers exceed a set threshold, a veto signal is sent to reject incoming triggers[1]. This prevents the memory buffer from filling up, which would result in a loss of synchronization

[1]See Section 5.3.1 for more details about the trigger system.

between the digitizers. During the operation, none of the data sets required adjustments for dead time.

Because these data were collected in a low overburden environment, the ambient neutron rate and spectrum must be subtracted to obtain the true neutron rate. During the ^{252}Cf data collection, two long data sets were run without the source. The ambient neutron rate should be approximately stable throughout the measurements, and so will manifest as a constant offset in the efficiency data. The average rates during these two runs are listed in Table 6.1

6.2.3 Results from ^{252}Cf calibrations

For the efficiency measurements, data were collected at seven different distances. A measurement of the ambient neutron background was also performed to allow for accurate background subtraction. The results from these data sets are shown in Table 6.1 and Figure 6.4. The Monte Carlo results listed have been adjusted by the (84±10)% ^{3}He detection efficiency discussed in Section 2.4.4.

Table 6.1: Data from efficiency measurements taken with ^{252}Cf neutron source above FaNS-2. The ambient neutron rate has been subtracted from these data.

Distance (cm)	Date	Exposure (s)	Fractional Solid Angle (%)	Rate above 2 MeV (n/s)	MCNP (n/s)
238.31	5/18/13	3600	$(3.33 \pm 0.1) \times 10^{-3}$	0.264±0.03	0.30±0.03
199.45	5/17/13	3600	$(4.73 \pm 0.1) \times 10^{-3}$	0.406±0.03	0.41±0.04
161.35	4/29/13	3600	$(7.17 \pm 0.1) \times 10^{-3}$	0.612±0.04	0.62±0.06
130.87	5/20/13	3600	$(1.07 \pm 0.1) \times 10^{-2}$	0.886±0.05	0.92±0.09
110.55	5/18/13	3600	$(1.48 \pm 0.1) \times 10^{-2}$	1.181±0.05	1.24±0.1
100.39	4/24/13	3600	$(1.78 \pm 0.1) \times 10^{-2}$	1.569±0.06	1.48±0.15
85.15	5/20/13	3600	$(2.43 \pm 0.1) \times 10^{-2}$	1.799±0.06	1.99±0.2
Ambient	5/3/13	36000	N/A	0.346±0.01	N/A
Ambient	5/18/13	36000	N/A	0.347±0.01	N/A

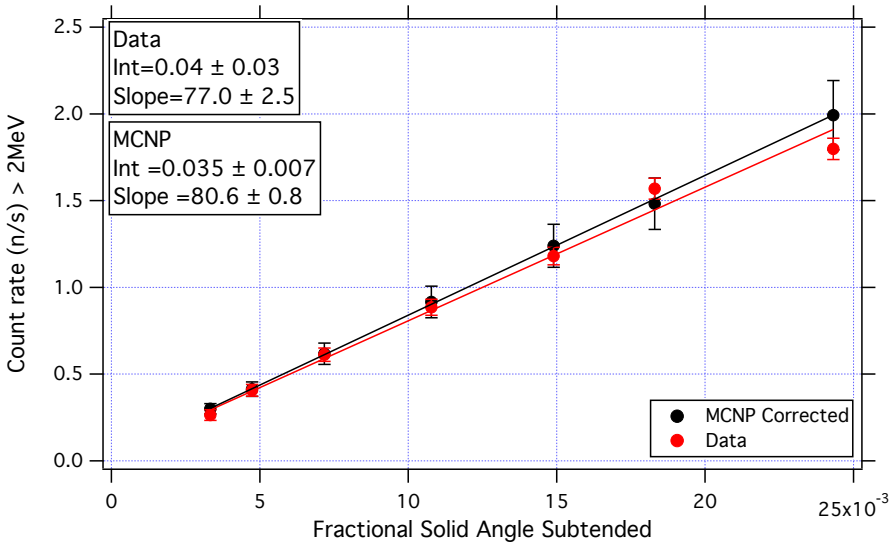

Figure 6.4: The resulting detected neutron rate (after subtracting the ambient neutron rate) versus subtended solid angle for a ^{252}Cf source at multiple distances (red) with statistical error bars. Also shown are the MCNP predictions for each distance (black) after the ^{3}He detection efficiency of 84% has been applied. The MCNP error bars are due to the uncertainty in this correction.

There is very good agreement between the data and MCNP observed in these measurements. This result lends confidence that the model of FaNS-2 accurately reproduces the measured data. The MCNP response will be used later to convert the measured ambient neutron rate into an incident neutron flux.

6.2.4 Efficiency measurement

To obtain the efficiency, a linear fit is performed to the detected rate versus solid angle data shown in Figure 6.4. The y-offset from the resulting fit is the room-return from neutrons that scatter from the walls or floor and back into the detector. The observed room-return rate is consistent with zero, which reinforces the benefit of working in the Low Scatter room. Effectively none of the neutrons

detected scattered from of the walls or floor and into the detector. As discussed in Section 3.4.2, the slope of the fitted line is proportional to the efficiency divided by the source activity:

$$\varepsilon_{E_n>2\ MeV} = \frac{slope}{\Gamma_s} = \frac{77 \pm 2.5 \text{ n/s}}{2137 \pm 85 \text{ n/s}} = (3.6 \pm 0.15)\%. \tag{6.3}$$

6.2.5 Discussion of ^{252}Cf calibrations

The (3.6±0.15)% efficiency for neutrons with energies above 2 MeV measured with the FaNS-2 detector is consistent with the simulated efficiency from MCNP for the same experimental threshold and setup. By accurately reproducing the measured data, the MCNP is shown to give meaningful results. This reinforces the use of MCNP to estimate the response of FaNS-2 to the broad neutron energy spectrum from cosmic ray interactions. This will be discussed in the next chapter.

6.3 Measurements with mono-energetic neutron generators

With a capture gated neutron spectrometer, neutrons that do not thermalize and capture are not included in the data. Thus, any neutron that partially scatters in the detector, and then leaves, is rejected. Therefore, instead of having a broad spectrum of neutron energies from a mono-energetic source, FaNS-2 produces a peak at the incident neutron energy. To confirm this, two mono-energetic neutron generators have been measured with FaNS-2.

6.3.1 Overview of Generator Technology

As discussed in Section 3.4.1, the mono-energetic neutron generators are compact accelerators based on deuterium/deuterium and deuterium/tritium fusion reactions:

$$D + D \rightarrow {}^{3}\mathrm{He} + n + 3.3\ \mathrm{MeV}, \tag{6.4}$$

$$D + T \rightarrow {}^{4}\mathrm{He} + n + 17.6\ \mathrm{MeV}, \tag{6.5}$$

which result in 2.5 MeV and 14.1 MeV mono-energetic neutrons, respectively. The generators accelerate deuterium into either tritium or deuterium to produce these reactions. They are used to test the energy reconstruction and resolution of FaNS-2. A diagram of a generator is shown in Figure 6.5.

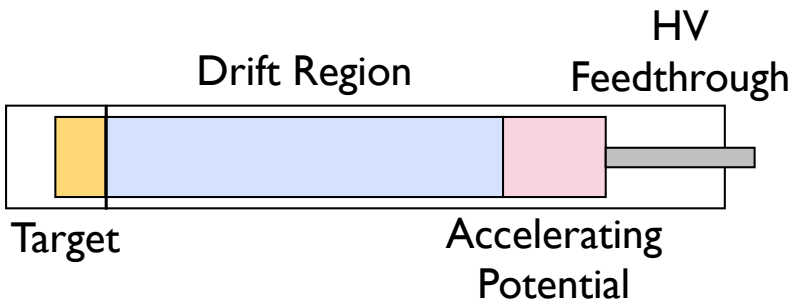

Figure 6.5: A simple schematic of a neutron generator. Either deuterium gas or a mixture of deuterium and tritium gas is accelerated into a fixed target. When two nuclei hit each other, they can fuse. Both of these reactions emit neutrons of a specific energy.

The generators are PC-controlled over serial cables. From there, any of the settings of the generators may be adjusted, including Beam Current, Accelerating Voltage, Duty Cycle, and Power. The total number of neutrons emitted roughly

scales linearly with the beam current. However, the dependence on accelerating potential is more complicated. Figure 6.6 shows the neutron yield for both DD and DT generators as a function of incident deuterium energy, as quoted from an IAEA report on neutron generators [146]. The absolute neutron yield from the generators is not reproducible and is therefore not used in this analysis.

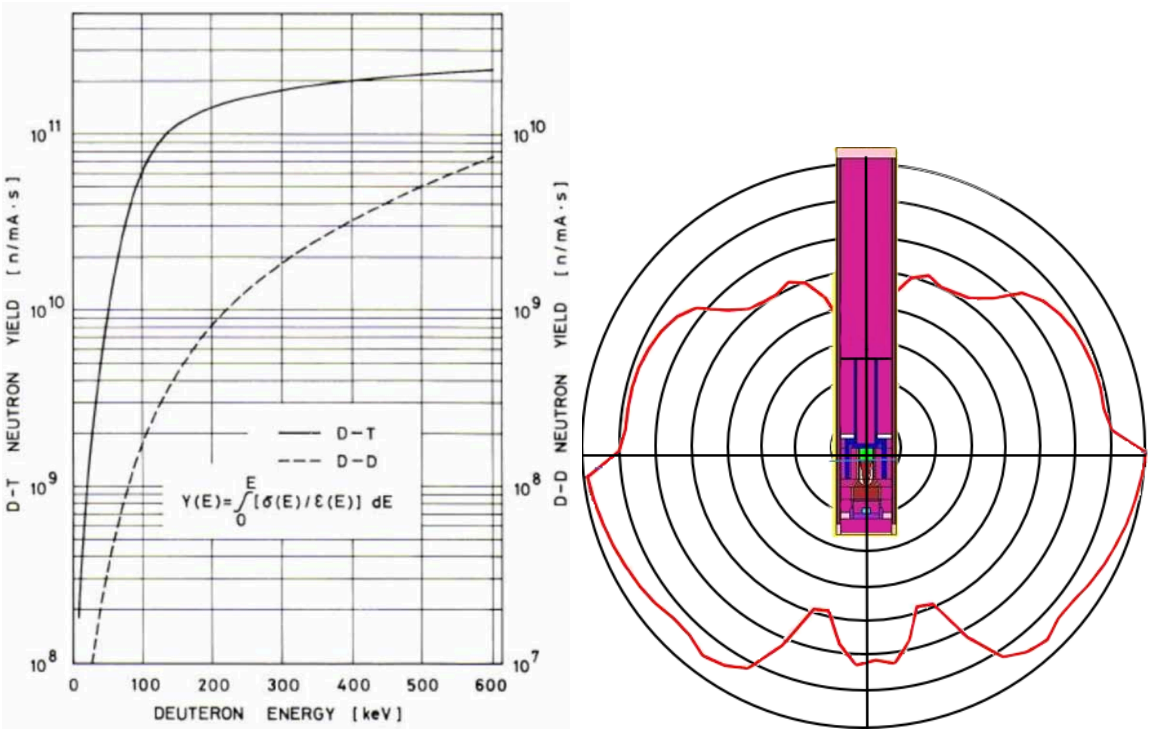

Figure 6.6: Left:The neutron yield for DD and DT reactions as a function of incident deuterium energy [146]. Right: The relative angular distribution (red) of emitted neutrons from a DT generator [147].

There is an angular dependence of the emitted neutron energy that depends on the incident deuteron energy. Figure 6.7 shows the angular dependence as a function of deuteron energy for both the DD and DT generators [146]. For the measurements made with the FaNS detectors, the incident deuteron energy was set

between 10-30 keV, below the energies shown in the figures. At these energies, the angular variation is minimal, and has not been adjusted for in this analysis.

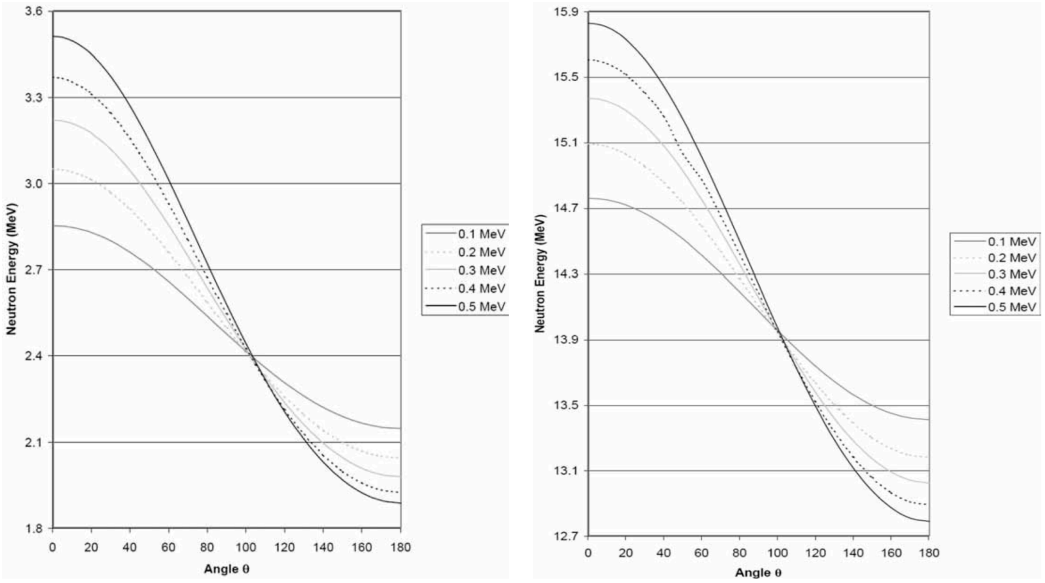

Figure 6.7: The angular dependence of the emitted neutron energy for multiple deuteron energies (0.1 - 0.5 MeV), for the DD (left) and DT (right) neutron generators. Note, for the FaNS detectors, the generators were operated at 10-30 keV deuteron energies, further reducing the angular dependence. Figures from Reference [146].

Measurements were made with both the DD and DT neutron generators directly above FaNS-2. The generators were mounted approximately 20 cm from the top of the FaNS-2 detector to minimize the number of neutrons that scatter from the floor and back into the detector. Figure 6.8 shows a schematic of the experimental setup. For this operation, the NIST DT generator was out of commission, and a replacement was borrowed from the Materials Science and Engineering department at the University of Maryland[2]. The replacement is a newer model (Thermo Scien-

[2]The authors would like to thank Dr. Richard Livingston, Prof. Mohamad Al-Sheikhly, and Mary Dorman for all their help with the loan of the DT generator. This work would not have been possible without it.

tific model P385 compared to model P325 [17]) but is functionally equivalent to the NIST-owned generator used with FaNS-1.

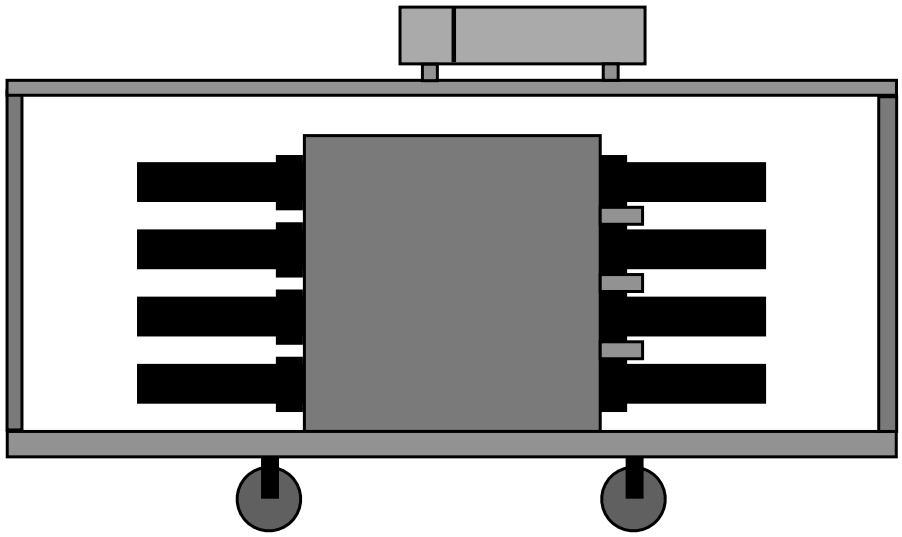

Figure 6.8: A schematic of the neutron generator mounted on top of the FaNS-2 detector. The vertical line on the generator is the target plane where the fusion occurs; this is centered overtop of the detector to provide symmetric illumination.

The neutron generators are designed for high neutron rate operations, such as neutron activation analysis of material composition [148, 149]. However, FaNS-2 is not designed to measure rates above ∼50 n/s. When operating a generator so close to the detector, care must be taken to minimize the total neutron flux emitted by the generators. Both the DD and DT generators were operated at settings below the manufacturer recommendation to minimize the neutron flux. This reduces pileup events where multiple neutrons capture in the same trigger window.

6.3.2 Proton recoil data

As discussed in Chapter 1, one of the standard techniques of neutron detection is detecting the recoil protons from neutron scatters in liquid scintillator [68,85,114, 150–152] . These detectors tally the energy deposition of any proton scattered by an incident neutron. This includes partial energy depositions, where the neutron exits the detector volume without thermalizing. Thus the resulting energy spectra from mono-energetic source are typically broad, with many low-energy deposition events.

To compare capture-gated results with proton recoil-type detectors, data were collected with no capture requirement in place. The photomultiplier tubes on the top layer of scintillator were allowed to free trigger. Any neutron that scatters in the detector will generate light that is detected by the PMTs. These signals are recorded and stored for off-line analysis. Figure 6.9 shows the deposited energy spectrum from these data. Since the distribution of energy deposition is determined by kinematics, the high-energy edges of the energy spectra represent a neutron thermalizing in a single scatter.

Both of these spectra show a broad energy response. The DD response, which is lower in energy, has significant gamma backgrounds that dominate the spectrum. Since plastic scintillator has no capability to remove gamma interactions via pulse shape discrimination, it is not possible to operate these detectors in a mixed radiation field. These spectra are discussed later when they are compared to the FaNS-2 measured spectra from the generators.

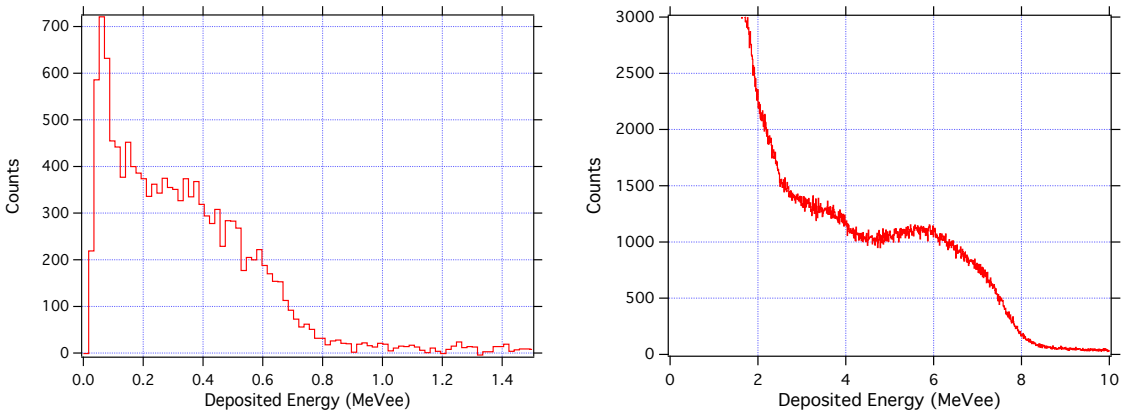

Figure 6.9: The deposited energy spectra from the top layer of scintillator in FaNS-2 during free triggering of the PMTs from the DD (left) and DT (right) neutron generators. Note: the DD data have had gamma backgrounds subtracted from this spectrum.

6.3.3 DD Measurements

Measurements with the DD generator were made over the course of a few days in April 2013. After a brief search for the optimum settings, the DD generator was operated at a beam current of 30 μA and an accelerating potential of 30 kV. The final data set used in this analysis constitutes the results from approximately two hours of data with a trigger rate of $\sim$27 /s.

To obtain the lowest energy threshold in analysis, the PMTs were operated at a higher gain setting than previously discussed. Full scale in the data acquisition was set to 5 MeV$_{ee}$, or roughly 9.6 MeV$_n$. The scintillator bars were calibrated using the source calibration procedure noted in the previous chapter. In analysis, a threshold of 200 keV$_n$ per scintillator block is applied. This is equivalent to 30 keV$_{ee}$, and is approximately 6 photoelectrons. This allows for the inclusion of multiple scatters

that would have been lost with a higher threshold. The "real+random" and "random only" energy spectra are shown in Figure 6.10.

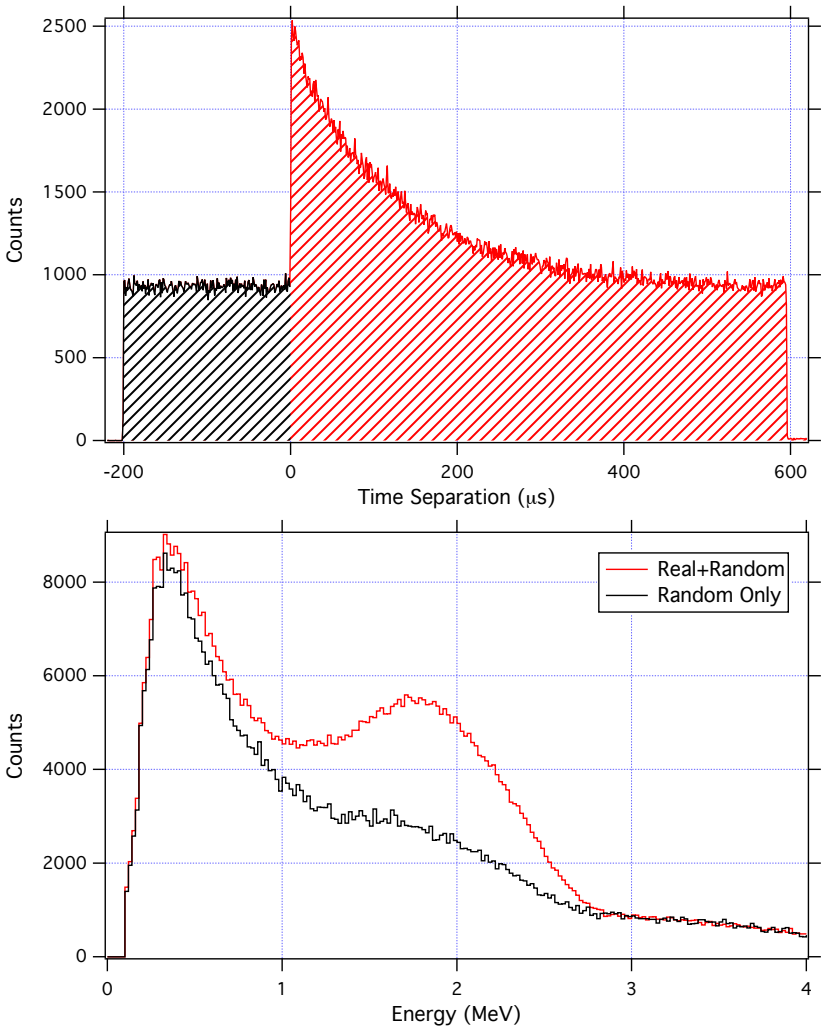

Figure 6.10: Top: The timing spectrum from the DD measurements after all cuts have been made. The shaded regions shown the "random" (black) and "real+random" (red) portions of the data. Bottom: The "random" and "real+random" energy spectra for the DD neutron generator data. Note: The "random" spectrum has been scaled to match the relative time acceptance (200μs compared to 600μs)

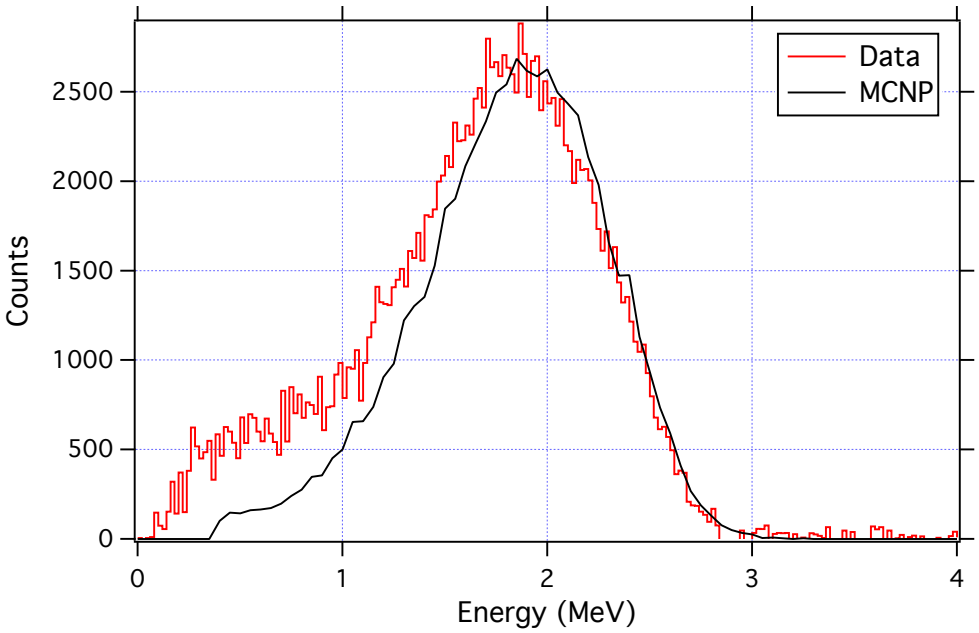

Figure 6.11: The DD neutron energy spectrum after subtracting random coincidences. Overlaid is a comparison to the MCNP predicted spectrum.

The background subtracted DD spectrum, shown in Figure 6.11, exhibits a clear peak with an upper edge of 2.5 MeV, as expected. Nice agreement is observed in the shape and location of the spectrum. There are excess counts at low energies compared to the Monte Carlo, that may be due to neutrons that scatter inside the generator before being emitted. Currently, there is no attempt made to model the inner-workings of the generators.

6.3.4 DT Measurements

The DT generator was mounted directly above FaNS-2 in the same position as the DD generator; the target plane was centered above the detector at a height of 20 cm. After a thorough search of the operational parameter space, the generator's

beam current was set to 10μA and the accelerating potential set to 10 kV. Despite concerns that the generator would not be stable at such low accelerating potential and beam current settings, it performed well[3].

During the operation of the DT generator, the PMTs were set to have full scale of the data acquisition at 20 MeV_{ee}, or 28 MeV_n. The gains of the PMTs had drifted subsequent to the previous calibrations with a ^{60}Co source. A recalibration of the detector was performed using the muon energy deposition peak. Muons are minimally ionizing particles, and deposit $\sim$2 MeV of light for every centimeter transversed in plastic scintillator. The scintillator segments are 9 cm wide, so the muon peak is expected to be at $\sim$18 MeV. MCNP can track muons and accurately calculate energy losses, so a muon spectrum was generated with MCNP, shown in Figure 6.12a, for a single scintillator bar to use for this calibration. This spectrum was fitted to the scintillator spectra from muon calibrations with FaNS-2. The resulting calibrated muon spectra for the FaNS-2 segments are shown in Figure 6.12b. The calibrations, in units of integral per MeV, are listed in Appendix B.

The energy range was chosen to ensure that the upper edge of the proton recoil distribution would fit entirely on the full scale. Data were collected for 5 hours, during which approximately 150,000 triggers were recorded. In between the hour-long runs, 100 s of free trigger data were collected with the scintillator bars.

Figure 6.13 shows the timing spectrum and the "real+random" and "random only" energy spectra from the DT generator operation. The majority of the random

[3]Many thanks are also owed to Fabian Schully at Thermo Scientific who helped operate the generators in such a non-standard way.

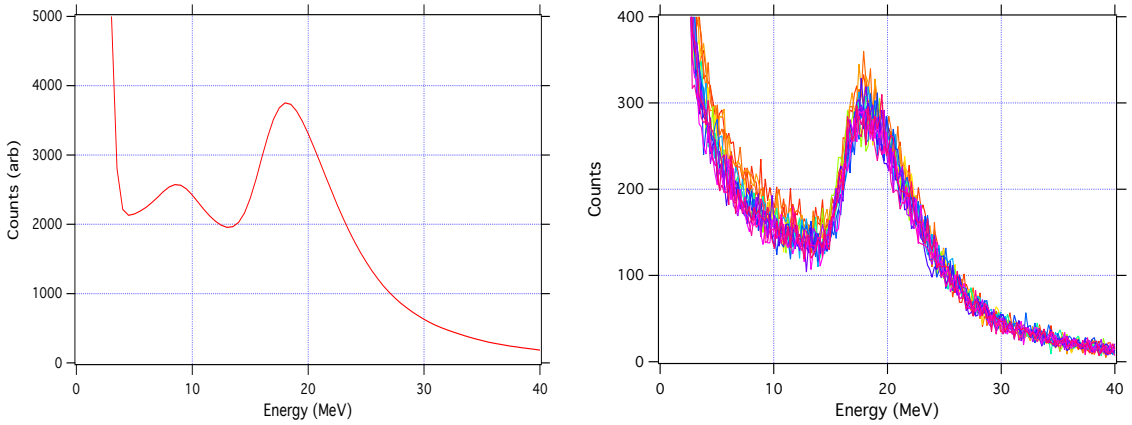

Figure 6.12: Left: The MCNP-generated spectrum of deposited muon energies in a single segment of FaNS-2 scintillator. Note the peak is at approximately 18 MeV. Right: The resulting muon spectra from each scintillator bar (shown in a variety of colors) after recalibration.

coincidences are at lower energies than the peak. The energy spectrum obtained after subtracting the random coincidences is shown in Figure 6.14. The peak-to-valley ratio of the background subtracted spectrum is approximately 7:2, which is a large improvement over FaNS-1. However, there is still a low-energy portion of the spectrum that remains after subtracting random coincidences. This is due to inelastic carbon recoil events that do not produce light in the scintillator.

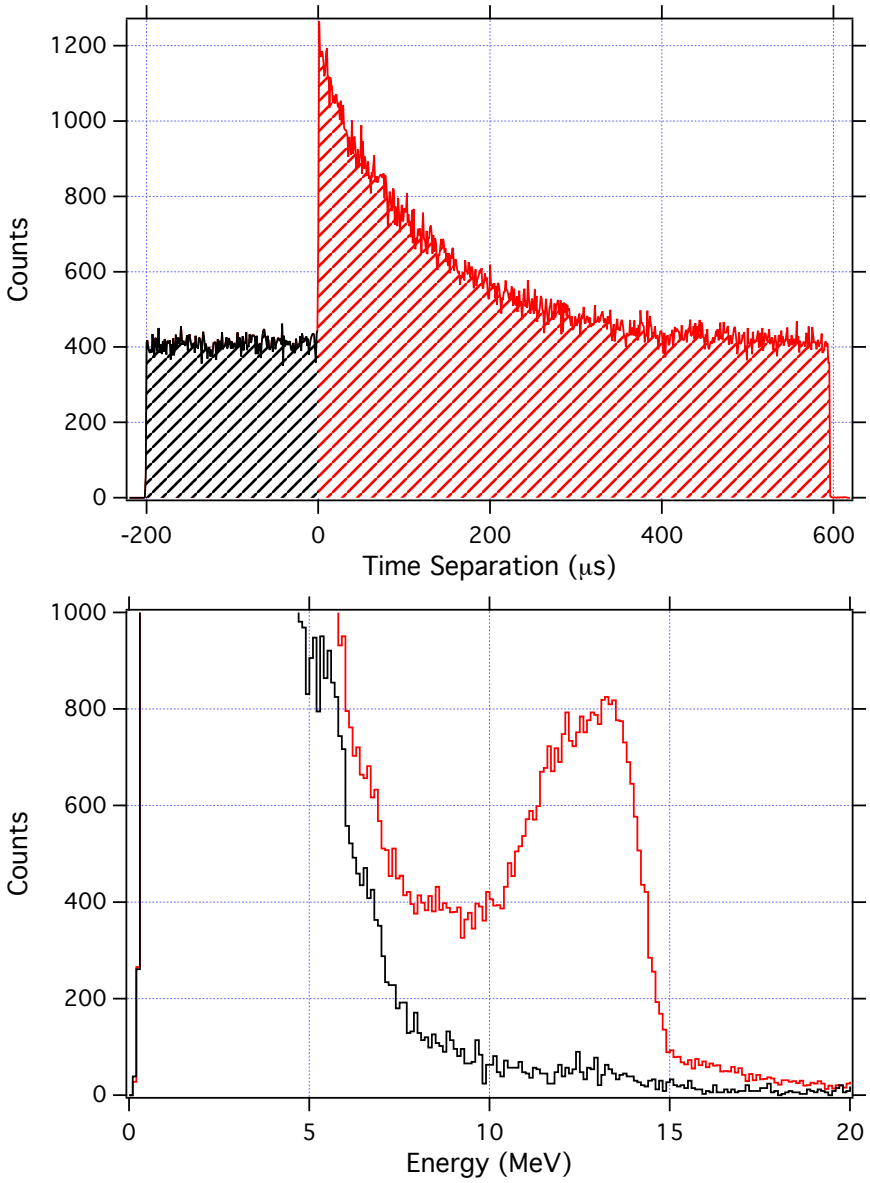

Figure 6.13: Top: The timing spectrum for data from the DT generator, with the random and real+random cuts shaded in black and red, respectively. Bottom: The energy spectra for the random and real+random events from the DT neutron generator data. Note: The random spectrum has been scaled to match the relative time acceptance (200μs compared to 600μs).

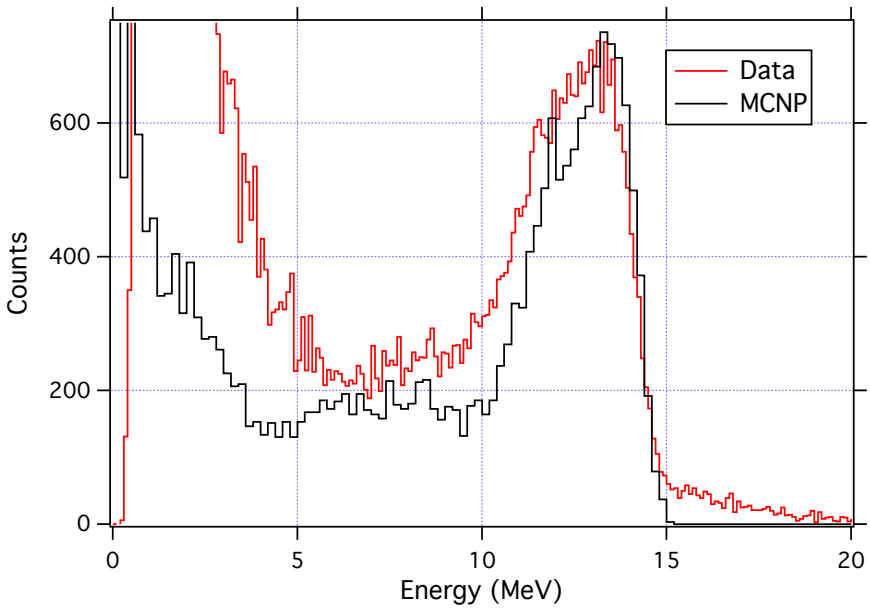

Figure 6.14: The detected neutron energy spectrum in FaNS-2 from the DT monoenergetic neutron generator after the subtraction of random coincidences. Also shown is the MCNP predicted neutron spectrum from the DT generator. Overlaid is the MCNP simulation of the DT energy spectrum. Note the good agreement of the upper edge of the full energy peak.

The MCNP simulation of these data is also shown in Figure 6.14. There is quite good agreement between the data and Monte Carlo at the location of the full energy peak. However, discrepancies in the width of the peak and the low energy behavior of the spectrum are observed. The data display a wider full energy peak than the Monte Carlo predicts. This could be caused by a number of issues, including errors in the Monte Carlo simulation of neutron energy loss and scattering, inaccuracies in the light response function, or inaccuracies in the calibration between detectors.

There is also a portion of events in the data with energies above the neutron peak. These events consist of a neutron that inelastically scatters on carbon, which then emits a gamma. The gamma is treated as a proton recoil event, and its energy

is reconstructed higher than it really is, leading to an event with energies above the full-energy peak. The lack of corresponding events in the Monte Carlo arises from a problem with MCNP's handling of gamma rays. As discussed in Section 5.6, MCNP treats gamma production on a statistical basis. When many events have been simulated, the relative branching ratios are correct, however, on an event-by-event basis, this may not be true. Events were observed that contained neutron capture gammas from both ^{3}He and aluminum, implying that a single neutron captured on two different nuclei. To avoid this issue, gamma production was turned off in the simulation. It is speculated that this leads to certain features in the data not being reproduced in the Monte Carlo, including the excess in events in the low energy tail and in the tail above the 14 MeV peak. A transition to a Monte Carlo that does not use the same statistical treatment of cross sections could resolve this issue.

6.3.5 Discussion of results

6.3.5.1 Multiplicity

For neutrons from the DT generator, a large fraction of events scatter in multiple scintillator segments before being captured by a ^{3}He counter. It is an interesting test of the energy reconstruction method to separate out single site interactions from multiple segment events. Figure 6.15 shows the separate energy spectra for different multiplicity events, ranging from single multiplicity events to threefold multiplicity events.

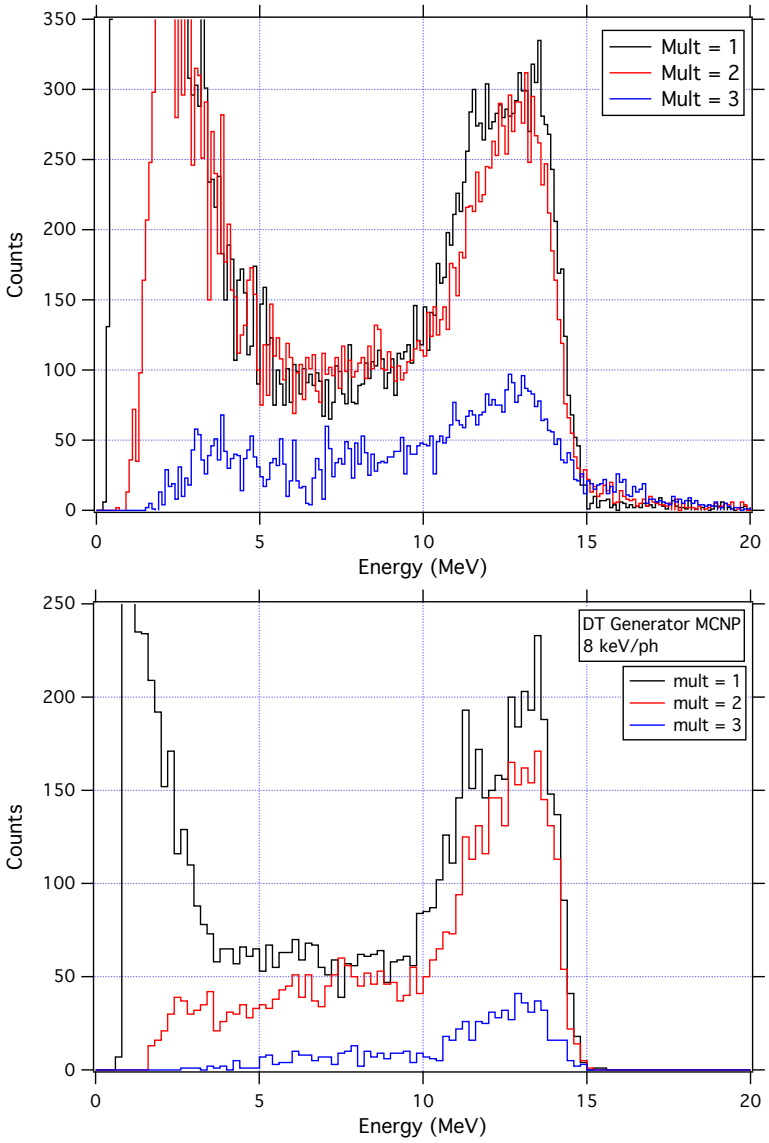

Figure 6.15: The separate DT neutron spectra for events that contain energy depositions in (1,2,3) scintillator segments for the experimental data (top) and the Monte Carlo (bottom). Note that the reconstructed peaks are in the same location, an indication that the energy reconstruction method is working as expected.

The distribution of multiplicities may be characterized by the integral of the peak in the DT spectra. The limits of the integration used here are (6, 15) MeV. The comparison of the ratios of the multiplicities between data and Monte Carlo is shown in Table 6.2.

Table 6.2: A comparison between DT data and Monte Carlo of the fraction of total events with each multiplicity with energies between 6-15 MeV.

	Mult=1	Mult=2	Mult=3
Data	0.45 ± 0.01	0.41 ± 0.01	0.14 ± 0.01
MCNP	0.52 ± 0.01	0.40 ± 0.01	0.08 ± 0.01

An interesting deviation from simulation is observed in the low energy portion of the DT energy spectrum. A large number of events are in the low energy tail of the *multiplicity* = 2 energy spectrum. MCNP does not predict such a tail. It is not yet clear why this is the case. A possible explanation stems from the removal of gamma rays from the simulation. This also leads to any secondary gamma emission from inelastic carbon recoils to be excluded. These events would show up in higher multiplicities and at low energies. Work is currently being done to understand this discrepancy. Apart from the low energy portion of the two-fold multiplicity energy spectrum, the Monte Carlo and data agree rather well.

6.3.6 Segmentation effect on DT spectral shape

As discussed previously, the segmented nature of FaNS-2 allows for improved neutron energy reconstruction. By separating the multiple scatters of a neutron's thermalization, and reconstructing each independently, the non-linearity effects of multiple scattering are reduced. To highlight the segmentation benefit, a comparison between data reconstructed with and without segmentation is shown in Figure 6.16.

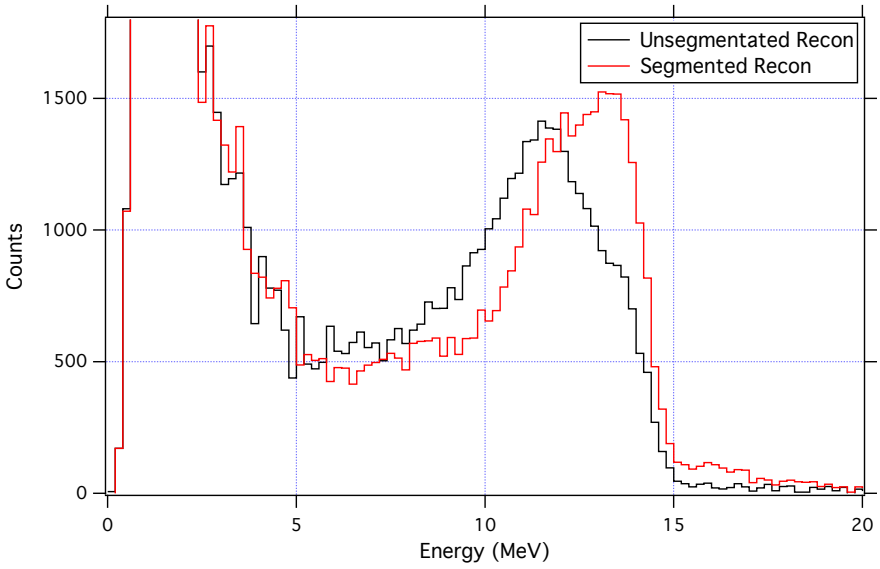

Figure 6.16: The reconstructed energy spectra for DT monoenergetic neutrons with (red) and without (black) utilizing the segmented nature of FaNS-2. Note the shift in location and overall broadening of the peak.

As demonstrated with the finely segmented simulation data in Figure 2.9, a shift in location and overall broadening of the peak is observed. Even with the relatively large segments of FaNS-2 (9 cm $\times$ 9 cm $\times$ 56 cm compared with the 1 cm^3 segments in the simulation), a significantly improved spectrum is obtained.

6.3.6.1 Threshold dependence of the reconstructed energy spectrum

An interesting consequence of a segmented detector is that the final energy spectrum depends on the threshold. In a large, single volume of scintillator, such as was discussed in Chapter 1, all light is collected if the sum of that light is over threshold. However, in FaNS-2, if an experimental threshold per scintillator bar is set, any scatters below that will not be included in the final analysis. An event that suffers from this effect is shown in Figure 6.17.

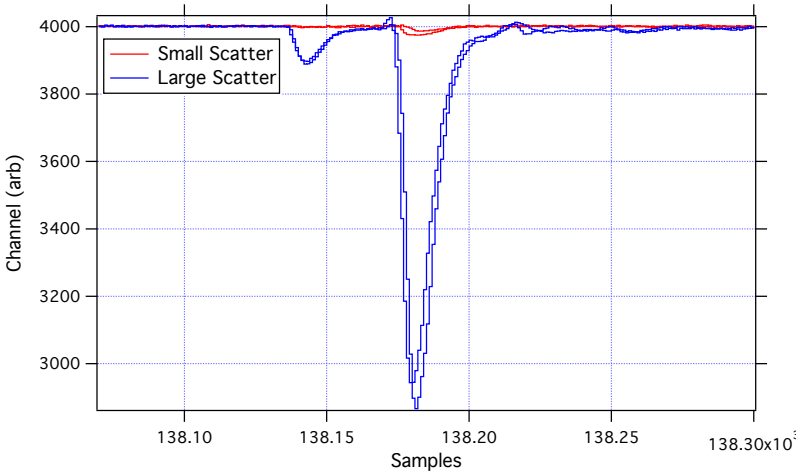

Figure 6.17: An example of an event that contains one large (blue) and one small (red) neutron scatter. With a low enough threshold, the deposited energy would be reconstructed to approximately 14 MeV. However, if an experimental threshold of 1 MeV is placed, the small scatter is lost and the reconstructed energy is correspondingly lower. Note: the traces for each PMT are shown for the scintillator bars.

This event has a large scatter and a small scatter. If both signals are above the experimental threshold, the reconstructed energy of this event is approximately 14 MeV. However, if an experimental threshold of 1 MeV is placed on each scintillator bar, the small signal is lost. The reconstructed energy of this event would then be 13 MeV. If this happens to a significant number of events, it will distort the shape of the full energy peak.

To highlight this effect, the threshold is varied in analysis, and distortion of the full energy peak for both the DD and DT data is seen. In Figures 6.18 and 6.19 the effect of increasing the threshold applied to each scintillator segment is shown. A decrease in peak resolution and a shift downward in the reconstructed peak location for both data sets are observed.

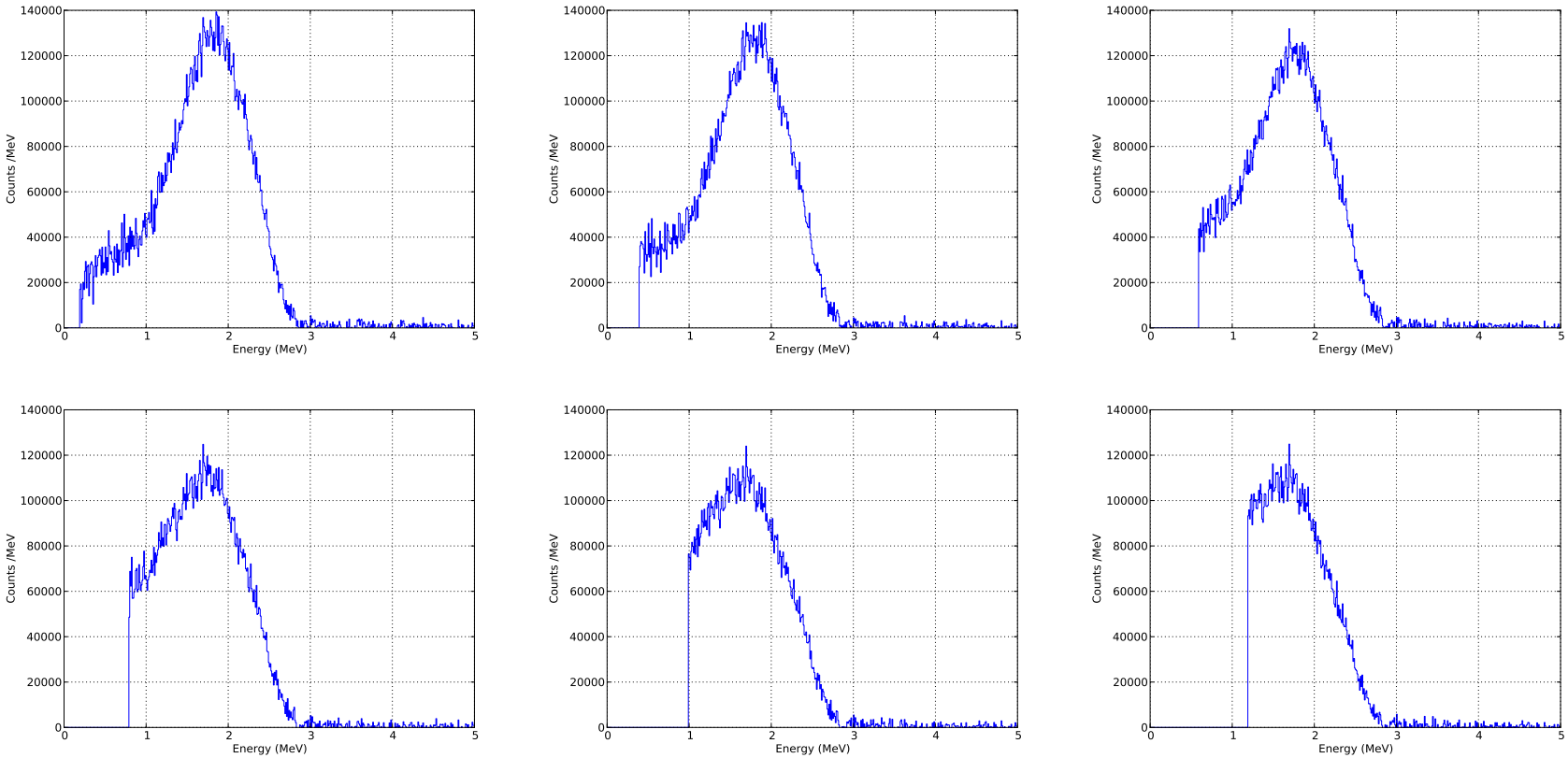

Figure 6.18: DD data analyzed with six different energy thresholds (0.2 MeV, 0.4 MeV, 0.6 MeV, 0.8 MeV, 1 MeV, and 1.2 MeV) applied to each scintillator bar. Note how the location of the peak shifts down and the spectrum broadens as the threshold increases.

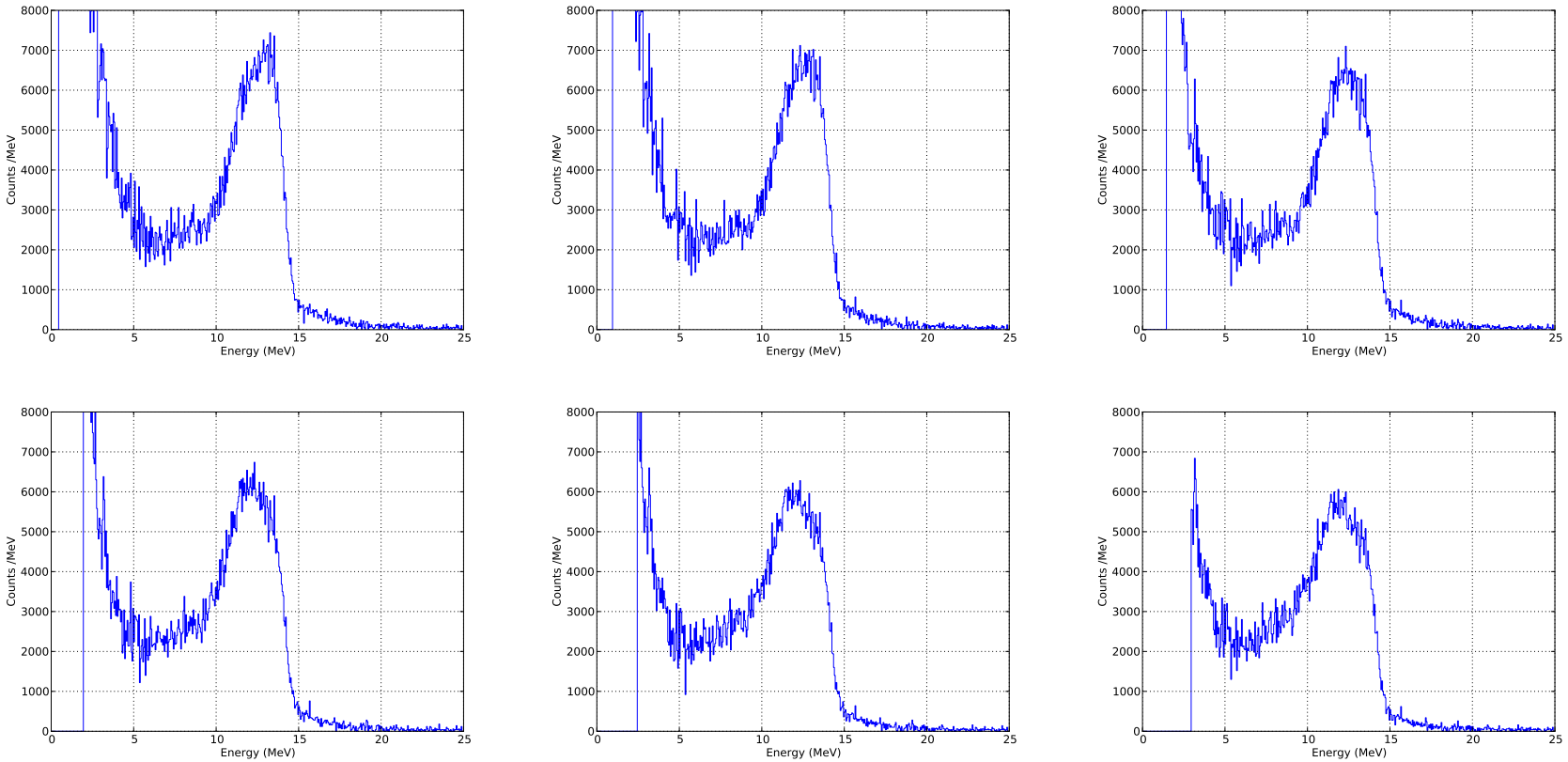

Figure 6.19: DT data analyzed with six different energy thresholds (0.5 MeV, 1.0 MeV, 1.5 MeV, 2.0 MeV, 2.5 MeV, and 3.0 MeV) applied to each scintillator bar. Note the decrease in fidelity of the full energy peak and the sloping of the upper edge as the threshold increases.

A clear distortion of the upper edge of the full energy peak is observed that increases with higher thresholds. For the 2.5 MeV neutrons, the effect is already visible at 400 keV. By 1 MeV, the DD spectrum is noticeably shifted down and features a significant loss of peak-to-valley ratio. For the DT data, the full energy peak not only shifts down, but also changes shape. Initially, the peak has a sharp upper edge at ∼14 MeV, but as the threshold increases, that upper edge is reduced, and a more prominent "peak" feature appears at ∼12 MeV.

The threshold dependence of the peak reconstruction is an important lesson of the segmented detector. To ensure that the correct energy spectrum is recorded, even at higher energies, it is vital that thresholds be as low as possible to collect as many neutron scatters as possible. For the measurement of the ambient fast neutron spectrum presented in the next chapter, the thresholds have been placed as low as possible to improve energy reconstruction.

6.3.6.2 Depth of interaction

Information about the location of energy depositions in the detector is determined using the segmented geometry of FaNS-2. The distribution of energy deposition and location of neutron captures for both neutron generators can be characterized. Figure 6.20 shows a schematic of the scintillator bars (blue) and the ^{3}He counters (green) when viewed from on end of FaNS-2. The neutron source is positioned above.

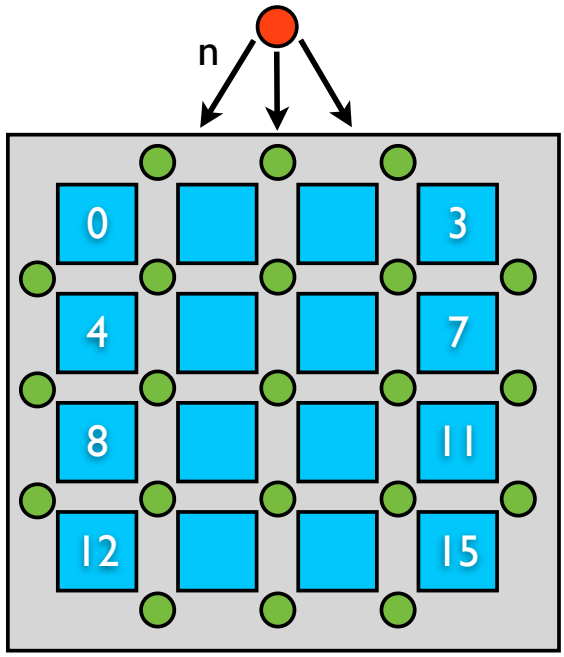

Figure 6.20: A schematic of FaNS-2 viewed from one end. The scintillator bars are shown in blue and the ^{3}He counters are in green. Here a neutron source has been placed above the detector. This is the same layout as the figures demonstrating the depth of interaction for DD and DT neutrons.

Using the same layout as in Figure 6.20, Figures 6.21 and 6.22 show the deposited energy and helium captures by location for the DD and DT generator, respectively. Note the concentration of events at the top of the detector where the generators are located. This shows that most of the events at DD and DT energies do not penetrate deep into the detector. However, it is clear that the DT neutrons interact more deeply in the detector than those from the DD generator. It is therefore possible to use the detector to look for hotspots of neutron emission in the surrounding environment.

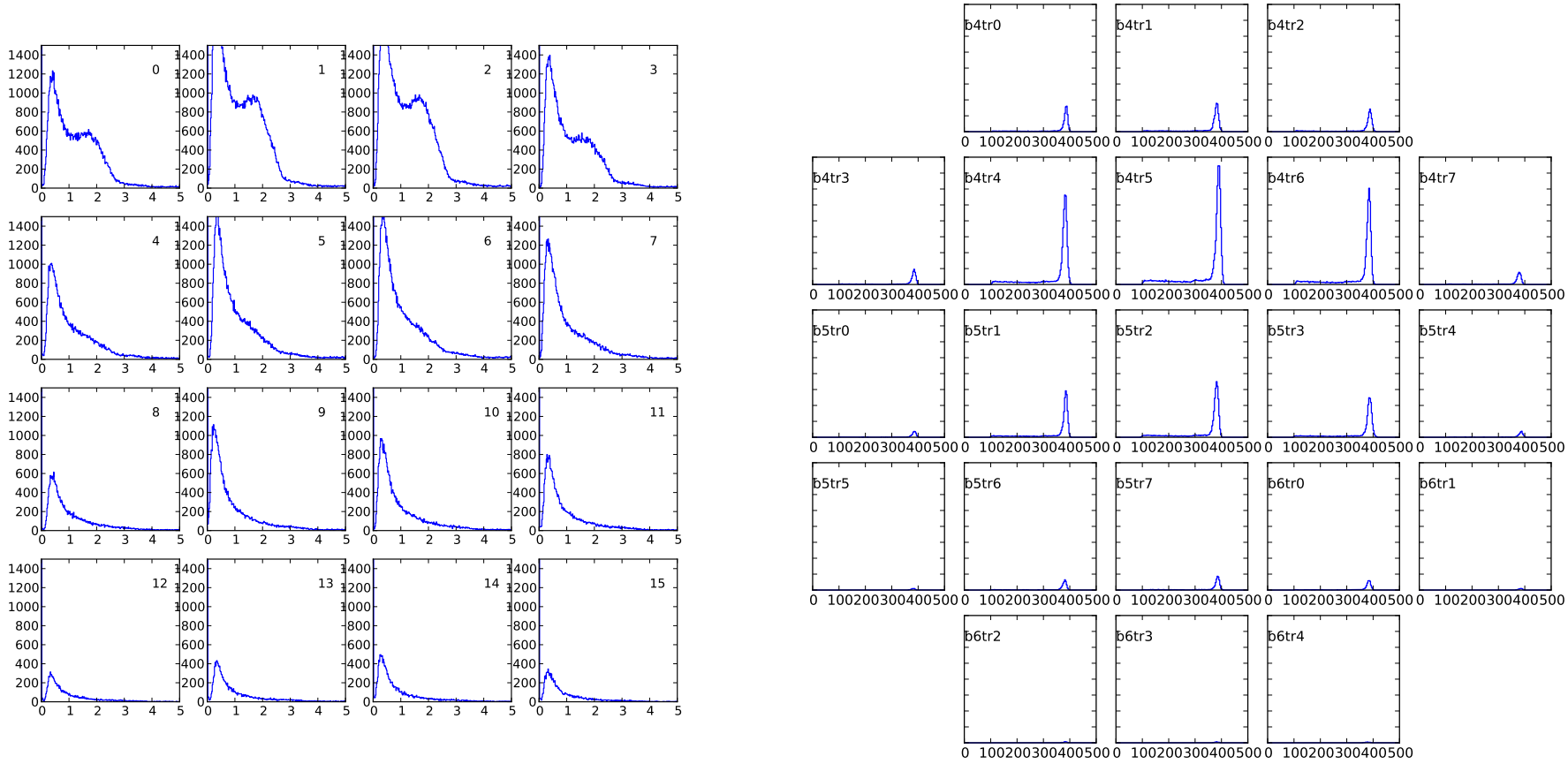

Figure 6.21: The energy deposited by 2.5 MeV neutrons in each scintillator bar (left), and the histograms of the ^{3}He detectors for the same data (right). Larger ^{3}He peaks towards the top and center of the detector are due to a greater number of neutron captures in these detectors.

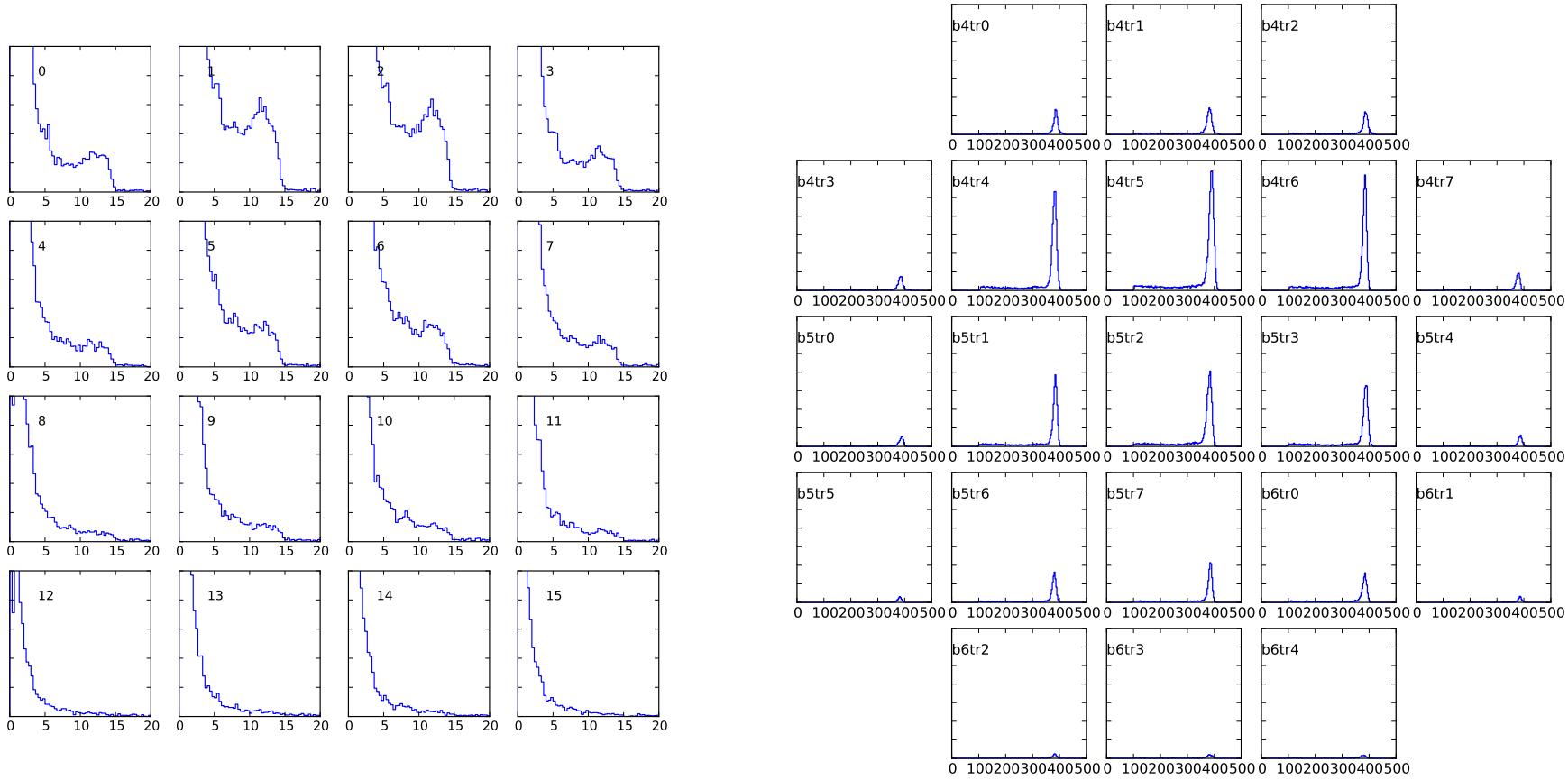

Figure 6.22: The energy deposited by 14 MeV neutrons in each scintillator bar (left), and the histograms of the ^{3}He detectors for the same data (right). Larger ^{3}He peaks towards the top and center of the detector are due to a greater number of neutron captures in these detectors.

An example of the benefit of this feature is found in the work of Reference [153]. A neutron detector was operated in the CUPP laboratory at the Pyhäsalmi Mine in Finland. An anomalous neutron rate was observed at one of the four depths at which the detector was operated. After extensive work shielding the detector, it was discovered that the granite powder covering the walls in one of the lab spaces contained higher levels of U/Th than expected. A directionally sensitive detector like FaNS-2 would have exhibited an excess of events on the side of the detector facing the wall.

6.3.6.3 Post DT operation scintillator spectra

After the operation of the DT generator, 100 s of free trigger data were again collected every hour, this time with the generator off. Over the following day, an exponential decay of the trigger rate in the scintillator bars was observed. Figure 6.23 shows the evolution of the file size for each of the hourly calibration files following the DT operation.

Figure 6.24 shows a comparison between the scintillator spectrum immediately following the shut down of the generator to the spectrum from before the generator was operated. These spectra are from a single scintillator bar that is directly below the location of the generator.

A large increase in the detected scintillator rate is observed directly after operation of the generator. Specifically, the scintillator bar directly below the generator exhibits a peak at approximately 2.5 MeV and a significant increase throughout

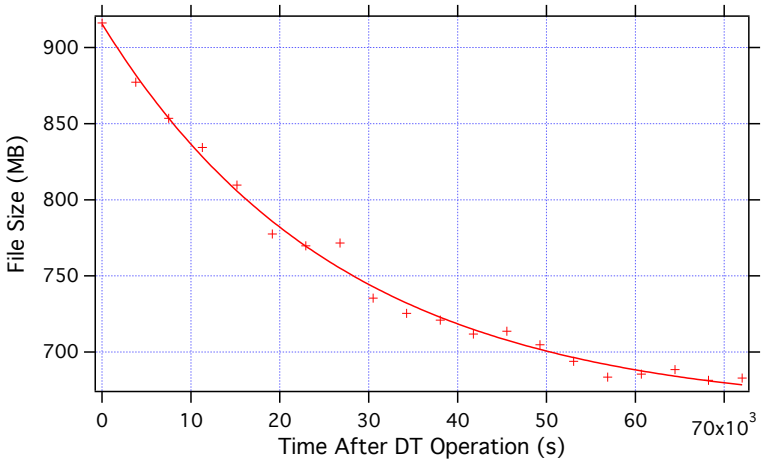

Figure 6.23: The file size (in MB) for each of the 100 s calibration files taken each hour after DT operation was completed. A larger file size indicates an increase in the trigger rate. There is a clear exponential decay in the data rate, with a half-life of approximately 10.75 hours.

the rest of the spectrum below 3 MeV. Above that energy, there is no appreciable change in the spectrum.

The manual for the generator indicates that activation of the generator target occurs after long periods of operation [154]. Therefore, the most likely source of the extra events is neutron activation of the surrounding material, namely aluminum and copper. The detector and the neutron generator are both encased in aluminum, while the target inside the generator is composed of copper. These two elements have isotopes produced with neutron activation that emit radiation in this energy range. The half-lives of ^{28}Al and ^{63}Cu are 2 minutes and 12 hours respectively. The observed half-life of the decay in the free-trigger rate of the scintillator is approximately 10.75 hours. This is more consistent with copper activation than aluminum.

The increase in gamma backgrounds due to activation of the surrounding material does not affect the measurement of the neutron spectrum. The additional

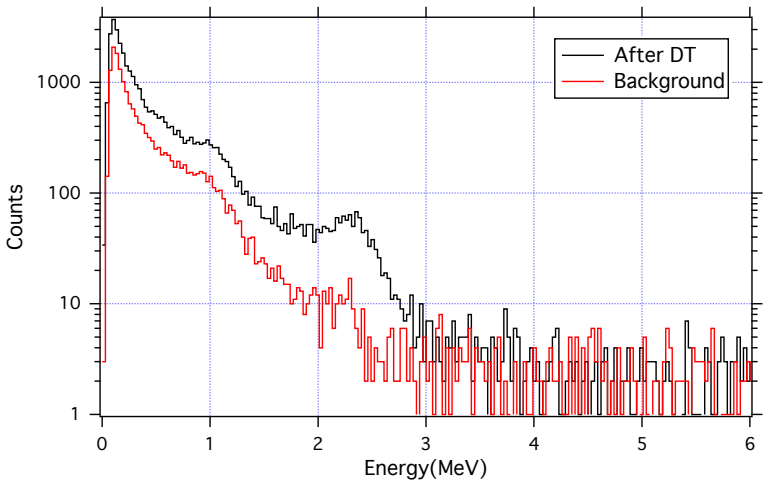

Figure 6.24: A comparison of the gamma spectra recorded in 100 s with a single scintillator bar of FaNS-2 before (red) and after (black) maximum operation of the DT generator. There is a significant difference in the spectral shape, as well as the absolute normalization. This is attributed to neutron activation of the surrounding material.

gammas are at sufficiently low energy that they do not interfere with the neutron peak region and are efficiently removed through subtracting random coincidences.

During the course of operation, no increase in the random coincidence rate is observed. It is therefore likely that the activation occurred during initial testing of the generator. NIST Health Physics required an initial test of the maximum neutron output for the generator to determine the allowable running conditions. At peak operation, the generator produces 10^8 n/s, while typical operation for FaNS-2 was closer to 10^3 n/s. It is speculated that this peak operation, which was not performed with the DD generator, could have activated the surrounding material, leading to this effect.

6.4 Source conclusions

FaNS-2 has been successfully calibrated for efficiency using a ^{252}Cf source with activity known to 2%. The data show good agreement with Monte Carlo once threshold effects have been taken into account. FaNS-2 is found to be (3.5±0.2)% efficient for neutrons above 2 MeV. This represents a factor of three improvement over FaNS-1 to low energy fast neutrons.

The detector has also been exposed to two monoenergetic neutron generators in an environment that minimizes backscattered neutrons. The spectra display highly peaked distributions that do not require unfolding to correctly identify incident neutron energies. A dramatic reduction in the low energy tail is observed in the DD neutron spectrum as compared to the measurement performed in the CNIF with FaNS-1. This is due to a reduction of room-return neutrons interacting in the detector. There is a similar reduction of the low energy tail in the DT data, but due to the presence of inelastic scattering from carbon, the tail is not completely suppressed. For the DD neutron generator, with energy of 2.5 MeV, FaNS-2 has a resolution of about 1 MeV, or about 40%. For the DT generator, with energy of 14 MeV, FaNS-2 shows a FWHM of 3.5 MeV, or a resolution of 25%.

Chapter 7

Measurement of the Surface Fast Neutron Spectrum and Flux at NIST

After characterizing FaNS-2 with calibrated sources at NIST, the detector was deployed to measure the ambient cosmic ray induced neutron spectrum. As discussed in Chapter 4, fast neutrons created in cosmic ray showers can have energies that exceed 10 GeV. FaNS-2 is designed to have sensitivity to neutrons with energies greater than 1 GeV, a factor of five higher than FaNS-1.

This chapter focuses on the measurement of the fast neutron spectrum and flux performed at NIST, Gaithersburg. First, the nature of ambient fast neutrons at the surface, including their source and spectral shape, is presented followed by a description of the detector's location and run conditions. Then follows a measurement of the cosmic ray induced neutron spectrum and flux made by FaNS-2. Finally there is a discussion of the results and future work for the spectrometer.

7.1 The surface fast neutron spectrum

As discussed in Chapters 1 and 4, the ambient fast neutron energy spectrum is extremely broad, ranging from thermal to very high energy neutrons. These neutrons are generated in the upper atmosphere by high energy cosmic rays. Incident protons create showers of particles, including neutrons, electrons, gammas, protons,

and muons, that propagate down to sea-level. The CRY Cosmic Ray Generator simulation package [20] is a tool to help understand the relative rates of these events. This package generates showers that can be imported into MCNP or another particle transport code to simulate a detector's response.

Figure 7.1 shows the produced spectra for neutrons, protons, gammas, and muons generated by showers in the CRY package. The normalization is based upon a total surface area of 50 cm × 50 cm, which mimics the top surface of FaNS-2. No particle transport has been done here; the energies of each particle type have simply been tallied.

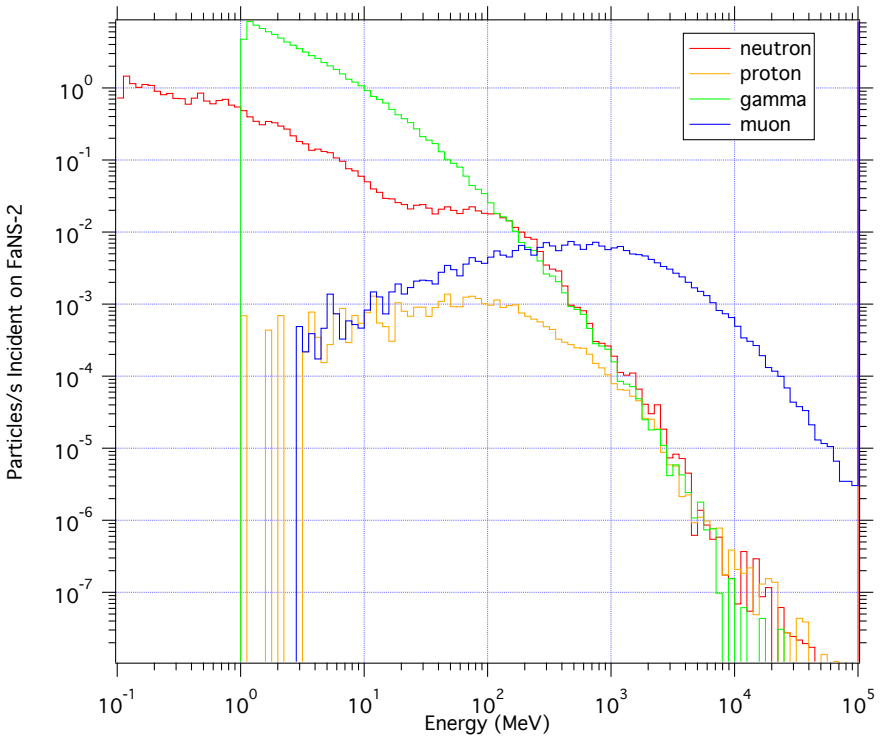

Figure 7.1: The spectra of cosmic-ray induced particles incident on a 50 cm × 50 cm area at sea level. Note that at energies above 1 GeV, there are roughly equal numbers of neutrons, protons, and gammas.

A total of 2×10^6 shower events that cross a 50 cm $\times$50 cm square at sea-level have been simulated, representing 6.59 hours of exposure. Table 7.1 shows the effective rates of different particles incident on the 50 cm $\times$ 50 cm square.

Table 7.1: The rate of particle interactions from showers simulated for gammas, electrons, protons, muons, and neutrons incident on a 50 cm $\times$ 50 cm square at sea-level.

Particle	Particles / s
Gamma	41.0
Electron	7.4
Muon	28.8
Proton	0.5
Neutron	7.3

Because the CRY simulation generates each shower as a single entity, it is possible to look at the rate of correlated particles entering the detector region for a single shower. Table 7.2 shows the rate of events with multiplicities up to n = 6. Higher multiplicities would be possible with a larger simulation.

Table 7.2: The simulated rate of multiple particle interactions from showers incident on a 50 cm $\times$ 50 cm square at sea-level.

Multiplicity	Rate (1/s)	Rate with neutron in Shower (1/s)
1	83.6	7.3
2	0.5	0.05
3	0.06	0.007
4	0.01	0.002
5	0.002	0.0005
6	0.0005	N/A

A total of 0.9% of neutron events, 0.06 /s, occur coincident with other particles. This equates to approximately 230 events per hour that contain a neutron

plus a second particle. FaNS-2 cannot easily distinguish between multiple particle interactions. Therefore, a low energy neutron accompanied by a higher energy muon or a proton will have its energy misidentified. The substantially higher detection efficiency of low energy neutrons compared with high energy neutrons will bias high energy data.

To study this effect, the real neutron energy of a shower event and the observed energy of the event have been calculated for each shower. For all particles besides muons, the observed energy is taken to be the energy of the particle. Muons, however, are minimum ionizing particles. Therefore, each muon has been treated as if it deposited 150 MeV, which is roughly the maximum energy a muon can deposit in the detector. A comparison between the two energy spectra, real and observed energies, is shown in Figure 7.2. Detection efficiency has not been accounted for in this figure, which will enhance the discrepancy.

To properly address this issue, the CRY simulated showers should be directly used as the input to the MCNP simulation of the detector. This would take into account the various energy depositions from all incident particles and the relative efficiencies. However, this would require a complete reworking of the simulation, and is not feasible for this work. This effort is ongoing.

7.2 Monte Carlo simulation of the neutron spectrum

As with FaNS-1, a thorough simulation was performed of the FaNS-2 detector exposed to the ambient fast neutron spectrum. The MCNP model of the detector

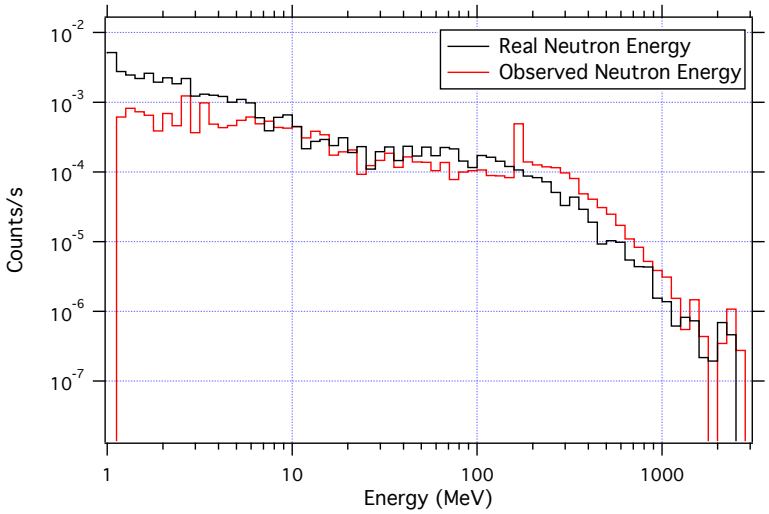

Figure 7.2: A comparison of the energy spectra for shower events that contain neutrons. Shown are the spectra of the real neutron energy and the observed neutron energy that includes energy depositions from other coincident particles. Note how the observed spectrum shifts low energy neutrons to higher energies. The peak at ∼150 MeV is from the minimum ionization energy of muons in FaNS-2.

was discussed earlier in Chapter 6, including a validation of the ^{252}Cf efficiency using a calibrated source.

7.2.1 Input neutron spectrum

To perform the simulation, an input spectrum of fast neutrons must be chosen. As with FaNS-1, the input fast neutron spectrum for the MCNP is that provided by Annex A of the JEDEC standard JESD89A [117]. This spectrum is based upon a measurement of the ambient fast neutron spectrum performed in New York City [23] combined with a calculation of the surface spectrum performed with the FLUKA simulation package [22].

This measurement was made using an array of Bonner spheres surrounding ^{3}He proportional counters, as discussed in Chapter 1. Each element of the array

had a different thickness of moderator and therefore a different energy sensitivity. Response functions for each detector were calculated using MCNP. The detectors were operated simultaneously, and the various count rates tallied. The relative count rates in each detector were then unfolded to produce the incident neutron spectrum.

This process relies upon an input reference neutron spectrum that is modified according to the measured count rates in each detector. The reference spectrum used in Reference [23] was generated by a FLUKA simulation of primary cosmic rays incident on the upper atmosphere. These primary cosmic rays generate air showers, and the resulting particles are tracked down to sea-level. The measured spectrum is generated by adjusting broad ranges of the input spectrum to match the experimental count rates. Therefore, fine structure in the reference spectrum is preserved in the reported spectrum, despite the inability of the measurement to directly observe it. The authors of both papers estimate the uncertainty in the high energy portion of the spectrum to be approximately 15%, though they do not actually quote error bars.

The absolute normalization of the incident spectrum is exceptionally complicated and depends on latitude, longitude, geomagnetic cutoff, weather, solar cycle, and surrounding environment. The JEDEC standard outlines a method for scaling the New York reference spectrum to other locations and conditions, shown in Equation 7.1:

$$\frac{d\phi(E)}{dE} = \frac{d\phi_0(E)}{dE} \times F_A(d) \times F_B(R_c, I, d), \tag{7.1}$$

where $d\phi_0(E)/dE$ is the reference spectrum in New York, d is the atmospheric depth, R_c is the vertical geomagnetic cutoff rigidity, I is the relative count rate of a neutron monitor measuring solar modulation, $F_A(d)$ is a function describing the dependence on altitude, and $F_B(R_c, I, d)$ is a function describing the dependence on geomagnetic location and solar modulation.

An online utility has been provided that utilizes the JEDEC formulae to calculate the overall shift to the reference spectrum [155]. The utility takes as input the latitude and longitude of NIST Gaithersburg, 39.13° N, 77.226° W, the altitude of 105 m, and the solar modulation during operation. These combined provide the correction factor for $d\phi_0(E)/dE$ at NIST, as shown in Table 7.3.

Accounting for the solar cycle is subtle; the neutron flux is linearly enhanced when solar activity is low. The total swing of cosmic ray intensity from solar minimum to maximum is approximately 10%. Although 2013 is near the maximum of solar cycle #24[1], it has been a relatively quiet period of solar activity [157]. Therefore, the solar activity level is estimated at 25%, and an error bar associated with the effect on the overall shift will be included.

The calculated shift, including the uncertainty from solar modulation, is 1.05 ± 0.04. This correction will be applied when comparing the final flux measurement to the JEDEC spectrum.

[1]Solar activity generally follows an 11 year oscillatory cycle. At peak periods of activity, the amount of charged particles emitted is enhanced. This leads to an increase in the magnetosphere shielding of the earth, which in turn decreases the number of cosmic rays that penetrate the earth's atmosphere. The solar cycles are numbered, beginning with Solar Cycle #1 in March of 1755. The most active solar cycle was #19, which peaked around 1960. Aurora were observed as far south as New Jersey [156].

Table 7.3: The parameters used in calculating the scaling factor for the reference neutron spectrum at NIST.

Parameter	Value	% Change from [23]
Latitude	39.13° N	-1%
Longitude	77.226° W	0%
Altitude	105 m	+10%
Solar Modulation	$(25 \pm 25)\%$	-(4±3)%
Total Change		+5%

7.2.2 Description of the FaNS-2 simulation

The MCNP simulation of FaNS-2 in the ambient neutron field was performed by throwing an isotropic distribution of neutrons from a spherical source plane of radius 1 m centered around the detector[2]. A schematic of the source configuration is shown in Figure 7.3.

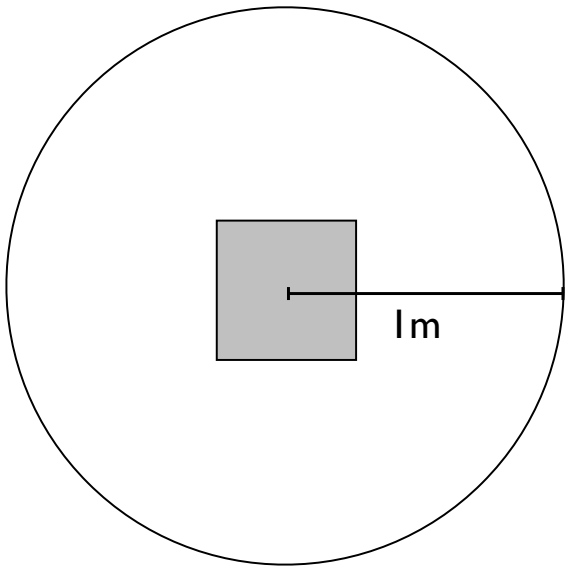

Figure 7.3: A schematic of the source configuration used to simulate the ambient neutron field for FaNS-2; the detector is shown in grey. The source plane is a sphere of radius 1 m and centered just below the base of the detector.

[2]For a spherical source plane, a $\cos^2\theta$ distribution yields an isotropic fluence inside the sphere.

The input energy spectrum includes ground effects already, therefore the concrete pad upon which the detector sits is not included. Otherwise, double counting would distort the spectrum at low energies. To decrease simulation time, a truncated energy spectrum consisting of neutrons above 0.122 MeV was used. A total of 5×10^7 neutrons were thrown at the detector. It is possible to remove the materials from the MCNP simulation and average the neutron fluence throughout the detector volume. For a spherical $cos^2\theta$ source, the fluence is uniform throughout the volume. Using the size of the source surface, the total fluence is:

$$\phi = \frac{n}{\pi r^2}. \tag{7.2}$$

Note, the denominator is πr^2, *not* $4\pi r^2$ as naively expected. The fluence is related to the cross-sectional area, not the surface area. This yields a fluence of 1592 n/cm^2 of neutrons above 0.122 MeV, which was verified by the MCNP average fluence simulation. To compare with the experimental data, a total fluence above the experimental threshold of 2 MeV is found to be 1106$\pm$30 n/cm^2. The uncertainty here is from the coarse binning of the input neutron spectrum.

7.3 Detector location

As discussed in Section 4.1, FaNS-1 was installed in a trailer outside of Building 245 at NIST to measure the ambient fast neutron spectrum. Operating a detector in the trailer presented a number of issues. Although the detector was protected from rain, there were large temperature swings during the short run with FaNS-1; the

internal temperature of the trailer reached greater than 40° Celsius during FaNS-1 operation. Though FaNS-2 was ready to be deployed in the trailer in December, 2012, the trailer does not have a heating system. As a result, the decision was made to measure the cosmic ray induced neutrons from within the Low Scatter room itself.

The Low Scatter room, as discussed in Section 6.1, provides a low overburden environment that is climate controlled and fully instrumented with AC power. The detector was situated on a small concrete pad in the far corner of the lab, farthest away from the concrete walls of the building. Figure 7.4 shows an aerial view of the detector's location (marked with the red 'X'). This location minimized any shielding caused by the concrete structure of Building 245, while still providing a stable operating environment.

Figure 7.4: An aerial view of the west side of the Radiation Physics Building (Building 245) at NIST, Gaithersburg. The location of FaNS-2 is marked by the red 'X'.

7.3.1 ^{3}He-based backgrounds

The ambient thermal neutron rate is monitored with a bare ^{3}He proportional counter of the same model internal to FaNS-2. This detector may trigger the data acquisition in the same way as the other ^{3}He counters. This gives a constantly running external thermal neutron monitor, as well as a convenient tool to test against correlated backgrounds. Since this detector is separated from the scintillator array, there should be no correlated neutron events. This hypothesis can be tested by looking at the timing spectrum for events that are triggered by the background ^{3}He tube, shown in Figure 7.5a. No timing correlation is observed between the bare ^{3}He counter and the FaNS-2 plastic scintillator.

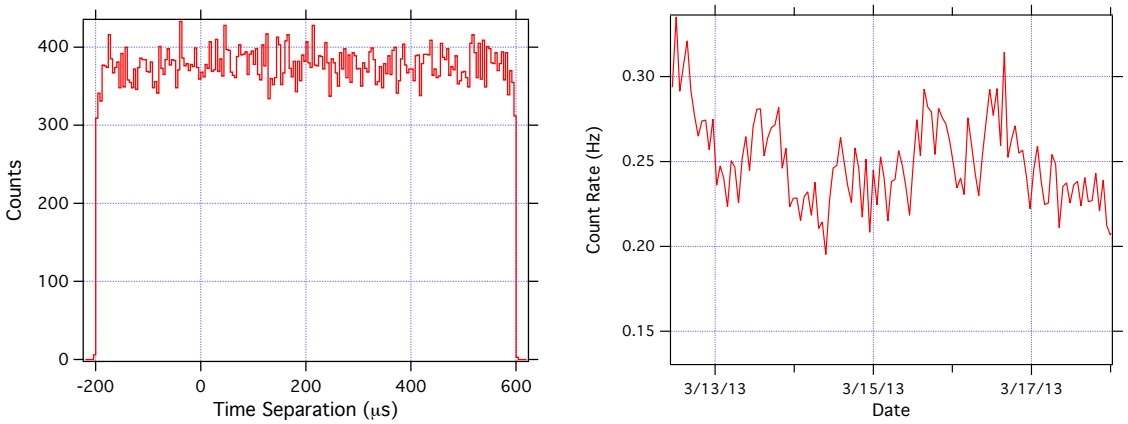

Figure 7.5: Left: The timing spectrum between the external ^{3}He counter and the scintillator array. As expected, there is no evidence for correlated events with the external ^{3}He counter. Right: A section of the ^{3}He trigger rate for the bare detector. The average observed rate is (0.25±0.04) Hz.

This ^{3}He counter was used to monitor the thermal neutron count rate throughout the operation of FaNS-2. Fluctuations in the rate could be caused by changes in the ambient neutron field or by the introduction of a neutron source to the lab

area. Figure 7.5b shows the thermal neutron rate as a function of time during the operating period for FaNS-2. Over the period shown, an average bare ^{3}He trigger rate of (0.24±0.04) Hz was observed.

There are also backgrounds from other interactions in the ^{3}He counters, including alpha particle emission from the detectors' internal walls, microdischarges, and electron/gamma interactions. The rates of these in FaNS-2 are shown in Table 7.4. The alpha background rates are detector dependent and not uniformly distributed across all ^{3}He counters.

Table 7.4: Rates of various ^{3}He event types, including neutron capture, alpha detection, and microdischages. These were measured using an 11 hour subset of the data. The statistical uncertainties on each are less than 1 %.

Event Type	Rate (1/s)
Neutron Capture	1.43
Alpha (E > 1 MeV)	0.03
Microdischarges	0.10
β/γ Interactions	0.19

7.3.2 Gamma backgrounds from local radioactivity

Data were broken into hour-long runs, each of which was preceded by calibration data. First, gamma calibration data were collected with synchronous triggering between all scintillator digitizers and with a low threshold. Then, the trigger threshold was increased and muon calibration data were collected. During most of the operation, a NaI gamma detector was also operated to monitor the ambient background gammas. A sample energy spectrum of the ambient gamma radioactivity, measured by the NaI detector, is shown in Figure 7.6a.

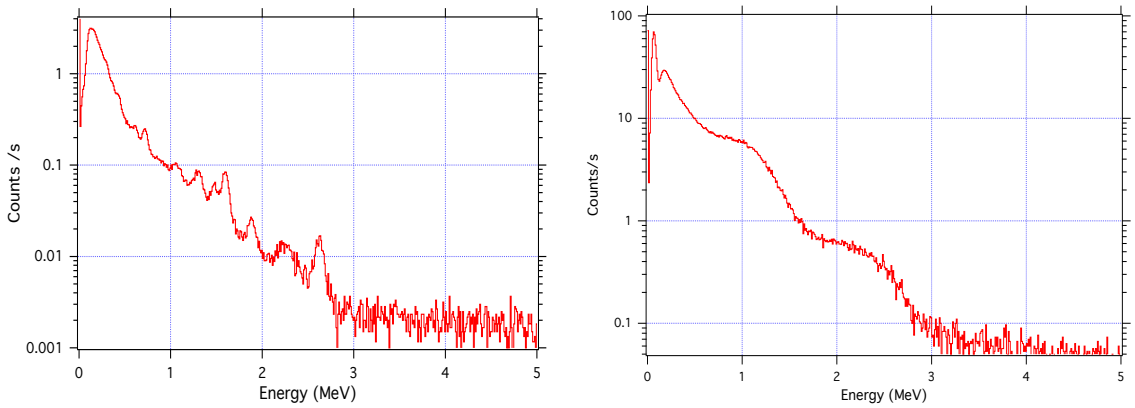

Figure 7.6: Left: A sample of the NaI-measured gamma radioactivity of the operating location in the Low Scatter room. The calibration is generated by fitting the upper most peak to the 2.614 MeV gamma from ^{208}Tl. Right: An energy spectrum of the ambient radiation in the Low Scatter Room collected by the full FaNS-2 array.

This gamma spectrum shows two prominent energy peaks, one at 1.4 MeV from ^{40}K and one at 2.6 MeV from ^{208}Tl. The smaller peaks are the multiple lines of ^{214}Bi. Figure 7.6b shows an equivalent gamma spectrum collected with the full FaNS-2 array in the Low Scatter room. The main features of the FaNS-2 spectrum are the two edges at $\sim$1.4 and $\sim$2.6 MeV from ^{40}K and ^{208}Tl.

The multiplicity distribution of the scintillator data is shown in Table 7.5. The rates show that the majority of scintillator interactions are single-scintillator events, but a sizable fraction are spread across higher multiplicities. There are also a non-zero number of events that have very high multiplicities, including those which interact in every scintillator segment.

7.3.3 Measurement of the muon flux

A key measurement that was not performed with FaNS-1 is the muon flux. Cosmic rays collide with the atmosphere and produce pions that decay in flight

Table 7.5: The distribution of multiplicities for free-triggering of the scintillator bars. These data are from a 200 s sample of calibration data, and the statistical uncertainties are all less than 5%.

Multiplicity	Rate (1/s)
1	1473.1
2	287.3
3	53.2
4	21.0
5	11.1
6	4.8
$\geq$7	3.3

to muons. The muon rate is therefore an interesting handle on the rate of these cosmic ray showers that also create fast neutrons. A number of measurements of the cosmic-ray induced neutron flux have reported their final result in units of n/μ [158–160], therefore, benchmarking the measurement of the muon rate with FaNS-2 is an important tool for future measurements.

To directly measure the muon energy spectrum, a very large detector comprised of heavy material is required. FaNS-2 is not ideally suited for this style of measurement. However, measuring the muon flux for energies above a threshold is possible. The detector is approximately 40-50 cm thick, depending on the angle of incidence. Therefore, for a minimum-ionizing muon, a minimum of 80-100 MeV is required to fully traverse the detector. Muon tracks that only cross part of the detector will have lower total energies.

To select muon events, PMT clusters that have a combined energy greater than that of the highest background gamma (^{208}Tl with 2.6 MeV) are selected. Signals

above this cannot be attributed to local radioactivity gammas and are most likely cosmogenic in origin.

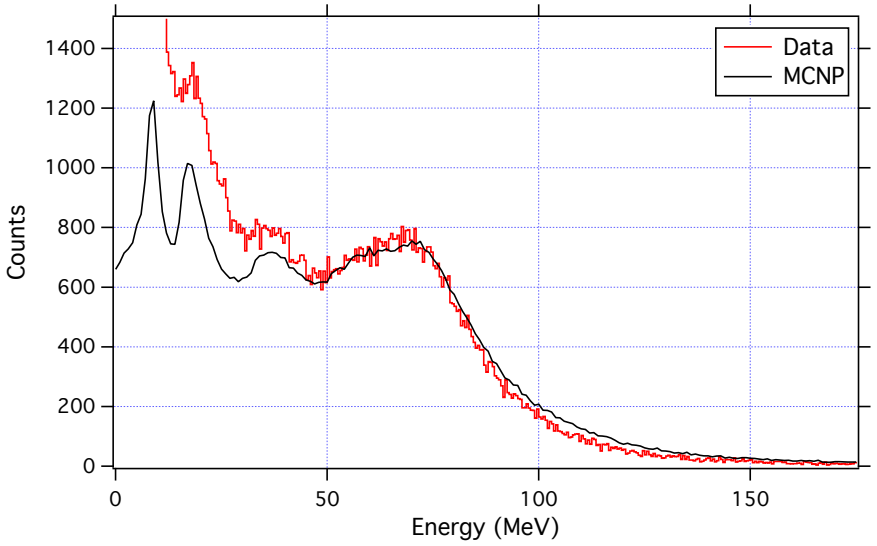

Figure 7.7: A comparison of the muon spectrum obtained with FaNS-2 (red) to that simulated in MCNPX (black). There was an effective threshold in this analysis of ∼5 MeV that cuts out part of the lowest peak in the Monte Carlo spectrum.

Figure 7.7 shows the comparison between the simulated muon spectrum generated in Monte Carlo and the measured spectrum. There is good agreement of the shape of the muon spectrum above 40 MeV. This simulation was performed by throwing a simulated surface muon spectrum from a large, planar $cos^2\theta$ distribution above the detector. This should act as a reasonable approximation for the surface muon spectrum. The difference between the simulation and data at energies below 40 MeV is most likely due to gammas and electrons generated in air showers, as discussed earlier.

By integrating the spectrum above 50 MeV, where the data and MCNP agree, a rate of muon interactions in the detector is determined to be ∼23 /s at the surface.

Selecting this energy range effectively eliminates the contribution of gammas and electrons to the rate.

When the detector is operating in an underground environment, the muon energy spectrum will harden and become more downward going, due to increased shielding for larger incident angles. Therefore, the measurement of the surface spectrum will act as an important baseline with which to compare future measurements.

7.3.4 Observation of shower events

During the muon calibration runs, a few events were observed with exceptionally high energies. These events have high multiplicities, with more than 10 of the 16 scintillator blocks triggering. Two examples of such events are shown in Figure 7.8.

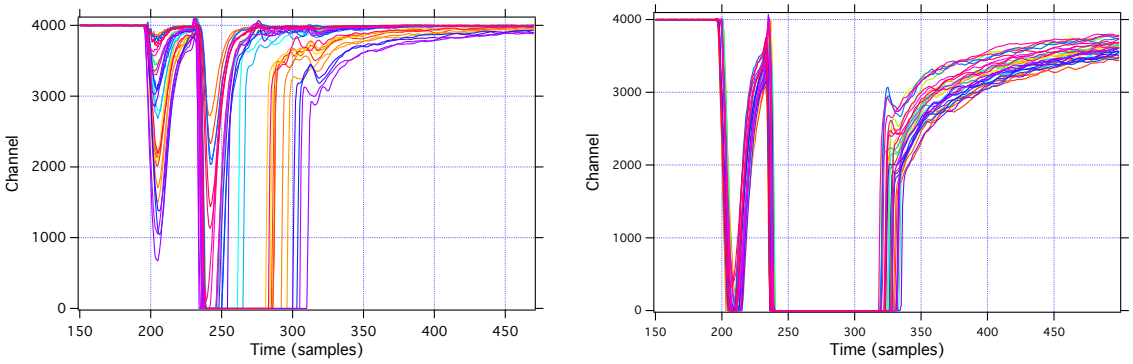

Figure 7.8: The traces from two events recorded during FaNS-2 muon calibration runs. Left: An event with a reconstructed energy of approximately 1.4 GeV. Right: An event with a deposited energy of 3.2 GeV, in which every scintillator bar in FaNS-2 is saturated.

It is unlikely that a single particle can account for all of the deposited energy in this event. A more probable explanation is the interaction of multiple high energy

particles in the detector. These could be from air showers generated in the upper atmosphere or showers from interactions in the material of the surrounding room.

To quantify these events, the rate of events with deposited energies greater than 500 MeV is determined from a subset of data. In a 5000 s long data selection, a total of 68 events occur that pass this criterion, for a rate of (49±6) / hour. This will be compared with future underground data as a check of the origin of these events. The use of scintillator paddles for a muon-tag would act as a tool to exclude such events. Three paddles could be placed around the detector (two above and one below) to identify both stopped and through-going muons. Events which occur in coincidence with a muon could be separated from the main data set and studied independently.

The rates of different scintillator events, separated by energy, are listed in Table 7.6. It is clearly seen that the dominant portion of the scintillator rate is below 3 MeV. These events are due to local radioactivity; the highest energy gamma commonly emitted in the U/Th decay chains is from ^{208}Tl at 2.614 MeV. At energies above 3 MeV, the event rate decreases by more than a factor of 20.

7.3.5 Barometric fluctuations of cosmic ray induced neutron rate

Data were collected periodically over six months from December 2012 through May 2013. These dates included large variations in the precipitation, outside temperature, and barometric pressure. These will all contribute to a slight time variation

Table 7.6: Rates of scintillator events with various total energies. These were measured with a 200 s subset of calibration data, and each has statistical uncertainties below 10%. Energies below 3 MeV are typically dominated by gamma backgrounds from local radioactivity. Between 3 and 50 MeV, the field is mixed between cosmogenic gammas and muons. Above 50 MeV, the dominant interaction is from muons.

Energy Range	Rate (1/s)
E $\leq$ 3 MeV	(1.84$\pm$0.003)$\times 10^3$
E $\geq$ 3 MeV	94$\pm$1
E $\geq$ 10 MeV	69.0$\pm$1
E $\geq$ 50 MeV	31.6$\pm$2
E $\geq$ 100 MeV	3 $\pm$0.07

of the data that will be averaged out by including a wide range of these conditions in the analysis.

The external temperature and barometric pressures varied greatly during the operation. Information on local weather conditions was gathered from a weather station at the Muddy Branch Park in Gaithersburg, MD using the Weather Underground website [161]. The weather station is situated approximately 1.1 km from the detector's location. These hourly recordings should provide a reasonable proxy for the outside conditions at NIST.

A correlation between barometric pressure and detected neutron rate has been observed by many neutron detectors [162–165]. FaNS-2 has also shown substantial fluctuations in the detected fast neutron rate, after background subtraction. The fluctuations have a spread of approximately 20%. It is possible to compare the

fluctuations observed with FaNS-2 to those observed by the nearest Neutron Monitor Database (NMDB) station located in Newark, DE [166][3].

The NMDB is a network of approximately 80 standardized neutron detectors stationed across the globe to monitor primary cosmic ray fluence. Each detector consists of thermal neutron detectors surrounded by layers of polyethylene and lead, as shown in Figure 7.9. This gives the neutron detector sensitivity to a broad range of energies.

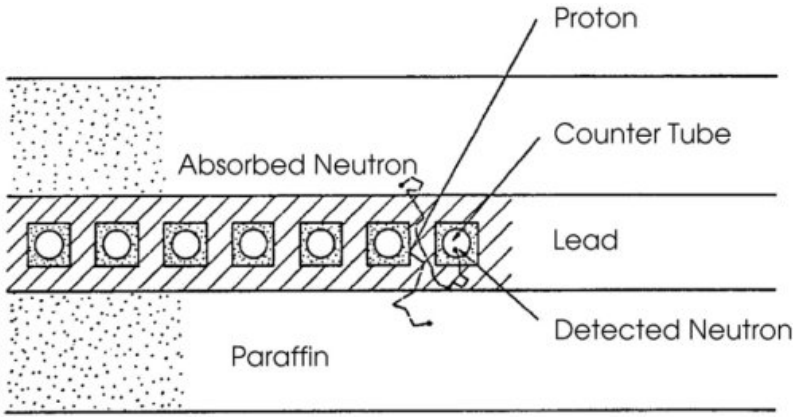

Figure 7.9: A schematic of the shielding surrounding the thermal neutron detectors for a standard Neutron Monitor. From outside in, there is a layer of polyethylene, followed by a layer of lead, and finally an innermost layer of polyethylene. This layering provides a high response to high energy neutrons. Figure from Reference [167].

The NMDB provides the realtime data of each station for general use, including a warning system of solar activity [166]. Figure 7.10a shows the data recorded by the NMDB station in Newark, DE during the same period as FaNS-2 in Figure 7.10b.

It is possible to correct the detected count rate for the barometric pressure using a simple linear regression. Variations in the neutron rate at sea-level for the Newark station can be parameterized as $\beta = 0.735 \pm 0.01\%$ change per millibar

[3]The neutron monitor data from Newark/Swarthmore are provided by the University of Delaware Department of Physics and Astronomy and the Bartol Research Institute.

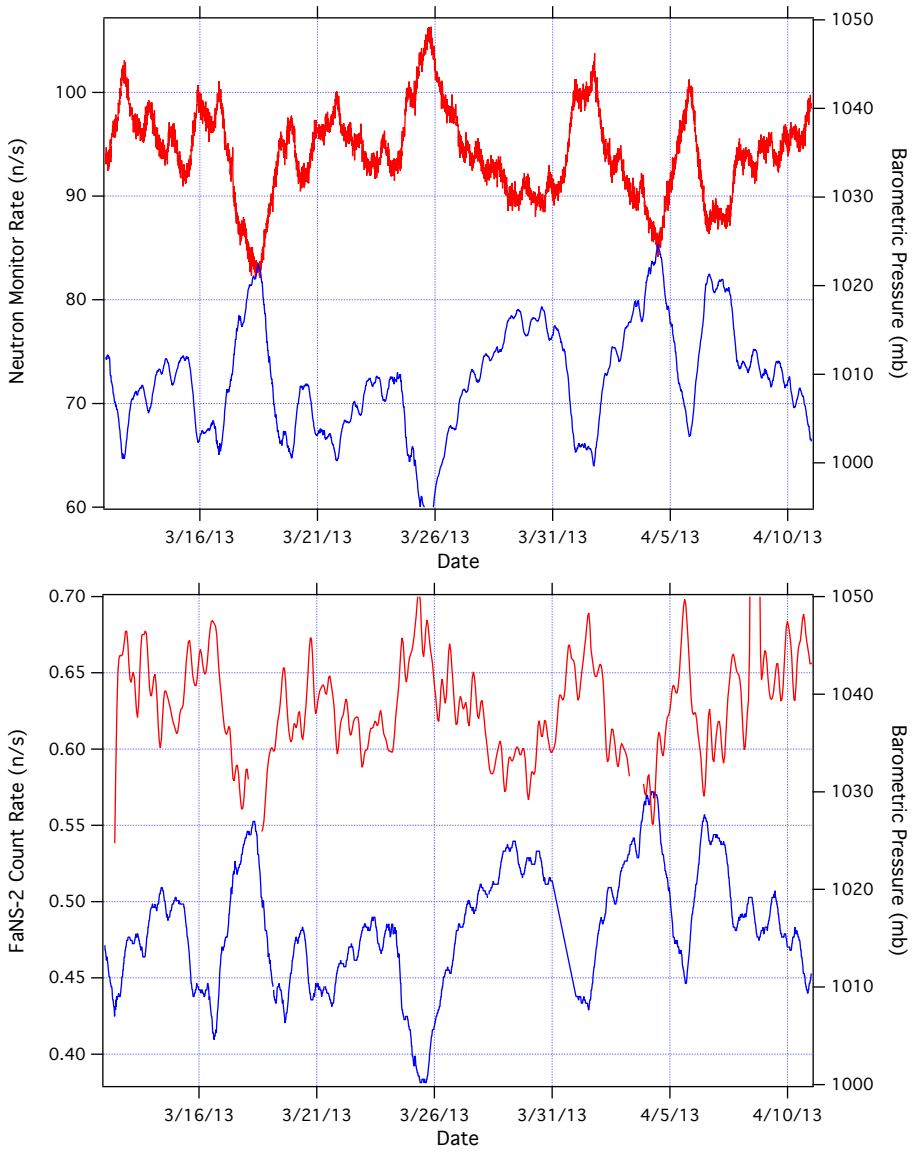

Figure 7.10: Top: The recorded neutron rate (red) and barometric pressure (blue) from the NMDB station in Newark, DE [166]. Bottom: The post-background subtraction FaNS-2 neutron count rate (red) and external barometric pressure (blue) as functions of time.

change in the barometric pressure [168].

$$dN = -\beta \times dP \tag{7.3}$$

$$dN = -(7.35 \pm 0.1) \times 10^{-3} \times dP \tag{7.4}$$

Using the same barometric coefficient, the FaNS-2 rates have been corrected for the local pressure fluctuations. The uncorrected and corrected neutron rates, with comparisons to the Newark, DE data, are shown in Figure 7.11. Though separated by ∼160 km, the rates of the two detectors track each other very well.

The variation in neutron energy spectrum with barometric pressure has not been well studied, and is outside the scope of this work. For the measurement of the flux and spectrum of comsic-ray induced fast neutrons at NIST, no correction for pressure will be applied. The data cover a wide range of pressures, and the effect is assumed to average out.

7.4 Calibrations

As was discussed in Chapter 5, the calibrations used for FaNS-2 have been determined with a ^{60}Co gamma source inserted at key locations in the detector. Hourly calibration data were collected throughout the surface data collection to track any fluctuations in the calibrations with time[4]. Figure 7.12 shows the variation of calibration factors as a function of time during the surface operation. There is

[4]Ideally, periodic calibration checks would have been performed with the ^{60}Co source. However, complications with source usage at NIST prevented this from occurring.

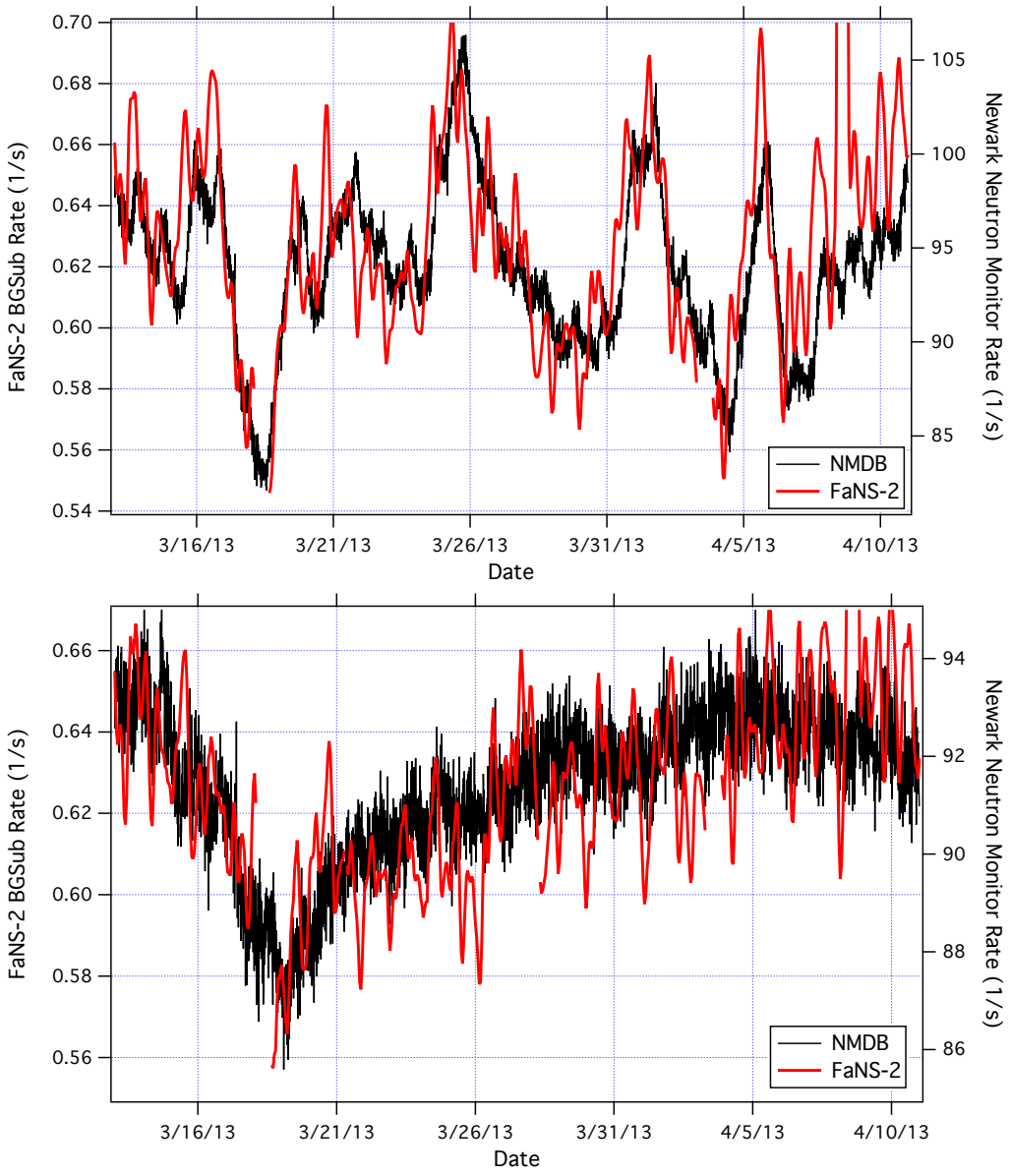

Figure 7.11: Top: The raw count rate of the NMDB neutron monitor compared with the background subtracted fast neutron rate for FaNS-2. Bottom: After a correction for the local barometric pressure has been applied to the raw count rates shown in the top figure. The remaining feature is attributed to solar activity.

very little drift in the calibrations, with the exception of one channel. Data have been excluded for the period of time that this channel varied than 10% away from its starting calibration factor. Since there are only minor fluctuations, the calibration factors obtained from source calibration are used throughout the presented data.

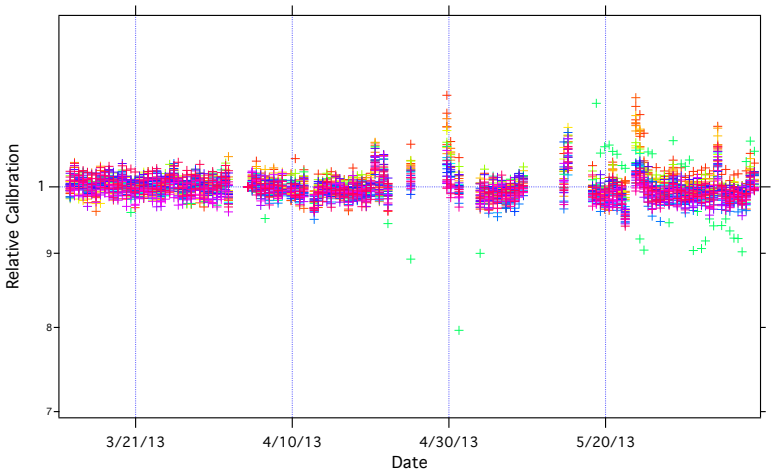

Figure 7.12: The calibration factors as a function of time for FaNS-2 during ambient neutron data collection. Note that only one channel (shown in teal) displays any appreciable fluctuations.

7.5 Data summary

Data were collected for 1345 hours, or 4.842×10^6 s. During this time, approximately 9×10^6 events were collected for a total trigger rate of $\sim$2 /s. Table 7.7 shows a summary of the data files used in this analysis. For FaNS-2 surface data, the primary gain setting tunes the attenuated PMT signals to a 200 MeV_{ee}saturation point for the attenuated signals. This puts the absolute upper limit of the full detector at approximately 3 GeV.

Table 7.7: The run details for each data series of ambient neutron data used in this analysis.

Data Series	Start Date	Elapsed time
CD30	12/27/2012	68400 s
CD31	12/28/2012	212400 s
CD32	12/31/2012	223200 s
CD36	1/7/2013	75600 s
CD67	3/7/2013	75600 s
CD68	3/12/2013	468000 s
CD69	3/18/2013	1119600 s
CD70	4/1/2013	147600 s
CD73	4/3/2013	3600 s
CD74	4/3/2013	630000 s
CD85	5/3/2013	324000 s
CD100	5/18/2013	133200 s
CD116	5/22/2013	414000 s
CD118	5/27/2013	986400 s

7.6 Measured fast neutron spectrum with FaNS-2

Using the same procedure outlined in Chapter 5, these data sets are analyzed using the FaNS-2 Python software. Individually, cuts on the ^{3}He energy, ^{3}He rise-time, and scintillator energy are applied to these data. The effects of these cuts are outlined in Tables 7.8 and 7.9. Separately, Table 7.10 shows the effect of combining the PMT and ^{3}He cuts, and the relative rates of "random only" and "real+random" events separated by the time separation.

Table 7.8: Details of the ^{3}He cuts applied to a sample of ambient neutron data and their effect on the data. Each cut has been applied individually, and then combined.

	Total Events:	1624526
Cut Parameter	Cut Range	Events After Cut
^{3}He Energy	0.2 MeV < E < 0.8 MeV	1497889
^{3}He Spark Cut	$\tau_r > 0.1$ μs	1491996
^{3}He β Cut	Diagonal in τ_r vs E	1342668
	All ^{3}He Cuts	1308226

Table 7.9: Details of the PMT cuts applied to a sample of ambient neutron data and their effect on the data. Each cut has been applied individually, and then combined.

	Total Events:	1624526
Cut Parameter	Cut Range	Events After Cut
Scintillator Energy	E > 1.0 MeV	1188445
Prompt Δt Cut	Removal of $0 < \Delta t < 2$ μs	1604823

Table 7.10: The effect of combining the ^{3}He and PMT cuts on the sample data. Also shown are the effects of placing the timing cuts to separate out the "random" and "real+random" events. Finally, the background subtracted number is shown.

Total Events:	1624526
	Events After Cut
^{3}He and PMT	965612
Real + Random	778510
Random Only	187101
After subtraction	217207

The most substantial cut in the data results from applying the energy threshold on the PMT signals. This rejects many events that are either due to noise or low energy signals in the PMTs. Since each trigger of the data acquisition contains multiple events, this cut helps to eliminate many of the random coincidences.

After placing the above cuts, the data are split into "random only" and "real + random" time-to-capture events. Figure 7.13a shows the histogram of the time-to-capture for each signal that passed the above cuts. Figure 7.13b shows the energy spectra of the "random only" and "real + random" timing events.

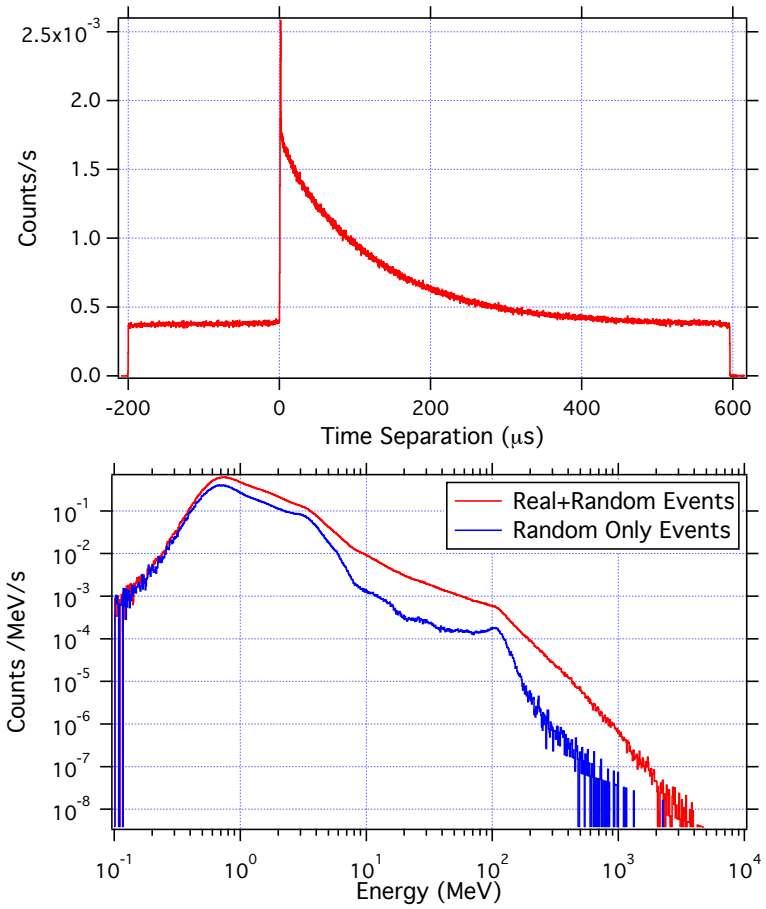

Figure 7.13: Top: The timing spectrum from a Low Gain data series. Note, the prompt peak in the timing spectrum ($0 < \Delta t < 2$ μs) has been removed from analysis. Bottom: The energy spectra of the "random only" (blue) and "real + random" (red) events.

The "random only" energy spectrum is then subtracted from the "real + random" energy spectrum to obtain the final neutron energy spectrum, shown in

Figure 7.14. Also shown in this figure is the result from the Monte Carlo simulation of FaNS-2 exposed to the ambient neutron spectrum, as discussed above.

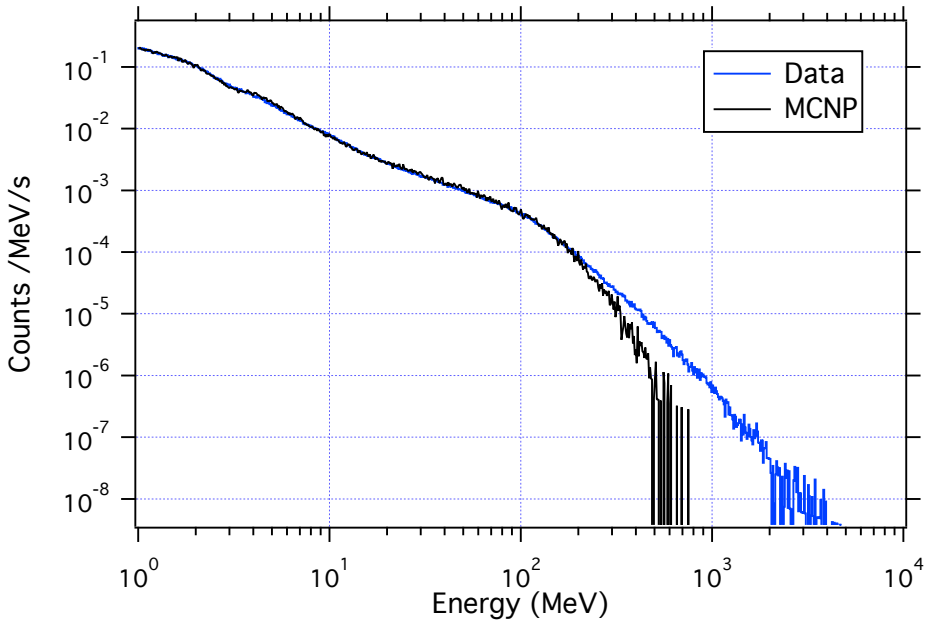

Figure 7.14: The background subtracted neutron spectrum measured with FaNS-2 over the course of six months. Overlain is the MCNP prediction of the FaNS-2 response to the JEDEC spectrum [23]. The MCNP normalization has been floated to highlight the similarities between the data and Monte Carlo spectral shapes.

Figure 7.14 shows the comparison between the measured spectrum and the MCNP simulation. There is very good agreement between the shape of the spectra for energies ranging from 1 to ∼200 MeV. The neutron spectral shape is roughly 1/E; thus, by displaying the spectrum as $E \times d\phi/dE$, or lethargy, it is possible to accentuate the small features in the spectrum. Figure 7.15 shows the data and MCNP in this display.

There are two features in the surface spectrum that merit further discussion. At 2 MeV and 4 MeV, inflections in the simulated and detected spectrum are observed. The energy region between 0.5 MeV and 10 MeV is referred to as the

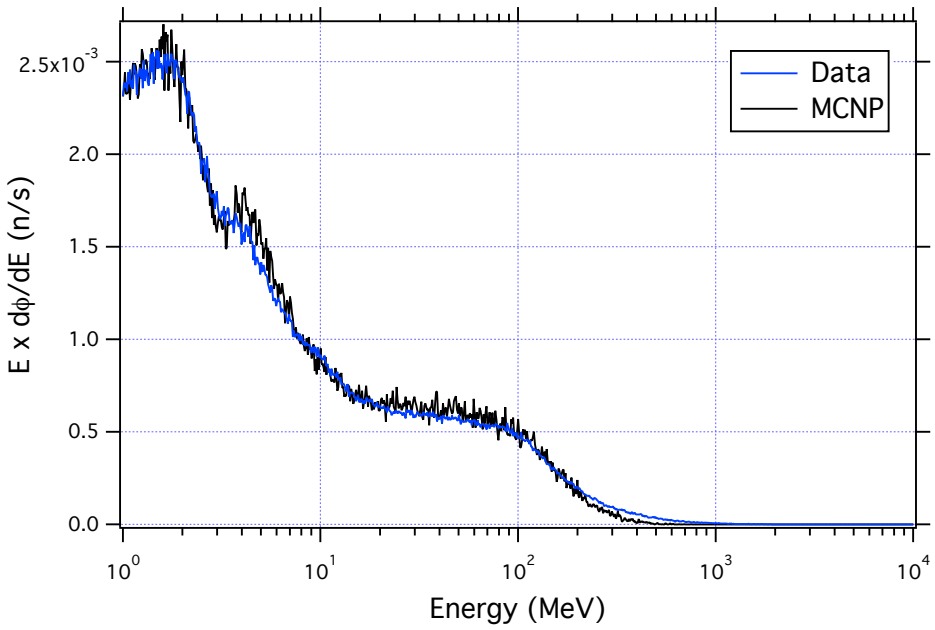

Figure 7.15: The simulated (black) and detected (blue) $E \times d\phi/dE$ spectra for FaNS-2 at the surface. The MCNP normalization has been floated to highlight the spectral similarities between the data and simulation.

"evaporation peak", because these neutrons are generally created by neutron emission of excited nuclei in the atmosphere[5]. The structure of the evaporation peak is determined by the many resonances of nitrogen and oxygen, the dominant nuclei in the atmosphere [21, 22]. These features are too fine to be visible by Bonner sphere spectrometers, but have been included in previous reported spectra because they are present in the a priori spectrum for unfolding [23, 170]. FaNS-2, however, has directly resolved these features. This demonstrates one of the major benefits of using a segmented capture-gated spectrometer to measure the cosmogenic neutron spectrum. To the authors' knowledge, this is the first direct measurement of these features.

[5]A thorough treatment of the theory of nuclear evaporation can be found in Reference [169].

To compare the measured spectrum with Monte Carlo, Table 7.11 shows the detected and simulated fluxes above multiple thresholds. At energies above 200 MeV, a significantly higher rate of events is observed than is predicted by the simulation.

Table 7.11: The integrated rates (in neutrons/s) of neutrons above each of five thresholds (1, 10, 100, 200 MeV and 1 GeV). Also listed are the equivalent rates predicted by the MCNP simulation of the JEDEC spectrum. The MCNP data shown use the same normalization as in Figures 7.14 and 7.15.

Threshold (MeV)	Neutron Rate (/s)	MCNP Rate (/s)
1 MeV	0.510	0.517
10 MeV	0.153	0.154
100 MeV	0.029	0.0257
200 MeV	0.0087	0.0046
1 GeV	0.00022	0

7.7 Measurement of the fast neutron flux above multiple thresholds

To obtain the total neutron flux above a given threshold, the difference in the number of "real+random" and "random only" events is computed. For an experimental threshold of 2 MeV_n, a total of 3.471×10^6 events are found with time separations between (2, 595 μs) and 5.79×10^5 events are found with time separations between (-200, 0 μs). The time ranges have been selected to reject prompt coincidences, which are frequently caused by non-neutron interactions. Subtracting the random events from the real+random events yields $(1.753\pm0.002)\times10^6$ neutrons over background during an observation period of 4.842×10^6 seconds.

From the Monte Carlo simulated fluence of 1.58×10^3 n/cm^2, 1.145×10^5 events that pass all experimental cuts are observed. Including the 84% ^{3}He detection efficiency from Section 2.4.3, this yields an efficiency of:

$$\epsilon = \frac{1.14 \times 10^5 \ n}{1.10 \times 10^3 \ n/cm^2} \times (0.84 \pm 0.1) \tag{7.5}$$

$$\epsilon = 87 \pm 13 \ n/(n/cm^2), \tag{7.6}$$

where the efficiency here has dimensions of neutron detected per unit fluence. As opposed to an efficiency of neutrons detected per source neutron, this notation has the benefit of removing any dependence on the simulated source location from the efficiency. The uncertainty in the response is dominated by the uncertainty in the ^{3}He detection efficiency. For comparison, the response simulated for FaNS-1 is 10.3 n/(n/cm^2), which is almost a factor of nine lower than that of FaNS-2.

Table 7.12: The main uncertainties in the FaNS-2 measurement of the surface fast neutron flux.

Source	Uncertainty
Exposure Time	0.01%
Statistics	0.2%
Threshold	5%
MCNP Response	15%

Using this efficiency, the measured neutron rate is converted into an incident neutron flux, shown in Equation 7.7. Table 7.12 lists the main sources of systematic and statistical uncertainties. The same procedure can be performed for multiple

thresholds, and the results of which are listed in Table 7.13.

$$\Phi(E_n > 2 \text{ MeV}) = \frac{(1.753 \pm 0.003) \times 10^6 \ n}{4.842 \times 10^6 \ s \times (87 \pm 13) \ n/(n/cm^2)} \tag{7.7}$$

$$\Phi(E_n > 2 \text{ MeV}) = (4.16 \pm 0.6) \times 10^{-3} \ n/cm^2/s \tag{7.8}$$

Table 7.13: The measured flux above multiple thresholds, using the MCNP to estimate the sensitivity and fluence as determined by MCNP. The MCNP fluence is calculated by integrating the portion of the input neutron spectrum above each threshold. The sensitivity includes the ^{3}He detection efficiency discussed earlier.

Threshold MeV	MCNP Fluence n/cm^2	MCNP Counts	Sensitivity n/(n/cm^2/s)	BG Subtracted Counts	Detected Fluence n/cm^2/s
2	1104.7	114489	87±13	1.753×10^6	$(4.16\pm0.6)\times10^{-3}$
10	816.2	48594	50±8	7.397×10^5	$(3.05\pm0.4)\times10^{-3}$
20	739.2	34684	40±6	5.248×10^5	$(2.75\pm0.4)\times10^{-3}$
50	656.2	18754	24±3	2.943×10^5	$(2.53\pm0.4)\times10^{-3}$
100	396.4	7970	17±2	1.392×10^5	$(1.70\pm0.3)\times10^{-3}$
200	239.6	1473	5±1	4.204×10^4	$(1.68\pm0.3)\times10^{-3}$

7.8 Discussion

The ambient fast neutron spectrum at sea-level has been measured from 2 MeV to 1 GeV using FaNS-2. The measured spectrum spans nine decades, from 0.3 neutrons/MeV/s to 10^{-9} neutrons/MeV/s. For neutrons with energies above 2 MeV, a total flux of $\Phi(n) = (4.16 \pm 0.6) \times 10^{-3}\ n/cm^2/s$ is observed. For comparison, the JEDEC parameterization yields a flux of $4.89 \times 10^{-3}\ n/cm^2/s$ above 2 MeV at sea-level and mid-solar cycle. Applying the correction discussed in Table 7.3 of Section 7.2.1, this is equivalent to a flux of $(5.1 \pm 0.2) \times 10^{-3}\ n/cm^2/s$ at NIST, where the uncertainty is only from the solar-cycle conversion. The JEDEC flux does not have any stated error bars, it is difficult to estimate how well the two measurements compare.

However, a recent measurement, discussed in Chapter 1, has made a measurement of the flux above two different energy thresholds, 10 and 20 MeV [30]. Their measurement was performed at Gran Sasso National Lab in L'Aquila, Italy, located at 42°25′11″ N, 13°31′2″ E, rigidity cutoff of 6.3 GeV, and 970 m above sea-level, during a period of solar minimum. The detector consisted of a single large volume of liquid scintillator doped with gadolinium, a neutron capture agent. Using the same procedure laid out in Section 7.2.1, a correction to their measurement can be made to allow for a comparison with the FaNS-2 data at NIST. The correction from L'Aquila to NIST is found to be 1/1.64 [155]. Their corrected flux measurements are compared with FaNS-2 in Table 7.14.

Table 7.14: A comparison between the LNGS and FaNS-2 measurements of the neutron flux above 10 MeV and 20 MeV.

Energy Range	LNGS Flux $n/cm^2/s$	Corrected LNGS $n/cm^2/s$	FaNS-2 Flux $n/cm^2/s$
$E_n > 10$ MeV	$(4.7\pm0.5) \times 10^{-3}$	$(2.9\pm0.3) \times 10^{-3}$	$(3.05 \pm 0.4) \times 10^{-3}$
$E_n > 20$ MeV	$(4.2\pm0.4) \times 10^{-3}$	$(2.6\pm0.3) \times 10^{-3}$	$(2.75 \pm 0.4) \times 10^{-3}$

Very good agreement is seen between the measured fluxes of the two experiments. The FaNS-2 spectrum is statistically superior and extends to both higher and lower energy neutrons. The two measurements have similar quoted uncertainties, though both experiments are systematics limited. The dominant uncertainties in the LNGS measurement are from energy calibrations and the non-linearity of the scintillator. For FaNS-2, the dominant uncertainty is from the characterization of the ^{3}He proportional counter sensitivity. Improvements to the understanding of the ^{3}He counters would greatly improve the quoted uncertainties.

During the course of six months, the detector was stable and operated extremely well. FaNS-2 has demonstrated the ability to measure very high energy neutron events while still having sensitivity to low energy neutrons with good energy resolution. The comparison between FaNS-2 data and the MCNP simulation is now discussed, along with a comparison between the two FaNS detectors.

7.8.1 Comparison to Monte Carlo

Though there are many fluctuations in measurements of the total flux of cosmic-ray induced neutrons, the relative shape of the energy spectrum is similar across measurements. Thus, the Monte Carlo has been used to determine

the weighted response (in neutron detected per neutron fluence) for FaNS-2 in the cosmic-ray induced neutron field. This response has then been applied to the detected neutron rate to obtain a measurement of the incident neutron flux.

Between 1 and 200 MeV the data and Monte Carlo spectra agree very well, including the nuclear evaporation features at 2 MeV and 4 MeV that appear in both spectra of Figure 7.15. Bonner sphere measurements lack the energy resolution required to observe these resonances, but FaNS-2 has been able to directly observe them. Above 200 MeV, a significant discrepancy is observed in the shapes of the spectra. There are three main possibilities that could explain these discrepancies:

1. MCNP does not correctly propagate neutrons with such high energies.

2. The detector is observing interactions that are not included in the simulation.

3. The input energy spectrum of neutrons is inaccurate.

Each of these explanations offers insight into the understanding of the FaNS-2 data. The first item, that MCNP does not accurately handle neutrons with energies above 200 MeV, is certainly plausible. MCNP was designed for studying nuclear reactors and as such focuses on fission-like neutron energies (< 10 MeV). The advent of MCNPX has helped extend the reach of the simulation above 150 MeV. However, after 150 MeV, MCNPX relies on models for neutron production and propagation, as opposed to tables that have been verified. It is not yet clear how much validation has been done for the models of nuclear interactions at these energies.

Secondly, there is evidence that FaNS-2 is detecting multiple particles from the same air shower event. Rough estimates indicate approximately 200 events

containing a neutron plus a second particle are incident on the detector every hour. Further study using the CRY simulation package could demonstrate the plausibility of them causing the excess. Similarly, the generation of neutrons within the detector from other high energy particles, including muons, protons, and electromagnetic cascades, could be a source of these events. FaNS-2 cannot distinguish between low-energy neutrons accompanied by other high energy particles and an original high energy neutron. The addition of muon-tagging scintillator paddles in future work could help identify events with multiple particles, for separate study.

Finally, there is also the possibility that the chosen input spectrum is not a good representation of the ambient neutron spectrum at NIST. As discussed in Chapter 1, there is much uncertainty in the shape of the cosmogenic neutron spectrum, especially at energies above 100 MeV. For instance, the spectrum from Ziegler et al. has a significantly higher rate of high energy neutrons than the spectrum used in this simulation [45,171]. Other measurements do not often quote their uncertainties, so it is difficult to estimate the confidence that should be placed in them.

The largest uncertainty for FaNS-2 is that from the Monte Carlo simulated response. Improvements to the simulation could reduce this uncertainty and improve the measurement. Specifically, a better characterization of the ^{3}He counters would reduce the uncertainty in their response. This would require calibrating the response of these detectors to a known neutron field, which is a significant undertaking. An experiment is currently being planned to directly measure the ^{3}He proportional counters' response to a monochromatic neutron beam at NIST. This could provide important information about how the detectors perform and their overall sensitivity.

A supplementary Monte Carlo of the detector in a different simulation environment, like Geant4 or FLUKA, would also enhance confidence that the detector is being modeled correctly. At high energies it is known that MCNP has difficulties that may preclude it from accurately reproducing the FaNS-2 response. These other Monte Carlos have been better benchmarked than MCNP and can perform more advanced detector modeling.

7.8.2 Comparison to FaNS-1

One important cross-check of the FaNS program is the comparison between the two detectors. Though FaNS-1 only observed the surface neutron spectrum for a few days, it was still possible to measure the spectrum out to 150 MeV. Figure 7.16 shows the final spectra from the two detectors.

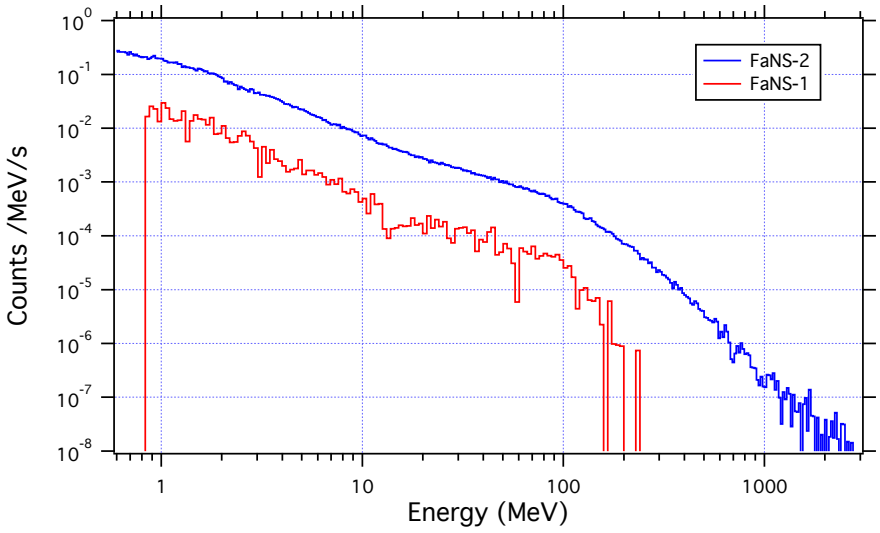

Figure 7.16: A comparison of the background subtracted neutron energy spectra recorded with FaNS-1 (red) and FaNS-2 (blue). The spectra are shown in neutrons/s, and no attempt to account for detector acceptance or efficiency has been done.

As discussed in Section 4.1.3, the measured surface fast neutron flux, for neutrons greater than 1 MeV, from FaNS-1 is $\Phi(n) = (4.0 \pm 1) \times 10^{-3}$ n/cm^2/s. This can be compared with the FaNS-2 measurement, above 2 MeV, of (4.6$\pm$0.6) $\times$ 10^{-3} n/cm^2/s. The uncertainty from threshold effects has been reduced for FaNS-2, primarily due to the work done studying the photon statistics of the detectors and their inclusion in the Monte Carlo. The driving uncertainty for both detectors is the simulated response to the surface neutron spectrum. Both detectors have similar spectral shapes; a steep slope from 1 MeV to 10 MeV, a slight leveling off from 10 MeV to 100 MeV, and finally a steep slope for neutrons with energies above 100 MeV. The ratio of the two spectra is consistent with expectations from the Monte Carlo simulated responses. This comparison highlights the improvements in sensitivity and energy range made when designing the FaNS-2 detector.

7.9 Conclusions and future work

The FaNS-2 detector has been deployed in a low overburden environment at NIST, Gaithersburg. The ambient fast neutron energy spectrum and flux have been measured over the course of six months of operation. The results of these measurements are reported along with a characterization of the environment in which they were performed. Measurements of the ambient gamma and thermal neutron backgrounds have also been performed. These measurements assist in the understanding of the random coincidence rate and shape of the random coincidence energy spectrum.

A dependence of the flux on atmospheric conditions is observed, most notably on the barometric pressure. Fluctuations in the barometric pressure lead to significant variations in both the trigger rate of the detector and the detected flux of fast neutrons, as is shown in Figure 7.11. These fluctuations are anti-correlated with the pressure and can be attributed to the variation in the effective shielding provided by the atmosphere. The fluctuations observed with FaNS-2 have been compared with those observed by the NMDB neutron monitor in Newark, DE. A method for adjusting the detected rate for barometric pressure has been demonstrated, though it is not used in the final FaNS-2 result.

A new measurement of the ambient fast neuron spectrum is presented. Though good agreement with the shape of Monte Carlo simulations for neutrons below 200 MeV is observed, above this energy, a substantial increase in the measured neutron flux is found compared to the simulation. Work is underway to characterize the source of this discrepancy, although three potential sources have been discussed. These include 1) errors in the particle transport of MCNP at energies above 200 MeV, 2) inclusion of events in the detector that are not accounted for in the simulations, such as multiple particle interactions from air showers, and 3) errors in the input fast neutron spectrum for the Monte Carlo. Any of these three may contribute to the discrepancy between the reported data and the simulation. An expansion of the Monte Carlo to include these effects could help to understand the discrepancy.

As discussed in Chapter 1, a reliable measurement of the surface fast neutron spectrum is important to many areas of research, including those designing shielding

systems and modeling activation of detector components for low background experiments. There are currently broad uncertainties associated with the surface neutron spectrum, and this improved measurement could help reduce them.

The main uncertainty in the total flux is from the simulation of the detector response, much of which is due to the correction for the overall sensitivity of the ^{3}He proportional counters. To improve this uncertainty, new measurements in controlled environments must be performed and simulated to ensure the Monte Carlo is accurately reproducing the true efficiency of the detectors. A measurement on a thermal neutron beam is currently being planned, and could lead to an improved understanding of the inner-workings of the ^{3}He counters and their efficiency.

FaNS-2 has been shown to have good energy resolution for neutrons at 14 MeV. An important piece of future work, however, is to simulate the response of FaNS-2 to a broad range of mono-energetic neutrons, thereby generating a response matrix for the detector. It would then be possible to unfold the detected spectrum and produce a spectrum of the incident neutron energies. This would account for efficiencies that vary with energy and the ability of the detector to reconstruct energies. This spectrum could then be used by other researchers in their work. This is an important task, and one that is being actively pursued.

FaNS-2 performed extremely well while operating in the Low Scatter room at NIST. These measurements further understanding of the ambient fast neutron spectrum at sea-level, as well as demonstrate the sensitivity and performance of the detector.

Chapter 8

Outlook and conclusions

The field of neutron spectroscopy has long been based upon two standard detection techniques: Bonner sphere arrays and liquid scintillator proton recoil detectors. Though very successful, these detector types each have drawbacks. Bonner sphere arrays do not directly detect neutron energy, but rather depend on using multiple moderated thermal neutron detectors with different energy acceptances. Liquid scintillator recoil detectors, on the other hand, detect the energy deposited by any neutron that interacts in the detector, most of which are only partial energy depositions. Neither of these two detectors are ideally suited to neutron spectroscopy. By combining the two techniques, a capture-gated spectrometer demands full energy deposition while directly measuring the incident neutron energy. The FaNS detectors have successfully demonstrated the power of this combination, and have been deployed to characterize various neutron sources.

The design, development, and deployment of two fast neutron spectrometers based on plastic scintillator and ^{3}He proportional counters is discussed in this thesis. The two detectors, FaNS-1 and FaNS-2, have measured a variety of neutron environments ranging from high-rate calibration to high energy cosmogenic neutron fields and finally to rare-event underground neutron fields. In each environment, the detectors have performed exceptionally well. In this final chapter a summary

of the FaNS results is presented along with a discussion of the future of the FaNS program.

Monoenergetic neutron measurements made with the FaNS detectors highlight the ability of capture-gated neutron spectrometers to directly measure the energy spectra of different neutron sources. Even with coarse segmentation, it is possible to accurately reconstruct the neutron peaks from both DD and DT generators. The future measurement of an Am-Be neutron source, which has many small peaks in its energy spectrum, could further show the effectiveness of the FaNS technique.

The FaNS-1 measurements performed at the Kimballton Underground Research Facility show how capture-gated spectroscopy can be applied to low signal to background environments, where the fast neutron to gamma ratio is approximately 10^{-6}. This measurement will be used by the other researchers at KURF as inputs to their simulations, and can be used in the design of future detectors and operations in the lab.

The performances of the FaNS detectors at ground level at NIST demonstrate that a segmented fast neutron detector can directly measure neutron energies ranging from 1 MeV to beyond 1 GeV. The FaNS-2 measurement of the neutron flux agrees well with the recent measurement reported by Reference [30] once location effects have been taken into account. This represents a major improvement over Bonner sphere arrays that cannot directly measure energies and liquid scintillator recoil detectors that cannot resolve spectral features. This new measurement of the surface fast neutron spectrum and flux will improve understanding of neutron-induced interactions that are problematic for numerous low-background experiments.

Capture-gated neutron spectrometers have been shown to provide significant improvements over previous detector technology. A few potential measurements that can be made with the FaNS detectors will now be discussed.

8.1 Current and future measurements

As calibrated, high-sensitivity neutron spectrometers, both FaNS detectors remain in operation at NIST. FaNS-1 is being used to characterize the fast neutron backgrounds generated by the NIST National Bureau of Standards Reactor (NBSR), a 20 MW research reactor, as part of an effort to design an experiment to detect reactor antineutrinos at NIST [172,173]. The νPROSPECT experiment aims to test previous reactor antineutrino anomalies through an ultra short baseline oscillation measurement. They will be deploying two large neutrino detectors at distances of $\sim$2 m and $\sim$15 m from a research reactor. The ratio of neutrino inverse beta-decay events between the two detectors can determine whether there is any deviation from the expected rate that could be due to an oscillation into a fourth generation sterile neutrino. This collaboration also plans to perform a precision measurement of the reactor antineutrino energy spectrum. Fast neutron backgrounds present at a surface-level reactor are possibly a debilitating background for this type of experiment, since the signature of an inverse beta-decay event is also a delayed neutron capture.

FaNS-1 is ideally suited to measure this background; it is a compact detector with high sensitivity and dynamic range. The detector has been fitted with

an improved housing and will be deployed at three different reactor sites to help determine the location for the νPROSPECT experiment. The detector will then be used to characterize the reduction of neutron backgrounds as shielding components are installed.

FaNS-2 has been deployed in a shallow underground (20 m.w.e.) lab at NIST to measure muon-induced neutrons in a shallow environment. This depth is sufficient to eliminate any hadronic component of the cosmogenic radiation. Thus the only sources of neutrons in the lab should be local radioactivity and muon-induced neutrons from interactions in the nearby environment. There have been a small number of measurements of the muon-induced neutron yield at similar depths [159,174], but almost no data exist on the energy spectrum of neutrons from this process.

The average muon energy increases with increasing depth, due to lower energy muons stopping in the overburden. Therefore, it is interesting to measure neutron production at different depths and map variations in the neutron/muon yield and the energy spectrum of muon-induced neutrons. After operating at 20 m.w.e., FaNS-2 could be installed at a lab of approximately $\sim$100-300 m.w.e. deep. However, there is a limit to the depth at which it is practical to operate FaNS-2. At a depth similar to KURF, the expected muon-induced neutron flux above 10 MeV is 7×10^{-9} n /cm^2/s, approximately a factor of $5{\times}10^5$ lower than the surface neutron flux. Using the simulated surface sensitivity of FaNS-2, (87$\pm$13) n/(n/cm^2/s), the expected detection rate would be $\sim$20 neutrons/year. To effectively measure a neutron spectrum, FaNS-2 would need to operate for at least five years. A better use of FaNS-2 would be to measure at multiple depths from 20 m.w.e. to 400 m.w.e. and

provide insight to the energy dependence of the neutron yield and spectrum. This can be used to benchmark simulations and improve understanding of the physics behind muon-induced neutron production. There are a number of other interesting measurements that can be performed with these detectors, a few of which will be discussed further here.

8.1.1 Muon-induced neutrons from a fixed target

As discussed in Chapter 1, there is a demand for precision knowledge of cosmogenic activities in materials for low background experiments. In particular, dark matter and neutrinoless double-beta decay experiments require very low background materials for use in their shielding and detector construction. Activation during fabrication and transport at sea-level can create irreducible backgrounds that could cause severe problems for these experiments. Better knowledge of the muon-induced neutron processes would greatly benefit this effort [39, 43].

There are still many features in the production of neutrons from muon interactions, including spallation and negative muon capture, in different materials that are difficult to characterize. Specifically, the yield and energy spectrum of muon-induced neutrons in lead, copper, and polyethylene are important parameters for designing shielding for underground experiments. Stopped muon interactions are of great interest because they are difficult to reject or shield against in shallow experiments. Neutron production from stopped muons is generated by a significantly different physical process than muon-spallation. Therefore a precision measurement

of the two muon-induced neutron yields would improve the understanding of both processes. Though measurements of the neutron yield have been performed, there have not been measurements of the neutron energy spectrum from these processes. It is possible to measure the neutron production from these materials using FaNS-2. One could position a target consisting of a $25 \times 25 \times 50$ cm^3 block of a target material between muon paddles (two on top and one below) next to FaNS-2. A significant number of muons will be stopped in the target, so having two paddles above the block ensures that these events may be isolated from through-going muon interactions.

A schematic of the proposed measurement is shown in Figure 8.1. Here, FaNS-2 is shown positioned $\sim$50 cm from a target consisting of lead. Neutrons produced by muons in the target are detected by FaNS-2, with the use of the muon-tag to identify potential events. Previous measurements of the neutron production from lead indicate that between 50 and 500 neutrons per day would be detected with FaNS-2.

Performing this measurement with multiple targets, as well as without a target, would eliminate many systematics of the measurement and provide insight to simulations and calculations of the neutron yield. The no-target run would eliminate correlated events generated by cosmic ray air showers, as discussed in Chapter 7.

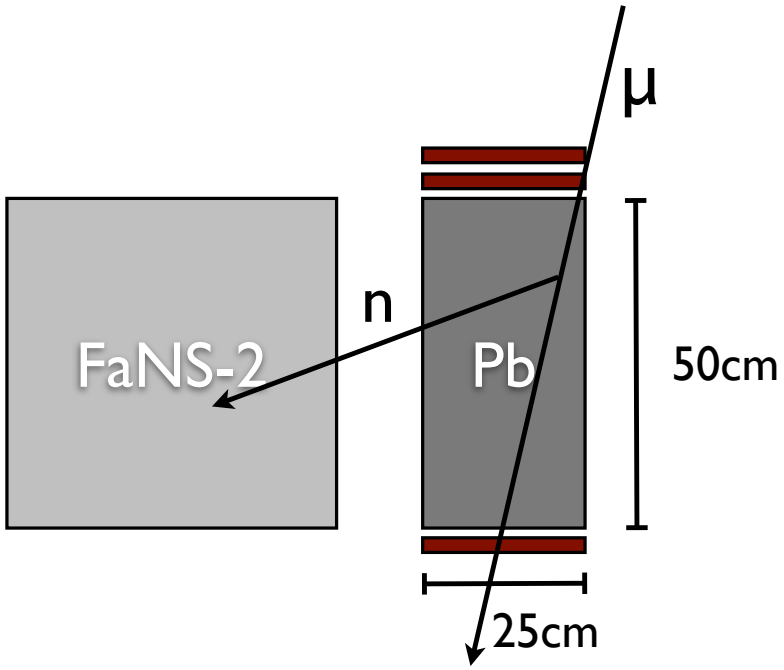

Figure 8.1: A schematic showing the layout of a potential muon-induced neutron measurement with FaNS-2. A target (here consisting of lead) is placed between muon paddles (red) and positioned next do FaNS-2. A muon traverses the target, and kicks out a neutron, that is detected by FaNS-2. The muon paddles provide a tag that identifies neutron interactions originating in the target.

8.1.2 Low activity neutron sources

Low background underground experiments often have need of low neutron activity sources ($\sim$ few /s) to calibrate and test their detectors. However, calibrating such a low activity source is difficult and not typically done by NIST. As a high sensitivity, calibrated neutron detector, FaNS-2 is well suited to measure the neutron output of low activity sources. NIST possesses a number of μg level sources that emit very low rates of neutrons ($<$1 /s) that have not been fully characterized. These sources can be detected in a relatively short operational period with FaNS-2. To test this technique a weak fission neutron source could be placed at various distances

from the detector. By looking at the required exposure necessary to confirm the source's presence, the total sensitivity of the detector can be demonstrated.

A proof of principle test has been performed that demonstrates the ability of FaNS-2 to make such measurements. A 200 μg Pu source, with calculated neutron activity of 0.2 /s, was placed 10 cm above the detector. Figure 8.2 shows a 2D histogram of background-subtracted ^{3}He count rates throughout the detector. Each square is a helium counter, arranged as they are physically in the detector.

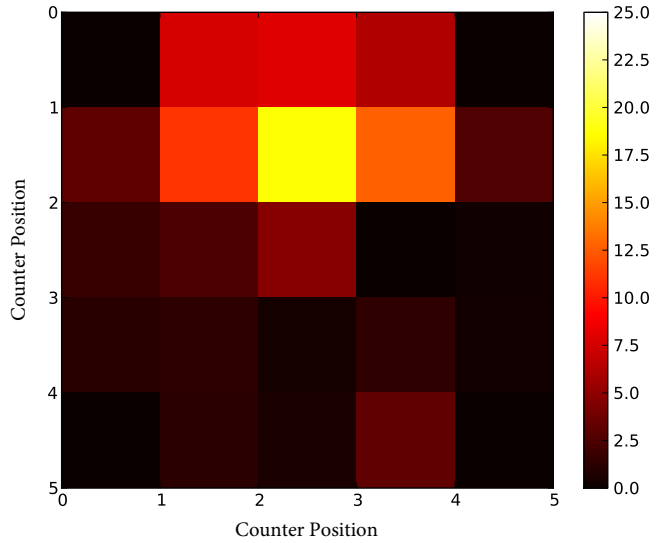

Figure 8.2: A 2D histogram showing the background-subtracted count rates (in counts/hour) of each ^{3}He counter with a 200 μg source placed above the detector.

There is clear evidence of the detection of neutrons emitted from the source, seen by the excess count rates in the top of the detector. This test demonstrates that FaNS-2 is able to detect very low rates of neutrons from a low activity source. It also clearly shows the directionality of the detector; the ^{3}He counts are all located towards the top of the detector, where the source is located. For certain source

sizes, it may also be possible to insert the source into the center of the detector to detect all emitted neutrons. Using the calibration insert that was discussed in Section 5.5.4, a source smaller than 3 cm may fit inside the detector. This could also be used to study correlated emission of multiple neutrons per spontaneous fission event.

8.1.3 Neutron energy spectra at multiple overburdens

As discussed with FaNS-1, the muon-induced neutron energy spectrum and flux are two very important parameters for underground experiments. By measuring the spectrum at a variety of overburdens, FaNS-2 could provide much information for simulations and help to decrease uncertainty in the rate of such interactions in underground labs.

The dominant technique for estimating the muon-induced neutron background at underground laboratories is through simulations. These simulations are not well benchmarked, especially with regard to the energy spectrum of generated neutrons. By making measurements at a series of depths, with the same detector, the production processes can begin to be cross-checked. Two sites for shallow operation of FaNS-2 have been identified, one at 20 m.w.e. and the other at 100 m.w.e. FaNS-2 is currently operating in the 20 m.w.e. shallow lab on site at NIST, Gaithersburg. The data currently being collected will be compared against simulations and a few muon-induced neutron yield measurements that have been performed at similar depths [159, 174].

Another possibility is to install FaNS-2 in a laboratory with a variable overburden, such as the Aberdeen tunnel where the Daya Bay experiment is currently operating. A horizontal access tunnel, this location could provide a finely varying overburden, from 270 m.w.e to 1250 m.w.e. with minimal difficulties for relocation.

8.2 FaNS Conclusions

The design, construction, calibration, and operation of two capture-gated fast neutron spectrometers consisting of plastic scintillator and ^{3}He proportional counters is demonstrated in this thesis. The two detectors were calibrated to have a 1.3% and 3.4% efficiency for detection of ^{252}Cf-like neutrons. Through the use of monoenergetic neutron generators, this technique was shown to provide a substantial improvement in the energy response over traditional neutron detectors.

While operating at the NIST, FaNS-1 successfully performed a measurement of the ambient fast neutron spectrum at sea-level of neutrons from 1 MeV to 150 MeV. This is the first such measurement with a capture-gated spectrometer. The measured spectrum agrees well with a prediction from Monte Carlo that uses a previously measured spectrum as its input. This measurement demonstrates the detector's sensitivity to high energy neutrons.

FaNS-1 made an important measurement of the ambient neutron flux and energy spectrum at the the Kimballton Underground Research Facility in Ripplemead, VA. The detected spectrum appears to be similar to that of (α,n) neutron sources, and it is posited that the source of these neutrons is predominantly from

(α,n) events of U and Th in the surrounding rock. Measurements are currently being performed by a group at KURF to measure the U and Th content of the rock that may help to confirm this conclusion.

The upgraded detector, FaNS-2, has improved upon many aspects of FaNS-1. With a significantly larger active volume, FaNS-2 has a correspondingly higher sensitivity and extended energy range. During its operation at NIST, FaNS-2 has been able to measure the ambient neutron spectrum from 2 MeV to beyond 1 GeV. Excellent agreement is shown with a Monte Carlo simulation up to 200 MeV, at which point data and MCNP diverge. The root cause of this discrepancy is currently being investigated.

The FaNS-2 detector has now been installed in the shallow underground Californium Neutron Irradiation Facility (CNIF) at NIST. Located at approximately 20 m.w.e deep, the lab provides an excellent location to study the neutron spectrum. Simulations indicate that 20 m.w.e. significantly reduces the flux of neutrons generated in the atmosphere from cosmic-ray-induced air showers. Only muons are sufficiently penetrating to reach the detector in the CNIF. Thus, this is an excellent location to collect data from muon-induced neutrons. By comparing the underground spectrum to that measured at the surface, the high energy events generated in air-showers may be isolated. This will give insight to the discrepancy between the detected and simulated energy spectra.

FaNS-2 is a highly sensitive detector for a wide range of neutron energies. This makes it an ideal detector for studying neutron spectra in various underground settings. By collecting data at multiple depths, it will be possible to map out the

depth dependence of the fast neutron spectrum and yield. Such a measurement will provide important feedback into the low-background physics community to help benchmark existing simulations.

Appendix A

FaNS-2 Operation Procedure

The FaNS-2 detector is complicated, so it is helpful to have instructions for starting up the detector and normal operation. There are two main programs required to start up FaNS-2: 1) the high voltage control to bias the detectors, and 2) the data acquisition to control the digitizers. We will outline the use of each of these programs here.

A.1 High voltage control

The PMTs and ^{3}He detectors are biased using two separate Wiener MPOD Mini high voltage crates. Each crate contains a controller card that is accessed over ethernet. The PMT crate has IP address of 10.10.0.1 and the ^{3}He crate is 10.10.0.2. To monitor the status of the crates, you navigate to that address in a web browser, where an overview of the channels' high voltages and currents are updated every few seconds. A screenshot of that display is shown in Figure A.1.

Separately, there is a command-line interface to monitor and control the high voltage settings based upon the open library SNMP (*Simple Network Management Protocol*). This interface is more convenient for automated monitoring and allows for full control of the voltages for each channel. The scripts for controlling the high

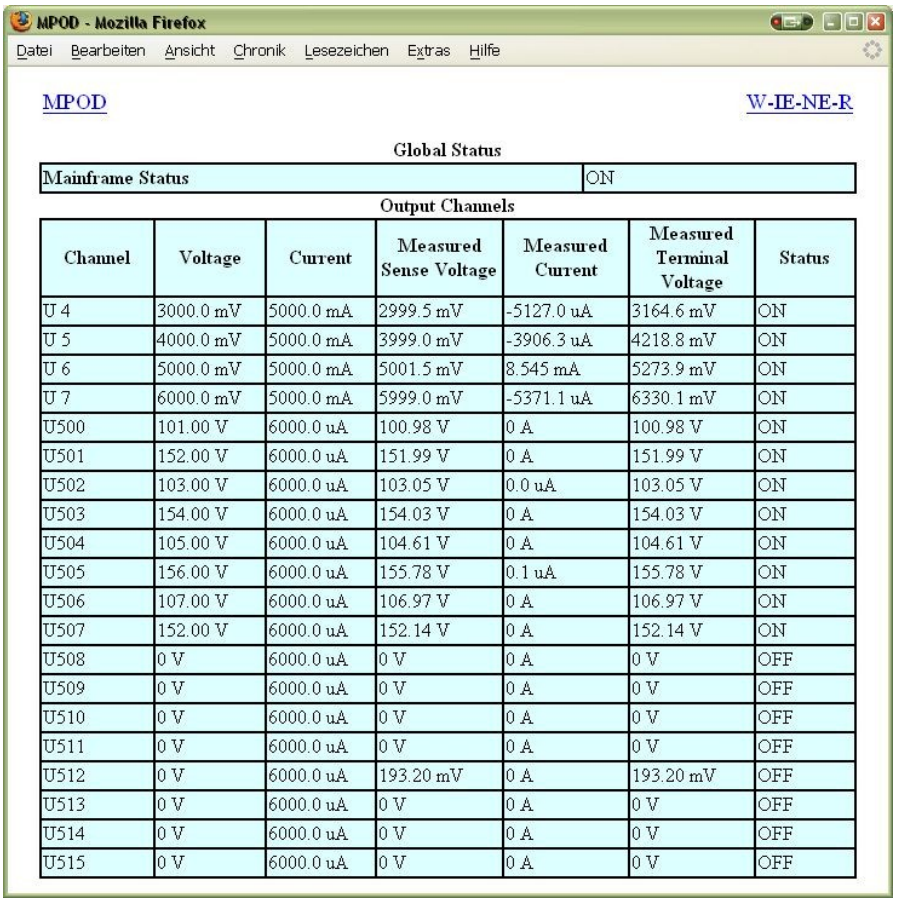

Figure A.1: The web interface for monitoring the HV settings from the MPOD Mini crate. This is found by navigating to the crate's IP address in a web-browser.

voltage are included at the end of this manual. SNMP can easily be installed on Ubuntu using apt-get:

```
sudo apt-get install snmp
```

Wiener provides a .MIB file that contains the functions for communicating with the MPOD Mini crate. This file must be located in either the working directory or the `/usr/local/share/snmp/mibs` directory. On the current DAQ computer, it is located in this directory, allowing the commands to be issued from any working directory.

A object-oriented wrapper for the SNMP commands has been written in Python. The Python file is called `highVoltage.py` and is located in the home directory of the `fn-daq` user. The *highVoltage* class contains all of the operations that are anticipated, including a cold start up that loads the previous voltages, a shut down procedure, and functions to check and set voltages. The control can be operated using the `IPython` command line interface, exhibited here:

```
fn-daq@FNDAQ:~/ ipython
>>> from highVoltage import highVoltage
>>> pmt = highVoltage('10.10.0.1')
```

The *pmt* instance of the *highVoltage* class will then be ready to set voltages. The available functions for the class are listed here:

- `voltagesFromFile(fileName)`: Reads in the voltage settings from a given file, `fileName`, and returns two arrays. The first array is a channel listing, while the second array contains the voltages.

- `voltagesToFile(fileName)`: Writes the current voltage settings for each channel to the file, `fileName`, in the format that is read by `voltagesFromFile`.

- `setVoltage(channelArray, voltageArray)`: Takes two arrays, containing channels and voltages, and sets the voltages. The arrays must be the same length, but can contain any number of channels. This is convenient for setting voltages on a layer of the detector.

- `checkVoltages(channelArray)`: If given a `channelArray`, this function returns the measured voltages on those channels. If no `channelArray` is specified, it returns the voltages for the whole crate.

- `startUp(fileName=‘‘LastUsedPMTSettings.txt’’)`: Reads the settings from the given file, if none is provided it uses the settings stored in `LastUsedPMTSettings.txt`, and applies them to the crate.

- `shutDown`: Writes the current settings to the file, `LastUsedPMTSettings.txt`, and then ramps all voltages to zero.

An example use of these functions is shown here:

```
>>> pmt.checkVoltages()
>>> pmt.checkVoltages([0,1,2,3])
>>> pmt.voltagesToFile(‘PMTVoltages.txt’)
```

The `highVoltage.py` script may also be called from the command-line to start up or shut down both the PMT and ^{3}He high voltage crates. This is done by calling the following from the home directory:

```
fn-daq@FNDAQ:~/python highVoltage.py on
fn-daq@FNDAQ:~/python highVoltage.py off
```

The `on` command will read the voltages stored in `LastUsedHe3Voltages.txt` and `LastUsedPMTVoltages.txt` and apply them to the system. The `off` command stores the current settings in those files and then ramps down the system. The program will check to ensure that the voltages are down before returning. It is important to note that the on and off options work on the whole system, so make

sure the detector is light-tight and ready for voltages. A sample high voltage control script is shown here:

```
from highVoltage import highVoltage

# Create instances for each crate
pmt = highVoltage('10.10.0.1')
he3 = highVoltage('10.10.0.2')

# Read voltages from files for each crate
pmtCh, pmtV = pmt.voltagesFromFile('PMTVoltages.txt')
heCh, heV = he3.voltagesFromFile('He3Voltages.txt')

# Take those voltages and apply them to the crates
pmt.setVoltages(pmtCh, pmtV)
he3.setVoltages(heCh, heV)

# Check the voltages (This will print to screen the returned voltages)
pmt.checkVoltages(pmtCh)
he3.checkVoltages(heCh)
```

These commands can be run from a script on the command-line or from within the Python interpreter. This flexibility is a huge asset for controlling the system.

There is a script that runs periodically that checks the high voltages for each crate and writes them to a log file. The frequency is controlled by `cron`, and is currently set to run every five minutes. The log files, called `PMT_HV.log` and `He3_HV.log` are stored in the home directory. Their format is a UNIX timestamp[1] followed by a comma-separated list of tuples containing the channel number, measured current, and measured voltage:

```
time0, (ch0, current, voltage), ... , (chN, current, voltage)
time1, (ch0, current, voltage), ... , (chN, current, voltage)
```

where N is the total number of channels in the crate.

[1]The UNIX timestamp is in units of seconds since January 1, 1970 GMT.

A.2 DAQ Digitizer Control

The CAEN V1720B digitizers are controlled by a custom software package called *Caen* that resides in `/home/fn-daq/Desktop/`. After the program is launched it can either be controlled locally using the on-screen interface, or by running a Python control function, an example of which is shown in Appendix D. The Python interface is also object-oriented and is setup by creating an instance of the *caenSocket* class. This class sends commands and receives replies from the *Caen* program over IP using the loopback IP address of the computer (`127.0.0.1`) and Port `50001`. To begin a control session, do the following:

```
from caenSocket import caenSocket
s = caenSocket()
```

Functions have been written that wrap the allowed commands so that they can easily be operated. The allowed commands are listed here:

- `start(boardID)`: Takes a `boardID` number and sends the start command
- `stop(boardID)`: Takes a `boardID` number and sends the stop command
- `readIni(boardID, iniFile)`: Takes a `boardID` number loads the `iniFile` that contains board settings. Note: iniFile is a string.
- `getElapsedTime(boardID)`: Takes a `boardID` number and returns the current elapsed time in the run
- `getElapsedCounts(boardID)`: Takes a `boardID` number and returns the current number of counts in the run

- `setPresetTime(boardID, setTime)`: Takes a `boardID` number and sets the run time to `setTime`
- `setPresetCounts(boardID, setCounts)`: Takes a `boardID` number and sets the max counts in the run to `setCounts`
- `zeroTime(boardID)`: Takes a `boardID` number and zeros the time counter
- `zeroCounts(boardID)`: Takes a `boardID` number and zeros the event counter
- `setSkip(boardID, skipCount)`: Takes a `boardID` number and sets the number of events for the display to skip to `skipCount`
- `writeHist(boardID, fileName)`: Takes a `boardID` number and writes the current histogram data to `fileName`. The data is in IGOR format with the wave names set to `boardID, channelNumber`. Ex: b0w7. Note: fileName is a string.
- `writeData(boardID, fileName)`: Takes a `boardID` number and sets the file for raw data to be written to `fileName`. Note: fileName is a string. To release the file, use this function with `fileName = ‘’` (an empty string).

For each of these commands `boardID` refers to the individual board number, ranging from zero to seven. If `boardID` = -1, the command will apply to all boards being controlled by the Coordinated Panel. Which boards are being controlled is a setting in the `iniFile`. The `iniFile` for a coordinated run contains the settings for all controlled boards. An example of a function call is shown here:

```
s.setPresetTime(-1, 100)
```

This will set the preset run time of the acquisition to 100 s. A small sample run procedure is shown here:

```
from time import sleep
from caenSocket import caenSocket

# Initialize the caenSocket instance
s = caenSocket()
# Read the settings from the iniFile
s.readIni(0, board0.ini)
# Set a preset time of 500s
s.setPresetTime(0, 500)
# Set a max counts of 20000
s.setPresetCounts(0, 20000)
# Set the DAQ to write binary data to ‘‘testData.dat’’
s.writeData(0, ‘‘testData.dat’’)

# Zero the time and counts (Not necessary, but makes sure that
# the run starts clean)
s.zeroTime(0)
s.zeroCounts(0)

# Starts acquisition
s.start(0)

# Sleeps the control program until the run is over, and then
# sleeps a few more seconds to make sure it’s done
sleep(500)
sleep(5)

# Stops the acquisition (Not strictly necessary, but just makes
# sure it’s stopped)
s.stop(0)

# Releases the binary file so that it is no longer being written to
s.writeData(0, ‘’)

# Writes the final histograms to file
s.writeHist(0, ‘testHist.itx’)

# Closes the acquisition session
```

```
s.close()
```

The main control script is located in the home directory, and is split into three types of operation: 1) gamma calibration, 2) muon calibration, 3) neutron data. Both the calibration runs are currently set to be 100 s long, which has typically been sufficient to obtain statistics while not seriously increasing down time of the experiment. The calibration data are coordinated, with all PMT digitizers being controlled. The neutron data is a coordinated run with all seven digitizers controlled. These data typically are set for 3600 s, which is a convenient chunk of time and data. Typical file sizes for the calibration runs are 500 MB for low-threshold gamma data, and 30 MB for high trigger threshold muon data. The ambient neutron data at the surface is typically 500 MB, while the file sizes underground are more like 50 MB. These numbers vary with thresholds, both for trigger and the Zero-Length Encoding options.

A.3 Restart procedure

Occasionally, the DAQ becomes non-responsive and requires a hard-reboot. This is the clean start up procedure if that should happen.

- Turn off the PC
- Turn off the VME crate
- Wait a few minutes (just in case)

- Turn back on the PC, it should boot into Ubuntu. Log in `usr: "fn-daq"`
- Open a terminal, and navigate to `/home/fn-daq/CAEN_Stuff/A3818Drv/src/`
- Execute `sudo sh a3818_load` This loads the driver for the optical fibre controller card. Note, the `sudo` command temporarily elevates the user to have superuser privileges.
- Turn back on the VME crate
- On the desktop, there is a folder named

  `Caen-build-desktop-Desktop_Qt_4_7_4_for_GCC__Qt_SDK__Debug`

  Open this folder by double clicking on it. Inside that folder is the executable for the DAQ, named Caen, double click on it to open the program. It should not pop up any errors[2].
- In the terminal, navigate to `/home/fn-daq/Desktop/`
- in that terminal execute `python <fileName>`. Where `fileName` is the name of the current control script being used.
- It should prompt you for a directory name, choose an apropriate name that includes the next run number. Hit `<return>`
- It will prompt for the base-name of the files, the default is date/time.

[2]NB: The display is slightly messed up, and at startup, won't display any traces. At the top left of the display, there are the radio buttons for selecting which channels are displayed. When you start up the program, channels 4 and 7 are not selected. When you select them, the display should start working. You have to do this for each of the 7 display panels.

- It should begin acquisition of the gamma data for the 4 PMT digitizers (on the left side of the crate).
- After 100s, it should move on to the muon data for another 100s
- The program should then load the ini file for normal DAQ, and you should click on the "coord" radio button to view the run stats of that acquisition. There should be traces showing up for each trigger, which should be coming in about 2 Hz.

This should be sufficient to restart the data acquisition. The high voltage is not be effected by this procedure, and should still be at the set voltages. If this fails for some reason, they will have to be reset using the procedure outlined earlier.

Appendix B
PMT Calibrations for FaNS-2

Table B.1: The calibrations used for FaNS-2 in units of (pulse integral per MeV).

PMT (board, channel)	High Gain (integral/MeV)	Low Gain (integral/MeV)	Full/Att Ratio
(0, 0)	8370.55	1973.90	10.734
(0, 1)	8542.09	2001.11	11.037
(0, 2)	8431.51	2120.74	11.208
(0, 3)	8649.19	2071.07	11.158
(0, 4)	8570.83	2090.31	11.233
(0, 5)	8512.49	2095.93	11.216
(0, 6)	8453.27	2075.08	11.039
(0, 7)	8377.52	2056.54	10.875
(1, 0)	8077.11	1996.24	10.826
(1, 1)	7932.56	1819.57	11.279
(1, 2)	8569.08	2252.02	11.459
(1, 3)	8480.27	2071.60	10.623
(1, 4)	8448.92	2044.87	10.642
(1, 5)	8541.22	2148.37	11.408
(1, 6)	8047.50	1982.78	10.302
(1, 7)	8023.99	1987.31	11.212
(2, 0)	7902.96	1826.32	11.137
(2, 1)	7974.36	1995.05	10.565
(2, 2)	8690.12	2368.65	11.524
(2, 3)	8691.86	2304.89	10.778
(2, 4)	8322.66	1971.42	10.865
(2, 5)	8400.16	2244.30	10.937
(2, 6)	8205.11	1951.10	10.711
(2, 7)	8424.54	2136.77	10.995
(3, 0)	8377.52	2090.67	10.750
(3, 1)	8461.98	1953.85	11.064
(3, 2)	8305.25	1996.23	10.630
(3, 3)	8007.45	2024.24	10.565
(3, 4)	8563.86	2032.55	10.366
(3, 5)	8462.85	2115.59	10.651
(3, 6)	7922.11	1813.69	10.561
(3, 7)	8044.02	2000.27	10.399

Appendix C
Channel Map for FaNS-2

Table C.1: The channel map for the PMTs in FaNS-2. The PMT high voltage crate has IP:10.10.0.1.

PMT	Data Acquisition	High Voltage
Left 0	b0tr0	100
Right 0	b0tr1	0
Left 1	b0tr2	101
Right 1	b0tr3	1
Left 2	b0tr4	102
Right 2	b0tr5	2
Left 3	b0tr6	103
Right 3	b0tr7	3
Left 4	b1tr0	104
Right 4	b1tr1	4
Left 5	b1tr2	105
Right 5	b1tr3	5
Left 6	b1tr4	106
Right 6	b1tr5	6
Left 7	b1tr6	107
Right 7	b1tr7	7
Left 8	b2tr0	108
Right 8	b2tr1	8
Left 9	b2tr2	109
Right 9	b2tr3	9
Left 10	b2tr4	110
Right 10	b2tr5	10
Left 11	b2tr6	111
Right 11	b2tr7	11
Left 12	b3tr0	112
Right 12	b3tr1	12
Left 13	b3tr2	113
Right 13	b3tr3	13
Left 14	b3tr4	114
Right 14	b3tr5	14
Left 15	b3tr6	115
Right 15	b3tr7	15

Table C.2: The channel map for the ^{3}He detectors in FaNS-2. The ^{3}He High Voltage crate has IP:10.10.0.2

^{3}He Tube	Data Acquisition	High Voltage
0	b4tr0	0
1	b4tr1	1
2	b4tr2	2
3	b4tr3	3
4	b4tr4	4
5	b4tr5	5
6	b4tr6	6
7	b4tr7	7
8	b5tr0	8
9	b5tr1	9
10	b5tr2	10
11	b5tr3	11
12	b5tr4	12
13	b5tr5	13
14	b5tr6	14
15	b5tr7	15
16	b6tr0	100
17	b6tr1	101
18	b6tr2	102
19	b6tr3	103
20	b6tr4	104

Table C.3: The channel map of the background monitoring detectors

Detector	Data Acquisition	High Voltage
^{3}He	b6tr5	^{3}He PS ch 105
NaI	b6tr7	Rackmount PS

Appendix D
Python data acquisition control for FaNS-2

```
from caenSocket import caenSocket
from FileCompletedEmail import fileCompEmail
import time
import os
import sys

s = caenSocket()
nIters = 2000
secsPerRun = 3600
secsPerCal = 100
secsPerMuCal = 100
board = -1  # -1 indicates the control of all boards currently being sync'd

# Booleans to turn on or off calibration data
calRun = 1
muonRun = 1
NaIRun = 1

# Prompt user for data location
dirName = raw_input('Name for Data Directory?\nDefault = none\n')

if dirName != '':
    if dirName[-1] != '/':
        dirName += '/'

print dirName

dateFormat = "%Y-%m-%d %H-%M-%S"

baseName = raw_input('Basename for data run?\nDefault = Date/Time\n')
useDate = 0
if baseName == '':
    print 'Using date/time'
    useDate=1

dataLocation = "/media/FaNS2Data1/" + dirName

# Open logFile for writing
logFile = open(dataLocation + 'logFile.log','a')

logFile.write('Starting acquisition at: ' + time.strftime(dateFormat) + '\n')
logFile.flush()

# Create directory if it doesn't exist
if os.path.isdir(dataLocation) ==0:
    os.mkdir(dataLocation)

# Location of each iniFile
calIniLocation = "/home/fn-daq/Desktop/"
syncCalIniLocation = "/home/fn-daq/Desktop/"
bgIniLocation = "/home/fn-daq/Desktop/"

# Loop for acquisition
for iters in xrange(nIters):
    date = time.strftime(dateFormat)
    if emailSent:
        fileList = []
        mcaList = []

    # PMT Calibration (Gamma)
    if calRun == 1:
        calIniFile = calIniLocation + "022013-gammaCoord.ini"
        s.setPresetTime(board, secsPerCal)
        s.setPresetCounts(board, 0)

        s.setSkip(board, 10000)
        s.zeroTime(board)
        s.zeroCounts(board)
        s.readIni(board,calIniFile)
        if useDate:
            dataName = dataLocation + "GammaSync-" + date + ".dat"
        else:
            dataName = dataLocation + baseName + "-" + str(iters) + "_GammaSync.dat"
        fileList.append(dataName)

        s.writeData(board,dataName)
        print "\nStarting gamma run ", str(iters), "at ", time.strftime(dateFormat), "\n"
        sys.stdout.flush()
        logFile.write("\nStarting gamma run ", str(iters), "at ", time.strftime(dateFormat), "\n")
        logFile.flush()

        s.start(board)
```

```
    time.sleep(secsPerCal+5)
    s.stop(board)

    s.writeData(board, " ")
    elapsed = s.getElapsedTime(board)
    numEvents = s.getElapsedCounts(board)
    for i in range(4):
        mcaName = dataName[0:-4] + "-b" + str(i) + ".mca"
        s.writeHist(i, mcaName)
        mcaList.append(mcaName)
        s.zeroHist(i)
    s.zeroTime(board)
    s.zeroCounts(board)
    print numEvents, " Events in ", elapsed, " seconds \n"
    sys.stdout.flush()
    logFile.write(print numEvents, " Events in ", elapsed, " seconds \n")
    logFile.flush()

# MUON Calibration
if muonRun == 1:
    syncCalIniFile = syncCalIniLocation + "100512-muon.ini"
    s.setPresetTime(board, secsPerMuCal)
    s.setPresetCounts(board, 0)
    s.setSkip(board, 10)
    s.zeroTime(board)
    s.zeroCounts(board)
    s.readIni(board, syncCalIniFile)
    if useDate:
        dataName = dataLocation + "Sync-" + date + ".dat"
    else:
        dataName = dataLocation + baseName + "-" + str(iters) + "_Sync.dat"
    fileList.append(dataName)
    s.writeData(board, dataName)
    print "\nStarting muon run ", str(iters), "at ", time.strftime(dateFormat), "\n"
    s.start(board)
    sys.stdout.flush()
    logFile.write("\nStarting muon run ", str(iters), "at ", time.strftime(dateFormat), "\n")
    logFile.flush()
    time.sleep(secsPerCal+5)
    s.stop(board)
    s.writeData(board, " ")
    elapsed = s.getElapsedTime(board)
    numEvents = s.getElapsedCounts(board)
    for i in range(4):
        mcaName = dataName[0:-4] + "-b" + str(i) + ".mca"
        s.writeHist(i, mcaName)
        mcaList.append(mcaName)
        s.zeroHist(i)
    s.zeroTime(board)
    s.zeroCounts(board)
    print numEvents, " Events in ", elapsed, " seconds \n"
    sys.stdout.flush()
    logFile.write(numEvents, " Events in ", elapsed, " seconds \n")
    logFile.flush()

for i in range(7):
    s.zeroTime(i)
    s.zeroCounts(i)
    s.setPresetTime(i, 0)
    s.setPresetCounts(i, 0)
    s.zeroHist(i)


# Data Run
s.setPresetTime(board, secsPerRun)
s.setPresetCounts(board, 0)
s.zeroTime(board)
s.zeroCounts(board)
iniFile = bgIniLocation + "121112-nCoord-twoLink-bareHe_NaI.ini"
s.readIni(board, iniFile)
s.setSkip(board, 100)
if useDate:
    dataName = dataLocation + "BG-" + date + ".dat"
else:
    dataName = dataLocation + baseName + "-" + str(iters) + ".dat"
fileList.append(dataName)
s.writeData(board, dataName)
print "\nStarting run ", str(iters), "at ", time.strftime(dateFormat), "\n"
logFile.write("\nStarting run " + str(iters) + "at " + time.strftime(dateFormat) + "\n")
logFile.flush()
s.send("start " + str(board))
sys.stdout.flush()

oldNumEvents = 0
for i in range(secsPerRun/10):
    numEvents = s.getElapsedCounts(board)
    elapsed = s.getElapsedTime(board)
    print repr(numEvents) + " recorded in " + repr(elapsed) + ' seconds\n'
    print 'Data rate = ' + repr((numEvents - oldNumEvents)/10.) + ' counts/s\n'
    sys.stdout.flush()
    logFile.write(repr(numEvents) + " recorded in " + repr(elapsed) + ' seconds\n')
```

```
            logFile.write('Data rate = ' + repr((numEvents - oldNumEvents)/10.) + ' counts/s\n')
            logFile.flush()
            oldNumEvents = numEvents
            time.sleep(10)
        time.sleep(secsPerRun%10 + 5)

        s.stop(board)
        s.writeData(board, " ")
        elapsed = s.getElapsedTime(board)
        numEvents = s.getElapsedCounts(board)
        for i in range(7):
            mcaName = dataName[0:-4] + "-b" + str(i) + ".mca"
            s.writeHist(i, mcaName)
            mcaList.append(mcaName)
            s.zeroHist(i)
        s.zeroTime(board)
        s.zeroCounts(board)
        print "Complete File: " + numEvents, " Events in ", elapsed, " seconds \n"
        sys.stdout.flush()
        logFile.write("Complete File: " + numEvents, " Events in ", elapsed, " seconds \n")
        logFile.flush()

        try:
            fileCompEmail(fileList,mcaList)
            emailSent = 1
        except:
            print "Cannot send email at " + str(time.strftime(dateFormat))
            print "Continuing with run."
            sys.stdout.flush()
            logFile.write("Cannot send email at " + str(time.strftime(dateFormat)) +
            logFile.write('Continuing with run')
            logFile.flush()
            emailSent = 0
logFile.close()
s.close()
```

Bibliography

[1] J. S. Nico *et al.*, Physical Review C **71**, 055502 (2005).

[2] J. S. Nico *et al.*, Nature **444**, 1059 (2006).

[3] M. Dewey *et al.*, Nuclear Instruments and Methods in Physics Research Section A: Accelerators, Spectrometers, Detectors and Associated Equipment **611**, 189 (2009).

[4] D. Pushin, M. Arif, M. Huber, and D. Cory, Physical Review Letters **100**, 250404 (2008).

[5] M. Huber *et al.*, Physical Review Letters **102**, 200401 (2009).

[6] A. Ioffe *et al.*, Physical Review A **58**, 1475 (1998).

[7] J. Byrne, *Neutrons, Nuclei and Matter: An Exploration of the Physics of Slow Neutrons* (Dover Publications, 2011).

[8] P. Harris *et al.*, Physical Review Letters **82**, 904 (1999).

[9] C. O'Shaughnessy *et al.*, Nuclear Instruments and Methods in Physics Research Section A: Accelerators, Spectrometers, Detectors and Associated Equipment **611**, 171 (2009).

[10] M. B. Chadwick *et al.*, Nuclear Data Sheets **112**, 2887 (2011).

[11] J. Beringer *et al.*, Physics Review D **86**, 10001 (2012).

[12] G. F. Knoll, *Radiation Detection and Measurement*, 2nd ed. ed. (Wiley, New York :, 1989).

[13] J. Chadwick, Nature **129**, 312 (1932).

[14] D. M. Mei, C. Zhang, and A. Hime, Nuclear Instruments and Methods in Physics Research Section A: Accelerators, Spectrometers, Detectors and Associated Equipment **606**, 651 (2009).

[15] D. Mei and C. Zhang, Neutron yield in materials, `http://neutronyield.usd.edu/`, 2013.

[16] J. W. Marxh, D. J. Thomas, and M. Burke, Nuclear Instruments and Methods in Physics Research Section A: Accelerators, Spectrometers, Detectors and Associated Equipment **366**, 340 (1995).

[17] T. F. Scientific, Neutron Generators, `http://www.thermoscientific.com/ecomm/servlet/productscatalog_11152_L11191_82242_-1_4`.

[18] NSD-Gradel-Fusion, 14.1 MeV Neutron Generators, http://www.nsd-fusion.com/14mev.php.

[19] I. Adelphi Technology, Neutron Generator Products, http://www.adelphitech.com/products/products_overview.html.

[20] C. Hagmann, D. Lange, and D. Wright, Cosmic-ray shower generator (CRY) for Monte Carlo transport codes, in *Nuclear Science Symposium Conference Record, 2007. NSS'07. IEEE* Vol. 2, pp. 1143–1146, IEEE, 2007.

[21] S. Roesler, W. Heinrich, and H. Schraube, Radiation research **149**, 87 (1998).

[22] S. Roesler, W. Heinrich, and H. Schraube, Radiation Protection Dosimetry **98**, 367 (2002).

[23] M. S. Gordon *et al.*, Nuclear Science, IEEE Transactions on **51**, 3427 (2004).

[24] T. Nakamura, T. Nunomiya, S. Abe, K. Terunuma, and H. Suzuki, Journal of Nuclear Science and Technology **42**, 843 (2005).

[25] H. Kornmayer, H. H. Mielke, J. Engler, and J. Knapp, Journal of Physics G: Nuclear and Particle Physics **21**, 439 (1995).

[26] W. Hess, H. Patterson, R. Wallace, and E. Chupp, Physical Review **116** (1959).

[27] M. KOWATARI *et al.*, Journal of Nuclear Science and Technology **42**, 495 (2005).

[28] M. Takada, K. Yajima, H. Yasuda, T. Sato, and T. Nakamura, Journal of Nuclear Science and Technology **47**, 932 (2010).

[29] K. Yajima and H. Yasuda, Radiation Measurements **45**, 1597 (2010).

[30] A. Bonardi, M. Aglietta, G. Bruno, W. Fulgione, and A. A. Bergamini Machado, Astroparticle Physics **34**, 225 (2010).

[31] N. Mascarenhas, J. Brennan, K. Krenz, P. Marleau, and S. Mrowka, IEEE Transactions on Nuclear Science **56**, 1269 (2009).

[32] M. Moser, J. Ryan, L. Desorgher, and E. Flückiger, Proceedings of the 29th International Cosmic Ray Conference. August 3-10 **2** (2005).

[33] D. F. Smart and M. A. Shea, Advances in Space Research **44**, 1107 (2009).

[34] E. Heidbreder, K. Pinkau, C. Reppin, and V. Schonfelder, Journal of Geophysical Research **76**, 2905 (1971).

[35] T. Luu and C. Hagmann, Lawrence Livermore National Laboratory Report No. UCRL-TR-226323, 2006 (unpublished).

[36] D. M. Mei and A. Hime, Physics Review D **73**, 53004 (2006).

[37] D. Measday, Physics Reports **354**, 243 (2001).

[38] M. Plett and S. Sobottka, Physical Review C **3**, 1003 (1971).

[39] S. R. Elliott, V. E. Guiseppe, B. H. LaRoque, R. A. Johnson, and S. G. Mashnik, Physics Review C **82**, 54610 (2010).

[40] D. M. Mei, S. R. Elliott, A. Hime, V. Gehman, and K. Kazkaz, Physics Review C **77**, 54614 (2008).

[41] D. Leonard *et al.*, Nuclear Instruments and Methods in Physics Research Section A: Accelerators, Spectrometers, Detectors and Associated Equipment **591**, 490 (2008).

[42] K. Adler *et al.*, Community Material Assay Database, `www.radiopurity.org`, 2013.

[43] V. E. Guiseppe, S. R. Elliott, N. E. Fields, and D. Hixon, (2012), 1209.4412.

[44] I. Barabanov *et al.*, Nuclear Instruments and Methods in Physics Research Section B: Beam Interactions with Materials and Atoms **251**, 115 (2006).

[45] J. F. Ziegler, IBM Journal of Research and Development **40** (1996).

[46] E. Kouzes, R. T. Aguayo, J. L. Orrell, D. J. Reid, and J. E. Fast, Pacific Northwest Nuclear Laboratory Report No. PNNL-21302, 2012 (unpublished).

[47] A. Gould, The Astrophysical Journal **321**, 571 (1987).

[48] G. Steigman and M. S. Turner, Nuclear Physics B **253**, 375 (1985).

[49] J. Angle *et al.*, Physical Review Letters **100**, 021303 (2008).

[50] V. Kudryavtsev, N. Spooner, and J. McMillan, Nuclear Instruments and Methods in Physics Research Section A: Accelerators, Spectrometers, Detectors and Associated Equipment **505**, 688 (2003).

[51] E. Armengaud *et al.*, Astroparticle Physics **47**, 1 (2013), arXiv:1305.3628v1.

[52] E. Tziaferi *et al.*, Astroparticle Physics **27**, 326 (2007).

[53] H. Wulandari, J. Jochum, W. Rau, and F. von Feilitzsch, arXiv preprint hep-ex/0401032 (2004), 0401032.

[54] E. Aprile *et al.*, (2013), 1306.2303.

[55] J. A. Formaggio and C. Martoff, Annual Review of Nuclear and Particle Science **54**, 361 (2004).

[56] Z. B. Yin, D. M. Mei, and S. Elliott, Nuclear Physics A **834**, 823c (2010).

[57] L. Reichhart *et al.*, A measurement of the muon-induced neutron yield in lead at a depth of 2850 m water equivalent, in *Low Radioactivity Techniques 2013* Vol. 219, pp. 219–222, 2013.

[58] V. Kozlov *et al.*, Astroparticle Physics **34**, 97 (2010).

[59] M. Aglietta and L. Collaboration, arXiv preprint hep-ex/9905047 , 1 (1999), 9905047v1.

[60] LVD Collaboration, arXiv preprint hep-ex/9905047 , 1 (1999), 9905047v1.

[61] R. Persiani, M. Garbini, G. Sartorelli, and M. Selvi, Measurement of the muon-induced neutron yield in liquid scintillator and stainless steel at LNGS with the LVD experiment, in *Low Radioactivity Techniques 2013* Vol. 235, pp. 235–238, 2013.

[62] H. Araújo *et al.*, Astroparticle Physics **29**, 471 (2008).

[63] V. Chazal *et al.*, Nuclear Instruments and Methods in Physics Research Section A: Accelerators, Spectrometers, Detectors and Associated Equipment **490**, 334 (2002).

[64] A. Lindote, H. Araújo, V. Kudryavtsev, and M. Robinson, Astroparticle Physics **31**, 366 (2009).

[65] S. Agostinelli *et al.*, Nuclear Instruments and Methods in Physics Research Section A: Accelerators, Spectrometers, Detectors and Associated Equipment **506**, 250 (2003).

[66] A. Thompson, personal communication, 2013.

[67] N. Magalotti, V. Lacoste, L. Lebreton, and V. Gressier, Radiation Protection Dosimetry **125**, 69 (2007).

[68] L. Lebreton, A. Zimbal, and D. Thomas, Radiation Protection Dosimetry **126**, 3 (2007).

[69] R. L. Bramblett and T. Bonner, Nuclear Physics **20**, 395 (1960).

[70] R. L. Bramblett, R. I. Ewing, and T. Bonner, Nuclear Instruments and Methods **9**, 1 (1960).

[71] C. Pioch, V. Mares, and W. Rühm, Radiation Measurements **45**, 1263 (2010).

[72] D. J. Thomas and A. V. Alevra, Nuclear Instruments and Methods in Physics Research Section A: Accelerators, Spectrometers, Detectors and Associated Equipment **476**, 12 (2002).

[73] D. Bartlett *et al.*, Nuclear Instruments and Methods in Physics Research Section A: Accelerators, Spectrometers, Detectors and Associated Equipment **476**, 386 (2002).

[74] M. Luszik-Bhadra, F. DErrico, O. Hecker, and M. Matzke, Nuclear Instruments and Methods in Physics Research Section A: Accelerators, Spectrometers, Detectors and Associated Equipment **476**, 291 (2002).

[75] B. Fisher *et al.*, Nuclear Instruments and Methods in Physics Research Section A: Accelerators, Spectrometers, Detectors and Associated Equipment **646**, 126 (2011).

[76] A. S. Ido, M. R. Bonyadi, G. R. Etaati, and M. Shahriari, Applied Radiation and Isotopes **67**, 1912 (2009).

[77] J. K. Dickens, Oak Ridge National Laboratory Report No. ORNL-6436, 1988 (unpublished).

[78] R. Koohi-Fayegh, S. Green, and M. C. Scott, Nuclear Instruments and Methods in Physics Research Section A: Accelerators, Spectrometers, Detectors and Associated Equipment **460**, 391 (2001).

[79] X. Yuan *et al.*, ArXiv e-prints (2013), 1304.7356.

[80] D. M. Drake, W. C. Feldman, and C. Hurlbut, Nuclear Instruments and Methods in Physics Research Section A: Accelerators, Spectrometers, Detectors and Associated Equipment **247**, 576 (1986).

[81] J. Czirr and G. L. Jensen, Nuclear Instruments and Methods in Physics Research Section A: Accelerators, Spectrometers, Detectors and Associated Equipment **284**, 365 (1989).

[82] J. N. Abdurashitov *et al.*, Nuclear Instruments and Methods in Physics Research Section A: Accelerators, Spectrometers, Detectors and Associated Equipment **476**, 318 (2002).

[83] C. Bass *et al.*, Applied Radiation and Isotopes **77**, 130 (2013).

[84] J. N. Abdurashitov *et al.*, Nuclear Instruments and Methods in Physics Research Section A: Accelerators, Spectrometers, Detectors and Associated Equipment **476**, 322 (2002).

[85] N. Zaitseva *et al.*, Nuclear Instruments and Methods in Physics Research Section A: Accelerators, Spectrometers, Detectors and Associated Equipment (2011).

[86] J. B. Birks, Proceedings of the Physical Society. Section A **64**, 874 (1951).

[87] R. L. Craun and D. L. Smith, Nuclear Instruments and Methods **80**, 239 (1970).

[88] G. V. O'Rielly, N. R. Kolb, and R. E. Pywell, Nuclear Instruments and Methods in Physics Research Section A: Accelerators, Spectrometers, Detectors and Associated Equipment **368**, 745 (1996).

[89] M. Berger, J. Coursey, M. Zucker, and J. Chang, Stopping-power and range tables for electrons, protons, and helium ions, `http://www.nist.gov/pml/data/star/index.cfm`, 2011.

[90] A. Enqvist, C. C. Lawrence, B. M. Wieger, S. A. Pozzi, and T. N. Massey, Nuclear Instruments and Methods in Physics Research Section A: Accelerators, Spectrometers, Detectors and Associated Equipment **715**, 79 (2013).

[91] N. S. Bowden *et al.*, Nuclear Instruments and Methods in Physics Research Section A: Accelerators, Spectrometers, Detectors and Associated Equipment **609**, 32 (2009).

[92] R. Batchelor, R. Aves, and T. H. R. Skryme, Review of Scientific Instruments **26**, 1037 (1955).

[93] W. R. Mills, R. I. Caldwell, and I. L. Morgan, Review of Scientific Instruments **33**, 866 (1962).

[94] A. Sayres and M. Coppola, Review of Scientific Instruments **35**, 431 (1964).

[95] A. Izumi and Y. Murata, Nuclear Instruments and Methods **94**, 141 (1971).

[96] D. Sim, `en.wikipedia.org/wiki/File:Detector_regions.gif`.

[97] N. Takeda and K. Kudo, IEEE Transactions of Nuclear Science **42**, 548 (1995).

[98] J. F. Ziegler, M. D. Ziegler, and J. P. Biersack, Nuclear Instruments and Methods in Physics Research Section B: Beam Interactions with Materials and Atoms **268**, 1818 (2010).

[99] H. H. Andersen, J. F. Ziegler, J. P. Biersack, and U. Littmark, *The Stopping and Ranges of Ions in Matter* (Pergamon Press, 1977).

[100] W. R. Leo, *Techniques for Nuclear and Particle Physics Experiments: A How-To Approach*, 2nd ed. ed. (Springer-Verlag, 1994).

[101] B. Beltran *et al.*, New Journal of Physics **13**, 73006 (2011).

[102] T. Langford *et al.*, Nuclear Instruments and Methods in Physics Research Section A: Accelerators, Spectrometers, Detectors and Associated Equipment **717**, 51 (2013).

[103] K. M. Heeger *et al.*, IEEE Transactions of Nuclear Science **47**, 1829 (2000).

[104] J. Leake, S. Croft, R. McElroy, and K. Lambert, Optimizing ^{3}He tube design for various operational conditions: A review of the design parameters of ^{3}He gas proportional counters used for neutron detection, www.canberra.com/pdf/Literature/optHe-3tubes-Paper.pdf, 2007.

[105] T. Gooding and H. Pugh, Nuclear Instruments and Methods **7**, 189 (1960).

[106] J. A. Grundl *et al.*, Nuclear Technology **32**, 315 (1977).

[107] P. Finnerty *et al.*, Nuclear Instruments and Methods in Physics Research Section A: Accelerators, Spectrometers, Detectors and Associated Equipment **642**, 65 (2010), 1007.0015.

[108] B. A. Raue *et al.*, Physical Review **C53**, 1005 (1996).

[109] GaGe Applied Technology, Octopus CompuScope 82XX, www.gage-applied.com/digitizers/GaGe-Digitizer-OctopusCS82XX-PCI-PCIe-Data-Sheet.pdf.

[110] P. Wiener and B. Corp., MPOD Mini, http://www.wiener-d.com/products/46/91.html.

[111] Iseg High Voltage, EHS High Voltage Modules, http://www.iseg-hv.com/en/products/product-details/product/21/.

[112] Wavemetrics, IGOR Pro, http://www.wavemetrics.com/products/igorpro/igorpro.htm.

[113] W. Mannhart and F. R. Braunschweig, Physics of Neutron Emission in Fission , 305 (1989).

[114] S. A. Pozzi, J. A. Mullens, and J. T. Mihalczo, Nuclear Instruments and Methods in Physics Research Section A: Accelerators, Spectrometers, Detectors and Associated Equipment **524**, 92 (2004).

[115] L. Linpei, Radiation Protection Dosimetry **5**, 227 (1983).

[116] R. B. Schwartz and C. M. Eisenhauer, Radiation Protection Dosimetry **55**, 99 (1994).

[117] JEDEC Solid State Technology Association Report No. JESD89A, 2006 (unpublished).

[118] M. Reginatto, P. Goldhagen, and S. Neumann, Nuclear Instruments and Methods in Physics Research Section A: Accelerators, Spectrometers, Detectors and Associated Equipment **476**, 242 (2002).

[119] L. Pibida, M. Unterweger, and L. Karam, Applied Radiation and Isotopes **64**, 1271 (2006).

[120] C. Aalseth *et al.*, Nuclear Instruments and Methods in Physics Research Section A: Accelerators, Spectrometers, Detectors and Associated Equipment **652**, 692 (2011).

[121] C. Grieb *et al.*, Nuclear Physics B - Proceedings Supplements **221**, 349 (2011).

[122] J. Xu *et al.*, p. 21 (2012), 1204.6011.

[123] M. F. Kidd, J. H. Esterline, and W. Tornow, Bulletin of the American Physical Society **55**, 1 (2010).

[124] Omega Engineering, Inc., 8-Channel USB Thermocouple Data Acquisition Module, `http://www.omega.com/DAS/pdf/TC-08.pdf`, 2013.

[125] Omega Engineering, Inc., Real-Time Temperature and Humidity Monitor, `http://www.omega.com/DAS/pdf/OM-EL-USB-RT.pdf`, 2013.

[126] N. Johnson, private communication, 2011.

[127] Eljen Technologies, EJ-200 Plastic Scintillator, `http://eljentechnology.com/index.php/products/plastic-scintillators/48-ej-200`.

[128] E. T. Enterprises, XP2262, `http://my.et-enterprises.com/pdf/XP2262.pdf`.

[129] V. Popov, Nuclear Instruments and Methods in Physics Research Section A: Accelerators, Spectrometers, Detectors and Associated Equipment **505**, 316 (2003).

[130] D. Androić *et al.*, Nuclear Instruments and Methods in Physics Research Section A: Accelerators, Spectrometers, Detectors and Associated Equipment **646**, 59 (2011).

[131] D. S. Armstrong *et al.*, Physics Review Letters **95**, 92001 (2005).

[132] P. Components, *Photomultipliers Data Handbook* (Phillips, 1990).

[133] S. Williamson, GuideM Light Propagation Simulation.

[134] H. Breuer, personal communication, 2013.

[135] 80/20 Inc., 80/20 Product Catalog, `www.8020.net`.

[136] Shieldwerx, Flexi-Boron SWX-238, `http://www.shieldwerx.com/assets/swx-238.pdf`.

[137] CAEN Technologies INC, A1422 Digitizer, `http://www.caen.it/csite/CaenProd.jsp?parent=13&idmod=604`.

[138] CAEN Technologies INC, V1720 Digitizer, `http://www.caen.it/csite/CaenProd.jsp?parent=11&idmod=570`.

[139] H. W. Bertini, Nuclear Physics **87**, 138 (1966).

[140] L. S. Waters, Los Alamos National Laboratory (2002).

[141] D. M. Gilliam, A. T. Yue, and M. S. Dewey, Calibration of a manganese bath relative to 252Cf nu-bar, in *Reactor Dosimetry State of the Art 2008 - Proceedings of the 13th International Symposium* Vol. 1, pp. 361–367, Singapore, 2009, World Scientific Publishing Co. Pte. Ltd.

[142] J. M. Adams, Nuclear Instruments and Methods in Physics Research Section B: Beam Interactions with Materials and Atoms **213**, 218 (2004).

[143] National Institute of Standards and Technology, Neutron Source Strength Calibrations, `www.nist.gov/pml/div682/grp03/neutron-source-calibrations.cfm`.

[144] L. Pibida, C.Heimbach, B.Norman, A. Thompson, and S.Dewey, NIST Technical Note **1788** (2013).

[145] D. Gilliam, personal communication, 2013.

[146] International Atomic Energy Agency, *Neutron Generators for Analytical Purposes*IAEA Radiation Technology Reports (International Atomic Energy Agency, 2012).

[147] J. Simpson, personal communication, 2013.

[148] J. Reijonen *et al.*, Nuclear Instruments and Methods in Physics Research Section A: Accelerators, Spectrometers, Detectors and Associated Equipment **522**, 598 (2004).

[149] D. L. Chichester, J. D. Simpson, and M. Lemchak, Journal of Radioanalytical and Nuclear Chemistry **271**, 629 (2007).

[150] CAEN Technologies, Inc., CAEN Technologies Inc. Report No. AN2506, 2012 (unpublished).

[151] M. Nakhostin, Nuclear Instruments and Methods in Physics Research Section A: Accelerators, Spectrometers, Detectors and Associated Equipment **672**, 1 (2012).

[152] F. Brooks and H. Klein, Nuclear Instruments and Methods in Physics Research Section A: Accelerators, Spectrometers, Detectors and Associated Equipment **476**, 1 (2002).

[153] J. N. Abdurashitov *et al.*, (2006), nucl-ex/0607024.

[154] T. F. Scientific, P385 Neutron Generator Operational Manual, 2010.

[155] SEU Test, Flux Calculation, http://www.seutest.com/cgi-bin/FluxCalculator.cgi.

[156] H. W. Dodson, E. R. Hedeman, and O. C. Mohler, Reviews of Geophysics **12**, 329 (1974).

[157] D. H. Hathaway, Solar cycle prediction, solarscience.msfc.nasa.gov/predict.shtml.

[158] F. Boehm *et al.*, Physics Review D **64**, 112001 (2001).

[159] R. Hertenberger, M. Chen, and B. L. Dougherty, Physics Review C **52**, 3449 (1995).

[160] L. B. Bezrukov, V. I. Beresnev, O. G. Ryajskaya, L. N. Stepanets, and G. T. Zatsepin, Investigation of Depth-Intensity Curve of Nuclear Events Induced by Muons, in *International Cosmic Ray Conference* Vol. 3, p. 1947, 1973.

[161] Weather Underground Inc., Weather History for KMIEASTL10, http://www.wunderground.com/weatherstation/WXDailyHistory.asp?ID=KMIEASTL10.

[162] J. A. Lockwood and H. E. Yingst, Physical Review **104**, 1718 (1956).

[163] H. Carmichael and M. Bercovitch, Canadian Journal of Physics **47**, 2073 (1969).

[164] L. I. Dorman, *Cosmic rays: variations and space explorations, Volume 1* (North-Holland, 1974).

[165] J. M. Clem and L. I. Dorman, Neutron monitor response functions, in *Cosmic Rays and Earth*, pp. 335–359, Springer, 2000.

[166] C. T. Steigies, NMDB Event Search Tool (NEST), www.nmdb.eu/nest/search.php, 2013.

[167] C. T. Steigies, Neutron Monitor Database (NMDB), www.nmdb.eu, 2013.

[168] P. Paschalis *et al.*, New Astronomy **19**, 10 (2013).

[169] R. Chasman, Physical Review **122**, 902 (1961).

[170] P. Goldhagen *et al.*, Nuclear Instruments and Methods in Physics Research Section A: Accelerators, Spectrometers, Detectors and Associated Equipment **476**, 42 (2002).

[171] J. F. Ziegler, IBM Journal of Research and Development **42**, 117 (1998).

[172] K. M. Heeger, B. R. Littlejohn, and H. P. Mumm, (2013), 1307.2859.

[173] Z. Djurcic *et al.*, (2013), 1309.7647.

[174] F. Boehm *et al.*, Physical Review D **62**, 92005 (2000).